THE UNIVERSITY OF QUEENSLAND

AUSTRALIA

Investigation of using firing time renewal processes for modelling and analysis of single point microelectrode recordings of the subthalamic nucleus.

Kristian James Weegink

B. Sci. Physics (Hons I), B. Sci. Chemistry

A thesis submitted for the degree of Doctor of Philosophy at

The University of Queensland in 2018

School of Mechanical & Mining Engineering

Abstract

Microelectrode recordings (MER) involve insertion of an electrode, approximately 50 micrometers at the tip, into deep brain structures and recording the electrical activity. It is commonly used in surgeries to accurately determine the location of a target for deep brain stimulation (DBS). A common target for this type of procedure is the subthalamic nucleus (STN), identified by a unique spiking pattern and a change in the background noise level compared to surrounding structures. This change in background noise level indicates that the noise is composed of neuronal sources.

This thesis aims to develop a model to determine what extent the volume of neurons around the electrode contribute to an MER. The potential usefulness of the model as a biomarker for the behaviour of the STN is then explored. The model for the STN MER involves simulating thousands of neurons by assuming they follow a renewal process. This assumption requires that the timing between a single neuron's spikes (inter-spike interval - ISI) are independent and identically distributed (IID). The model is tuned to intraoperative recordings to determine the best simulation parameters. To investigate the usefulness of the model as a biomarker of STN behaviour, the IID assumption is relaxed by introducing synchronization between neurons or changing their spike timings to be driven by a dynamical model of the basal ganglia. Fitting the parameters of the renewal process model to these extended models is then used to see if they can reliably describe the new behaviour.

The results show firstly that a volume of ~1mm^3, or on the order of 10,000 neurons, are required to simulate an STN MER that best describes patient data. This result indicates that the background noise of MERs is in fact partly caused by neuronal sources. The speed of the renewal model, faster than real time, allowed many simulations ($O(10^6)$) with different parameters to be created for tuning and verification of the model. The Weibull distribution is used as a parameterized ISI distribution for the renewal model and was found to reliably describe the simulations when the IID assumptions were relaxed. The first example of this was when neurons had synchronized firing times. In this case the Weibull distribution reliably fit the underlying ISI distribution for different realizations of the same simulation parameters. Finally, the thesis shows that using a neural mass model of the basal ganglia to generate the STN firing times, that the renewal model can differentiate between certain cortical inputs. This motivates future investigation into using the parameters from fitting a renewal model to an MER as biomarkers.

Declaration by author

This thesis is composed of my original work, and contains no material previously published or written by another person except where due reference has been made in the text. I have clearly stated the contribution by others to jointly-authored works that I have included in my thesis.

I have clearly stated the contribution of others to my thesis as a whole, including statistical assistance, survey design, data analysis, significant technical procedures, professional editorial advice, financial support and any other original research work used or reported in my thesis. The content of my thesis is the result of work I have carried out since the commencement of my higher degree by research candidature and does not include a substantial part of work that has been submitted to qualify for the award of any other degree or diploma in any university or other tertiary institution. I have clearly stated which parts of my thesis, if any, have been submitted to qualify for another award.

I acknowledge that an electronic copy of my thesis must be lodged with the University Library and, subject to the policy and procedures of The University of Queensland, the thesis be made available for research and study in accordance with the Copyright Act 1968 unless a period of embargo has been approved by the Dean of the Graduate School.

I acknowledge that copyright of all material contained in my thesis resides with the copyright holder(s) of that material. Where appropriate I have obtained copyright permission from the copyright holder to reproduce material in this thesis and have sought permission from co-authors for any jointly authored works included in the thesis.

Publications during candidature

Theoretical & Experimental Analysis of the Non-Markov Parameter to Detect Low Frequency Synchronisation in Time Series Analysis. (2011), John J. Varghese, Kristian J. Weegink, Paul A. Bellette, Terry Coyne, Peter A. Silburn, and Paul A. Meehan, Proceedings of the 33rd Annual International Conference of the IEEE EMBS, Boston, Massachusetts USA, August 30-September 3 2011, pp. 1500-1505. doi:10.1109/IEMBS.2011.6090743

Simulating micro electrode recordings from deep brain surgery for applications in a clinical framework. (2011), Kristian J. Weegink, John J. Varghese, Paul A. Bellette, Terry Coyne, Peter A. Silburn, and Paul A. Meehan, Abstracts of WFN XIX World Congress on Parkinson's Disease and Related Disorders. WFN XIX World Congress on Parkinson's Disease and Related Disorders, Shanghai, China, pp S225-S225. 1114 December 2011. doi:10.1016/S1353-8020(11)70957-9

An efficient stochastic based model for simulating microelectrode recordings of the deep brain. (2012), Kristian J. Weegink, John J. Varghese, Paul A. Bellette, Terry Coyne, Peter A. Silburn, and Paul A. Meehan, Proceedings of Biosignals 2012, International Conference on Bio-Inspired Systems and Signal Processing. 5th International Joint Conference on Biomedical Engineering Systems and Technologies (BIOSTEC), Vilamoura, Portugal, pp 76-84. 1-4 February 2012.
ISBN 9789898425898

Analysis of the non-Markov parameter in continuous-time signal processing. (2015), John J. Varghese, Paul A. Bellette, Kristian J. Weegink, Andrew P. Bradley, Paul A. Meehan, Phys. Rev. E., vol 89(2), p. 022109, 2015.
doi:10.1103/PhysRevE.89.022109

Spectral properties of neuronal pulse interval modulation. (2015), John J. Varghese, Kristian J. Weegink, Paul A. Bellette and Andrew P. Bradley, 2015 IEEE International Conference on Acoustics, Speech, and Signal Processing: Proceedings. International Conference on Acoustics, Speech, and Signal Processing (ICASSP) Conference, Brisbane, QLD, Australia, (1007-1011). 19-24 April 2015.

doi:10.1109/ICASSP.2015.7178121

Spikes from compound action potentials in simulated microelectrode recordings. (2015), Kristian J. Weegink, John J. Varghese, and Andrew P. Bradley, 2015 IEEE International Conference on Acoustics, Speech and Signal Processing (ICASSP). 2015 International Conference on Acoustics, Speech and Signal Processing, South Brisbane, QLD, Australia, pp 813-816. 19-24 April 2015. doi:10.1109/ICASSP.2015.7178082

A Parametric Simulation of Neuronal Noise from Microelectrode Recordings. (2016), Kristian J. Weegink, Paul A. Bellette, John J. Varghese, Peter A. Silburn, Paul A. Meehan and Andrew P. Bradley, IEEE Transactions on Transactions on Neural Systems and Rehabilitation Engineering, Vol 25, no. 1, pp 4-13, Jan. 2017. doi:10.1109/TNSRE.2016.2573318

Publications included in this thesis

Paper A. *An efficient stochastic based model for simulating microelectrode recordings of the deep brain.* (2012), Kristian J. Weegink, John J. Varghese, Paul A. Bellette, Terry Coyne, Peter A. Silburn, and Paul A. Meehan, Proceedings of Biosignals 2012, pp 76-84. 1-4 February 2012 – incorporated into Chapters 3 and 4.

Contributor	Statement of contribution
Kristian Weegink (Candidate)	Conception and design (60%) Analysis and interpretation (65%) Drafting and production (70%)
John Varghese	Conception and design (0%) Analysis and interpretation (10%) Drafting and production (10%)
Paul Bellette	Conception and design (10%) Analysis and interpretation (10%) Drafting and production (5%)
Terry Coyne	Conception and design (10%) Analysis and interpretation (0%) Drafting and production (0%)
Peter Silburn	Conception and design (10%) Analysis and interpretation (5%) Drafting and production (5%)
Paul Meehan	Conception and design (10%) Analysis and interpretation (10%) Drafting and production (10%)

Paper B. *Spikes from compound action potentials in simulated microelectrode recordings.* (2015), Kristian J. Weegink, John J. Varghese, and Andrew P. Bradley, 2015 IEEE International Conference on Acoustics, Speech and Signal Processing (ICASSP). 2015 International Conference on Acoustics, Speech and Signal Processing, South Brisbane, QLD, Australia, pp 813-816. 19-24 April 2015 – incorporated into Chapters 3 and 4.

Contributor	Statement of contribution
Kristian Weegink (Candidate)	Conception and design (80%) Analysis and interpretation (80%) Drafting and production (80%)
John Varghese	Conception and design (0%) Analysis and interpretation (10%) Drafting and production (10%)
Andrew Bradley	Conception and design (20%) Analysis and interpretation (10%) Drafting and production (10%)

Paper C. *A Parametric Simulation of Neuronal Noise from Microelectrode Recordings.* (2016), Kristian J. Weegink, Paul A. Bellette, John J. Varghese, Peter A. Silburn, Paul A. Meehan and Andrew P. Bradley, IEEE Transactions on Transactions on Neural Systems and Rehabilitation Engineering, Vol 25, no. 1, pp 4-13, Jan. 2017 – incorporated into Chapters 3 and 4.

Contributor	Statement of contribution
Kristian Weegink (Candidate)	Conception and design (60%) Analysis and interpretation (65%) Drafting and production (60%)
John Varghese	Conception and design (0%) Analysis and interpretation (10%) Drafting and production (10%)
Paul Bellette	Conception and design (10%) Analysis and interpretation (10%) Drafting and production (5%)
Peter Silburn	Conception and design (10%) Analysis and interpretation (5%) Drafting and production (5%)
Paul Meehan	Conception and design (10%) Analysis and interpretation (5%) Drafting and production (5%)
Andrew Bradley	Conception and design (10%) Analysis and interpretation (10%) Drafting and production (10%)

Paper D. *Bayesian Approach for Stationary Analysis of Microelectrode Recordings Using a Neural Mass Model of the Basal Ganglia.* (2018), Kristian J. Weegink, Paul A. Bellette, John J. Varghese, Andrew P. Bradley and Paul A. Meehan, submitted to IEEE Transactions on Biomedical Engineering, 2018 – incorporated into Chapters 3 and 4.

Contributor	Statement of contribution
Kristian Weegink (Candidate)	Conception and design (90%) Analysis and interpretation (70%) Drafting and production (75%)
John Varghese	Conception and design (0%) Analysis and interpretation (10%) Drafting and production (10%)
Paul Bellette	Conception and design (5%) Analysis and interpretation (10%) Drafting and production (5%)
Paul Meehan	Conception and design (0%) Analysis and interpretation (5%) Drafting and production (5%)
Andrew Bradley	Conception and design (5%) Analysis and interpretation (5%) Drafting and production (5%)

Contributions by others to the thesis

Paul A. Meehan and Andrew P. Bradley provided assistance with drafting and revisions of the thesis to contribute to the interpretation. John J. Varghese and Paul A. Bellette offered insight in interpretation of the results.

Statement of parts of the thesis submitted to qualify for the award of another degree

None

Research Involving Human or Animal Subjects

No animal or human subjects were involved in this research.

Acknowledgements

This thesis was made possible only because of the help and support of numerous people who I would like to thank for their contributions.

Paul Meehan: Thank you for your supervision, making the project possible, always making time for meetings and all the time spent reviewing the various iterations of my thesis.

Andrew Bradley: Thanks for your supervision, support and countless hours reviewing papers and my thesis, along with all the time you made available for me to ask technical, strategic and administrative questions.

Paul Bellette: Without your technical help and supervision, I doubt much of what I did would have happened. Thanks for all your time and brain power, as well as your encouragement and friendship.

John Varghese: You had no vested interest in this thesis except our friendship, but you still pushed me to get it completed. I would not have a thesis if you did not constantly check up on me and provide perspective and advice. I cannot thank you enough for all your help.

Miranda Goodwin: You absorbed so much of my projected stress and self-doubt that made completing this possible. Thank you for all your support and for putting up with my crazy adventures.

My Family and friends: Thanks to you all for your support. I would particularly like to thank my Mum and Dad for raising me and giving me every opportunity.

Financial support

This research was supported by an Australian Government Postgraduate Award Scholarship and a UQ Advantage Scholarship

Medtronic also provided support through a top up scholarship.

Keywords

Micro Electrode Recording, subthalamic nucleus, STN MER, neural signal processing, spectral analysis, filtered point process, renewal process, deep brain stimulation, neural mass model, biomarkers

Australian and New Zealand Standard Research Classifications (ANZSRC)

ANZSRC code: 090304, Medical Devices, 30%

ANZSRC code: 010406, Stochastic Analysis and Modelling, 40%

ANZSRC code: 010202, Biological Mathematics, 30%

Fields of Research (FoR) Classification

FoR code: 0903, BIOMEDICAL ENGINEERING, 30%

FoR code: 0104, STATISTICS, 40%

FoR code: 0102, APPLIED MATHEMATICS, 30%

Table of Contents

List of Figures and Tables

List of Abbreviations

AP – Action potential

BG – Basal ganglia

CDF – Cumulative distribution function

CAP – Compound action potential

CoV – Cofficient of variation

Ctx – Cortex

DBS – Deep brain stimulation

EAP – Extracellular action potential

EEG – Electroencephalogram

EM – Electromagnetic

FPP – Filtered point process

GPi – Globus palidus internal

GPe – Glodus palidu external

IID – Independent identically distributed

ISI – Interspike interval

KDE – Kernel density estimate

KS - Kolmogorov-Smirnov

LFP – Local field potential

MER – Mircoelectrode recording

NMP – Non-Markov parameter

ODE – Ordinary differential equation

OU – Ornstein–Uhlenbeck

PD – Parkinson’s disease

PDE – Partial differential equation

PDF – Probability density function

PSD – Power spectral density

RMS – Root mean squared

SNr – Substantia niagra pars reticulate

STN – Subthalamic nucleus

SUA – Single unit activity

1 Introduction

This thesis is a compilation of work completed during the investigation using firing time renewal processes for modelling and analysis of single point microelectrode recordings of the subthalamic nucleus. It is presented as a summary of the work completed for the thesis along with publications based on this work. First details of the background, motivation and aims is presented. A literature summary is then provided to identify the current state of the art in the field and how the work presented in this thesis builds on this. Subsequently, a summary of the publications made during the research for this thesis is provided. The methods used for the investigation are summarised and an overview of the results are then given. The conclusions of this work are presented in the final chapter along with limitations, future work and the novel contributions of the thesis. In addition to this summary of work, complete copies of the published works are provided in the appendix. All code used for this thesis is also available in the appendix and online (Weegink, 2017). This thesis presents a concise description of the work performed and includes full details for replication of the work available to enable further research using this foundation.

Contained in the rest of this section is a more descriptive outline of the thesis. This outline includes a summary of the background and motivation for performing the work within this thesis. The chapter concludes by defining the scope and objectives of this work.

1.1 Background and motivation

Decoding how neurons carry information is not just a question of philosophy but biological importance, as it can be used to create brain interfaces, characterize pathological processes or to diagnose disease (Reike, et al., 1997) (Bialek, et al., 1999) (Rouse, et al., 2011) (Hosain, et al., 2014) (Remple, et al., 2011). Detecting when a patient enters a diseased state would allow treatment to be tuned to when it is needed, a prime example of this is deep brain stimulation (DBS) where treatment is moving towards intelligent systems that use adaptive stimulus (Priori, et al., 2013) (Little, et al., 2013) (Hosain, et al., 2014) (Rouse, et al., 2011). This type of treatment could reduce side effects and improve the efficiency of the treatment.

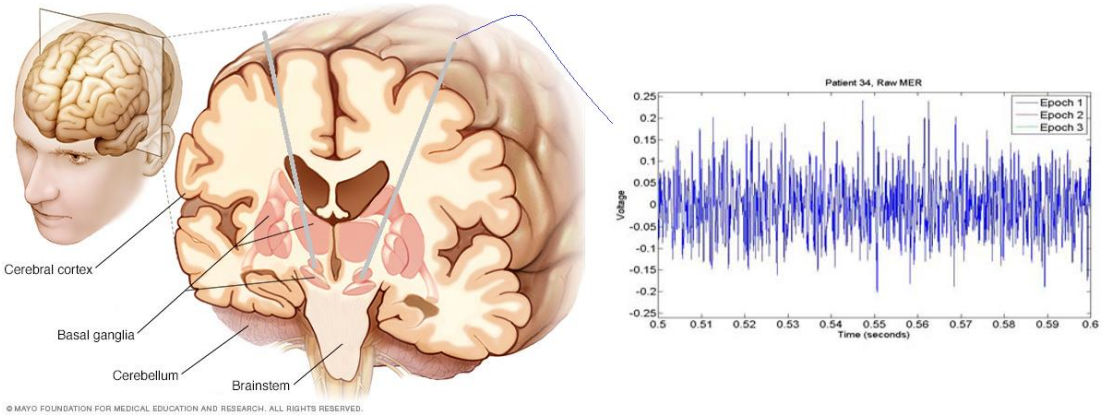

Figure 1 - The position of the microelectrodes when placed in the sub thalamic nucleus for DBS treatment of PD. The graph demonstrates a typical MER used in this thesis (adapted from (Mayo Foundation for Medical Education and Research (MFMER), 2017)).

Deep brain stimulation (DBS) is used to treat chronic neuro-psychological disorders by applying a localized current to a specific structure of the brain. A common disease treated with DBS is Parkinson's disease (PD) (Davie, 2008). Currently patients who are treated with DBS receive open-loop stimulation, where the stimulation is constant and adjustments are made in clinical visits (Moro, et al., 2006). To improve the positive outcomes of DBS, decrease the side effects and to increase the battery life, closed-loop stimulation (also known as adaptive DBS) is being developed (Rouse, et al., 2011) (Chen & al., 2010) (Parastarfeizabadi & Kouzani, 2017) (Priori, et al., 2013) (Little, et al., 2013) (Hosain, et al., 2014) (Rouse, et al., 2011). An overview of these two methods is shown in Figure 2. For adaptive DBS to work a biomarker, or combination of biomarkers, is required that indicates when the patient is in a normal or abnormal state (Eusebio & Brown, 2009) (Rouse, et al., 2011) (Chen & al., 2010). Biomarkers can range from accelerometers on limbs monitoring tremor or gait, micro-electrodes monitoring single cell behaviour to macro-electrodes monitoring large scale brain dynamics (Akingba & al., 2003) (Eusebio & Brown, 2009) (Hosain, et al., 2014) (Rouse, et al., 2011).

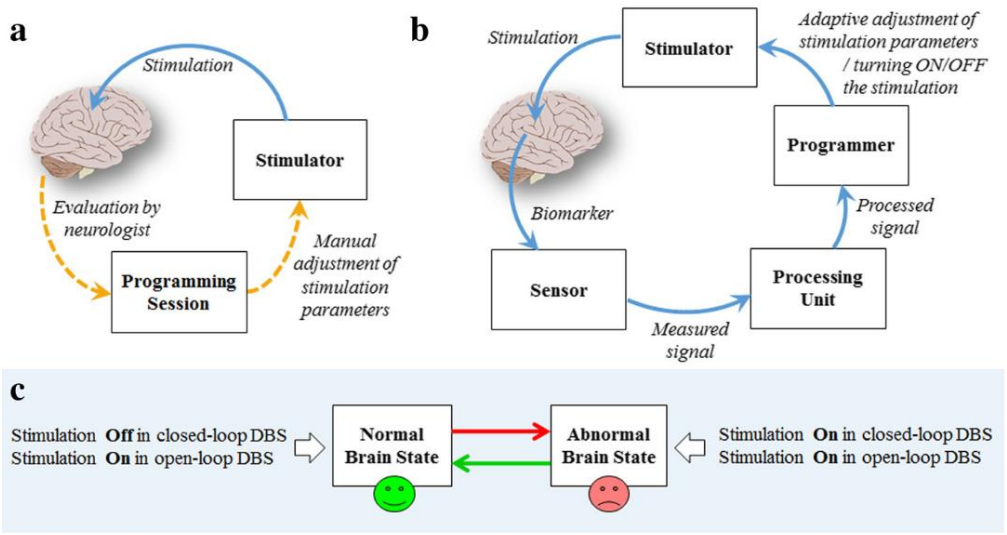

Figure 2 - Comparison of open and closed-loop DBS. a) The current method for tuning DBS for individual patients involves a trained clinician adjusting the settings of the stimulator during clinical visits. b) In closed-loop, also known as adaptive DBS, by detecting a biomarker that indicates an abnormal state the stimulator automatically adjusts the stimulation parameters. c) An example of a benefit of closed-loop DBS where the stimulation is only applied when it is needed, opposed to constant application in open-loop. From (Parastarfeizabadi & Kouzani, 2017).

Due to the invasiveness and dangers involved, there are very few opportunities to obtain electrical recordings from deep within the human brain. Deep brain recordings of extracellular activity using microelectrodes, Figure 3, are used to locate brain structures in surgeries to implant deep brain stimulation systems. The treatment involves localizing the subthalamic nucleus (STN) within the basal ganglia (BG) deep inside the brain using a combination of imagery and microelectrode recordings (MER) (Coyne, et al., 2006). The role of the MER is to assist the clinical team in identifying the target structure. By using their experience, the team can recognize the unique patterns of the STN by observing the spiking intensity, rate and background noise patterns (Camalier, et al., 2014) (Baker & al, 2004) (Burchiel & Israel, 2004) (Coyne, et al., 2006) (Snellings, et al., 2009).

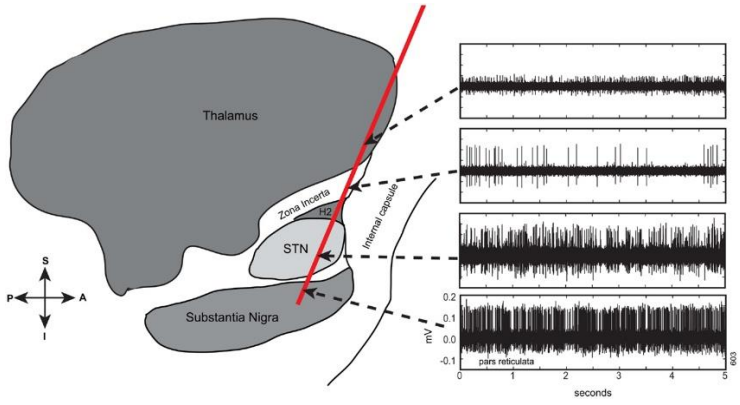

Figure 3 - Examples of how the spiking activity and the background noise changes as the MER enters different structures in the Basal Ganglia (Camalier, et al., 2014).

Extracellular recordings of the electrical activity have been used to determine brain functions since the invention of the microelectrode in 1921 (Israel & Schulder, 2004). MERs have been used to investigate *in vivo* neuron firing in animals and humans (Israel & Schulder, 2004). They have been used to locate different brain structures, map the somatotopy of motor and sensory structures within the brain and characterize the different firing rates and the firing patterns in healthy and diseased models (Israel & Schulder, 2004). These findings have led to the development of many methods of analysis and modelling of the electrode recordings. These models however fail to address the change in background noise, Figure 4, that neurologists can use to identify the STN.

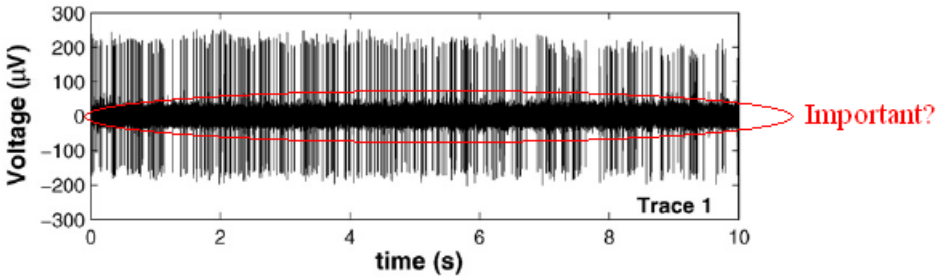

Figure 4 – A typical STN MER recording showing the spiking activity from the closest neuron and the background noise (circled in red) that neurologist may use to identify the location of the MER. Adapted from (Theodosopoulos, et al., 2004).

MERs are analysed by looking at the spiking behaviour of a single neuron that is recorded (Burchiel & Israel, 2004). A typical MER, shown in Figure 4, contains a strong spiking signal from the closest neuron/s and noise that can have maximum amplitude of 10-50% of the spiking amplitude (Heinricher, 2004) (Garonzik, et al., 2004). Figure 5 shows how an MER consists of the contribution of slow oscillations from the neurons located further from the electrode, known as the local field potential (LFP), as well as high frequency spikes from close neurons (Garonzik, et al., 2004) (Akingba & al., 2003). The recordings are filtered to remove the LFP, leaving the strong spikes and high frequency noise (Medtronic Inc., Minneapolis, MN) (Garonzik, et al., 2004) (Rasch, et al., 2009). The change in this high frequency noise with the electrode position leads to the possibility of the neurons in the LFP zone still contributing in the high frequency. The possibility of this background noise having a neuronal component means that MERs could be used as a biomarker of the collective behaviour of a group of neurons, instead of only targeting a single neuron. This raises the first question of the work performed for this thesis: What range do the neurons further from the electrode contribute to the MER background noise?

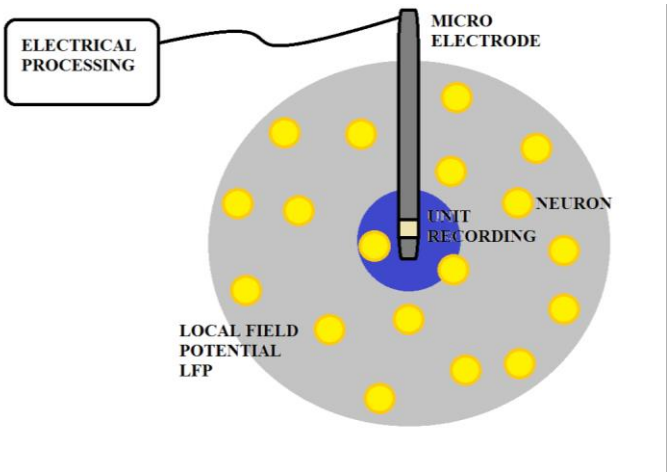

Figure 5 – How neurons contribute to an MER. The dark area represents the neurons that produce a strong spiking signal on the recording (unit recording) and the light gray area represents the neurons that contribute to the LFP.

Most theoretical efforts thus far have analyzed and modeled the recordings with high impedance electrodes for single-cell electrical activity (Burchiel & Israel, 2004) (Favre & Baumann, 2004) (Sarma & al., 2010) (Pedoto, et al., 2012) (Michmizos & Nikita, 2012). The analysis techniques involve isolating the firing times of individual neurons identifiable in the recording. These times can then be used to identify the statistics of the individual cell, or they can be compared to a stimulus or another recording to determine correlations. This type of analysis using a single electrode restricts the scope to a small number of neurons, one to three. To model these types of recordings nonlinear neuron models are used. These nonlinear models can be computationally expensive, thus restricting simulations to a small number of neurons, single to hundreds. To be able to answer the question of how neurons contribute to the background noise of the STN MER models of potentially on the order of 10^5 neurons may be required. The types of models discussed so far are unsuitable for this, therefore stochastic models will be used, specifically renewal process models. The renewal process characterizes the neurons by using a probability distribution to describe the interval between spike events, raising the second question addressed by this thesis: Can fitting the inter-spike interval probability distribution of renewal models to STN MERs be used as a potential biomarker?

With the increasing usage of DBS as a tool for treatment, the chance to explore the electrical activity of the deep brain becomes accessible. It is the purpose of this thesis that by modelling firing times as renewal processes simulations of STN MERs can be generated from tens of thousands of neurons. These models can then be used to analyze how further neurons contribute to the recording, how synchronization and brain dynamics affect the

spike time statistics and if they can be modelled suitably using the assumption of independent, identically distributed inter-spike interval times. Then the usefulness of renewal models for predicting underlying dynamics will be demonstrated.

Understanding how large volumes of neurons contribute to MERs and investigating how well renewal models can be used to determine underlying dynamics can identify methods to elucidate brain behavior. This work could potentially be used to predict the properties of brain behavior allowing better diagnosis of disease and could possibly be used in development of adaptive deep brain stimulation.

1.2 Scope and objective

Section 1.1 provided motivation for two research question that this thesis aims to answer:

1. What range do the neurons further from the electrode contribute to the MER background noise?
2. Can fitting the inter-spike interval probability distribution of renewal models to STN MERs be used as a potential biomarker?

To address these questions, I aim to investigate the use of renewal processes firing times for modelling and analysis of single point microelectrode recordings of the subthalamic nucleus. To do this I will develop and validate a computationally efficient simulation of STN MERs using a renewal process. The model will simulate the STN and surrounding structures. The neurons will be simulated using combined statistical and biologically inspired dynamical models. The microelectrode recording will be produced by using these neuron models developed and electromagnetic (EM) models for the interaction of the neurons with the electrode. Developing an efficient model will allow many simulations to be performed for tens of thousands of neurons which means significant statistics of the model behaviour can be produced and in future work could potentially be used to develop real time control of DBS.

The methodological approach of this thesis to help answer the research questions are:

- Develop a renewal model to simulate an MER of thousands of neurons with physically realistic coupling of neurons to the electrode that includes attenuation, extracellular filtering and electrical noise, with post processing.

- Verify and tune the MER model against intraoperative recordings of patients. Including investigate how the number of neurons contribute to the recording and the effect of firing statistics on the MER power spectrum using the model.
- Enhance the model by:
    - Relaxing the assumption of independence between neurons. This will allow correlations between neurons firing within the STN.
    - Relaxing the assumption of the ISI times being drawn from a distribution that is stationary in time (changing from time-homogeneous to time-inhomogeneous). This can be achieved by extending the evolution of the statistic of the MER model to include the relevant pathways in the BG and have connections to and from other parts of the brain into the BG.
- Investigate how well the renewal model developed in the first objective fits these enhanced models where the assumptions of the simple model are no longer valid.

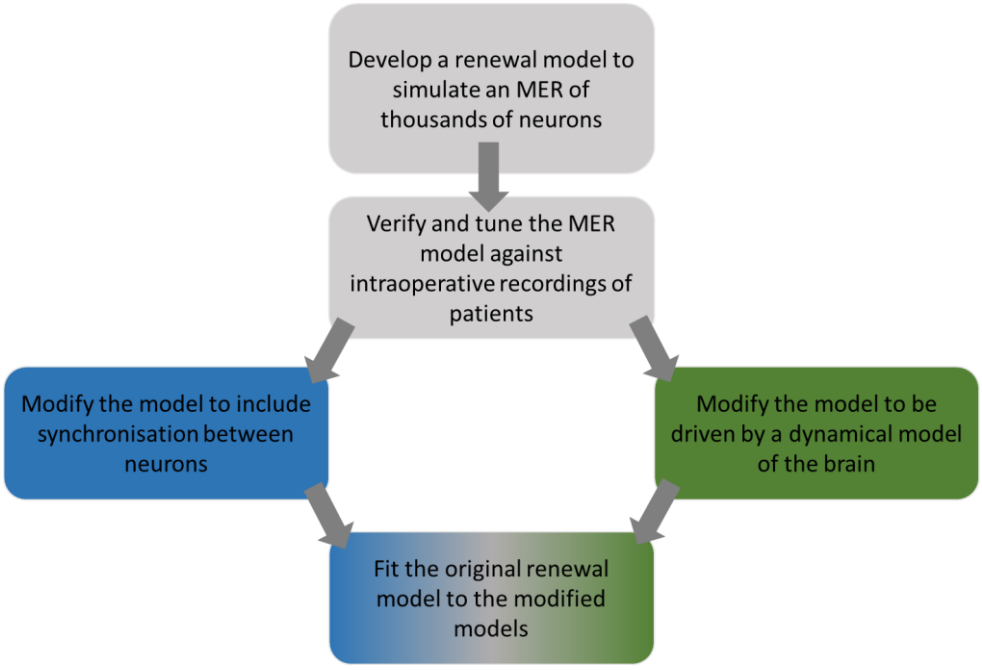

Figure 6 - Summary of the logical flow of the methodology of this thesis. By developing a model of an MER that uses renewal neurons and tuning the model against patient data the number of neurons that contribute to the high frequency noise in an MER can be determined. Modifying the model to include more biological realism can then be used to determine if the renewal model could be useful as a biomarker.

The scope of the work presented is to understand the neuronal origin of the high frequency noise in STN MERs by determining the volume of neurons that contribute to a recording. The ability to fit features of the MERs will be investigated under different assumptions of neuronal behaviour, specifically fitting the inter-spike interval from the power spectrum using a parametrized distribution. This thesis will not attempt to develop an increased

understanding of PD or the behaviour of the neural structures modelled. An application to DBS is also not included in this thesis, however a method for using the results contained for predictions of the neural state using a renewal model is given as an example for how this work could be extended for adaptive DBS.

1.3 Summary

This introduction has motivated the purpose of this thesis, to develop an efficient model of an MER that describes changes in the properties of the background noise. This will involve comparison of the model to patient data and development of analysis techniques using renewal processes. The rest of this thesis will be structured as follows:

- Literature Review – this chapter will contain a summary of the relevant literature related to neuron modelling, MER modelling, BG modelling and renewal models.
- Methods – this chapter describes the methods used for the models developed in this thesis and the techniques used to validate and analyse them.
- Results – all the results found during the development of this thesis are summarised including a discussion on the significance of these results.
- Summary of Papers – a short summary of each paper that contributes to this thesis.
- Conclusion – a summary of the contributions of this thesis are presented. This chapter also includes limitations and suggestions of future work based on the research within this thesis.
- Appendix – copies of the papers that have contributed to this thesis.

2 Literature Review

This chapter outlines briefly the current research available on models of the brain relevant to this thesis and it identifies gaps in knowledge that this thesis will fill. The aim of this review is to determine methods to identify how neurons contribute to the noise of an MER and to determine how renewal models could be used for analysis of MERs. To model an MER there are several factors that need to be considered: the behaviour of individual neurons, how the brain on a larger scale influences the behaviour of the neurons and how the neurons interact with the electrode and recording equipment. There is a large set of literature on neuron modeling, and neural network modeling, however for this thesis, previous models of the subthalamic nucleus (STN) and basal ganglia (BG) will be reviewed since the *in vivo* recordings available are acquired from the STN. The other set of models that will be reviewed are statistical models, specifically renewal models. Renewal models are considered due to their speed compared to dynamical models, as well as their ability to describe stochastic signals using a small set of parameters. Both properties would be important for development of closed loop DBS. This chapter is divided into the following sections: 2.1 Dynamical neuron models, 2.2 Renewal Process Models, 2.3 Models of the basal ganglia, 2.4 Neuron-Electrode Interaction and 2.5 Summary.

2.1 Dynamical neuron models

Figure 7 outlines the components of MERs that are commonly used for analysis, the local field potential (LFP), the multiunit activity and the single unit activity (Rasch, et al., 2009). One of the main uses of MERs is to identify single or multi-unit recordings. This means they identify the spiking behaviour of a single neuron close to the electrode tip, with a possibility of several neurons close and contributing to spikes in the MER. This highlights the importance of modelling individual neurons. The main feature of neurons that contribute to the spikes observed in MERs are action potentials (AP). The AP is characterised by a rapid change in the electrical potential across the neurons cell membrane, followed by a rapid reversal of the potential. The AP is of interest as it is thought that it is the method for neurons to transmit and process information.

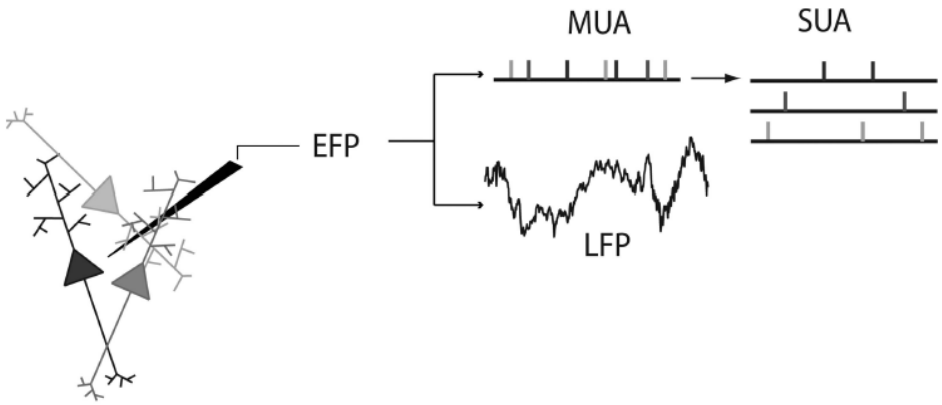

Figure 7 – The steps in acquiring the local field potential (LFP) and the single unit analysis (SUA) from a MER recording otherwise known as an extracellular field potential (EFP). From (Rasch, et al., 2009).

Methods of modelling an individual neuron can vary dramatically, from stochastic models that determine only the timing of AP events (Johnson, 1996) (Zelniker & al., 2008) (Sarma & al., 2010), to dynamical models that use differential equations to model the structures in the neuron that control the flow of charged particles across the cell membrane (Hodgkin & Huxley, 1952) (Terman, et al., 2002). The problem with modelling all the processes involved in the activation of the neuron individually with dynamical equations is that it can be computationally intensive with regards to the time to find numerical solutions. To overcome this different work has been performed to model the behaviour of neurons using dynamics to approximate mathematical features that are seen in the full model (Izhikevich, 2003) (Izhikevich, 2007). As the biological plausibility (the number of mathematical features simulated) of a model increases, the computational time to implement the model increases (Figure 8).

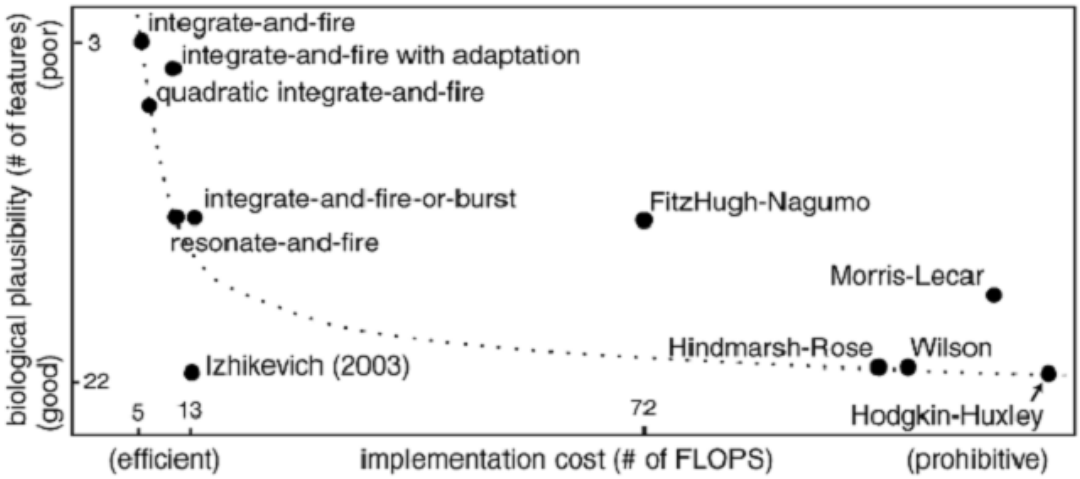

Figure 8 - A comparison of the computational cost to implement different models, versus their biological plausibility, from (Izhikevich, 2004).

Many of these models have been used for studies investigating the STN. These approaches include using the Hodgkin and Huxley (HH) equations for each neuron and simulating a small subset of neurons (Feng, et al., 2007) (Rubin & Terman, 2004) (Terman, et al., 2002), use of an Izhikevich model for each neuron to simulate a larger number of neurons for each structure (Kang & Lowery, 2011) (Michmizos & Nikita, 2012) and renewal models to evaluate the spike timings (Dummer, et al., 2014) (Rajdl & Lansky, 2015) (Camunas-Mesa & Quiroga, 2013). The findings, advantages, disadvantages and relation to this thesis of these models will be discussed.

The HH model for a neuron was originally described by Hodgkin and Huxley for the squid giant axon (Hodgkin & Huxley, 1952). It relates the membrane potential to the different membrane currents caused by activation and deactivation of different ion transporters. Numerous papers have been produced with slight modifications of this model to relate to the STN (Feng, et al., 2007), (Rubin & Terman, 2004), (Terman, et al., 2002). These models collectively can demonstrate the common pathalogical behaviour of beta band (10-30 Hz) synchronization in STN neurons for simulations of the Parkinsonian state that are not present in simulations of the normal state, shown in Figure 9.

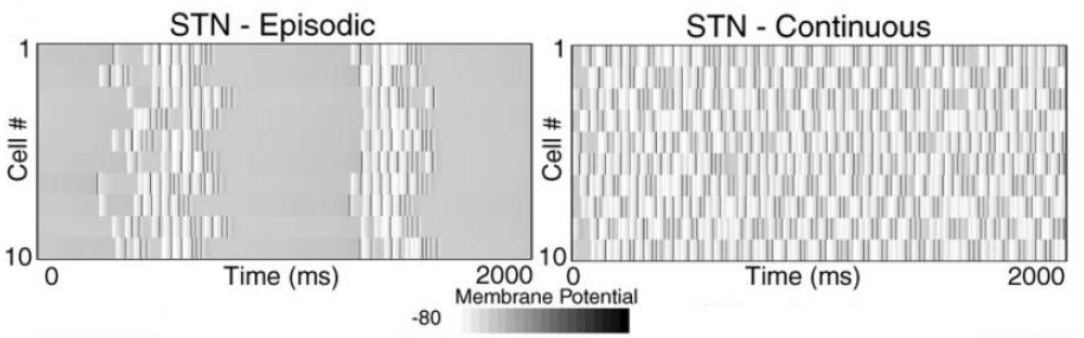

Figure 9 - The STN cell behavior in HH BG models with inputs describing the pathological state (Episodic) and inputs describing the normal state (Continuous), from (Terman, et al., 2002).

They can also show the arrest of this synchronization when DBS is applied. Computational limitations prevent the models mentioned so far from simulating a large number of neurons, allowing only a subset (the closest neurons to the electrode) to contribute to an MER simulation. This model has been analysed numerous times in the liturature and it's robustness and accuracy have been tested. It has been found to be a accurate model for representing an individual neuron (Pascual, et al., 2006).

The HH type of model is not the most suitable for creating a complete MER for this thesis due to the small number, ~10^1, of neurons simulated for the STN (Rubin & Terman, 2004) (Terman, et al., 2002). If the model is extended to see how large numbers, >10^5, of neurons contribute to the MER noise numerical solutions for simulations would take too long.

An advancement, in terms of cell number simulated, of the HH BG models is to use the Izhekevich model (Kang & Lowery, 2011). The Izhikevich model is a simplification of the HH type models by reducing them to a two-dimensional system of ordinary differential equations. This model has been shown to be very computationally effective, see Figure 8. These equations represent an approximation of the phase space of the HH based two dimensional models around the stationary point with the reset auxillary equation accounting for the trajectories outside of this region (Izhikevich, 2003). There are also several papers that have demonstrated the ability for the model to simulate the twenty common firing types of neurons, Figure 10 (Izhikevich, 2004). The model has also been used to efficiently simulate on a large scale, hundreds of neurons, that can display common neural network phenomena of spike timing dependant plasticity (Izhikevich, 2007) and synchronisation (Izhikevich, 2006).

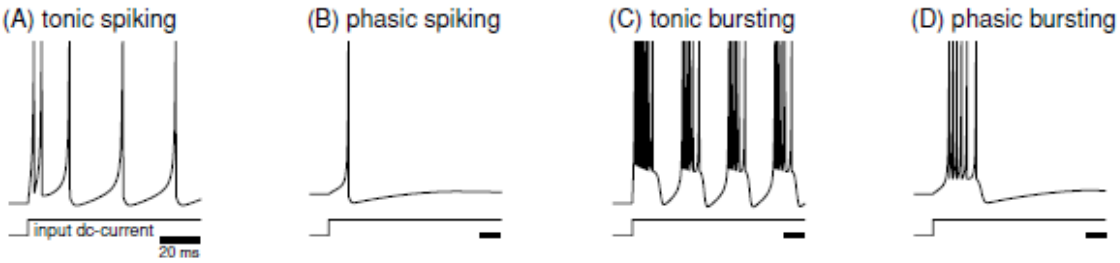

Figure 10 – Examples of the 4 out of 20 common firing behaviors of neurons achieved by the Izhikevich model. These four types of behavior represent common behavior of the STN. Adapted from (Izhikevich, 2004).

Due to the decrease in computational time per neuron, when compared to the HH model, this model allows a larger set of neurons to be modeled for each structure. A BG model for DBS has been produced using these equations that contains 200 STN , 200 GPi, 200 GPe and 200 thalamocortical neurons (Kang & Lowery, 2011). These numbers compare to approximately $5x10^6$ neurons contained in the human STN alone (Hardman, et al., 2002). With this model it was demonstrated that it could reproduce the beta band synchronicity given inputs describing the pathalogical state. The model was also able to describe the arrest of this behaviour in all the STN cells upon application of DBS to 1 and 2 neurons. This model also allowed the state of the STN cells to be monitored to determine the revival time of beta-band oscillations after ceasement of DBS (Kang & Lowery, 2011).

Using the Izhikevich model neuron simulations of up to 10^{11} neurons has been demonstrated (Izhikevich 2005). Although there is a large time improvement compared to the HH model, the large scale simulation took over 1 month to calculate the dynamics. For real simulations the Izhikevich model can be used to generate accurate statistics for the spike timing of ~10^3 neurons. This improved computational time still prevents investigation of how a large number of neurons, ~10^5, contribute to an MER. This model still presents a computation cost significant enough to prevent investigation of how a large number of neurons, >10^4, contribute to an MER. Another problem when using this model to generate MERs is the shape of the waveform generated for the AP. The AP is added to the simulation by addition of a spike when a threshold voltage is reached. This affects the appearance of the MER power spectrum because it does not accruately model the frequency components of AP. Due to the random nature of the MER recordings analysis using the power spectrum is prefered over using techniques directly on the time series. The analysis of the Izhikevich model, and hence the problems associated with using the Izhikevich method for modelling MERs are discussed later in this chapter, see Chapter 2.2.2.

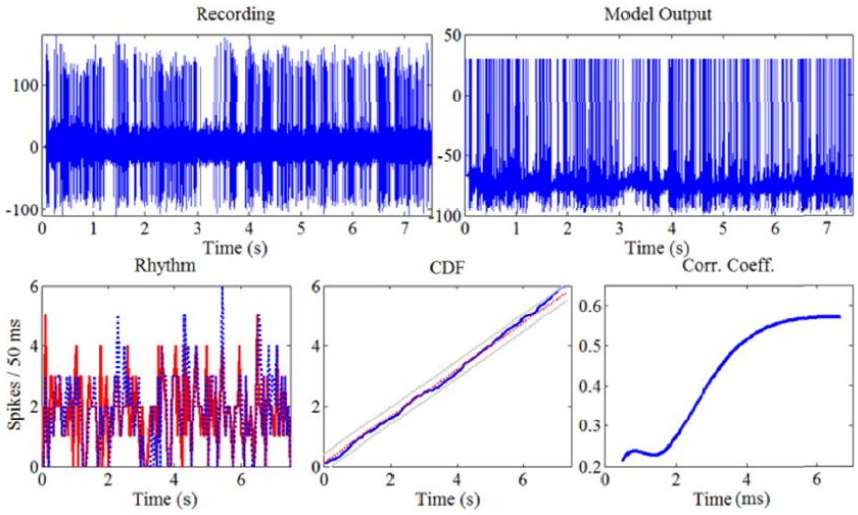

Figure 11 - a) A comparison of the CDF from a MER with the CDF from a model for the single unit driven by the MER LFP. b) The Cross-correlation between the binary spike trains for the MER and the Model, from (Michmizos & Nikita, 2012).

To demonstrate potential analysis of MERs using the Izhikovich model another study that has showed that given the LFP as a parameterized input, it could reproduce the single unit behaviour from the recording (Michmizos & Nikita, 2012). The model was verified by comparing the cumulative distribution function (CDF) for the spike statistics, through a plot of recorded CDF versus model CDF. An accurate reproduction of the single unit produces a 45^{o} line shown in Figure 11. Binary spike trains were also produced from the model and the cross-correlation was used to validate the results. The model produced the single unit behaviour with 95% confidence 70% of the time. This type of behaviour from a model would be desierable for MER monitoring, as the initial state of the neurons may not be known in a real recording. Data from the real MER could then be used to set up the initial state of the model, and the simulation could then track the MER behaviour. To do this analysis the spikes need to be isolated in the time domain using spike sorting, since the only feature of the recording reproduced is the spike times. While these papers demonstrate the LFP of the MER contains information on the spike times of the neurons, it removes the noise from the LFP and neuron spike trains and does not include it in the modelling. It is this noise that can be used to identify the STN during surgery, and so may be more than just uncorrelated fluxuations (Coyne, et al., 2006).

Other work has demonstrated how LFPs can drive single unit activity (SUA) (Santaniello, et al., 2004) (Rasch, et al., 2008). By looking at a parameterized third order model of a spiking neuron (Santaniello, et al., 2004) showed that the LFP can be used to produce accurate spike timings and shape. To produce the SUA the LFP was used to drive a model that

produced the spike shapes and times for STN neurons. The LFP was acquired by using a low pass filter on *in vivo* recordings. The parameterized LFP was then fed into a third order dynamical model, Figure 12, where the parameters were found by extracting the spikes from in vivo recordings by using a wavelet filter to find the spike times and shape. The spike times were then used to generate the cumulative distribution function which was also used to fit the model.

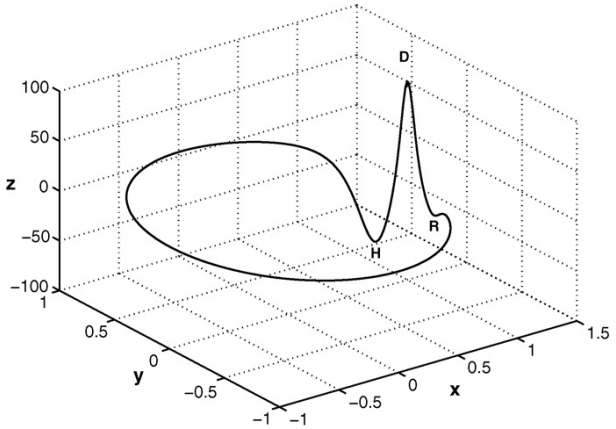

Figure 12 - The third order ($\dot{x}, \dot{y}, \dot{z}$) dynamical model fitted to single unit activity of a MER, which can then be used to reproduce MERs. The output is given by z(t) with the addition of LFP noise. The refractory, depolarization and hyperpolarization cell phases correspond to the R, D and H respectively. From (Santaniello, et al., 2004).

The work by Santaniello, *et al*. is another example of how the spike timing of a neuron seen by an MER can be generated using the LFP. This contrasts with using the Izhikevich model to demonstrate how the SUA can describe the LFP. However, both methods indicate that the LFP comprises of information related to the spike time statistics. Although this model can reproduce a MER that has the same statistics as an experimentally acquired MER, it required the inputs from the experimental MERs, and does not dynamically predict their evolution.

The previous models reviewed described methods for modelling spikes using the LFP, there is a set of literature that describes the process in the other direction, generating the LFP using the spike times (Rasch, et al., 2009). A linear method is used to estimate the convolution kernel that when applied to the SUA produces the LFP. Using recordings from 545 recordings from seven different monkeys of ~4 mins length, the convolution kernel ($h(t-\tau)$) was estimated that would generate the LFP, Figure 13, from a function describing the SUA ($x(\tau)$) using the estimated LFP:

$$L_{est}(t) = \int_0^T d\tau h(t-\tau)x(\tau), \tag{1}$$

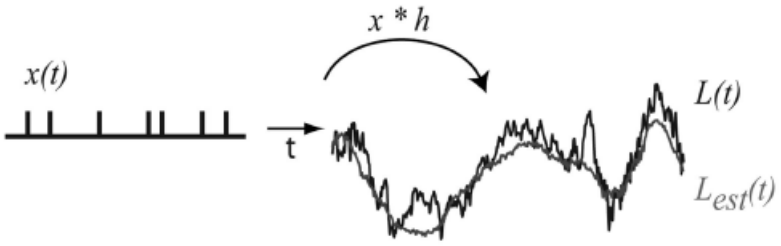

Figure 13 – The reproduction of the LFP using the single unit spike train, from (Rasch, et al., 2009).

This method once again assumes a fixed correlation between the LFP and the single unit, however in contrast to (Santaniello, et al., 2004) and (Rasch, et al., 2008) who showed that the LFP can reproduce the SUA, this work shows that the single unit activity can describe the LFP. This work does not reproduce accurate MER simulations instead it can be used to generate an LFP after processing an experimental MER using spike sorting to determine the spike times. This demonstrates that spikes contribute to the LFP, with correlations up to 0.6, it fails to identify high frequency contributions to the MER noise since the LFP is extracted using a low pass filter with a 300Hz corner. This removes any contribution from the extracellular action potential (EAP) of further neurons, only realizing the slower network behaviour. The contribution from neurons whose SUA is not captured by the MER is also not considered in this model.

The main problem with these dynamical models when developing a MER is fitting the model parameters with a small amount of data. To be useful in the diagnosis of disease, confirmation of location, or applied to feedback controllers for adaptive DBS the ability to quickly determine the model parameters is important. Another important feature is to have as few model parameters as possible. The minimum number of parameters helps to reduce the complex information that is being sort, such as patient state. The models presented so far contain a large number of parameters for characterizing the behvaiour of a single neuron, and extending them to a large number of neurons $(> O(10^4))$ creates a combinatorial increase as the number of parameters increase when the connectivity between each neuron ($\sim O(10^3)$ conections per neuron) is considered.

The types of models reviewed in this section are satisfactory for reproducing features of recordings after online analysis and they demonstrate how different components of MERs, spikes or LFP, can be predicted by using the other. These models do not attempt to reproduce MERs of more than a small number, 1-100 neurons. To investigate how a large number, on the order 10^4, neurons contribute to an STN MER the models presented so far in this section present a problem due to their computational time required for a numerical solution. The HH model does present the most accurate way of producing the STN action potential shape, so it is used for the work in this thesis in conjunction with a statistical model for the spike timing, see Chapter 4.2.2.

2.2 Renewal Process Models

How the neurons in the brain carry and encode information is one of the fundamental questions of neuroscience. There are several models a neuron's spikes could encode information (Bialek, et al., 1999). One approach, temporal encoding, relies on the precise timing of spikes in relation to a stimulus or neighbouring spike times (Bialek, et al., 1999). An alternate approach, developed using concepts from information theory, attempts to characterize the spike train by using the statistical distribution of the time between spikes (inter-spike interval, ISI) (Bialek, et al., 1999). This section describes how neurons have successfully been modelled using renewal models. There are three subsections: 2.2.1 introduces how renewal models have been used for simulating neurons, 2.2.2 outlines mathematical properties of renewal models that will be used in this thesis and 2.2.3 summarises properties of the STN that will be used to develop the model developed as part of this thesis.

2.2.1 Renewal process models for simulating neurons

One of the simplest forms of describing neuron behavior is in Perkel et al. who showed that neural activity can be described in terms of the statistics of the inter spike interval, ISI (the time between two consecutive spikes) (Perkel, et al., 1967) (Perkel, et al., 1967). The model that describes this behavior is known as a point process, where each event (spike) in time has a probability of occurring. A special case of point processes are renewal processes, where the ISI distributions are independent and identically distributed (IID) for all ISI times. There has been a relationship between the HH model and renewal models

established (Johnson, 1996). The resetting of the Na^+ and K^+ channels after an action potential is analogous to the renewal of the firing time. The Izhikevich model also has an explicit reset after neuron firing. Renewal process model has been used extensively in neuroscience for both experimental (Moore, et al., 1966) (Maimon & Assad, 2009) (Bastian & Nguyenkim, 2001) and theoretical work (Johnson, 1996) (Pawlas & Lansky, 2011) (Wilbur & Rinzel, 2983).

Renewal process models have been used in spike sorting to aid in clustering by maximizing the probability a neuron belongs to using Bayes rule (Pouzat, et al., 2004). However, there is evidence that not all neurons follow renewal statistics. The condition for ISI statistics following a renewal process has been looked at in work by Avil-Akerberg *et al.* In their work, they summarise the findings about neurons whose ISIs display non-renewal spiking statistics (Avil-Akerberg & Chacron, 2011). They compile thirty different studies that show non-renewal neurons, of note is that the STN was not included in this list. A specific study of STN cells showed that they can be modelled using a three-state point process (Zelniker & al., 2008). Although not a renewal model, since the ISI times are not IID, it was shown that the ISI statistics from intraoperative recordings of the STN can be modelled stochastically.

The renewal model only creates the timing of neuron firing. This type of model contains no action potential shape, representing only the timing of neuron firing events. To model the neuron electric field detected by an electrode a filtered point process (FPP) is needed. A FPP involves convolution of an action potential shape (the “Filter”) with the spikes that represent the neuron firing times. Although this type of model can simulate the waveform dynamics for super-threshold activity, it cannot predict any subthreshold activity for the neurons.

Due to the ability to simulate many neurons, the model for the MER developed in this thesis, described in Chapter 4.2, will involve simulating the neurons as renewal models and pooling their response at the electrode tip. Similar work to this has been done in (Dummer, et al., 2014), (Rajdl & Lansky, 2015) and (Camunas-Mesa & Quiroga, 2013), the latter of which was developed independently and parallel to the work in this thesis. While (Dummer, et al., 2014) and (Rajdl & Lansky, 2015) use a renewal model to simulate the neuronal input into a dynamical neuron, Chapter 4.2 will develop a model where the dynamical neuron is replaced with an extracellular medium/microelectrode model. The work in (Camunas-Mesa

& Quiroga, 2013) used a similar model to this, where they investigated the neuron-electrode interaction using a special type of renewal process known as a Poisson process.

2.2.2 Properties of renewal models

To begin this section a definition of renewal processes, as related to spike trains, will be formalized. Using this definition useful properties of renewal processes that relate to the research undertaken for this thesis will be presented.

First a series of positive times, T_i, that are independent, identically distributed random variables that have an expectation value ($\mathbb{E}[\,]$):

$$0 < \mathbb{E}[\mathrm{T_i}] < \infty. \tag{2}$$

This series of times represents the ISI times for a given neuron. The spike time (t_n) of the nth spike, where $n > 0$, can then be written as:

$$t_n = \sum_{i=1}^{n} T_i. \tag{3}$$

A random variable, N_t, can now be defined that counts the number of spikes up until a time t by considering the supremum of the set of spike times less than or equal to t:

$$N_t = \sup\{n: t_n \leq t\}. \tag{4}$$

Since renewal processes are often concerned with the number of events within a period, the renewal function is defined by:

$$m(t) = \mathbb{E}[N_t]. \tag{5}$$

To see the usefulness of the renewal function, consider when the ISI times are drawn from a probability density function $\big(f(t)\big)$, pdf, defined by the cumulative distribution function $\big(F(t)\big)$:

$$f(t) = \frac{dF(t)}{dt}. \tag{6}$$

The renewal function satisfies the renewal function:

$$m(t) = F(t) + \int_0^t m(t-s)f(s)ds. \tag{7}$$

Taking the derivative of the renewal function

$$\frac{dm(t)}{dt} = \frac{dF(t)}{dt} + \frac{d}{dt}\int_0^t m(t-s)f(s)ds.$$

$$\frac{dm(t)}{dt} = f(t) + \int_0^t \frac{dm(t-s)}{dt} f(s)ds\,. \tag{8}$$

Solving for $\frac{dm(t)}{dt}$ in terms of the ISI pdf gives:

$$\frac{dm(t)}{dt} = f(t) + \int_0^\infty f(t')f(t-t')dt' + \int_0^\infty \int_0^\infty f(t')f(t'')f(t-t'-t'')dt'\,dt'' + \cdots \tag{9}$$

This result is of interest because it shows how the renewal function can be written in terms of an infinite sum of nested convolutions of the ISI pdf. The nested convolutions represent the probability of a spike at time *t*. The first term is the probability of the first spike, the second term the probability of the second spike, etc. Hence, the derivative of the renewal function can be thought of as the probability density of any spike occurring at a given time, and is known as the renewal density function.

To represent a neuron with this model the ISI times can be drawn from a pdf. Using these times and given the action potential shape, g(t), the neuron time series can be written as:

$$V(t) = \int_0^\infty g(t - t') \sum_{n=1}^{\infty} \delta(t' - t_n)\, dt'\,, \qquad \forall\ t > 0 \tag{10}$$

The autocorrelation function of the single neuron time series, with a firing rate of ν, has been shown as a function of the renewal density function as:

$$R(t) = \nu \int_0^\infty g(t-t') \frac{dm(t)}{dt}\, dt'\,, \qquad \forall\ t > 0 \tag{11}$$

Taking the Fourier transform of $R(t)$ and by the Wiener–Khinchin theorem, the power spectrum of a filtered renewal process is given by (Banta, 1964):

$$P(\omega) = \nu G(\omega)\left[1 + Re\left\{\frac{H(\omega)}{1 - H(\omega)}\right\}\right], \qquad \forall\ \omega > 0 \tag{12}$$

where $G(\omega)$ is the action potential power spectrum, $H(\omega)$ is the Fourier transform of the ISI pdf, known was the characteristic function. Equation (12) can be extended to a sum of *N* renewal process neurons by including a distribution function (*A*) to represent the amplitude of each neurons contribution (Banta, 1964):

$$P(\omega) = N\langle A^2\rangle \nu G(\omega)\left[1 + Re\left\{\frac{H(\omega)}{1 - H(\omega)}\right\}\right], \qquad \forall\ \omega > 0 \tag{13}$$

This simple analytical model for predicting the power spectrum of a filtered renewal process with changes in the ISI probability function is used in Chapter 4.4 and 4.5 to parametrically characterise the MER simulations (details on the method provided in Chapter 4.3.2). An

interesting property of Equation (13) is that for a Poisson process the term in the square brackets becomes constant for all frequencies.

2.2.3 Renewal models of the subthalamic nucleus

The participants for the deep brain MER recordings are undergoing treatment for a pathological state that is treated by altering STN function. This could imply abnormal function of the STN relates to a change in the distribution of ISI time (Sarma & al., 2010) and could be used to monitor disease. Although neurons are often modelled using Poisson statistics, exponentially distributed ISI times, the STN can exhibit a range of different ISI distributions (Theodosopoulos, et al., 2004). A renewal model can still be used by modifying the ISI distribution for these different cases, for example bursting fire can be described using a stretched exponential distribution and periodic firing can be described by a Rayleigh distribution. A parameterized probability distribution that can give these common types of behaviour found in STN neurons, such as bursting, Poisson and periodic behaviour, is the Weibull distribution (Perkel, et al., 1967) (Perkel, et al., 1967) (McKeegan, 2002) (Li, 2011). By fitting parameters of the Weibull distribution, a renewal model could be developed for the STN.

Table 1 - THE MEAN FIRING RATE FOR STN CELLS TAKEN FROM MERS (Theodosopoulos, et al., 2004).

STN Mean Discharge Rate (Hz)	# STN cells recorded
34	102
37	248
39	45
41	24
46	213
33	200
59-69*	190

*Rate varied according to firing pattern observed.

One of the first hypothesis to adopt the approach of using the ISI statistics to characterise a neurons response was by Adrian and Zotterman (Adrian & Zotterman, 1926), where the first statistical moment, the firing rate, was used to characterize neurons activity in the presence of different stimuli. The mean firing rate for STN cells is well studied, shown in Table 1 (Theodosopoulos, et al., 2004). A problem with the rate hypothesis is that the ISI timing can vary while the same overall rate is produced. For the STN an example of this is the difference between a regular cell and a tremor cell, shown in Figure 14. The spontaneous discharge

characteristics for STN neurons change dependant on Parkinsonian state (Kuhn & al., 2009) (Theodosopoulos, et al., 2004) (Rubin & Terman, 2004). It has been found that while the mean firing rate increases with Parkinson's disease, the rhythmic and non-rhythmic burst firing increased from 69% to 79% of neurons. This means the rate alone cannot be used as a measure to always explain the neurons behaviour and more sophisticated coding schemes were needed (Stein, et al., 2005). This variability can be characterized using the next statistical moment in the form of the coefficient of variation (CoV) defined as the standard deviation of the ISI time divided by the mean ISI time (Tuckwell, 1979). The CoV is a normalized metric of the spread of neural firing times. The extension of analysis to measuring the CoV can describe the variability in ISI times and how they relate to the information capacity of a neuron (MacKay & McCulloch, 1952).

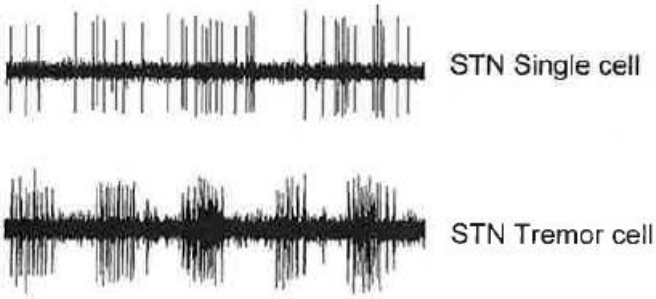

Figure 14 - The different cell behavior in STN cells. Standard STN single cell and an STN Tremor cell.

To decide what distribution is best to use for the renewal process used to generate the spike timing, the STN firing behaviour needs to be considered. Using the Weibull distribution for ISI times can generate common neuron firing behaviour found in the STN. The Weibull distribution is characterized by two parameters, the shape parameter and the scale parameter. The scale parameter controls the rate of neuron firing, while the shape parameter can be tuned to model periodic, burst or Poisson firing statistics. Another consideration for using the Weibull distribution is that the coefficient of variation (C_v) can also be fully described using only the shape parameter:

$$C_v = \frac{\sigma}{\bar{\mu}} = \frac{\sqrt{\Gamma\left(1+\frac{2}{k}\right)-\Gamma\left(1+\frac{1}{k}\right)^2}}{\Gamma\left(1+\frac{1}{k}\right)}, \qquad (14)$$

where $\Gamma(\ \ )$ is the gamma function, k is the Weibull shape parameter, $\bar{\mu}$ is the mean ISI time and σ is the standard deviation of ISI times. Because the coefficient of variation is a common metric for neural recordings and can be entirely described using the Weibull shape parameter, the Weibull distribution shape will be used to model the MERs. The shape

parameter will also be used to fit MERs to the model, described in Chapter 4.3.2. Using a single value to characterize the recording also opens avenues of future research where that variable could be used to confirm electrode location, diagnose disease or as a feedback state in adaptive DBS.

2.3 Models of the basal ganglia

The basal ganglia (BG) is a closed neural system that has been highly studied with applications for the treatment of movement disorders such as Parkinson's disease (Davie, 2008). The STN is a functional body of neurons that sits within the BG. In addition to inter-nucleus connections the neurons are also highly connected to surrounding structures in the BG. The anatomy of the BG, highlighting the type of connections neurons in one structure have with another, is shown in Figure 15 (Gurney, et al., 2001). This figure shows the inhibitory (GABA) projections and excitatory (glutamate) projections of the BG. D1 and D2 represents the (dopaminergic) cells in the striatum and have afferent excitatory pathways from the Cortex. From the straitum, D1 cells inhibit the globus palidus internal (GPi). The D2 cells inhibit the globul palidus external (GPe), which in turn inhibits the STN. The STN then has excitatory projections into the GPi. The GPe has inhibitory projections into the GPi and STN. The STN also has excitatory connections into the GPe and GPi. The GPi then projects into the thalamus and the brainstem. This seemingly simple model is successful at describing the pathophysiological processes, such as those involved in Parkinson's Disease (Albada & Robinson, 2009) (Albada & Robinson, 2009) (Liu, et al., 2017).

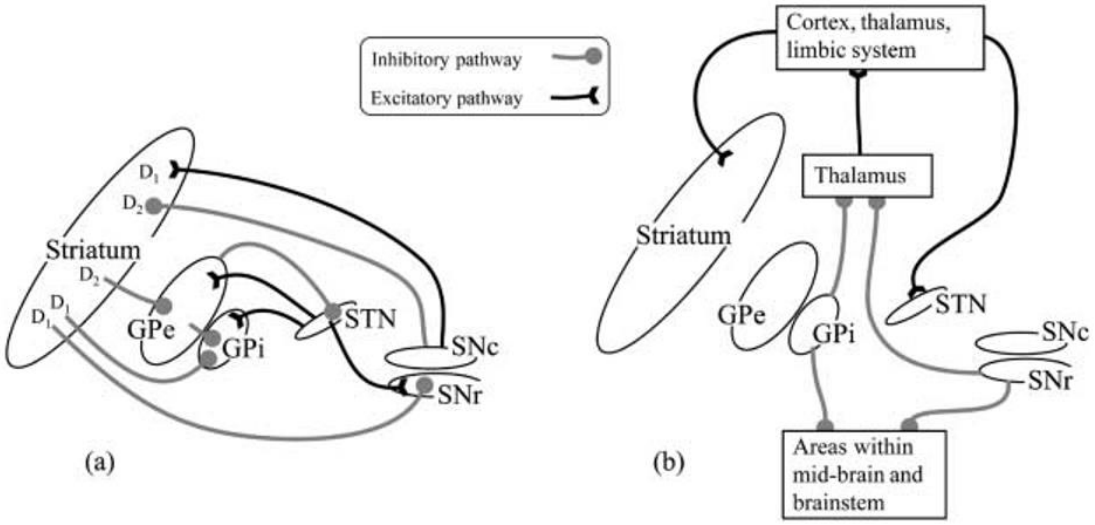

Figure 15 – Anatomy of the Basal Ganglia (a) The internal connections of the basal ganglia. (b) the external connections of the basal ganglia. From (Gurney, et al., 2001).

To appropriately model the STN firing times under different conditions, the STN connections within the BG and afferent connections to the BG need be modeled. The set of dynamical models presented in Chapter 2.1 can be extended to model the BG by including individual neurons simulated in the multiple structures. All the neuron models are then coupled to each other to represent the physical axonal connections between the different structures. This increases the computational time of the models significantly, as a large number of neurons are required for each structure involved. Because of this restriction in computational time, these types of models won't be considered.

The connectivity of the neurons within the BG leads to an extremely large number of states to model, $\mathbf{O}(10^4)$ – $\mathbf{O}(10^8)$ when considering neurons can have $\mathbf{O}(10^4)$ connections to other neurons. This is a problem when modelling parts of the brain as a dynamical system. When modelling these complex system, to reduce the size of this state space, a neural field model can be used (Albada & Robinson, 2009). These models borrow from the often-used mean field theory of physics to reduce a highly-interconnected structure of the brain down to the time evolution of the distribution of firing times throughout the structure. This reduces a many-problem body down to a one-body problem. These field models are often expanded into the distribution's moments, giving a second order ordinary differential equation for each moment (Albada & Robinson, 2009). Basal ganglia field models of the first moment, the mean firing rate, have been developed and are known as neural mass models (Albada & Robinson, 2009) (Albada, et al., 2009) (Liu, et al., 2017). These models have been used with great success for analysis of movement disorders that are treated with DBS. The

advantage of these models is to reduce the high dimensionality of the state space down to two states per brain structure, firing rate and change in firing rate.

To get a clearer understanding of how these models work the states of a neuron that describe its behaviour have to be established. Consider each neuron has a state *x* that describes the important variable of a neurons dynamics, such as the membrane potential (*V*), the membrane currents (*I*) and any other variable required:

$$x = \{V, I, \dots\}. \tag{15}$$

The evolution of the state of a single neuron can then be described using the Langevin equation:

$$\mathrm{d}v = f(x,t)dt + 2\sqrt{D(x,t)}\,dW, \tag{16}$$

where $f()$ is an arbitrary function and $2\sqrt{D(x,t)}\,dW$ represents a stochastic evolution following a Weiner process. The function $f()$ can be non-linear and the evolution of v is not deterministic. For this type of stochastic evolution the probability distribution of the possible states, $p(x,t)$, can be described exactly using the Fokker-Plank equation:

$$\frac{dp(x,t)}{dt} = -\frac{\partial}{\partial x}\left(\mathrm{f}(x,\mathrm{t})\mathrm{p}(\mathrm{v},\mathrm{t}) - \mathrm{D}\frac{\partial \mathrm{p}(x,\mathrm{t})}{\partial x}\right) \tag{17}$$

By assuming the afferent currents arriving at neurons have the same statistics the mean field approximation can be used to simplify Equation (18). The mean field approximation for neurons reduces the set of states to the distribution of membrane voltage (V) and membrane current $\left(I = \frac{dV}{dt}\right)$, mean firing rate $v(t)$ and the variance of the firing rate σ^2. Using the membrane resistance (R) and the membrane time constant (τ) the Langevin equation can then be reduced to:

$$RI = v(t) + \sigma\sqrt{\tau}dW. \tag{18}$$

The evolution in time of the neural field distribution can now be describe using:

$$\frac{dp(x,t)}{dt} = \frac{1}{2\tau}\sigma^2\frac{\partial^2 \mathrm{p}(x,\mathrm{t})}{\partial x^2} + \frac{\partial}{\partial x}\left[\frac{x(t)-v(t)}{\tau}p(x,t)\right]. \tag{19}$$

A common simplification of Equation (19) is to consider the distribution of states expanded into statistical moments (μ_i) using basis functions (η_i):

$$p(x,t) = \sum_{i=0}^{\infty}\mu_i\eta_i\,. \tag{20}$$

For neural models, it has been shown that these moments decay exponentially after perturbation leaving the zeroth moment, μ_0 the mean, also known as the mass. This allows description of the system by using a single value rather than a distribution and is known as a neural mass model. Performing this first order expansion about the statistical moments, resulting in a system of ordinary differential equations which approximately describes the average voltage for a body of neurons given by:

$$\dot{\mu_l} = y_l \tag{21}$$

$$\dot{y_l} = ab\left[\sum_k \alpha_{lk}\zeta(\mu_k(t-\tau_{lk})) - \left(\frac{1}{a}+\frac{1}{b}\right)y_l - \left(\frac{1}{ab}\right)\mu_l\right] \tag{22}$$

$$\zeta(\mu_l) = \frac{S_{max}}{1+e^{k(\theta-\mu_l)}} \tag{23}$$

where y_l is the mean membrane current of the target nucleus (l), μ_l is the mean voltage of the target nucleus, α_{lk} is the strength of coupling from the nuclei k to the target l and τ_{lk} is the axonal propagation delay, S_{max} is the maximum firing rate of the target, a is the decay time constant of the membrane and b is the rise time constant (both relate to R and τ in Equation (18)), θ is the potential that gives half the maximum firing rate and k controls the slope of the sigmoid to give realistic rates for a given input potential. Equation (23) turns the mean neuron membrane potential into a mean firing rate and is a common method to compensate the model's inability to couple the mean to higher order moments (Deco, et al., 2008). This set of differential equations, Equations (21), (22), (23) are the basis for Chapter 4.5.

The neural mass model only describes the evolution of neural dynamics on a temporal scale. The dynamics can be extended to include spatial extent by extending $v(t) \rightarrow v(t,x)$. This type of model is particularly important for structures with large spatial extent, such as the cortical sheet (Robinson, et al., 1997) (Robinson, et al., 2005). While these methods have been successful in describing experimental observations, it is not considered important for this study as it has been shown that the structures in the BG can be successfully modelled without including spatiotemporal dynamics (Albada & Robinson, 2009) (Albada, et al., 2009).

The neuron models being considered in this study for simulating STN MERs are statistical models. This prevents modelling of the BG by including neurons within structures other than the STN and conections between them. The BG neural-mass model provides a method for describing the behaviour of the BG and providing an instantaneous average firing rate of the

STN. For a single neuron this instantaneous firing rate describes the probability density of a spike occuring. This probability is distinct from the ISI probability distribution described in Chapter 2.2.2. It is however an equivalent probability density to the renewal density function in Chapter 2.2.2. To see the equvilance the rate, ν, can be thought of as the change in the number of spikes, N_t, in time:

$$\nu = \frac{dN_t}{dt}. \tag{24}$$

The renewal density function can also be described with the rate by combining equation (5), (23) and (24):

$$\frac{dm(t)}{dt} = \frac{d\mathbb{E}[N_t]}{dt} = \mathbb{E}\left[\frac{dN_t}{dt}\right] = \mathbb{E}[\nu] = \zeta(\mu_V). \tag{25}$$

This motivates fitting a renewal model to MER simulations in Chapter 4.3.2.

By modifying the MER simulations from Chapter 4.2 to have neuron firing times modulated by a BG neural-mass model, the validity of using the Weibull distribution to model ISI times in a renewal process model can be investigated. The methodology for developing this modification is in Chapter 4.5, with the results presented in Chapter 5.3.

2.4 Neuron-Electrode Interaction

The models discussed so far only consider the behaviour of the neurons that contribute to the recording but do not consider how the electric field of the neurons interacts with the extracellular medium between the neuron cell and the microelectrode. To investigate how further neurons could contribute to the background noise of an MER these extracellular effects need to be considered. Several studies have looked at the effects of the extracellular medium on the electric field produced by a neuron (Bedard & Destexhe, 2009), (Bedard, et al., 2006), (Bedard, et al., 2004), (Buzsaki, et al., 2012), (Gold, et al., 2006). These studies involve simulating the neurons at different distances from an electrode and filtering their contributions to generate the electrical response at the electrode.

To turn the neuron simulations into an MER the electric field picked up by the electrode needs to be developed. The simulations of extracellular recordings of neurons consider how neurons located at different positions interact with the electrode. The electrode senses the neuron spikes through the electric field that propagates from the neuron. This electric field is known as the extracellular action potential (EAP). The EAP is generated by ionic currents

around the active neuron that can change as different cellular processes occur (Bedard & Destexhe, 2009). As the EAP propagates through the extracellular medium to the electrode it will pass through regions with different conductivity and permittivity (Bedard, et al., 2004). This will cause filtering effects along with attenuation of the field. This means that the electrode will record a different EAP for each neuron depending upon the distance from the electrode and the media in between.

The models that are used to generate electrode recordings from this method are only performed using tens of neurons. This is due to the type of experiments modelled which involve capturing single neuron spike trains. Single unit recordings with multiple electrodes have been performed in a small region of a cat parietal cortex, due to the restriction on the number of simultaneous recordings, only the activity of tens of neurons is recorded.

The most recent work in propagation of electric fields in the brain made use of boundary element methods (Hofmanis & al., 2011). They found that the boundary element method was accurate when predicting the field from DBS near the skull, however an analytical dipole model with homogenous media for DBS was sufficient in predicting the field power across a large frequency range close to the DBS source. As this thesis only involves interactions between neurons and electrodes deep inside the brain, far from the skull, it appears suitable to use an analytical method for determining the electric fields.

The electrodes used to capture MERs have a 50 µm tip diameter. This tip size is larger than electrodes used for single cell recordings (~1 µm) and considerably smaller than the implanted electrode (~1 mm). This intermediate size allows the electrode to record high frequency electrical activity, associated with the behaviour of single neurons and apply electrical stimulation without causing damage to the surrounding tissue. However, a consequence of the microelectrode tip size is that it contains a large degree of background activity compared to a high impedance single neuron recording electrode (Humphrey & Schmidt, 1990).

This process modifies the frequency behaviour recorded by the electrode for that neuron. These effects change the power spectra of a neuronal recording and need to be considered when producing a model of MER power spectra. Finite element models (FEM) have been created to describe the electric field of neurons as it propagates through the extracellular

medium (Gold, et al., 2006). The FEM simulations show that the extracellular medium causes low pass filtering and attenuation of the potential measured at the electrode, shown in Figure 16. The spatial composition of the extracellular medium is required to use these methods and these methods are computationally expensive. Complications can be reduced by assuming average properties of the extracellular medium (Bedard, et al., 2004). This also removes the need to define the exact extra cellular composition for each neuron-electrode interface. The average extracellular filtering of the neuronal electric field at the electrode can be described by a complex transfer function relating the cellular current to the voltage recorded by the electrode, i.e. the impedance of the extracellular material (Bedard & Destexhe, 2009) (Bedard, et al., 2004). This assumes the neurons act as a point current source and a decoupled magnetic field. However, obtaining the transfer function for the extracellular medium is computationally expensive as a numerical integral needs to be calculated for each frequency component and for all neuronal positions.

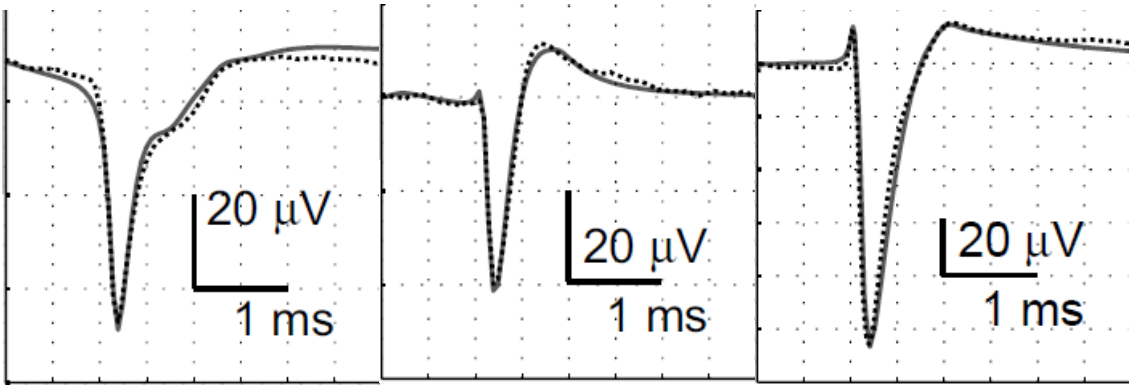

Figure 16 - Comparison of calculated EAPs (solid lines) with experimentally measured EAPs (dashed lines). These graphs show good agreement between the EAP calculated using Laplace's equation and that measured. From (Gold, et al., 2006).

A circuit model simplification of this extracellular filtering can be used to find a simplified form of the transfer function (James, et al., 2004), (McIntyre, et al., 2004).The effect of the radial distance to the electrode for each neuron is reduced to a "seal" resistance. This type of model also includes the frequency effects of the electrode geometry with Faradic resistance and capacitance. While the extracellular medium is known to be anisotropic over a scale of mm^3 (McIntyre, et al., 2004) there is currently no data available to model this anisotropy at sub-mm levels. Therefore, we assume the extracellular medium between the neuron and probe can be treated as isotropic.

2.5 Summary

Despite numerous studies that model the brain and electrode recordings, from single neuron models to large scale neural field models, and studies on analysis techniques on these same scales, from spike sorting to field potentials, there remains a gap: how large numbers of spiking neurons, $> \mathbf{O}(10^5)$, can contribute to an MER. Understanding how large volumes of neurons contribute to MERs will fill this gap in current scientific knowledge. The early results of Banta in the field of renewal models suggest that the electric field models can relate to the statistics of the inter-spike interval times. However, this connection relies on two conditions. First, the neuron action potential shape needs to be accurate. The Hodgkin and Huxley equation can generate an accurate action potential. This action potential could then be combined with the renewal model to represent the individual neuron behaviour. Second, the neuron behaviour needs to be well modelled by renewal statistics, where the ISI distribution remains stationary in time (time-homogeneous), which may not be the case when brain dynamics are considered. By investigating how well renewal models can be used to determine underlying dynamics will fill these gaps in scientific knowledge. This thesis addresses the deficits in knowledge highlighted above by developing a computationally efficient, renewal process model of STN microelectrode recordings and determining the ISI distribution by inverting the power spectrum of the electric field parametrically. Simulations using the model are tuned and verified using interoperative recordings from patients undergoing implantation of deep brain stimulation electrode. This work then investigates how modifying the IID properties of the model, by including effects such as synchronization and brain dynamics, affect the ability to fit a renewal model to an MER. This will help to identify the validity of using the renewal model of STN MER noise as a potential biomarker of large scale STN behaviour, an approach that has not previously been done.

3 Summary of Papers

Paper A (*An efficient stochastic based model for simulating microelectrode recordings of the deep brain. (2012), Kristian J. Weegink, John J. Varghese, Paul A. Bellette, Terry Coyne, Peter A. Silburn, and Paul A. Meehan, Proceedings of Biosignals 2012, International Conference on Bio-Inspired Systems and Signal Processing. 5th International Joint Conference on Biomedical Engineering Systems and Technologies (BIOSTEC), Vilamoura, Portugal, pp 76-84. 1-4 February 2012.*) contains details on a stochastic model for simulating STN MER recordings. The model simulates 10000's of neurons spike patterns as point processes using a Weibull distribution to describe the inter-spike interval times.

Paper B (*Spikes from compound action potentials in simulated microelectrode recordings. (2015), Kristian J. Weegink, John J. Varghese, and Andrew P. Bradley, 2015 IEEE International Conference on Acoustics, Speech and Signal Processing (ICASSP). 2015 International Conference on Acoustics, Speech and Signal Processing, South Brisbane, QLD, Australia, pp 813-816. 19-24 April 2015.*) contains an extension of the model presented in **Paper A** to account for synchronisation between neurons. The synchronisation is added stochastically using two different methods. The first method gives every neuron an equal probability of firing when a neuron fires. The second method uses a spatially weighted probability of firing when a neuron fires. It is found that the synchronisation doesn't affect the statistics found using the stationary model of this thesis. The other result is that the synchronisation can cause the field contribution from multiple neurons to build up creating a compound action potential (CAP). It is then investigated using spike sorting how the two different methods affect the number of CAPs can be disambiguated.

Paper C (*A Parametric Simulation of Neuronal Noise from Microelectrode Recordings. (2016), Kristian J. Weegink, Paul A. Bellette, John J. Varghese, Peter A. Silburn, Paul A. Meehan and Andrew P. Bradley, IEEE Transactions on Transactions on Neural Systems and Rehabilitation Engineering, Vol 25, no. 1, pp 4-13, Jan. 2017.*) the results from **Paper A** are extended to validate the STN MER model against patient recordings. The number of neurons simulated for the simulation to match the patient recording was found to be ~10,000. The Weibull shape parameter used to best describe the patient data was 0.8. This simple model with a large number of neurons was successful in describing the voltage amplitude

distributions, power spectral density estimates and phase synchrony of patient data while varying only one free parameter (The Weibull shape of the inter-spike interval distribution).

Paper D (*Bayesian Approach for Stationary Analysis of Microelectrode Recordings Using a Neural Mass Model of the Basal Ganglia. (2017), Kristian J. Weegink, Paul A. Bellette, John J. Varghese, Andrew P. Bradley and Paul A. Meehan, submitted to IEEE Transactions on Biomedical Engineering, 2017.*) the model from **Paper C** are extended to include the dynamics of the basal ganglia. A neural mass model is modified to include only first order effects from the time delays between BG structures. The STN dynamics from the neural mass model are then used to drive the MER model. The MER simulations are analysed using the inverse method that assumes stationary statistics. Using this method, it is found that depending on the cortical behaviour, the stationary assumption can be used to successfully analyse the recordings and calculate some properties of the neural mass model.

4 Methodology

Within this chapter the details of the methods used for modelling and analysing MER recordings are given, organized into six sections. Section 4.1, Patient data, contains the patient information and the measurement method used to obtain the microelectrode recordings of the STN during surgery. Section 4.2, Microelectrode model, describes how combining a renewal process for the STN neurons firing with electrical models for the coupling of the neuron to the recording equipment can be used to simulate STN MERs. Analysis methods used for experimental and simulated MERs are presented in 4.3 Validation and Analysis. Section 4.4, Neuron synchronisation, contains modifications to the model from section 4.2 to include synchronisation between neurons. Section 4.5, Brain dynamics, extends the neuron model from section 4.2 by introducing dynamics to the neuron firing times through a neural mass model that simulates the connectivity of the Basal Ganglia, driving the firing times of the STN via different cortical inputs. The final section, 4.6 Summary, provides a summary of the methodology for the investigation using firing time renewal processes for modelling and analysis of single point microelectrode recordings of the subthalamic nucleus.

4.1 Patient Data

Patient data is required to validate the model and for use in case study analysis. Due to the limited availability of deep brain recordings all the data used in this thesis has been acquired from patients undergoing surgical implantation of a DBS stimulator for the treatment of PD. The data used in this thesis was obtained through a collaboration across a large multidisciplinary team. The experiments were designed and performed for a separate study, after the completion of which the data sets were made available for this study. This prevented acquisition of new data sets to allow exploration beyond the initial results.

Nine participants (five male, four female) with idiopathic PD who were considered suitable for the implantation of bilateral permanent stimulator in the STN were included in this study. The patient age was 67 ± 5 years, with disease duration of 14 ± 6 years. Participants were all right handed and had no further neurological impairment. The participants had undergone psychiatric screening prior to DBS surgery. A summary of the patients is given in Table 2.

The dorsolateral aspect of the STN was targeted using a Cosman-Roberts-Wells frame-based stereotactic frame with coordinates based on CT images fused with 3T MRI t1 and FLAIR sequences. The electrode placement was confirmed inter-operatively by an MER. The surgical procedure is described in detail in (Coyne, et al., 2006). Tungsten microTargeting electrodes (model mTDWAR, FHC, Bowdoinham, ME) with a tip diameter of less than $50\mu m$ were used for the MER acquisition. The electrodes had a typical impedance of $0.5 \pm 0.15\ M\Omega$ at 1kHz. A LeadPoint© system (Medtronic Inc., Minneapolis, MN) was used to record the signals at a sampling rate of 24kHz. Three filters were applied (high pass:500Hz first order, low pass:5kHz first order and anti-aliasing:5kHz fourth order) as recommended by Medtronic. After the targeting electrode was inserted into the patient, they were examined for the stimulation effect on clinical signs (dyskinesia, tremor, rigidity, bradykinesia) and absence of adverse effects. To reduce patient variability if significant clinical symptoms were present, judged by the neurologist, data capture was not performed. After confirmation of the target the MERs were recorded. To further control for the variability in patient physiology and pathology each MER was recorded during resting phases, when the participant was lying still and not performing any cognitive or movement tasks. Recordings that contained movement artefacts and recordings from patients whose reaction time was less than a threshold were discarded.

Table 2 - SUMMARY OF PARTICIPANTS FOR WHOM MER RECORDINGS WERE USED FOR THE VALIDATION OF THE MODEL

Participant	Age	Gender	Education	Handedness	Disease Duration	Severity (H&Y)	UPDRS III score	Side of MER
32	73	M	14	Right	8	NA	NA	Left
38	58	M	11	Right	11	2	3	Bilateral
53	71	M	13	Right	16	4	20	Bilateral
61	71	F	10	Right	17	3	17	Bilateral
69	66	F	14	Right	22	NA	NA	Bilateral
74	65	F	7	Right	15	2	11	Bilateral
103	62	M	9	Right	20	2	8	Right
104	71	M	10	Right	3	NA	NA	Bilateral

Note: H&Y = Hoehn and Yahr; UPDRS = Unified Parkinson's Disease Rating Scale; NA not available.

4.2 Microelectrode Model

This section describes how each part of this model is created to simulate MERs and is based on **Papers A & C**. The STN MER simulations created as part of this thesis involves reducing the individual neurons to renewal processes, where the ISI times are drawn randomly and are independent and identically distributed (IID). The spike trains of tens of thousands of neurons can be generated using this method. The neurons are then distributed around the electrode tip. The shape of the action potential shape is super imposed at the spike times and biological filtering affects are applied based on the distance from the neuron to the electrode. The signals from all the neurons are combined, along with noise, and the effects of the recording equipment are applied. A summary of the MER model is provided in Figure 17 and the details are provided in the following sections.

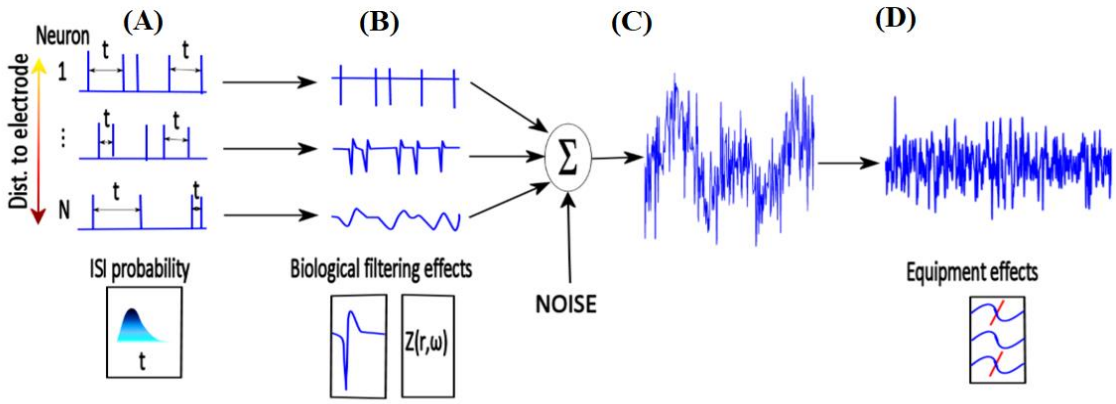

Figure 17 - Flow diagram summarizing how the MER simulations are performed. Neurons are generated around the electrode at different distances. (A) The spike times of the neurons is then generated by drawing the ISI times from randomly from a distribution function. (B) The effect of the electric field travelling through the extracellular medium is applied to each neuron individually. (C) The signal from each neuron is combined, and (D) then the filters used in the experimental acquisition are applied.

4.2.1 Neuron spike current

The STN firing times are modelled by assuming the ISI times form a random variable drawn from a Weibull distribution, Figure 17 (A), in time:

$$P(t) = \left(\frac{t - t_r}{\lambda}\right)^{c-1} \frac{c}{\lambda}\, e^{-\left(\frac{t-t_r}{\lambda}\right)^{c}} \quad for\ t > t_r \tag{26}$$

$$otherwise\ P(t) = 0, \tag{27}$$

where $P(t)$ is the probability density function for the ISIs and λ is the scale parameter that controls the firing rate. The shape parameter c controls the neuronal behaviour; with $c < 1$ generating burst firing, $c = 1$ Poisson statistics and $c > 2$ firing times with a common mode, as shown in Figure 18. In the limit of $c \to \infty$ periodic behavior emerges. The parameter t_r controls the refractory time of the neuron, preventing another action potential occurring within this period.

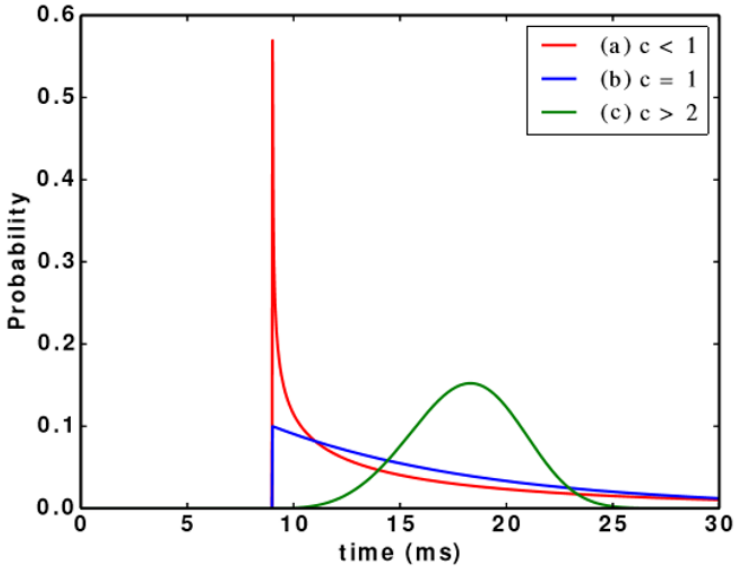

Figure 18 - Examples of how the shape parameter, c, modifies Weibull distributed ISI times. Example ISI distributions that describe (a) burst firing, (b) Poisson firing and (c) periodic firing.

The neuron spike timing consists of a time series of Kronecker-delta pulses which are first created by drawing the ISI times from the Weibull distribution. Shape parameter, *c*, values of 0.5, 0.8, 1, 10 and 100 are used to validate the model against patient data. The scale parameter used corresponds to a firing rate of 30Hz and a refractory time of 9ms was used based on (Theodosopoulos, et al., 2004). The spike timing is converted to a neuronal current time series by convolving the Kronecker-delta pulses with the action potential shape. This process is used by all the neurons simulated.

4.2.2 Action potential shape

To apply the extracellular filtering affects, Figure 17 (B), the shape of the action potential at the neuron is required. The action potential shape is generated by numerically solving a Hodgkin and Huxley model using a variable order solver. The Hodgkin and Huxley model parameters used were for the medium spiny neuron based on (Terman, et al., 2002):

$$C_m = \frac{dV}{dt} \tag{28}$$

$$C_m = -g_L(V - v_L) - g_K n^4(V - v_K) - g_{Na} m^3 h(V - v_{Na}) - G_T a^3 b^2(V - v_{Ca}) - g_{Ca} s^2(V - v_{Ca}) \tag{29}$$

where C_m is the membrane capacitance (1pF/μm^2); g_L, v_L are the leak conductance and reversal potential (2.25nS/μm^2 and -60.0mV respectively); g_K, v_K are the K^+ conductance and equilibrium potential (45nS/μm^2 and -80.0mV respectively); g_{Na}, v_{Na} are the Na^+ conductance and equilibrium potential (37.5nS/μm^2 and 55.0mV respectively); g_T is a low-threshold T-type Ca^{2+} conductance (0.5nS/μm^2); and g_{Ca}, v_{Ca} are a high-threshold Ca^{2+} conductance and a Ca^{2+} equilibrium potential (0.5nS/μm^2 and 140.0mV respectively). The gating variables *n*, *m*, *h*, *a* and *b* follow the ODE given in Equation (30), the physical parameters used are summarized in Table 3 (Terman, et al., 2002). The action potential produced is resampled at 24kHz to match the sample rate of the recording equipment.

$$\dot{x} = \alpha_x(V)(1 - x) - \beta_x(V)x. \tag{30}$$

Table 3 - SIMULATION PARAMETERS FOR THE HODGKIN AND HUXLEY MODEL OF THE STN.

Parameter	Value
C_m	$1\,pF/\mu m$
g_L	$2.25\,nS/m^2$
v_L	$-60.0\,mV$
g_K	$45\,nS/m^2$
v_K	$-80.0\,mV$
g_{Na}	$37.5\,nS/m^2$
v_{Na}	$55.0\,mV$
g_T	$0.5\,nS/m^2$
g_{Ca}	$0.5\,nS/m^2$
v_{ca}	$140.0\,mV$

4.2.3 Neuron-Electrode interaction

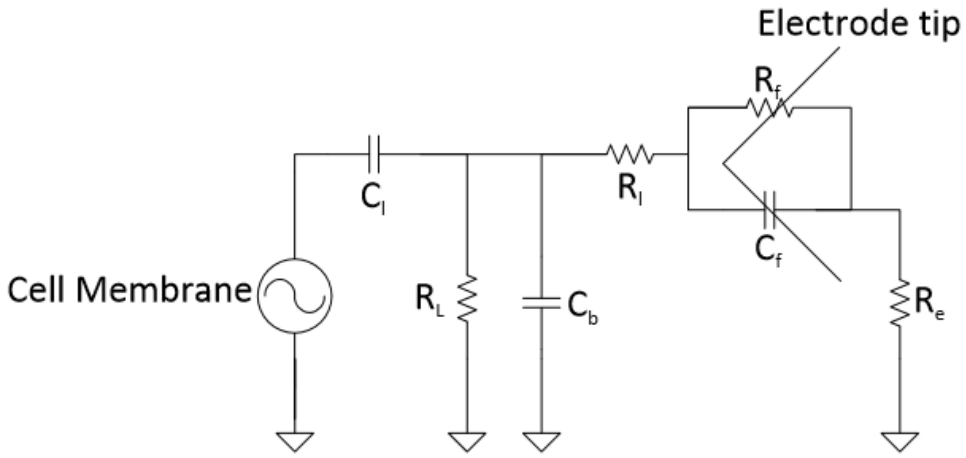

Figure 19 - Circuit diagram of the electrical model used for MER simulations. The cell membrane is treated as a signal generator that is coupled to the extracellular medium through a capacitor (C_l). R_l represents the resistance of the extracellular medium between the neuron and electrode. R_L and C_b model the leakage resistance and capacitance of the body. The electrode is modeled with faradic coupling, R_f and C_f, and a resistance R_e.

To couple each neuron to the electrode, Figure 17 (B), the extracellular effects need to be considered. To do this each neuron is modelled as a point source, by assuming the current is being generated from only the axon hillock and it is small ($\sim 1\mu m$) compared to the electrode tip ($\sim 50\mu m$). The current time series is then filtered using an impedance based on the distance of the neuron from the electrode to find the potential contributed by each neuron. This model assumes a far-field approximation to the electric field incident on the electrode. This allows us to sum the voltages linearly after they are found through the relation:

$$V_{\omega(r)} = I_\omega \, Z_{\omega(r)} \tag{31}$$

where I_ω is the frequency components of the current at the neuron. The impedance filter Z_ω is found by determining the transfer function $\frac{I_\omega}{V_\omega}$ for the circuit model for the neuron-electrode interaction, shown in Figure 19. This circuit model evaluates the propagation of the electric field through the extracellular medium, and is not an actual electron current. Circuit element values in this model depend on the radial distance between the electrode and neuron, the size of the electrode tip and the impedance of the electrode, where C_l is the membrane-electrolyte interface capacitance, R_L is the body resistance to ground (the spread of the field from the neuron), C_b is the body's capacitance, R_l is the resistance between the cell and the electrode (seal of the electric field by the neuron to the electrode (James, et al., 2004) (McIntyre, et al., 2004)), R_f and C_f are the electrode Faradic resistance and capacitance

and R_e is the electrode resistive load. The voltage for the recording, V_ω, is taken across the load resistance (R_e).

The neuron radial distribution, $N(r)$ where r is the distance from the electrode, is randomly generated using a uniform spatial distribution with density, $\rho = 10^5 cm^{-3}$ (Theodosopoulos, et al., 2004).

$$N(r) = 4\pi\, r^2 \rho \tag{32}$$

The complete time series from all neurons are then summed together linearly to create the potential across the electrode, Figure 17 (C). Thermal white noise (Johnson-Nyquist noise) is added to the electrode to match experimental conditions. The statistics of the noise are described by:

$$\langle V \rangle = 0,\ \langle V^2 \rangle = 4k_B T R(f) \Delta f \tag{33}$$

where k_B is Boltzmann's constant, T is the temperature (assumed to be average body temperature $37^o C$, $R(f)$ is the electrode resistance, Δf is the bandwidth of the recording and $\langle \ldots \rangle$ represents the time average. The product $R(f)\Delta f$ is calculated by integrating the product of $R(f)$ with the gain function $G(f)$ of the equipment over frequency:

$$R(f)\Delta f = \int_0^\infty R(f)G(f)\, df \tag{34}$$

To match simulations to the surgical conditions, Figure 17 (D), the simulated voltage time series is passed through three filters described in section 4.1. The filters are models of the two software filters with a 500Hz first order high pass, 5kHz first order low pass and the hardware 5kHz fourth order anti-aliasing filter. $G(f)$ is found by multiplying a flat unity power spectrum, $P(f) = 1$, by the filter gains.

4.3 Validation and Analysis

This section contains the methods used to validate the MER model by comparing features to what is seen in the patient recordings and contains the work in **Paper C**. The MER model is a top-down model, where details are added to the model so that it can reproduce features found in experimental data. Section 4.3.1 contains the validation methods used to determine what features of the patient data the model can reproduce. Section 4.3.2 has the details on how to fit the model to an MER, used to test how well the renewal model matches simulations where the IID assumption is relaxed in **Paper B** and **Paper D**.

4.3.1 Validation of modelled MERs using patient recordings

The validation of the model is broken into three sub sections. The sub-sections look at the distribution of signal amplitude in the time domain, linear fits of the modelled power spectral estimate to patient power spectral estimates and comparisons of synchronous phase components of the modelled MER to patient MERs. These tests assess how well the model describes the first order statistics of the patient recordings, the distribution of amplitudes in the time and frequency domain as well as the phase distributions in the frequency domain.

For the analysis in this section the tests are averaged over multiple recordings from the same patient and the two separate patient sides (left, right) were analysed separately. Patient recordings that contained movement artefacts, defined by amplitude > 10 mV, or had recording times less than 1s were removed from the analysis. After this removal process, 84 MERs from 14 patient-hemispheres are left.

4.3.1.1 Test of Voltage Distributions

In time, MERs are stochastic in nature, meaning two signals in the time domain cannot be compared by correlation of how their voltage changes in time. To perform a comparison in the time domain the distribution of voltages observed can be used. A two-sided Kolmogorov-Smirnov (KS) test is used on the distribution of the voltages in time. The KS test produces a p-value that the amplitudes for the patient recordings are drawn from the same distribution as the simulated MERs. The statistic is found by taking the supremum (maximum) of the distance between empirical cumulative distribution functions, $F_i(x)$, for the two distributions:

$$D = \sup_{\mathrm{x}} \left| F_{patient}(x) - F_{simulation}(x) \right| \qquad (35)$$

This test is symmetric for patient data compared to simulation, versus simulation compared to patient data. It is used as a goodness of fit for the simulation data fitting the patient data.

4.3.1.2 Power Spectrum Comparisons

Power spectra for the patient and simulated recordings are calculated using Welch's overlapping segment method with a Hamming window (Welch, 1967). The power spectra are estimated for five different simulation parameters, c = [0.5, 0.8, 1, 10, 100], and compared to the 14 patient-hemisphere recordings using linear regression. The linear

regression is performed between patient power spectral estimate, $P_{patient}(\omega)$, against the simulated power spectral estimate for each frequency:

$$P_{patient}(\omega_i) = a\, P_{simulation}(\omega_i)\ \forall\ \omega_i\ . \tag{36}$$

The correlation coefficient, R^2, was used to assess the goodness of fit for the simulation data fitting the patient data.

4.3.1.3 Phase comparisons

To compare the phase components, and to complete a comparison of the first order statistics of the patient and simulation MERs, the component synchrony measure (CSM), (Fridman, et al., 1984), is used:

$$CSM(\omega)\ =\ 1 - var\{\varphi(\omega)\}. \tag{37}$$

The individual recordings are divided into 100ms non-overlapping sections. The variance of the phase for each frequency for each section can be found using:

$$var\{\varphi(\omega)\} =\ 1 - \left[\frac{1}{N}\sum_{i=1}^{N}\cos\varphi_i\,(\omega)\right]^2 - \left[\frac{1}{N}\sum_{i=1}^{N}\sin\varphi_i\,(\omega)\right]^2 \tag{38}$$

where $\varphi_i(\omega)$ is the phase of the signal at frequency ω for signal segment *i*. The phase is found by taking the Fourier transform ($F[\,](\omega)$) of the signal segment ($x(t)$) and taking the inverse tangent of the ratio of the imaginary to real component, as,

$$\varphi_i(\omega) = \tan^{-1}\frac{Im\{F[x(t)](\omega)\}}{Re\{F[x(t)](\omega)\}}. \tag{39}$$

A KS test is then used between the distribution of CSM across all the patient recordings versus the distribution over an equal number of simulations to determine the goodness of fit.

4.3.2 Fitting the Model to an MER

To analyse the signals generated by the MER simulations we model the spike trains generated as renewal processes. For a renewal process the ISI times are independently drawn from a single probability distribution that does not change in time. Modelling the ISI times (*t*) as independent events drawn from a Weibull distribution, shown in Equation (40) (where k is the shape parameter and λ is the scale), allows a parametric method of fitting the model.

$$f(t;\lambda,k) = \frac{k}{\lambda}\left(\frac{t}{\lambda}\right)^{k-1} e^{-\left(\frac{t}{\lambda}\right)^{k}} \quad , \forall\ t > 0 \tag{40}$$

To differentiate between the Weibull shape parameter used for simulations, *c*, when the renewal model is being fitted to an MER, *k,* will be used for the shape parameter.

To find the shape parameter power spectral estimates of the simulated MER using Welch's method with five non-overlapping square windows are used. The inverse gain of the recording device is applied, using a regularization term that offsets the minimum gain to prevent amplification of noise. The power spectral estimate is then fit using least squares to the predicted power spectrum using the Marquardt-Levenberg algorithm. The predicted power spectrum of a renewal process ($P(\omega)$) is given by (Banta, 1964):

$$P(\omega) = A \cdot G(\omega)\left[1 + Re\left\{\frac{H(\omega,k)}{1 - H(\omega,k)}\right\}\right], \qquad \forall\ \omega > 0 \tag{41}$$

where $G(\omega)$ is the action potential power spectrum (found using the HH model presented in 4.2.2), $H(\omega,k)$ is the characteristic function of the Weibull distribution for shape parameter k, and A is a scaling factor that accounts for the rate, the number of neurons contributing to the signal, and the distance of the neurons to the electrode. Details on the derivation of Equation (41) is given in Chapter 2.2.2. The factor A creates a degeneracy between the rate, neuron distance and neuron number. This degeneracy means the rate parameter found with the least squares fit is unable to uniquely determine the rate used for the simulation. However, as the literature review showed, the coefficient of variation, an important metric in neural coding, is defined in terms of only the shape parameter. The rate parameter may not be important in characterizing the ISI distribution for the neural signals analysed and is thus ignored.

4.4 Neuron Synchronisation

To determine if synchronised firing between neurons affects the ability to fit the renewal model to the recordings, two methods of including synchronisation between neurons are added to the model from 4.24.2. This work is presented in **Paper B**.

A subset of synchronized neurons is defined at random during the initialization of the simulation. The neural spike times are generated following the same procedure as section 4.2. An additional renewal time series is generated using the same ISI distribution. At the

spike times of this additional time series a spike is added to the subset of neurons selected to be synchronized. If a neuron fires as part of a synchronized subset, the next firing time is reset and redrawn from the single neuron ISI distribution. The MER simulation is then completed using the methods in section 4.2.

To generate multiple synchronized sets of neurons, the process described above is repeated with a different group of neurons selected and a separate probability distribution for synchronized timing events generated. Neurons that synchronize in one group can still synchronize in another group. For spatial localization of groups, the neurons are selected using a Gaussian distribution in space, centred with a random distance from the electrode and a standard deviation that increases with the distance from the electrode, shown in Figure 20.

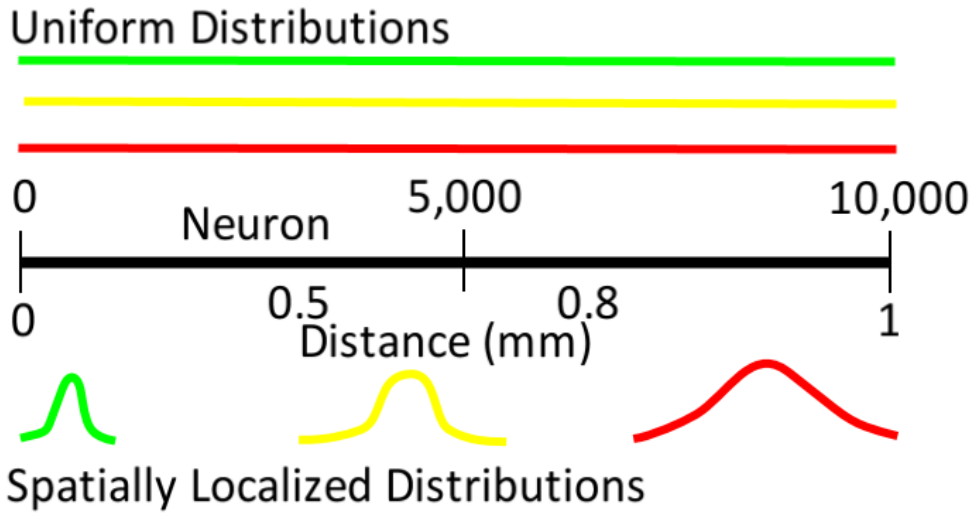

Figure 20 - Spatial distributions of the likelihood of neurons firing when another neuron fires. The top three lines represent the probability distribution function of a neuron coupling with equal likelihood to any other neuron. The bottom lines represent the probability distribution of a neuron coupling to neurons that are spatially close.

Previous analysis of STN recordings by Moran *et al.,* which looked at the differentiation of spiking activity and background spike activity, could not be used for this study due to the differences in impedance of the electrodes used and the acquisition hardware settings (Moran, et al., 2008). This difference in electrode required development of a study specific analysis method. The signal to noise ratio (SNR) of the spikes is calculated by taking the average peak amplitude for a spike above a user set threshold and comparing it to the root mean square (RMS) voltage of the noise. The spike sorting analysis of the recordings is performed using Osort (Rutishauser, et al., 2006), with compact support bi-orthogonal '1.5'

wavelet at individual wavelet scales corresponding to between 0.1 and 1ms. The clustering is unsupervised, with cluster validity checked by comparing spike timing to the synchronized times in the simulation.

4.5 Brain Dynamics

To investigate if the IID ISI times assumption of renewal processes is suitable for modelling of STN MERs the spike timings are generated by using a basal ganglia (BG) neural mass model. The microelectrode model from section 4.2 is modified to use these spike timings. This work can be found in **Paper D**.

4.5.1 Basal Ganglia model

For the neural mass model, the classical direct-indirect pathway model of the basal ganglia is used (Figure 21) (Albada & Robinson, 2009). This involves modelling the cortex with excitatory (Glutamate) projections into the D1 and D2 cells in the striatum. From the straitum D1 cells inhibit the globus palidus internal (GPi). The D2 cells inhibit the globul palidus external (GPe), which in turn inhibits the STN. The STN then has excitatory projections into the GPi. The GPe has inhibitory (GABA) projections into itself and the GPi. The STN also has excitatory connections into itself and the GPe. The GPi then projects into the thalamus and the brainstem, but this feature is not included in this paper. This seemingly simple model is successful at describing the pathophysiological processes, such as those involved in Parkinson's Disease (Albada & Robinson, 2009) (Albada, et al., 2009) (Liu, et al., 2017).

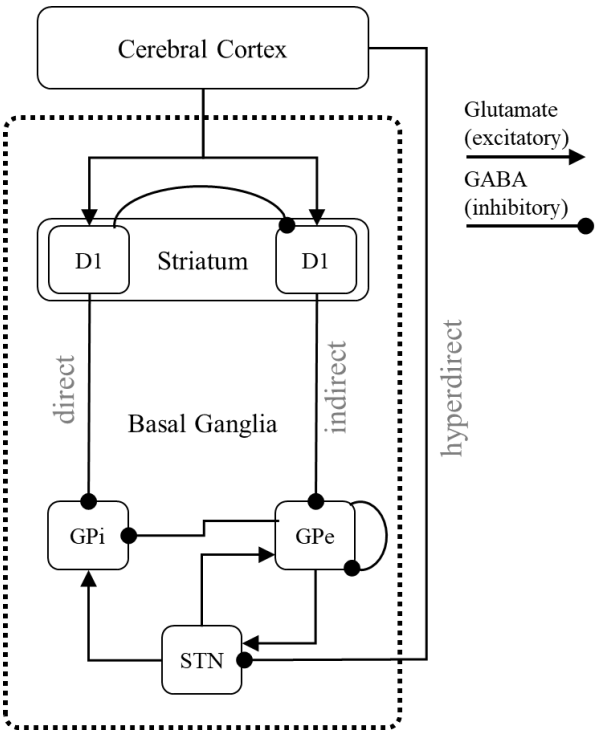

Figure 21 - Direct and indirect pathways in the Basal Ganglia. The neural mass model includes the connections of the pathways described here. In the Striatum two sets of dopaminergic cell groups are modelled, D1 and D2. The GPi, GPe and STN are modelled as single groups of cells. The Cerebral Cortex is the input to the model and several different classes of functions are used to see how their properties affect the STN MER.

A neural mass model involves modelling groups of neurons by using the Fokker-Plank equation to describe how the distribution of firing rates for a given group of neurons evolve over time and how different groups interact (Deco, et al., 2008). These types of equations can be simplified by performing a first order expansion about the statistical moments, resulting in a system of ordinary differential equations which describes their average firing rate for a group of neurons given by:

$$\dot{\mu_v} = y_v \tag{42}$$

$$\dot{y_v} = ab\left[\sum_k \alpha_{vk}\zeta(\mu_k(t-\tau_{vk})) - \left(\frac{1}{a}+\frac{1}{b}\right)y_v - \left(\frac{1}{ab}\right)\mu_v\right] \tag{43}$$

$$\zeta(\mu_v) = \frac{S_{max}}{1+e^{k(\theta-\mu_v)}} \tag{44}$$

where y_v is a dummy variable used to represent the second order system as a first order, μ_v is the mean voltage of the target nuclei, α_{vk} is the strength of coupling from the nuclei k to the target and τ_{vk} is the axonal propagation delay, S_{max} is the maximum firing rate of the target, a is the decay time constant of the membrane and b is the rise time constant, θ is the potential that gives half the maximum firing rate and k controls the slope of the sigmoid

to give realistic rates for a given input potential. The parameters used for the simulations using the neural mass model are listed in Table 4.

Equation (43) introduces the delays caused by axonal propagation between structures, τ. The delays increase the time for a numerical solution due to the different time scales involved preventing the use of variable time step solvers. When the delays are small compared to the characteristic times of the dynamics, the system can be approximated using perturbation analysis. All the delays are passed through the sigmoid function; therefore, a Taylor expansion of the sigmoid function can be performed, and sufficiently small terms can be truncated. The first expansion is performed around t:

$$\zeta\big(\mu_v(t-\tau)\big) = \zeta\big(\mu_v(t)\big) + (t-\tau-t)\frac{d\zeta\big(\mu_v(t)\big)}{dt} + \frac{(t-\tau-t)^2}{2!}\frac{d^2\zeta\big(\mu_v(t)\big)}{dt^2} + O(\tau^3) \tag{45}$$

$$\zeta\big(\mu_v(t-\tau)\big) = \zeta(\mu_v) - \tau\zeta'(\mu_v)\frac{d\mu_v}{dt} + \frac{\tau^2}{2!}\left[\zeta'(\mu_v)\frac{d^2\mu_v}{dt^2} + \zeta''(\mu_v)\left(\frac{d\mu_v}{dt}\right)^2\right] + O(\tau^3) \tag{46}$$

where $\zeta'(\mu_v(t))$ denotes the derivative with respect to μ_v and has been introduced into the equations using the chain rule and for convenience $\mu_v(t)$ is written as μ_v. Considering the faster time constant, the membrane potential gain, is on the order of 2ms, the τ^2 term is very small (three orders of magnitude) in comparison to the decay and rise times of the membranes (a = 160s^{-1}, b = 640s^{-1}). This allows us to neglect terms $O(\tau^2)$ and substituting into the dynamics for the neural structures yields a nonlinear first order differential equation:

$$\dot{y_v} = ab\left[\sum_k \alpha_{vk}(\zeta(\mu_k) - \tau_{vk}\zeta'(\mu_k)y_k) - \left(\frac{1}{a}+\frac{1}{b}\right)y_v - \mu_v\right] \tag{47}$$

This linearization decreases the time for a numerical solution which allows large numbers of simulations to be performed. The large number of simulations allows production of a large sample of the statistics using random processes for cortical simulation. It also allows Monte Carlo simulations to be performed for analysis of the system.

Table 4 - SIMULATION PARAMETERS FOR THE NEURAL MASS MODEL OF THE BASAL GANGLIA.

	Cortex	D1	D2	GPi	GPe	STN
S_{Max} (spikes/s)	-	65	65	250	300	500
k (mV^{-1})	-	0.3	0.3	0.2	0.2	0.2
θ(mV)	-	19	19	10	9	10
$\alpha_{D1,k}$ (mV s)	1.0	-	-	-	-	-
$\alpha_{D2,k}$ (mV s)	0.7	-	-	-	-	-
$\alpha_{GPi,k}$ (mV s)	-	-0.1	-	-	-0.03	0.3
$\alpha_{GPe,k}$ (mV s)	-	-	-0.3	-	-0.1	0.3
$\alpha_{STN,k}$ (mV s)	0.1	-	-	-	-0.04	-
$\tau_{D1,k}$ (ms)	2	-	-	-	-	-
$\tau_{D2,k}$ (ms)	2	-	-	-	-	-
$\tau_{GPi,k}$ (ms)	-	1	-	-	1	1
$\tau_{GPe,k}$ (ms)	-	-	1	-	1	1
$\tau_{STN,k}$ (ms)	1	-	-	-	1	-

4.5.2 Modifications to Microelectrode Model

To integrate the MER model with the neural mass model, the method for generating the spike times needs to be modified. The renewal model determines the firing times by drawing a random variable that describes the length of time until the neuron fires again. The neural mass model describes an instantaneous firing rate of the neural population. The instantaneous firing rate, ν, can then be turned into the firing times using an inhomogeneous Poisson process. The Poisson process, Equation (48), is a counting process of the probability of N spikes, *P(N=n)*, within a time (δt) and results in the firing times of the neurons being completely independent of each other, according to,

$$P(N = n) = \frac{(\nu \delta t)^n}{n!} e^{\nu \delta t} \quad (48)$$

This results in ISI times of a Poisson process being exponentially distributed (Weibull shape parameter of unity). The Poisson process can be extended to have a rate parameter as a

function of time ($\nu(t)$). This type of Poisson process is an inhomogeneous Poisson process. One example of an inhomogeneous Poisson process is the Cox process where the rate parameter is itself a stochastic variable. The importance of the Cox process for this study is that it has been shown that the firing times of the Cox process can be modelled using a Weibull distribution for the ISI times and it motivates fitting the neural mass simulations using the renewal model.

To calculate the firing times, the simulation is divided into times equal to the sample rate of the equipment, 24kHz. The instantaneous Poisson firing rates of the neurons in the STN (ν) are determined from the neural mass model at each time sample. Equation (49) is used to determine if there is at least one spike in the sampling time $\left(\delta t = \frac{1}{24000} s\right)$.

$$P(N \geq 1) = 1 - P(N = 0) = 1 - e^{\nu \delta t} \qquad (49)$$

After the firing times are determined the MER simulation is then completed using the methods in section 4.2.

4.5.3 Simulations

To simulate MER recordings, the cortical input to the model is required. The cortical input for the BG model can vary depending upon the patient state and task being performed. Although there are numerical models to simulate this, due to the ability of this input to change in a non-deterministic way (Brittain & Brown, 2014) (Kuhn, et al., 2008) (Marreiros, et al., 2013), it is more useful for this study to look at how the renewal model fits specific classes of cortical input functions. The four different cortical inputs ($\mu_{ctx}(t)$, shown in Figure 22) are: sinusoidal ($\mu_{ctx}(t) = C + B[\sin(Dt)]$), where B and D are varied, a Weiner process ($\frac{d\mu_{ctx}}{dt} = DW_t$), where D is varied and an Ornstein–Uhlenbeck (OU) process ($\frac{d\mu_{ctx}}{dt} = -\frac{1}{\tau}\mu_{ctx} + DW_t$) where τ is varied. These functions are chosen as they represent a deterministic process, a Gaussian process, and a Gauss-Markov process respectively.

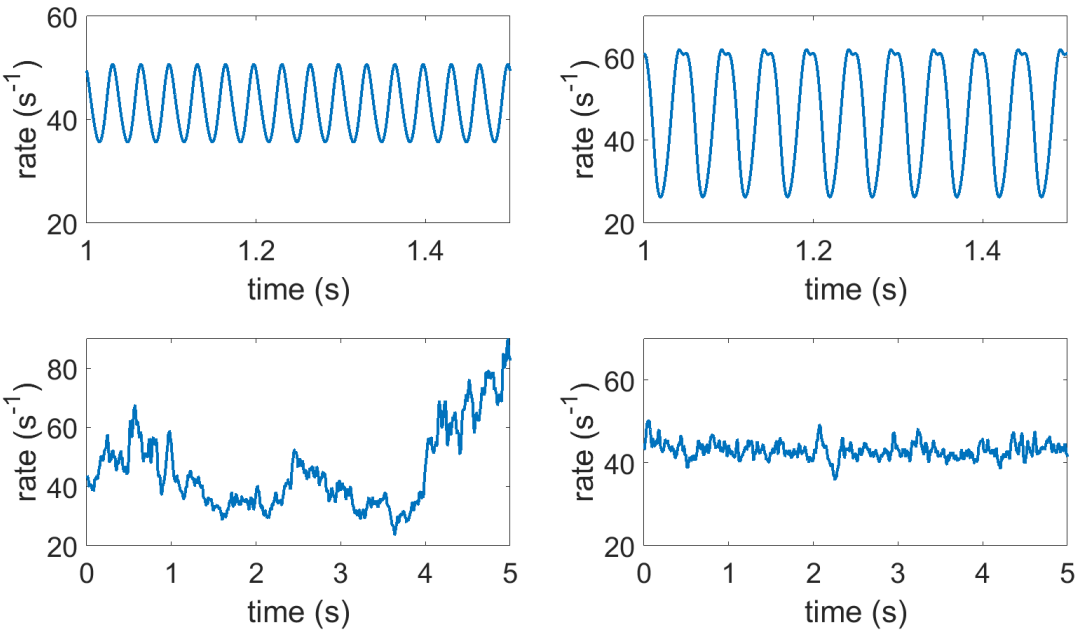

Figure 22 - Example rate evolution using different cortical inputs a) Varying the sinusoidal frequency, b) Varying the sinusoidal amplitude to the point that the non-linearities begin to affect the system c) varying the Diffusion constant of a Weiner process and d) varying the correlation time of a damped weiner process.

4.6 Summary

The methodology outlined here provides the necessary tools to investigate microelectrode recordings of the subthalamic nucleus using firing time renewal processes for modelling and analysis. The primary model developed, an outline of which is presented in Figure 17, uses a point process model where the ISI times are drawn from a Weibull distribution. A field of 10000 neurons is generated homogenously distributed around the electrode tip. The spike times for the neurons are convolved with an action potential shape which includes extracellular filtering effects based on the neurons distance to the electrode. All the neurons electrical signals picked up by the electrode are combined and recording equipment effects are added.

The point process model is a renewal process and hence assumes the neurons have IID ISI times. To investigate the effects these assumptions could have on a time homogeneous analysis of MERs the model is first extended to include synchronisation between different neurons, and second the firing times are generated using a neural mass model to simulate the dynamics of the BG. The synchronisation is included using two statistical models for neuron interaction shown in Figure 20. The models include a uniform probability of neurons

coupling and a spatially weighted probability of neurons coupling. The dynamics of the BG are modelled using a neural mass model which reduces the different brain components involved into an average firing rate of all the neurons within the structure. Three mathematically interesting cortical firing rate patterns are used to investigate potential changes in MERs; the cortical inputs include sinusoidal changes in the rate, the firing rate evolving as a Weiner process and as an OU process.

The theoretical models and experimental validation developed can provided new insights into the potential use of MERs in diagnosis of disease and brain machine interfaces such as adaptive DBS. In particular the model will help determine any neuronal sources that contribute to the high frequency background noise of MERs. Also, an investigation of fitting the renewal STN MER model to more complicated models will motivate further work into uses as a biomarker. The results of these investigations are presented in the following chapter.

5 Results

The important results of the methodology described in Chapter 4 to investigate microelectrode recordings of the subthalamic nucleus using renewal processes are contained within this chapter. The results and conclusions are presented in three sections. The first section, 5.1 Microelectrode Model, contains results from tuning of the MER simulations using the point process model combined with the electrical model of the neuron electrode interactions. Section 5.2, Neuron synchronisation, demonstrates the effects of the synchronisation models on MERs along with analysis of these effects. The next section, 5.3 Brain dynamics, presents verification of the reduced model. The final section, 5.4, contains a summary of the important results relevant to using renewal processes for investigating MERs and the novel contributions of these results.

5.1 Microelectrode Model

This section describes the results that relate to the selection of the MER model parameters, benchmarking the simulations and then validation of the simulations against patient MERs. Results from this section are from **Paper A** and **Paper C**. The results are presented in two sections, 5.1.1 Simulations contains the parameter selection, qualitative results from simulations and benchmarking the simulation performance. Section 5.1.2 has the quantitative comparison of the simulated MERs to the patient MERs.

5.1.1 Simulations

This section contains the results used to select model parameters, a qualitative look at the results of the simulations and benchmarking the time performance of the simulations. A discussion on the interpretation of the results is also provided.

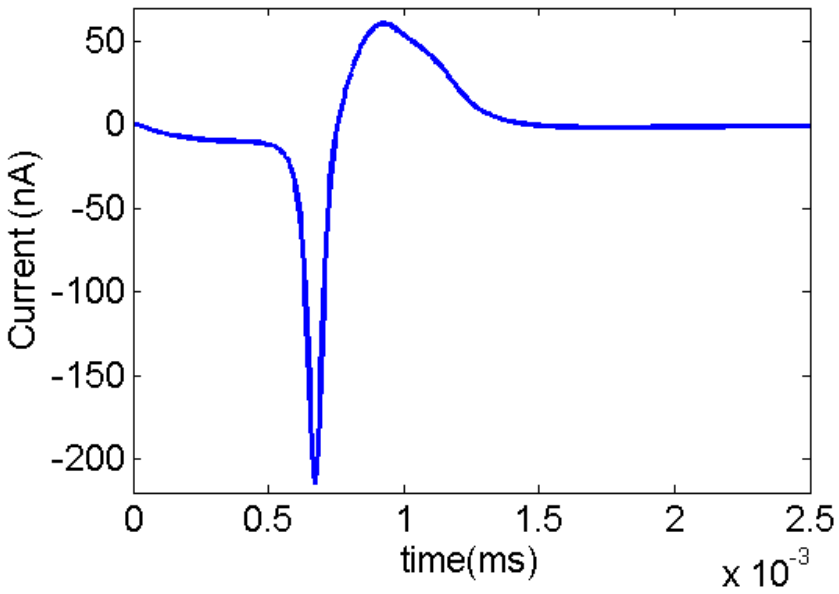

Figure 23 -The extracellular current used for each neuron generated using the Hodgkin and Huxley model of the STN pyramidal neurons in Equation (29) described in Chapter 4.2.2.

To be able to simulate the MERs the shape of the extracellular action potential (EAP) is required. A Hodgkin-Huxley type model was used to generate the EAP (see Figure 23) for a STN cell, based on the parameters outlined in the methodology. The equations were solved until the EAP settled to 0 nA and re-sampled to 24kHz. Figure 23 shows the waveform convolved with the spike times to produce the neuron currents.

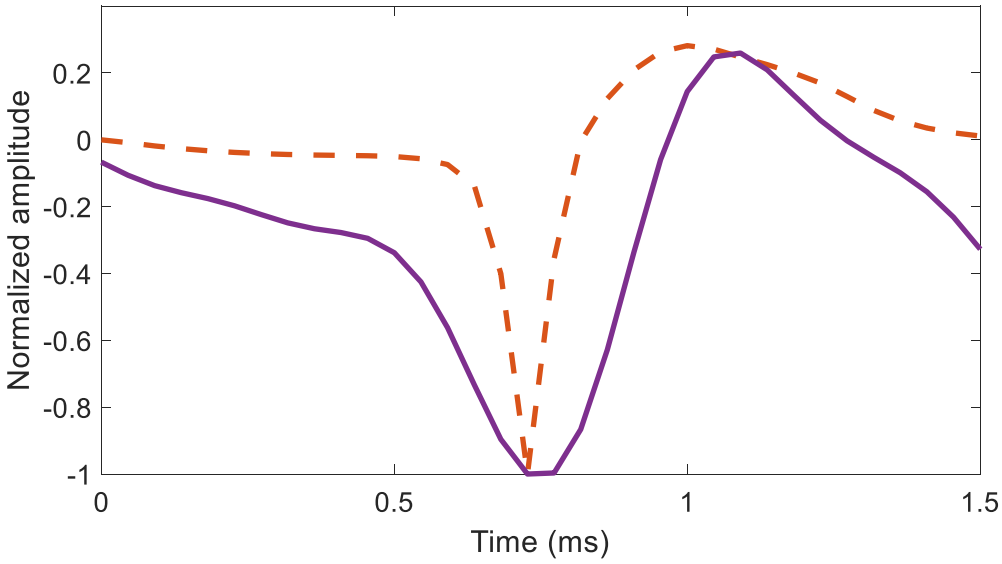

Figure 24 - Comparison of the simulation action potential current and the average spike detected in the patient MER.

Validation of the action potential current for the patients is not possible, due to the inability to do *in-vivo* recordings of the current. The shape of the action potential can be compared to the shape of the action potential detected at the microelectrode, Figure 24. The AP

detected by the microelectrode has a slower oscillation than the current waveform due to the filtering effects of the extracellular medium and the electronic equipment. The filtering effects make it difficult to make a quantitative assessment, however qualitative agreement for the timing and number of peaks is present.

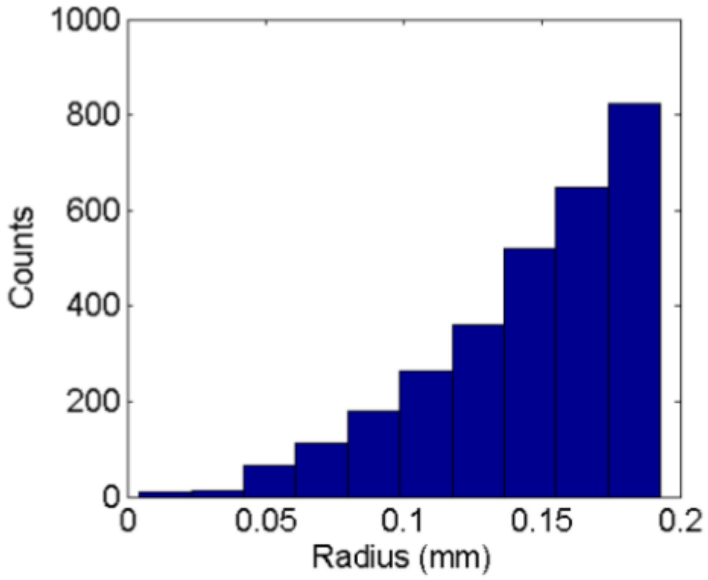

Figure 25 - A histogram of the neurons distance from the electrode used for the simulation. As the number of neurons is increased they are added further away from the electrode, increasing the volume simulated.

To determine the number of neurons required for the simulation to match patient recordings, 30s simulations are produced with different neuron numbers. Figure 25 shows the distribution of neurons around the electrode for a simulation. As neurons are added following Equation (7) using a constant density, they are placed further from the electrode. This means that the volume simulated is increased as neurons are added. Figure 26 shows how the root mean square (RMS) value of the simulated MERs changes as the neuron number is changed. Above 3,000 neurons the RMS value plateaus. The peak RMS value approaches $49\mu V$. This is within one standard deviation of the mean RMS value for all the patient recordings of $56 \pm 12\mu V$. These results correspond to a simulation volume of approximately 1mm^3, agreeing with the result found by (Camunas-Mesa & Quiroga, 2013).

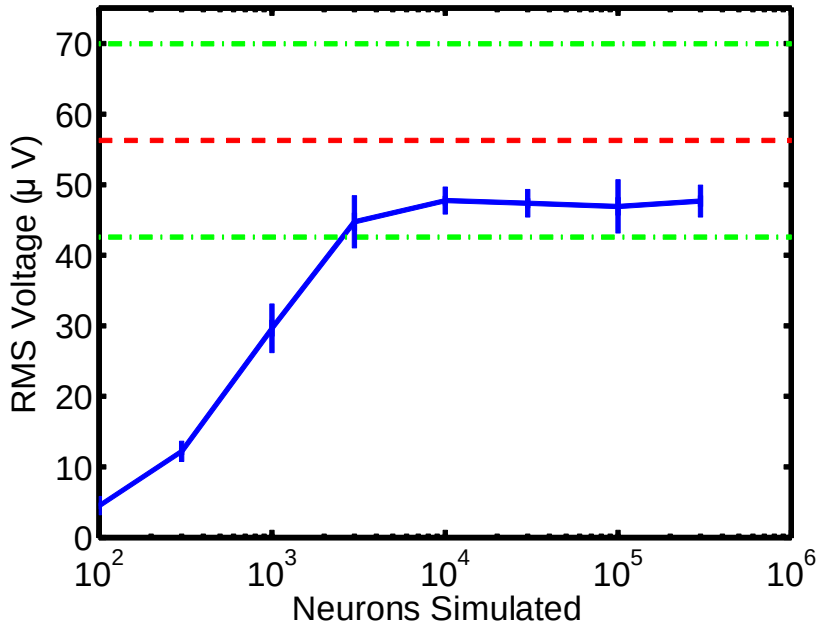

Figure 26 - The effect of changing the number of neurons simulated on the RMS value of the MER. The dashed lines represent the mean RMS (dark line) of patient recordings and one standard deviation (light line). The corner of the plateau corresponds to between 3,000-10,000 neurons, equivalent to ~1mm^3.

The change in RMS voltage, shown numerically in Figure 26, plateaus with a corner at 3,000 neurons. The variance in the RMS voltage is within one standard deviation of the experimental data above 10,000 neurons. Neurons added to the simulation over the 10,000 mark do not contribute significant energy to the recording. Additional neurons do not have a significant contribution to the model due the extracellular filtering effects. When the distance becomes too large their electric fields do not contribute to the recordings.

A homogenous cell distribution on the scale of the recordings, ~1mm^3, is used based on physiological studies of the STN (Israel, 2003). The physiology of the STN has a hard boundary of approximately 6.5 x 7.8 x 9 (W x L x D) mm, requiring simulations to only an appropriate distance from the STN edge. When a simulation approaches the edge of the STN the number of neurons contributing to the MER decreases, an example is shown in Figure 27. The curve characterizing the number of STN neurons captured by the electrode as it approaches the edge can be seen in Figure 28. Based on the Figure 28 curve the MER simulations, assuming homogenous cell distribution within the STN, are valid up to 0.15mm by maintaining the 3,000 neurons closest to the electrode. The reduced number of neurons simulated will increase the variance of the RMS Voltage as previously shown in Figure 26.

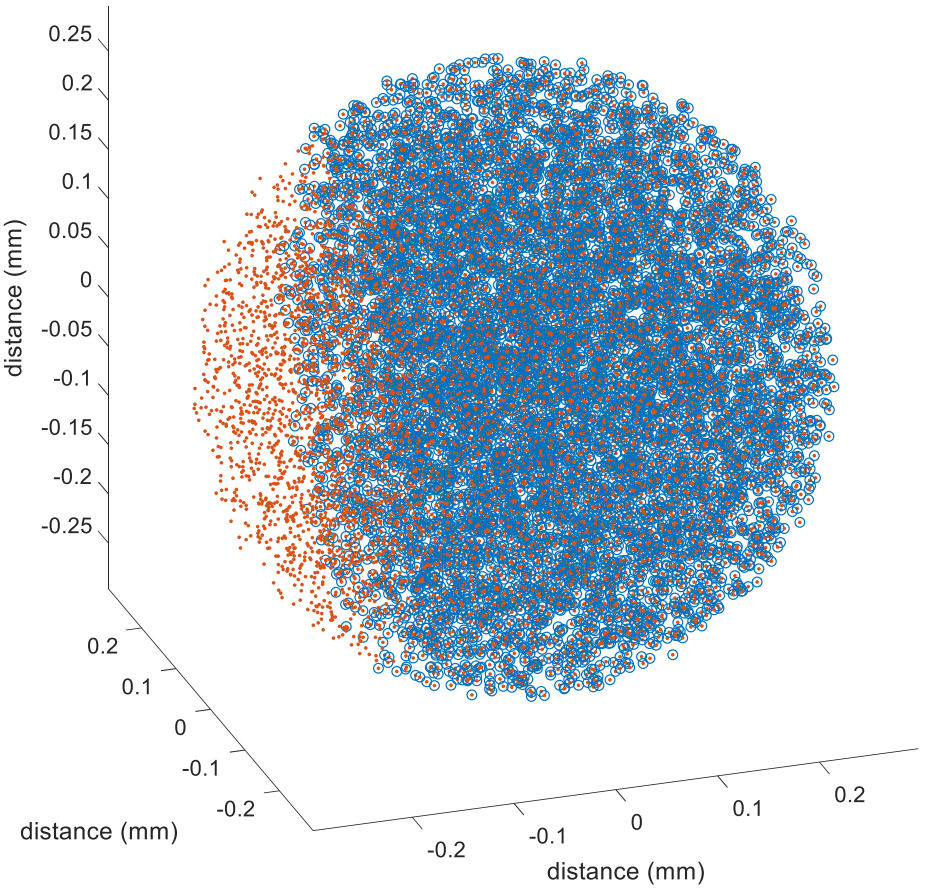

Figure 27 - The different volumes of neurons detected by the microelectrode when the electrode is placed into the bulk of the STN (dots) versus electrode placement 0.15mm from the edge of the STN (circles).

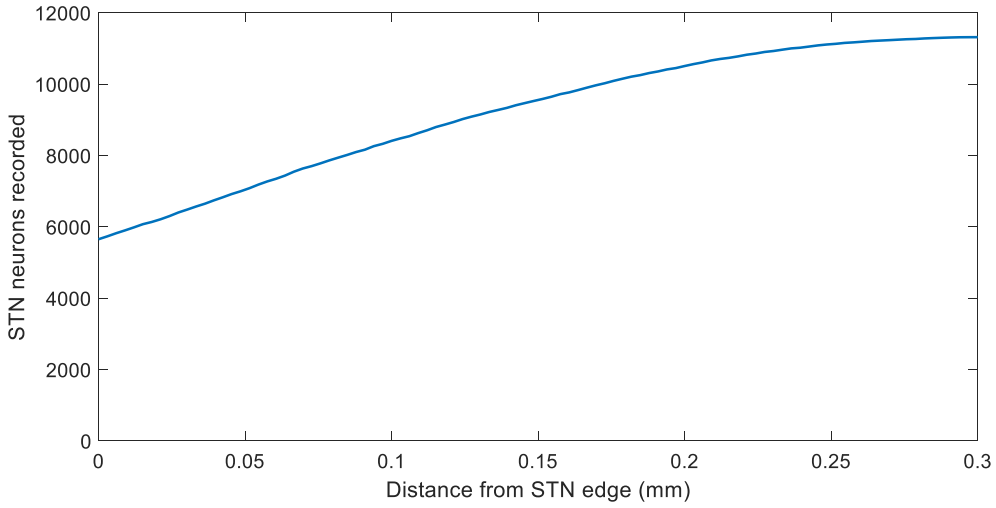

Figure 28 - Total number of neurons detected as a recording electrode approaches the edge of the STN.

Figure 29 shows comparisons of the patient DBS MER to a simulation with a Weibull shape parameter of *0.8* using *10,000* neurons. This comparison visually shows the difficulty to compare the simulation and patient recordings as a time series. A clearer comparison of how well the parametric MER simulation models the patient data PSD is shown in Figure 30.

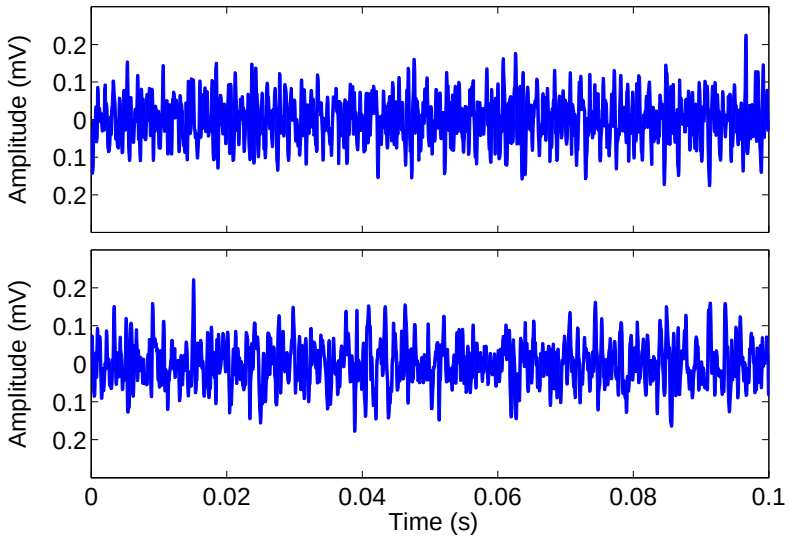

Figure 29 - Examples of a patient recording (top) and a simulated recording (bottom) with a simulation parameter *c=0.8*. It can be seen that the voltage time signals are stochastic in nature, making a direct comparison using these signals unfeasible.

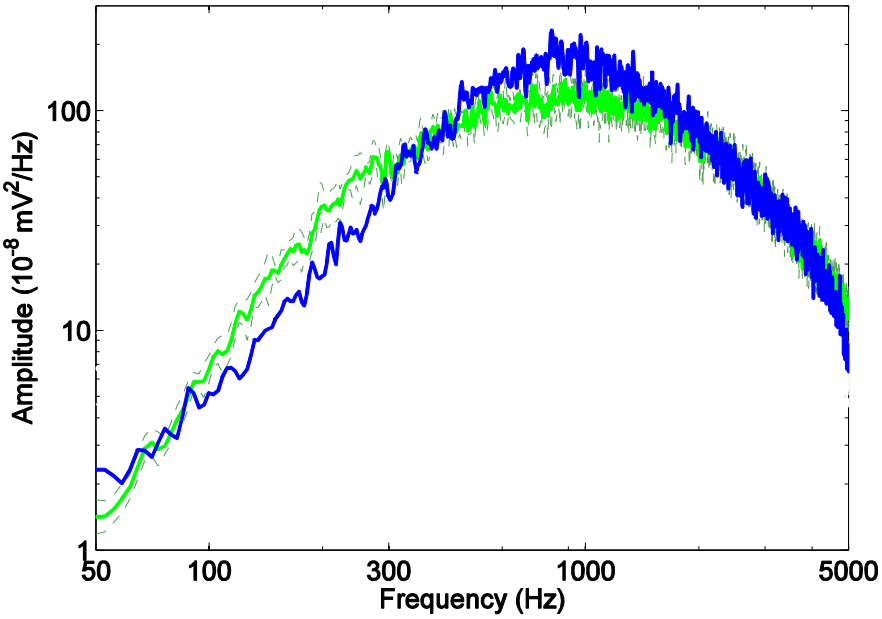

Figure 30 - Examples of the spectral estimates for P32L with *95%* confidence interval (dashed) and a simulation with *c=0.8* (Dark line). The shape of the power in the frequency domain can be used to verify the simulated MERs against patient data. The stochastic nature of the signals can be seen as noise.

To illustrate the speed advantages of the summed FPP model over a deterministic HH model, a comparison of the time required to compute an MER using the proposed electrode model and a coupled HH network is shown in Figure 31. The points are averaged over three data samples. The dashed line is a line with a slope of 1 to show that the computational order of the summed FPP is approximately *O(N)*, where *N* is the number of neurons. Due to

the long computation time, no simulations of the Hodgkin and Huxley network with over 1,000 neurons were performed. The comparison of the computational time compared to neuron number shows that the FPP model is significantly (100x) faster than the equivalent Hodgkin and Huxley network model.

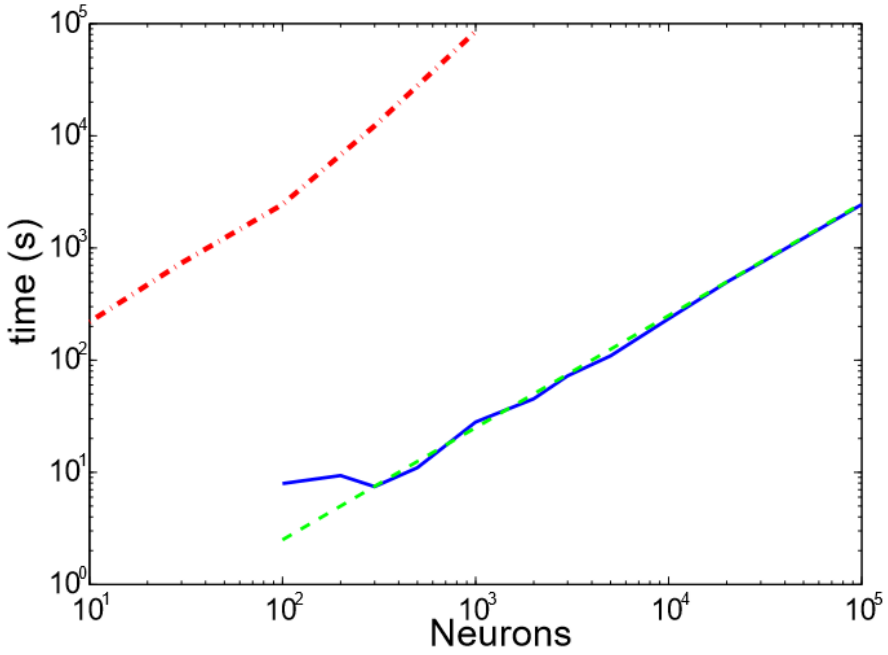

Figure 31 - The computational time to simulate an MER using the method presented in this paper (solid), a Hodgkin and Huxley neural network (dot dash). A line with slope one (dashed) is layered on top to indicate *O(N)*.

The computational time of the FPP model diverges from O(N) at low neuron number seen in Figure 31. This divergence from O(N) is due to the minimum time to initialize the simulation.

Other dynamic models of neurons, which reduce the complexity of the differential equations of the Hodgkin and Huxley model were not used to compare the computational time to this model. Computationally efficient spiking neuron (leaky integrate and fire and Izhikevich) models cannot produce accurate enough action potential shapes and are generally only used to produce the correct spike timing (Izhikevich, 2007). Because the PSD in the frequency range of interest has a contribution from the shape of the action potential these models were not considered. The model we have presented is a linear top-down model to analyse patient data via synthesis, where the complexity of spike timing is buried in the stochastic process. A similar `cut and paste' method for the spike shape can be used in the previous dynamical models where the spike timing is determined by the nonlinear dynamics.

However, using these models for parametric fitting to patient data, without pre-calculating accurate waveforms or ISI timings, would be a significant and computationally intensive task. This is because the dynamics of each neuron cannot be modelled individually since the network activity and neuron to neuron coupling is required to produce the individual neuron dynamics.

The time series data for three different simulation settings is presented in Figure 32, with a comparison to a real recording. From this it can be seen that c=1 appears to produce a MER most similar to the real recording. The windowed PSD for all three simulations and the patient recordings, seen in Figure 33, have three main regions. The first region is the filter drop off above 5 kHz. This feature is present in all four PSDs with good agreement between patient data and simulations.

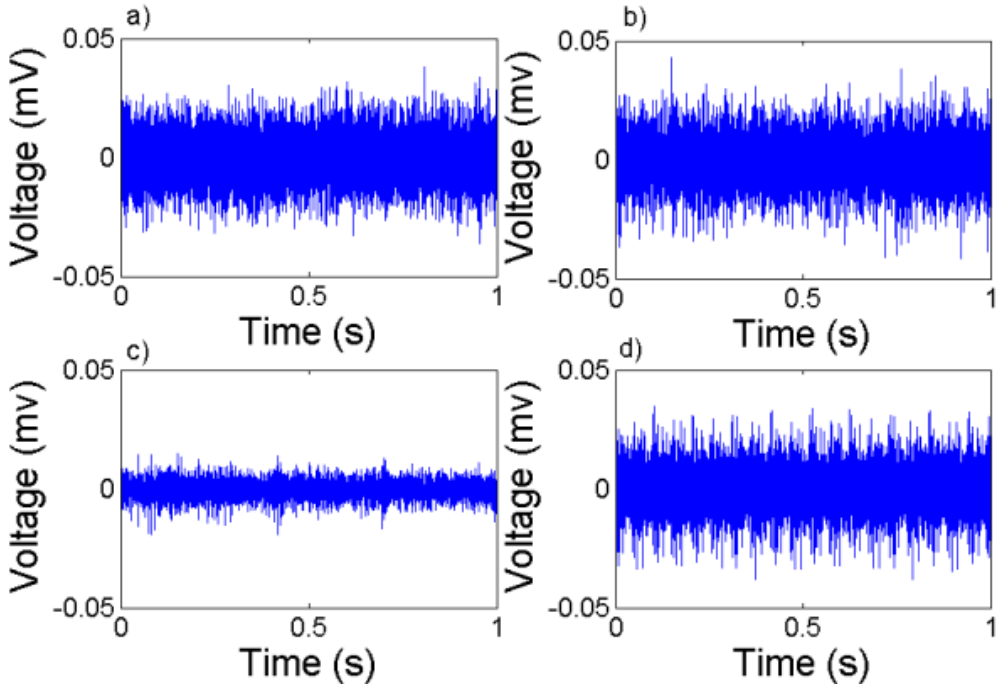

Figure 32 – Visual comparison of a) Patient MER to simulations with: b) c=1 displays a very similar appearance to the patient data, with no distinct pattern, c) c≪1 shows a decrease in the signal size, and several bursting events begin to emerge and d) c≫1 shows a periodic structure emerging in the spike occurrence.

The second region of interest in the power spectra is the behaviour at high frequencies (100-5000 Hz). The two simulations with $c \leq 1$ have good agreement with patient data in this region shown in Figure 33. The simulation with $c \gg 1$ has structure in this region that can be explained as harmonics of features in the low frequency region. The overall shape in this region is dominated by the waveform of the EAP.

The final region of interest is in the region below 100 Hz. This region is thought to contain information of the Local field potential (LFP). Experimentally this region has an electronic filter, with a slow drop off. For $c \gg 1$ this region has a sharp peak at 10 Hz, the simulated spike rate, and then has peaks at the harmonic frequencies of 10n Hz, where n is an integer. The other two cases have anomalous peaks in this region similar to the 20 Hz peak in the patient data. This beta band peak (12-30 Hz) has been seen in PD MER recordings previously and has been implicated in the pathological state (Eusebio & Brown, 2009). The model developed is an attempt to synthesise the experimental data using a top down approach, as such it does not intrinsically contain a biological mechanism that presents PD. Since the experimental data is from PD patients, the features produced in the simulations will be tuned for a PD state.

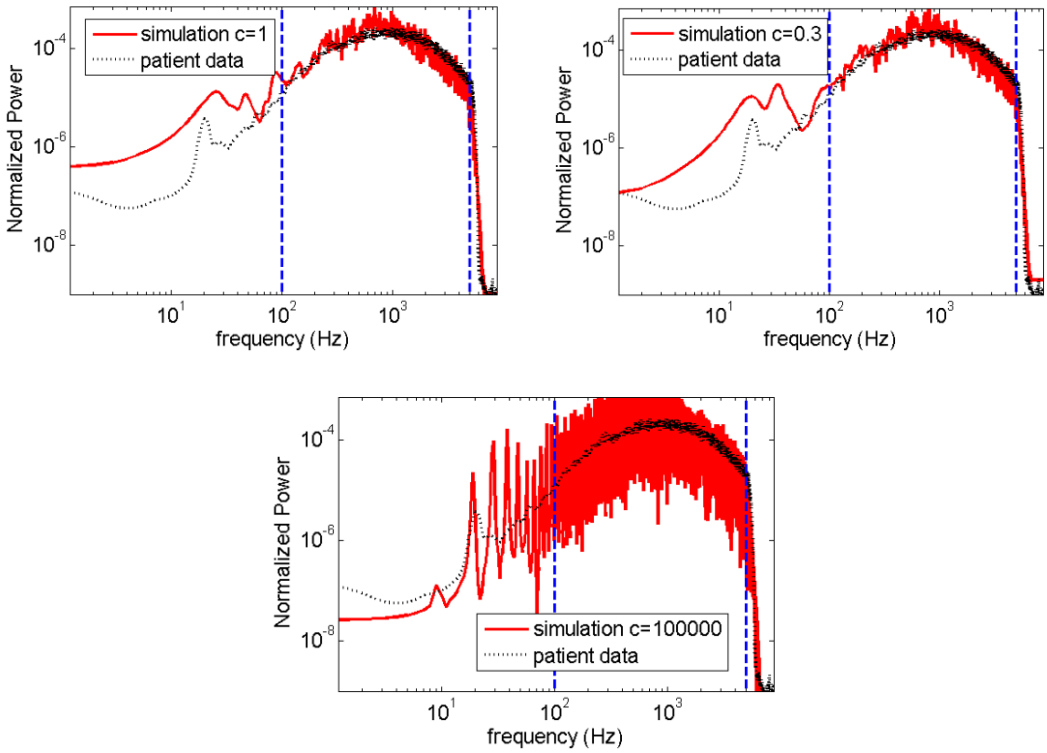

Figure 33 - Overlap of the real patient windowed PSD over the windowed PSD of the simulation for $c = 1$. Overlap of the real patient windowed PSD over the windowed PSD of the simulation for $c \gg 1$. Overlap of the real patient windowed PSD over the windowed PSD of the simulation for $c \ll 1$.

The thermal noise term added is white noise and as such adds the same power to every frequency, shifting the PSD up. This effect is removed by normalizing the power spectrum to integrate to unity. The other electrical effects; high and low pass filtering; do however alter the normalized power spectrum, seen by the sharp falloff in power in this region.

The power spectra appear qualitatively similar between 100-5000 Hz with differences in their structure below 100 Hz. The model is efficient at simulating the power spectrum of MERs in the band pass region. Figure 34 demonstrates how the power spectrum changes with the Weibull shape parameter. For the same recording length *c=0.5* (small dotted line) shows the least power density across the frequency band of interest in the patient recordings (unfiltered region, 500 Hz < ω < 5000 Hz). At the other extreme of *c=100* (dashed line) shows harmonic spikes. For *c=0.8* the PSD has a more spread out frequency distribution compared to the other simulations. The PSD for *c=1* follows the action potential power spectrum as expected from Carson's theorem for a Poisson process. Although *c=0.8* and *c=1* have a very similar shape of their ISI times distribution (exponential), they display different distributions of their power spectral estimates.

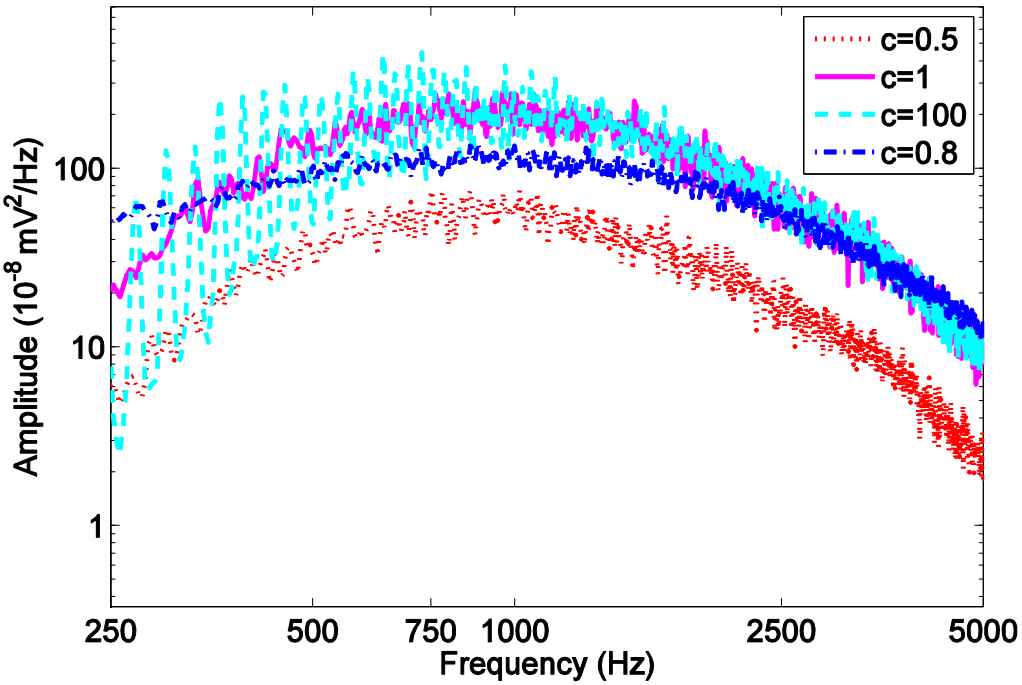

Figure 34 – Power spectral estimates for the simulations using *c=0.5*(dots) a decrease in overall power, *c=1*(solid), *c=100*(dashed) harmonics appearing and *c=0.8* (dot dash) a shift in the distribution of power across the frequencies.

Another method to qualitatively examine the spectral properties of a MER is to look at the spectrogram, Figure 35, and to observe changes in the power spectrum over time. From the spectrogram for the typical patient MER recording the PSD changes in time. These recordings show the feature in the beta band appearing and disappearing through the spectrogram. This behaviour can be seen for some of the simulations except for $c \gg 1$, the spectrogram appears periodic.

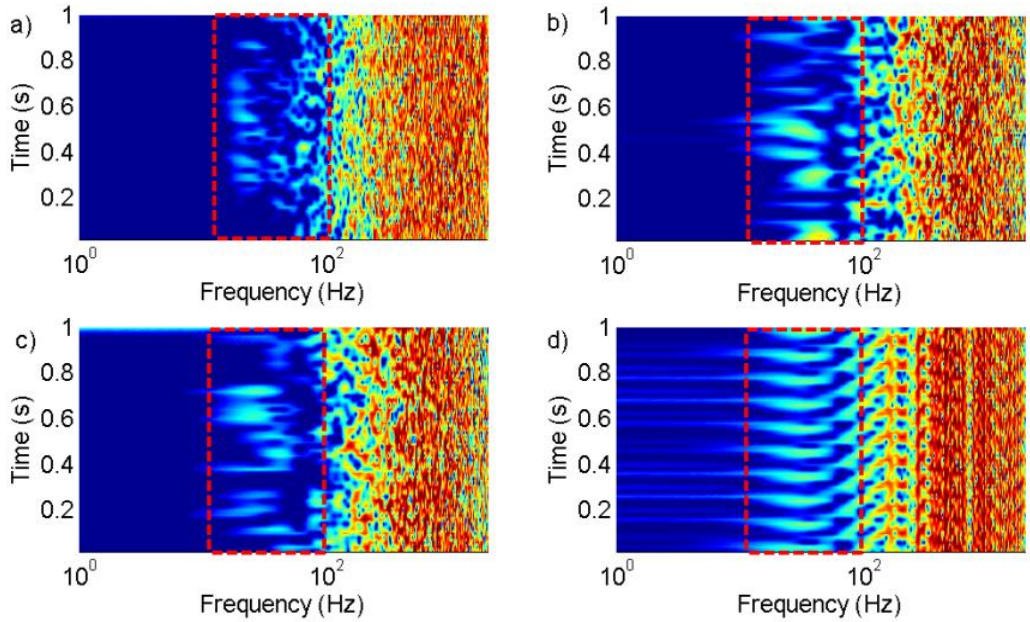

Figure 35 - Spectrograms with the region displaying beta band behavior boxed in red, a) patient MER showing transient beta band behavior, b) simulations $c \ll 1$ showing transient beta band behavior, c) $c = 1$ showing transient beta band behaviour and d) $c \gg 1$ showing periodic behavior.

This qualitative analysis suggests that $c \cong 1$ represents the patient data the best. This supports the idea that spiking behaviour in a large network appears Poisson like (Cateua & Reyes, 2006). The model proposed in this section only produces the timing and shape of action potentials. The model does not account for any of the oscillations in electrical activity below threshold before activation of the spike. This type of activity, called sub-threshold oscillations, are typically low frequency (1-100Hz). Slow oscillations are not clearly seen in the patient recordings due to the shape of the electrode ($50\mu m$ tip) and the high pass filter at 500Hz. Although it was found that $c \leq 1$ best represents the human data for patients with PD, in the current model it does not have a biological connection. The relationship between the non-stationary beta band behaviour ($c \leq 1$) and the brain dynamics will be discussed in section 4.3.

5.1.2 Validation

To perform a quantitative comparison and validation, of the simulated to patient MERs three different methods were used. These methods were used to build a comprehensive comparison between the patient and simulated recordings. The first order analysis, using

the voltage distribution, demonstrates matching behaviour of the probability distribution of voltage levels. The second order analysis, using the PSD, allows the correlation properties of the model and patient recordings to be analysed using different inter-spike interval statistics. The phase properties are used to verify the random phase assumption of a stochastic process.

Figure 36 shows a box-plot of p-values from the KS test on the voltage distributions of the 14 hemisphere recordings against simulation parameters *c=0.5* to *c=100*. Using the KS test as a distance measure, the closest simulated amplitude distribution to the patient recordings is *c=0.8* with a 0.97 mean correlation factor of simulations with patient data. There is also strong correlation with *c=100*. Simulations with other shape values, [0.5, 1, 10], also have a high correlation above 0.5.

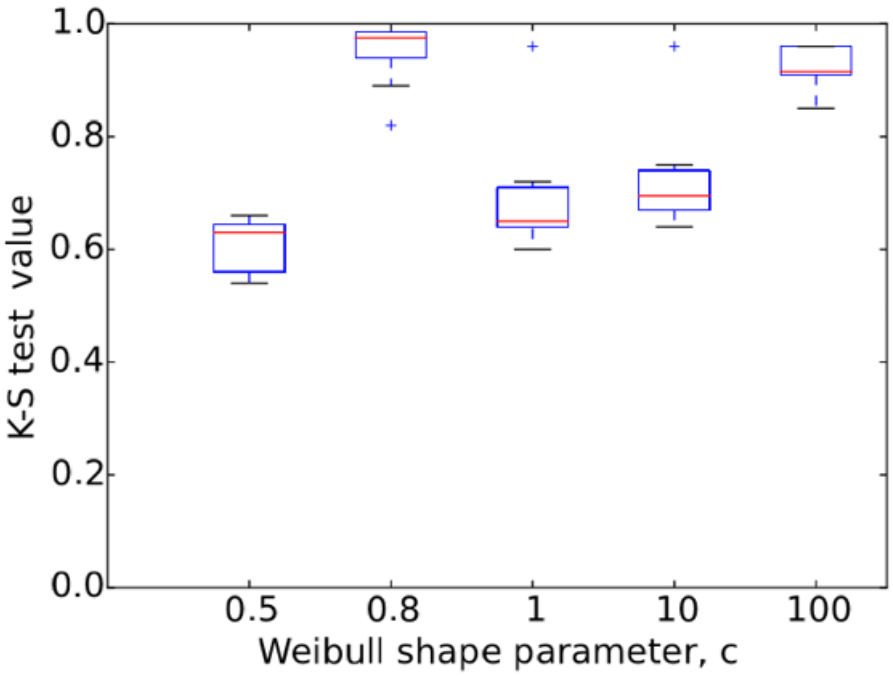

Figure 36 - Box plot of the KS test p-value of each patient voltage distribution matching the simulation distribution for each shape parameter. The Box represents the 25 and 75 percentiles, the lines represent the maximum and minimum values, the mid line represents the median value and the '+' represents outliers.

Linear regression of the simulated power spectral estimates against the patient MER PSD was used to assess the model fit to the patient recordings. Figure 37 shows a box plot of the correlation coefficient for the linear fit for the 14 patient-hemisphere recordings. The outlier point is patient 61 right side for all values of *c*. This figure also shows that the R^2 value is greater than 0.89 for all values of the shape parameter.

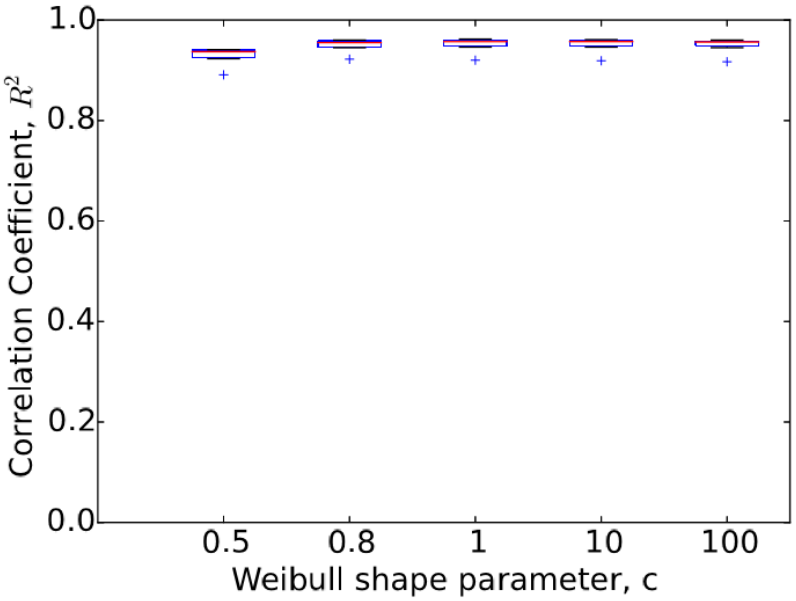

Figure 37 - Box plot of the R^2 value from fitting each patient spectrum to the simulated spectrums for different *c* values. The Box represents the 25 and 75 percentiles, the lines represent the maximum and minimum values, the mid line represents the median value and the '+' represents outliers.

The linear regression of patient and simulated power spectral estimates, with Weibull shape factor, *c*, ranges from 0.8 to 100 produces correlations with the patient recordings of better than 0.9 for all patients, except one (the + in Figure 37). Assuming constant action potential shape between patients, the changes in inter-patient PSD estimates are indicative of changes in the ISI statistics. Qualitatively it was shown in Figure 33 that simulations with *c=0.8* have the most similar PSD to a patient recording. The *95%* confidence interval is also plotted for five repeated recordings from the same patient. Figure 38 shows the linear regression of the PSD estimates for simulations using *c=0.8* against two different patients. This demonstrates the variation in patient recordings. For comparison, Figure 39 shows the regression of a patient PSD against white noise with equipment filtering effects. This regression has a low correlation coefficient, $R^2=0.0306$, indicating that the noise of the patient recordings contains structure not adequately modelled by filtered white noise.

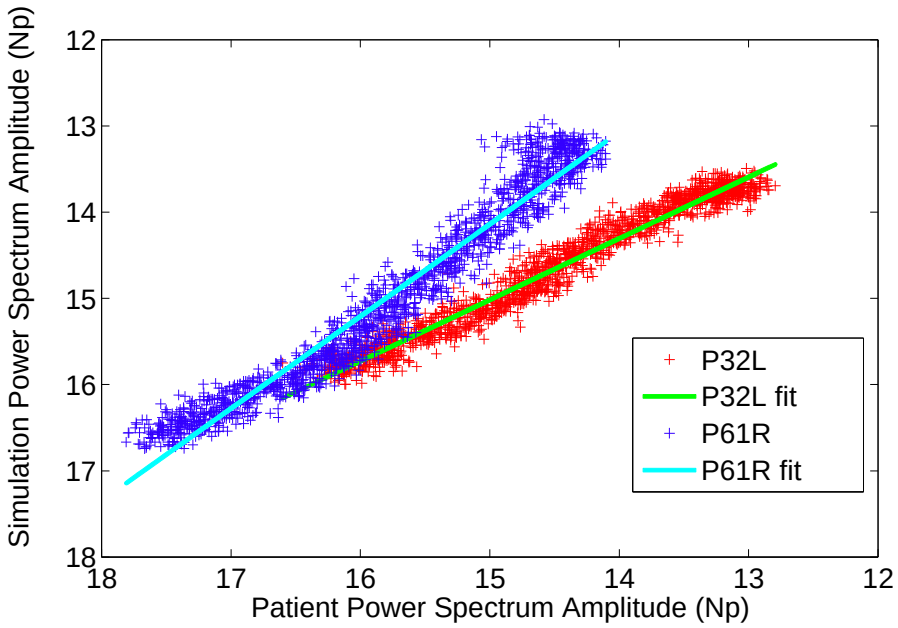

Figure 38 - Example of linear fits of the patient frequency power versus simulation frequency power for P32L (light) and P61R (dark). This shows a good correlation between the model and the patient data. However, the slope of the fit changes indicating the model parameters may need to be fitted to individual patients.

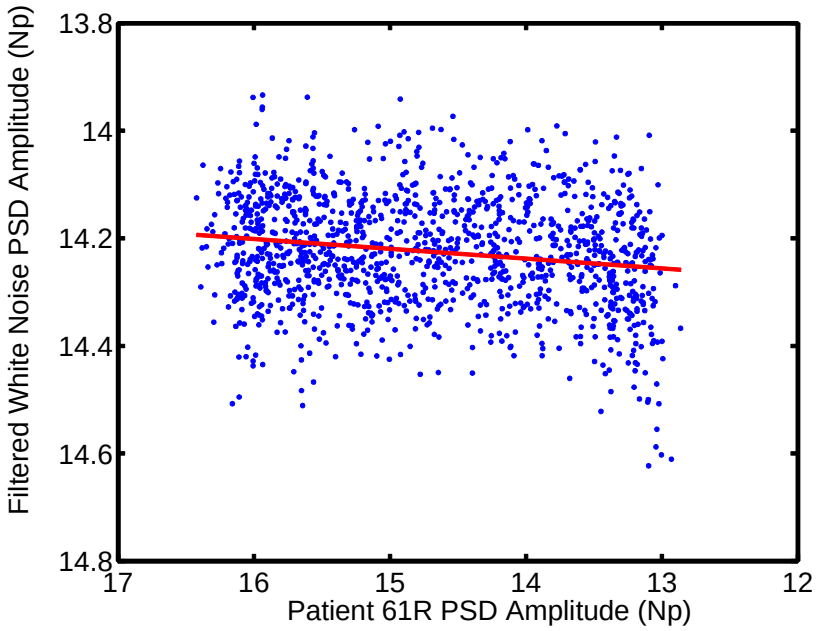

Figure 39 - Linear regression of the PSD of the P61R with white noise passed through the equipment filters. The regression line has the form *y = -0.0182x - 14.4920* with a correlation coefficient R^2=*0.0306*. This shows that the correlations in the patient data and simulations is not due to the filtering due to the equipment.

The tuning of the simulation shape parameters was performed by taking the average of the correlation tests for each patient. The other simulation parameters, including the electrode properties, the number of and distribution of neurons and the extracellular properties were not varied between patient comparisons. Some variation in fits between the different patient

data sets can be explained by these parameters, particularly the fact that an average electrode impedance of $0.5\ M\Omega$ at 1kHz was used for the model. The electrode impedance is different for each patient (Medtronic, n.d.). This model could be improved for individual patients by measuring the electrode impedance.

The component synchrony measure (CSM) was used to see if there are any features in the phase spectrum of the recordings. The amplitude of the largest peak in each CSM spectrum is shown in Figure 40 for both simulation and patient data.

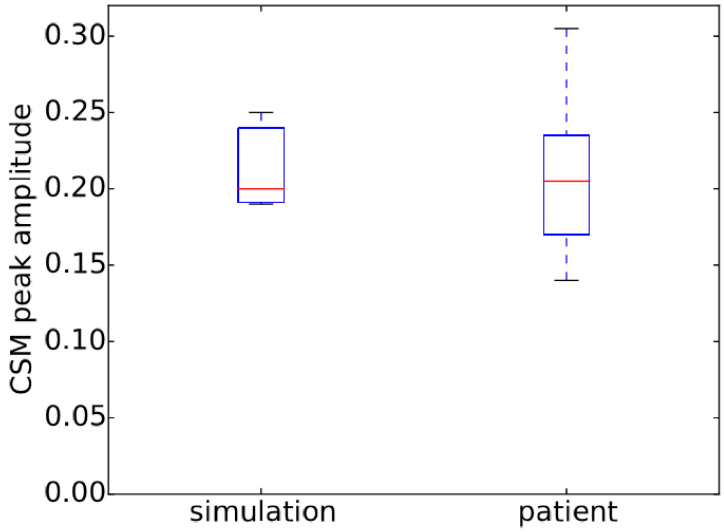

Figure 40 - Box plot of the amplitudes of the highest peak from each CSM spectra. The Box represents the 25 and 75 percentiles, the lines represent the maximum and minimum values, the mid line represents the median value and the '+' represents outliers.

Since a stochastic process in time will have random phase, the phase information should show no synchrony between any frequency components. CSM values above 0.5 show a significant amount of phase synchrony across the recordings at a specific frequency (Fridman, et al., 1984). Figure 40 shows there are no peaks above 0.3 in the CSM spectra for the patients or simulations, with patients being slightly more variable. This indicates that there is no phase synchrony present in either the model or patient recordings verifying the stochastic assumption for MERs. Using the KS test as a goodness of fit between the simulated CSM peaks and the patient CSM peaks gives a value of 0.73. This means they have similar distributions, but there is a difference in the distributions.

The difference in the distribution of CSM peaks in the model can be explained by an additional white noise source in the patient recordings that hasn't been modelled. A white

noise source would not affect the spectral colour, as it would add equal power across all frequencies, however it can add noise to the phase spectrum. This noise has a variance that scales with the amplitude of the source (Fridman, et al., 1984). This could increase the CSM peaks that are not above the significance of 0.5 and would be spread across a wider frequency range than the simulation currently displayed.

To see how the renewal model can be used to fit MERs the effects of the ISI statistics on the power spectrum were produced for a changing Weibull shape parameter. Figure 41 shows the frequency behaviour of Equation (41) for different values of c, if the aggregate renewal statistics (the ISI statistics averaged over all the neurons) follow a Weibull distribution for ISI times.

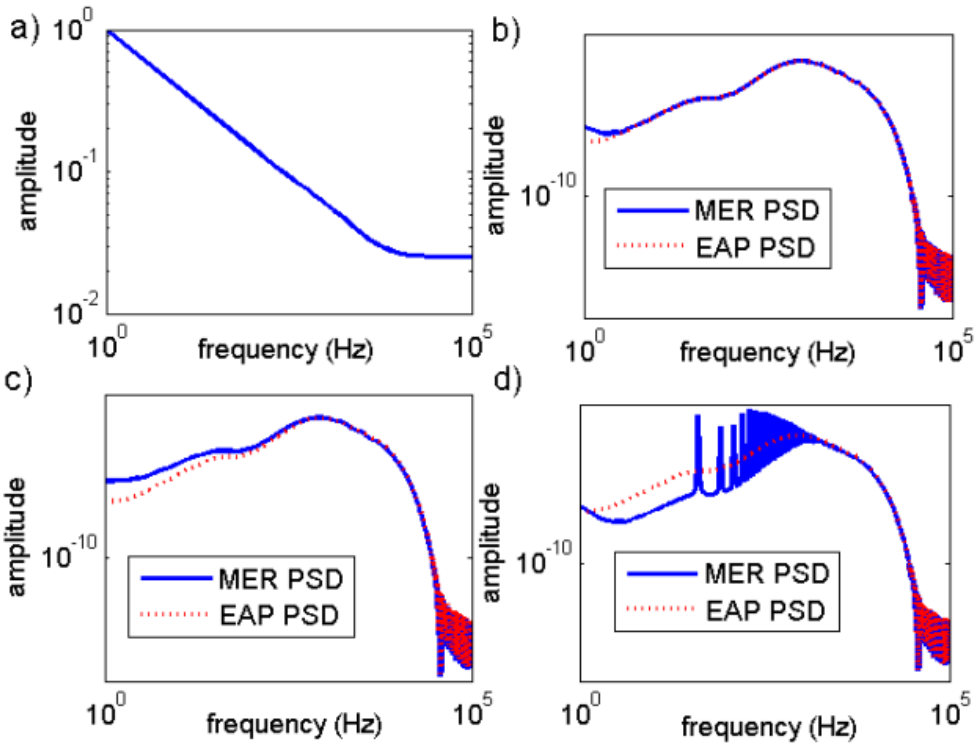

Figure 41 - a) The expected filter function of the extracellular medium taken over a population of 10,000 neurons. Inserts b)-d) show the comparison of the power spectrum of the EAP with the MER power spectrum from the analytical model, b) the MER PSD for $c = 1$ modelled by equation (9), it can be seen that for this distribution the results of the MER and EAP PSDs are in agreement, c) the MER PSD for $c \gg 1$ modelled by equation (9), d) the MER PSD $c \ll 1$ modelled by equation (9).

For $c \gg 1$ and $c = 1$ the frequency filtering effects due to the spiking statistics are minimal and will not add noticeable features in the power spectra at high frequencies. For $c \gg 1$ the 10 Hz peak with harmonic peaks in the numerical simulation can be seen in the frequency effects from the renewal statistics on the power spectra.

This analytical model doesn't consider the frequency filtering effects of neurons by the extracellular medium. These filtering affects need to be accounted for when fitting the renewal statistics. Figure 41 a) shows how the extracellular medium model acts as a low pass filter with this expected filter function. The shape of this extracellular filtering changes with distance to the electrode. To find the average contribution of a neuron, $G(\omega)$, to the MER the expected neuron distance for each frequency is found by taking the expectation value of the neuron distance, d_i, weighted by the extracellular filtering normalized to one, $Z(\omega)$.

$$G(\omega) = Z\left(\frac{1}{N}\sum_{i}^{N} d_i Z(d_i, \omega)\right) \tag{50}$$

To fit the shape parameter, many spikes need to have occurred to build up a representative sample of the ISI distribution. This means that the recordings need to run for a certain length before there are enough spike intervals to build up an estimate of the statistics. To determine what length of simulation is required, and hence what length of patient recording would be needed, simulations were produced drawing the firing times from Weibull distributions. The simulations used the neural shape and filtering effects for the STN MERs. The shape parameter was then determined from the simulations using $G(\omega)$ from Equation (50) and fitting the Weibull shape parameter. This was repeated 1000 times for 13 shape parameters. Figure 42 shows that over the expected range of shape values, 0.5 to 10, that a 3-10s recording is needed to obtain an error of estimated shape less than 10%. For the rest of the study 5s recordings are simulated to allow a large range of valid shape parameters.

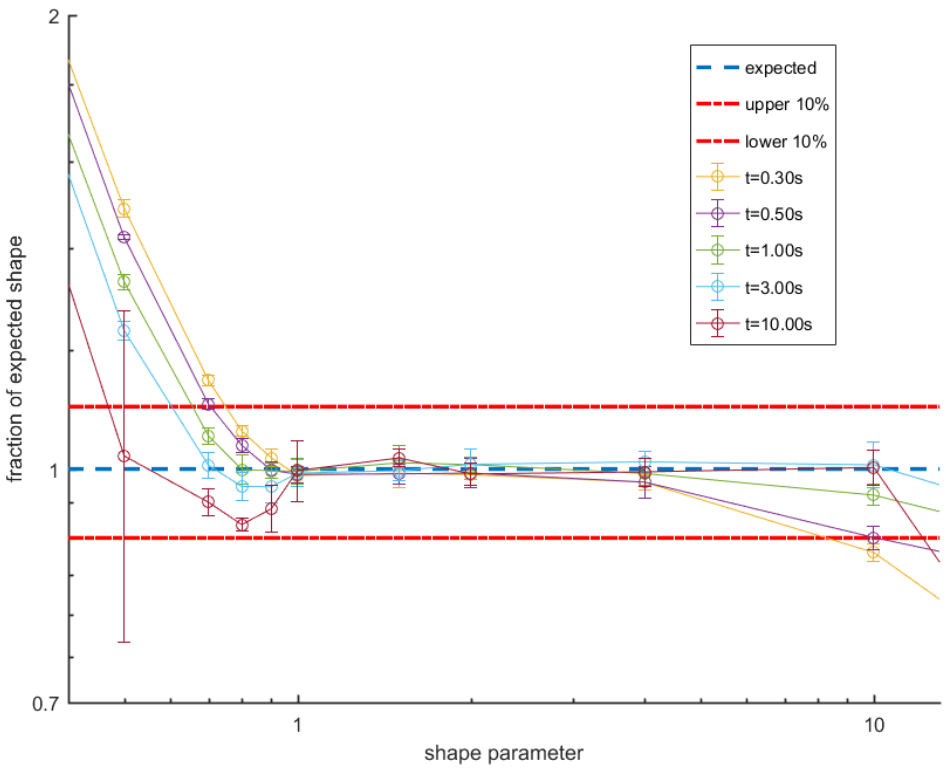

Figure 42 - Accuracy of Weibull shape prediction from 1000 MER simulations of varying time length. The blue dashed line corresponds to perfect prediction of the shape parameter, the red dashed lines are the upper and lower bounds of 10% accuracy. Simulations 1s and longer can predict the shape parameters larger than 0.6 and higher with greater than 10% accuracy.

5.2 Neuron Synchronisation

MER simulations were performed using each Weibull shape parameter for the ISI distributions in Figure 43 and Figure 44 for uniform and localized synchronisation respectively to investigate how well the renewal model can fit when the IID assumption is not valid. These figures show for 20 simulations of 2s what the ratio of the fitted shape parameter to the parameter used for the simulation. A kernel density estimate (KDE) is used to smooth the results.

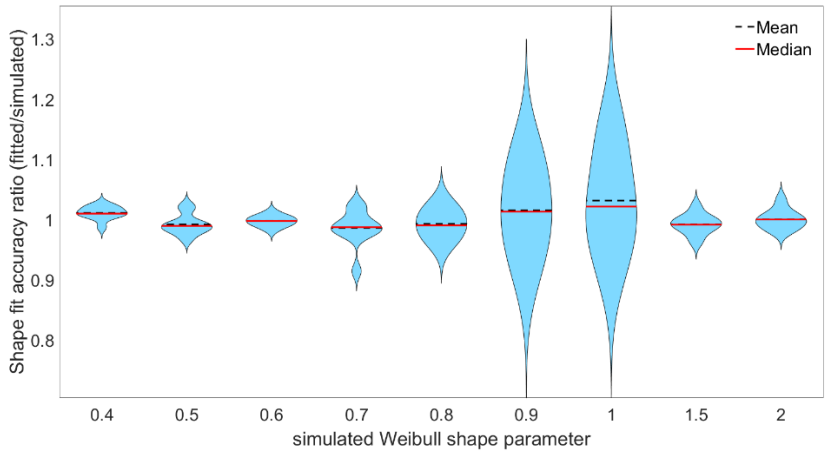

Figure 43 - Fitting accuracy of shape parameter to simulations using uniform synchronization. The width of the blue area represents kernel density estimates of the count distribution of predicted shape values. For 0.9 and 1 the variance is significantly larger than the other simulations. The reason for this increase is due to estimation noise from the small number of experiments. Their variance was still below 10%, indicating that uniform synchronization did not affect the ability to fit the renewal model.

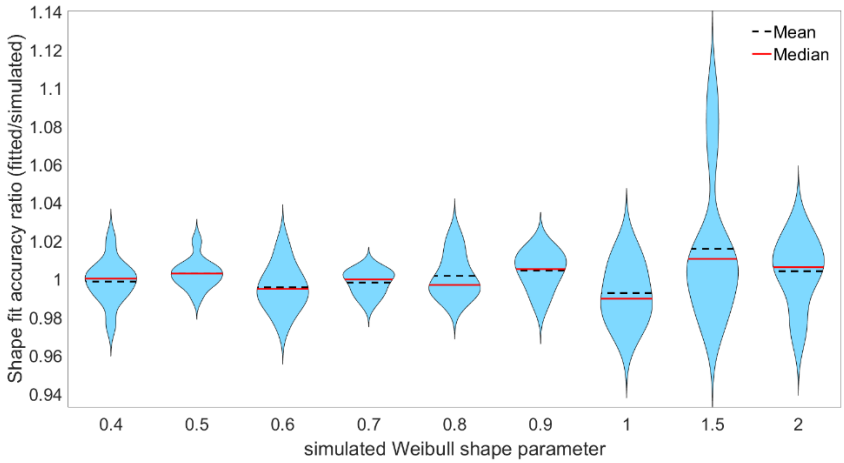

Figure 44 - Fitting accuracy of shape parameter to simulations using localized synchronization. The width of the blue area represents kernel density estimates of the count distribution of predicted shape values. For 1.5 the variance is larger than the other simulations. The reason for this increase is due to estimation noise from the small number of experiments. Their variance was still below 10%, indicating that localized synchronization did not affect the ability to fit the renewal model

For both forms of synchronisation, the fitted statistics match the statistics used for the generation of the simulation to within the accuracy of fitting the ideal simulations of a given time length (Figure 42). The distributions of fitted shape parameters are not all Gaussian distributed, and the variance changes significantly for the different shape parameters. These effects do not have a trend related to the shape parameter or synchronisation type, indicating that their cause is due to a small number of samples used to produce the figures. Because the values are bounded to within 10% of the simulation shape parameters, except for three values larger (~20%) there was no need to run more simulations. These results show that in the presence of synchronisation, causing the ISI times to no longer be

independent and identically distributed, the Weibull renewal model can be used to fit the MER.

An effect the synchronisation had on the MER simulation was to increase the apparent signal to noise ratio of the larger spikes. A raster plot, Figure 45, of the simulated neuron firings shows how the synchronized firing times correspond to a spike (compound action potential, CAP) with a large signal to noise ratio. In the raster plot two separate synchronized subsets can be seen. Although there are two subsets with the same percentage of total neurons synchronized, their spatial arrangement around the electrode are different. The effects of this spatial arrangement can be seen in the MER time series, where two different amplitude spike shapes are present.

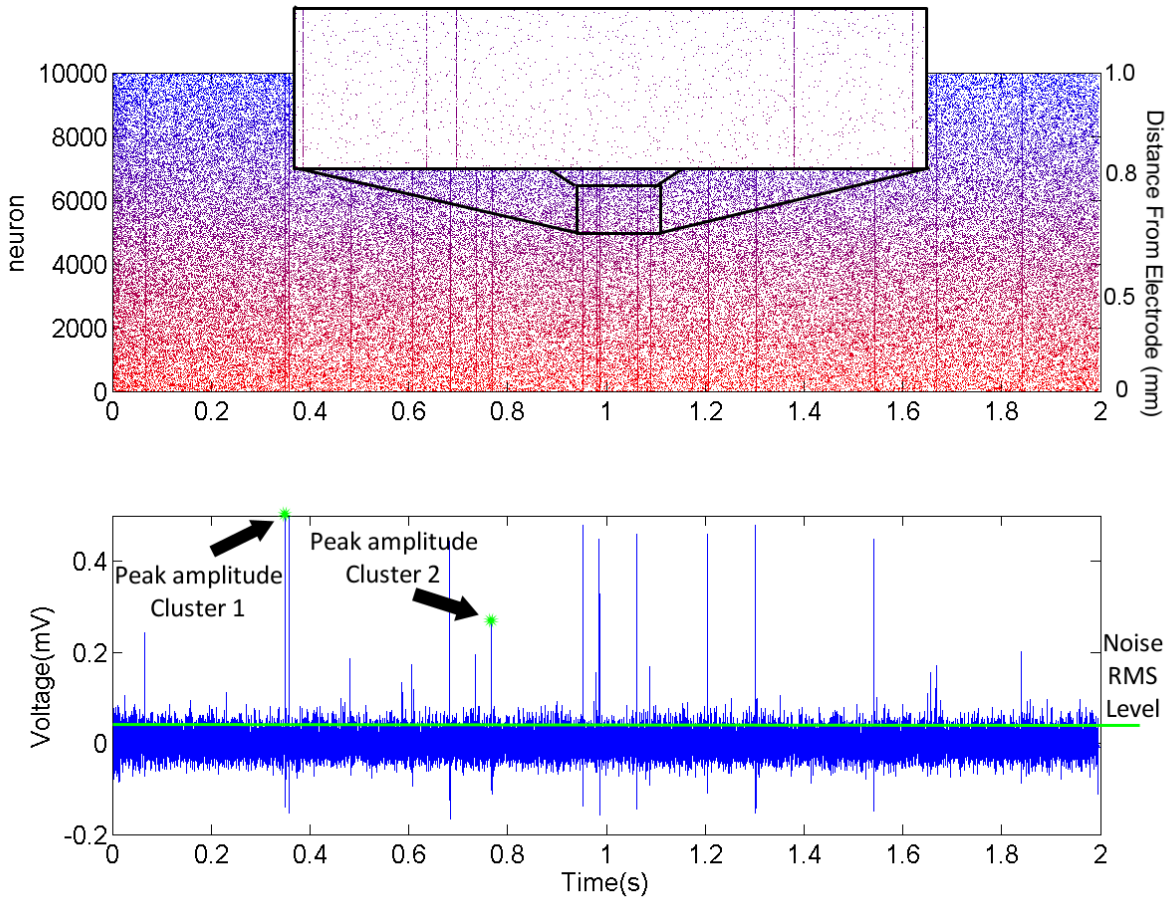

Figure 45 - Raster plot of active neurons with the electrode recording simulation generated using two groups of synchronized neurons. The top plot is a raster plot of spike times, where each dot represents a spike for a neuron at that time. The zoomed in section shows five synchronized firing events. The bottom plot is the voltage time signal recorded by the simulated microelectrode. Marked on it are the root mean squared level to indicate noise, and indicators of spikes from cluster 1 and cluster 2.

To test quantitatively the effect of synchronisation on the signal to noise ratio, 20 simulations were performed for different synchronisation percentages. As the number of neurons that are synchronized increases Figure 46 shows a linear increase of the mean peak amplitude

of the CAP spike, averaged over 20 simulations. The variance of the peak amplitude also increases significantly, depending on the spatial distribution of the sub-set of synchronized neurons, i.e. as more neurons are synchronized they are more likely to come from a wide spread of locations. Figure 46 shows synchronization over the biologically plausible range of 0-0.30 for the STN (Theodosopoulos, et al., 2004). For synchronization above 0.5 the mean peak signal amplitude becomes constant at $8.1 \pm 0.5mV$, with variance decreasing to zero when all neurons are synchronized.

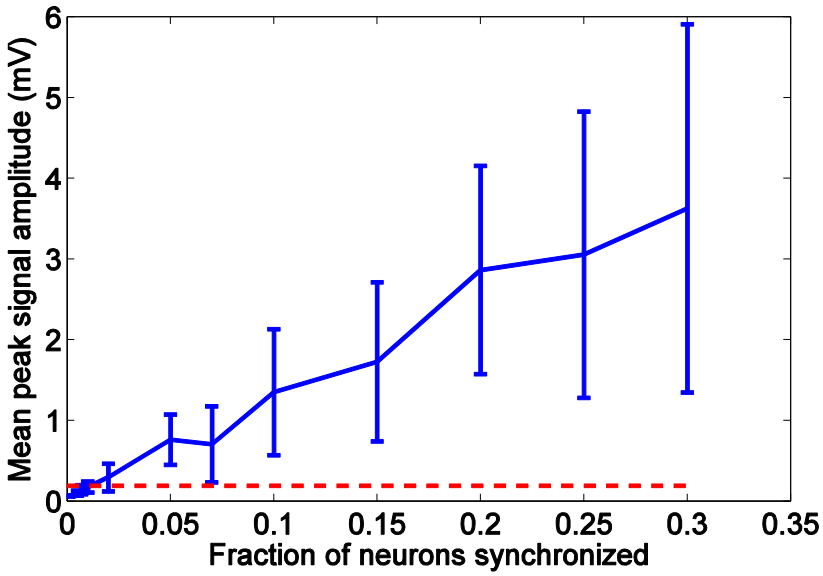

Figure 46 - Mean peak signal amplitude as the fraction of neurons in the synchronized sub-set changes. The mean is taken over 20 simulations and the error bars are one standard deviation. The dashed line represents the average RMS value of the recordings, shown in Figure 45.

Figure 46 shows that for no synchronization the simulations can have a peak signal amplitude above the RMS noise. For these cases, a neuron current source is located close enough to the electrode tip for its action potential to be significantly larger than the background noise and thus appear as a spike. In interoperative MERs this is often the case since the surgeon can adjust the electrode position until there is a strong spiking signal. This shows There are two methods to produce visible spikes in the MER simulations; it is possible for DBS MER spikes to represent single neuron activity or CAPs. The first method involves a neuron very close to the electrode (where the current source is adjacent to the tip of the electrode). The second method is to introduce synchronization and produce a CAP. For DBS MERs the spikes are often thought to be APs produced by single neurons. This work shows that even with extracellular filtering, CAPs could also cause spikes in the MERs.

To determine how different CAPs from different groups could be differentiated, spike sorting was used. Figure 46 shows when two sub-sets of synchronized neurons differ substantially in their spatial distribution, spike sorting can be successfully achieved. This occurs more often when the neurons are spatially localized, however it can occur when the two sub-sets are uniformly distributed, Figure 48.

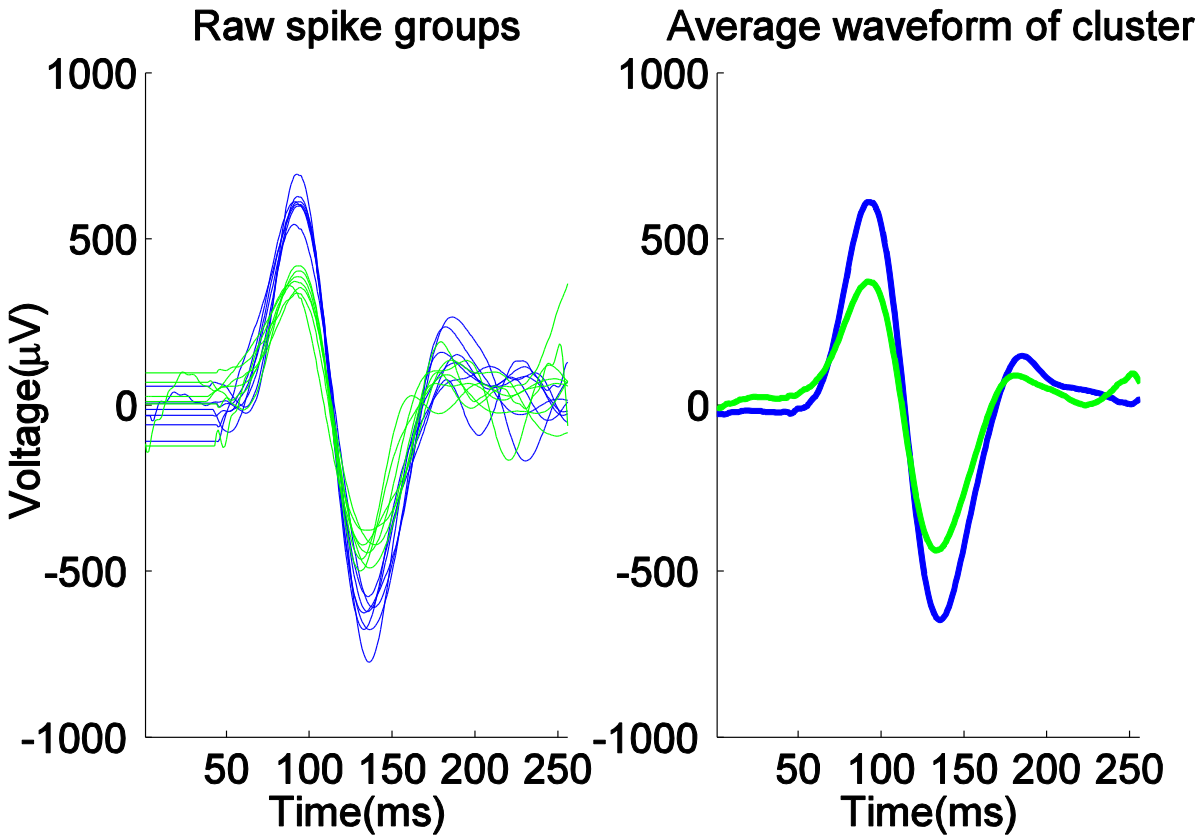

Figure 47 - Comparison of two CAPs after spike sorting from a simulation with synchronization percentage of 25% total synchronization. For this simulation, there were two synchronized subsets of neurons with each subset uniformly distributed across all the neurons and 12.5% of neurons in each set

Spike sorting techniques (outlined in Chapter 4.4), based on shape, amplitude and rate, were used to determine if the MER spikes all correspond to the same group, or multiple groups of neurons firing at different times (Rutishauser, et al., 2006). Figure 48 shows that when the synchronization of six neural subsets is changed from uniform across space, to spatially localized, the spike sorting algorithm can distinguish more clusters. For the uniform distribution only two to three clusters are found 50% of the time. For the spatially localized neural subsets more than four clusters are found 75% of the time.

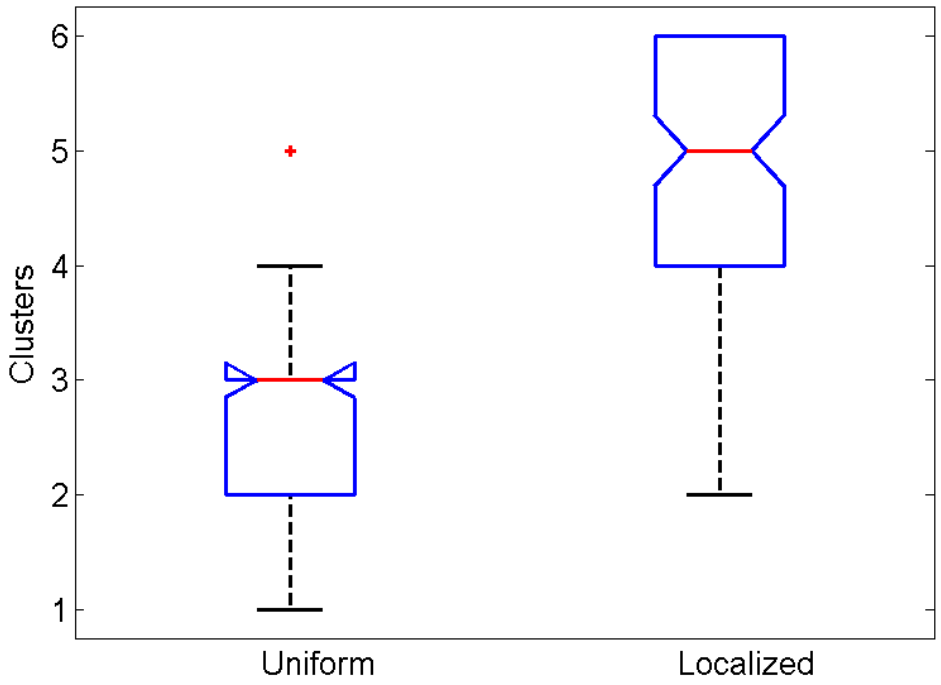

Figure 48 - The number of groups clustered for six spatially localized and six uniformly distributed subsets of synchronized groups of neurons over 100 simulations. The sticks represent the maximum and the minimum number of groups, the box represents the 25th and 75th percentile and the notch is the mean.

When synchronization was uniformly spread through the STN the spike sorting of different failed to produce the number of clusters that were simulated. This is due to the effective shape of the CAP produced by a subset of synchronized neurons either being too similar, or too small (cannot be differentiated from the background noise). The spike shape is an average effect of the action potentials, including extracellular filtering, from each neuron that is synchronized. As the distribution of the synchronized subsets has a uniform probability of selecting any neuron, the average spike shape for each subset is on average the same causing CAPs from different groups to be too similar to separate with spike sorting. On average neurons that are further away are more likely to be selected because the number of neurons increases with the square of the radial distance from the electrode, r^2. The further the neuron is from the electrode, the more the electric field is filtered by the extracellular medium, with an amplitude decay larger than $\frac{1}{r^2}$. This means the CAP shape is dominated by the closest neurons to the electrode. Therefore, the main difference between the two CAPs produced by a subset of synchronized neurons will be the total number of closer neurons, which will change the amplitude of the spike, as seen in the example in Figure 47.

When the synchronized subsets are defined to be spatially localized, rather than across all the STN, the compound action potentials are no longer dominated by the closest neurons. Rather they reflect the average AP at the mean spatial location of the cluster. This increases the success of the spike sorting because each CAP not only differs in amplitude but also in shape due to extracellular filtering. The cluster number from spike sorting still does not always match the number of synchronised groups simulated. This is due to the second effect, where the sum of the synchronised APs is less than the noise level of the simulation.

A point to note from Figure 48 is that the spike sorting never overestimates the number of synchronized subsets. This is due to the low likelihood of one or more neurons being initialised in the simulation close to the electrode tip. This is a limitation of this model since there is a minimum distance a neuron can be generated at. In practice, there is no limit to the neuron-electrode distance, and often the electrodes are moved into a position to allow distinct spikes to be seen above the RMS.

Applying spike sorting to the experimental MERs showed a mean firing rate of all patients 34.92±20.53 and CoV of 0.98±0.28 with an average of 3 clusters. Recordings with less than 15 spikes were discarded to produce an accurate estimate of the mean and CoV. A summary of spike sorting on the experimental data is presented in Table 5.

Table 5 - RESULTS FROM SPIKE DETECTION AND SORTING ON PATIENT DATA SHOWING MEAN FIRING RATE (HZ), COEFFICIENT OF VARIATION (COV) AND THE NUMBER OF CLUSTERS DETECTED.

Recording	Number of MERs	Mean firing rate	Mean CoV	Clusters
10	115	35.77±11.63	1±0.32	2
11	191	48.17±9.96	0.88±0.16	3
14	175	40.25±16.13	0.89±0.20	3
16	169	29.19±7.67	0.95±0.25	3
18	143	29.32±8.91	0.87±0.17	3
2	141	26.50±8.69	0.89±0.17	2

Using a single tip electrode, CAPs and close neurons cannot be differentiated. By using multiple MERs differences between CAPs and close neurons could be seen. This would be due to the different neuron-electrode distance, but a similar group-electrode distance. However, simultaneous MERs cannot be obtained in a target structure during current DBS surgery and the exact location of neurons around the electrode is also currently unmeasurable. These limitations, along with the spike mechanisms presented in this paper,

mean that it would be unlikely to differentiate between APs, a single synchronous neuronal subset and multiple uniformly distributed synchronous neuronal subsets. Due to this complication, DBS MER spikes are most sensibly considered as an indication of the target structures overall activity.

It is noted that the method used for adding the synchronization uniformly in this paper is artificial and not based on a biological mechanism. This was chosen only to demonstrate that with synchronization, the renewal model using Weibull ISI distributions can be fit to the simulations. It also demonstrated that sortable spikes can emerge from CAPs in MERs. The model was extended to include spatially localized synchronization to improve biological plausibility and making the CAPs differ in amplitude and shape. This distribution relates to the idea of somatotopy maps of the STN, which show that there is localized organization in the STN related to different movement tasks (Theodosopoulos, et al., 2004).

5.3 Brain Dynamics

In this section, we present the results from fitting the renewal model with ISI times following a Weibull distribution to different numerical simulations of MERs generated using the dynamics of the Basal Ganglia (BG). The linearized form of the BG model is validated and benchmarked against the complete model. The method for fitting the Weibull statistics is first tested using a Cox process, the results of which have been shown analytically in (Yannaros, 1994). Four different cortical inputs are then tested along with a discussion of the results from these experiments.

The linearized delay for the BG model (details in Chapter 4.5.1) was numerically solved for 5 s simulations, using a fixed time step (0.001 s) and a random cortical input. This decreased the solver time to 3.7±0.4 s from 51±11s for the BG model with axonal delays, Table 6. Solving the model with no delays had no significant speed increase (to within their measurement tolerance) over the linearized model, with an increase in the percentage error.

Table 6 - TIME PERFORMANCE AND ERROR USING THE FULL BG MODEL, ZEROTH ORDER AND FIRST ORDER APPROXIMATIONS.

Model	Solver time (s)	Maximum Error (fraction)
With delays	51±11	0
Without delays	3.1±0.5	0.18
Linearized delay	3.7±0.4	0.07

The decreased computational time is only advantageous if the numerical solution is still accurate (within 10%). Comparing the solution of this to the solution without delays allows accuracy of the linearized approximations of the model to be validated. Figure 49 shows the absolute error for the simulations using zero-time delay and the first order approximation. The maximum error fraction, $|y(t) - y_{0,1}(t)|$ where y is the numerical solution and $y_{0,1}$ indicate the zeroth and first order approximations, for the zeroth order (no delays) was 0.0018 and using the first order approximation the error reduced to $2.677e^{-4}$. The error level for the first order approximation is acceptable for simulating the MER, while significantly decreasing the time needed for a simulation.

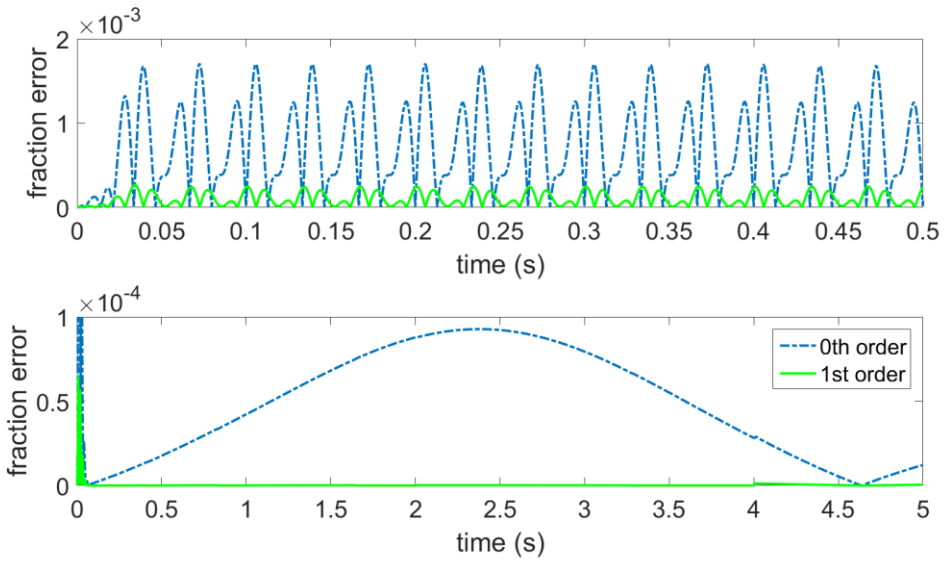

Figure 49 - Absolute error compared to the full model without delays for 0th and 1st order delay approximations for a) sinusoidal cortical input, B) linearly increasing cortical input.

To look at how an MER generated from a dynamical system (changing in time) can be modelled using the renewal model for an MER (time homogenous Weibull ISI distribution),

MERs were first simulated using a Cox process (doubly stochastic) to generate ISI times. By fitting the expected power spectrum of a renewal process MER with Weibull ISI statistics to the power spectrum of the simulation, it was found that as the Cox parameter is increased the average value of the Weibull shape parameter increased, as shown in Figure 50. This figure also shows the variance of the fit, over 300 simulations, increased with increasing Cox parameter.

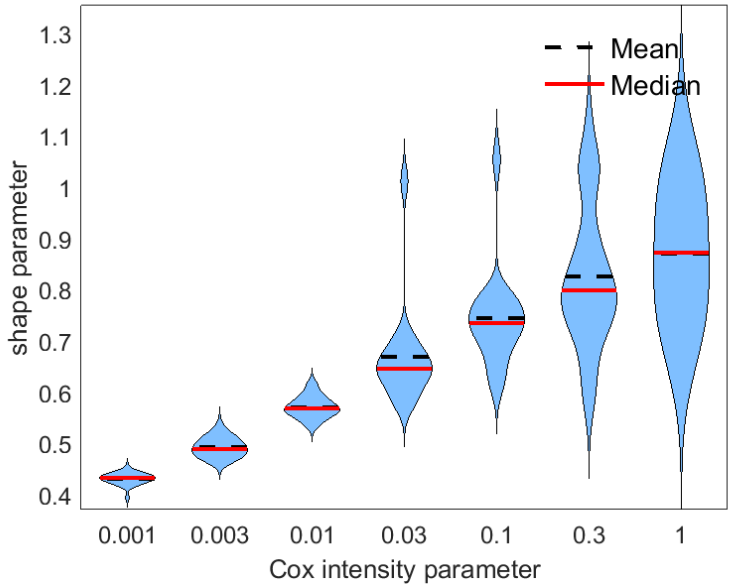

Figure 50 - Distribution of Fitted shape parameters over 100 Simulations for different Cox process intensity parameters. The width of the blue area represents kernel density estimates of the count distribution of predicted shape values. As the intensity parameter increases the shape parameter increases. The variance in fitting the shape parameter also increases.

The results show that the Cox process rate parameter is correlated with the shape parameter determined from the power spectrum. This result is expected based on the results of (Yannaros, 1994) and along with Figure 42 (renewal fitting against recording time) validates the method for finding the shape parameter. Based on Figure 42, a simulation time was chosen that would result in approximately 10% variance in the Weibull shape parameter, however when the Cox parameter was increased past 0.1 the variance of the fit increased beyond 10%. This result indicates that the non-stationary nature of the Cox process over the time length of the simulation is introducing variance of the shape parameter that cannot be accounted for using a stationary model.

For the neural mass model, the cortical input was first modelled using a continuous time stochastic process; the Weiner process. The Weiner process is a stationary Gaussian, meaning the random variable is drawn from a normal distribution that doesn't change in time. It can be seen in Figure 51 that the diffusion parameter has no effect on the expected

shape parameter. There was an increase in the variance of the fitted shape value as the diffusion parameter increased. Adding in a correlation time to the Weiner process creates an Ornstein–Uhlenbeck (OU) process. Using a fixed diffusion parameter of 30, the variance decreases as the correlation parameter (the inverse of the correlation time) is increased, see Figure 52.

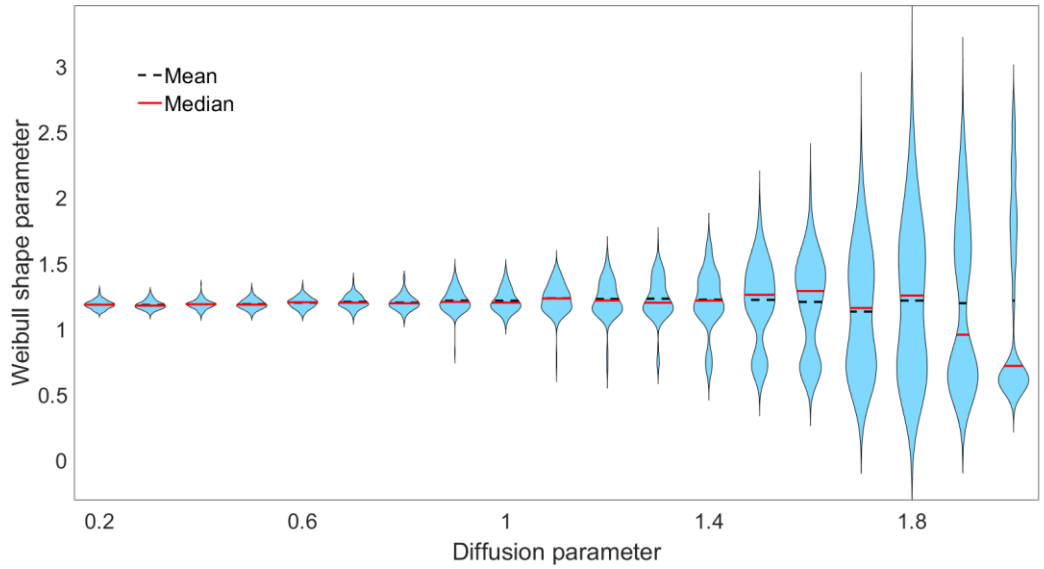

Figure 51 - Distribution of fitted shape parameters over 300 simulations for different diffusion parameters in a Weiner process. The width of the blue area represents kernel density estimates of the count distribution of predicted shape values. As the diffusion parameter increases there is no affect on the shape parameter. The variance increases significantly as the diffusion parameter is increased.

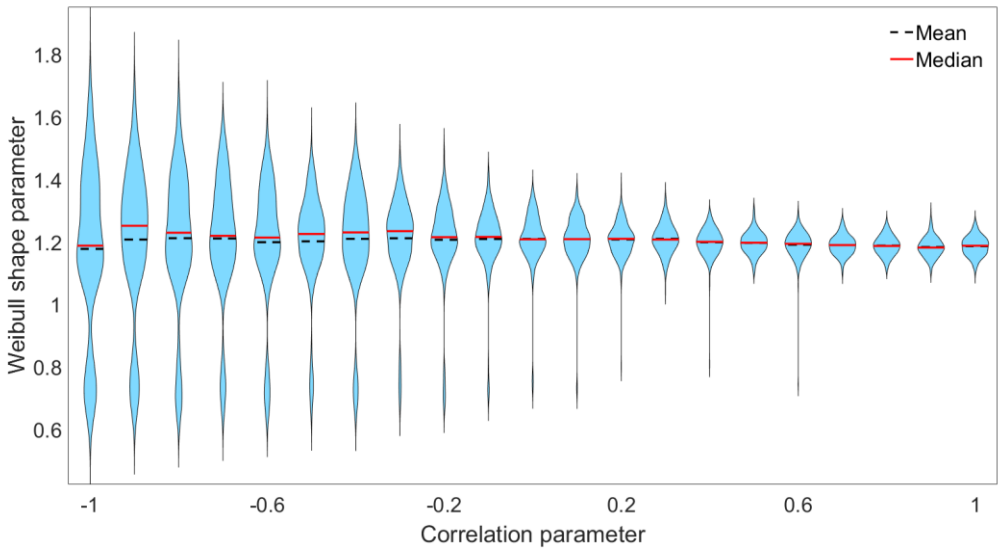

Figure 52 - Distribution of fitted shape parameters over 300 simulations for different correlation parameter for an Ornstein–Uhlenbeck process. The width of the blue area represents kernel density estimates of the count distribution of predicted shape values. The variance is large for small correlation parameters and reduces as the parameter is increased.

The cortical input was then changed to a sinusoid to mimic the oscillations common in the cortex. The frequency of oscillations was varied with a fixed amplitude of 1 spike/s and an offset of 14 spikes/s. Figure 53 shows that varying the frequency has no effect on the predicted shape parameter. Next, by fixing the frequency at 20 Hz and varying the amplitude has no effect on the predicted shape parameter, as seen in Figure 54.

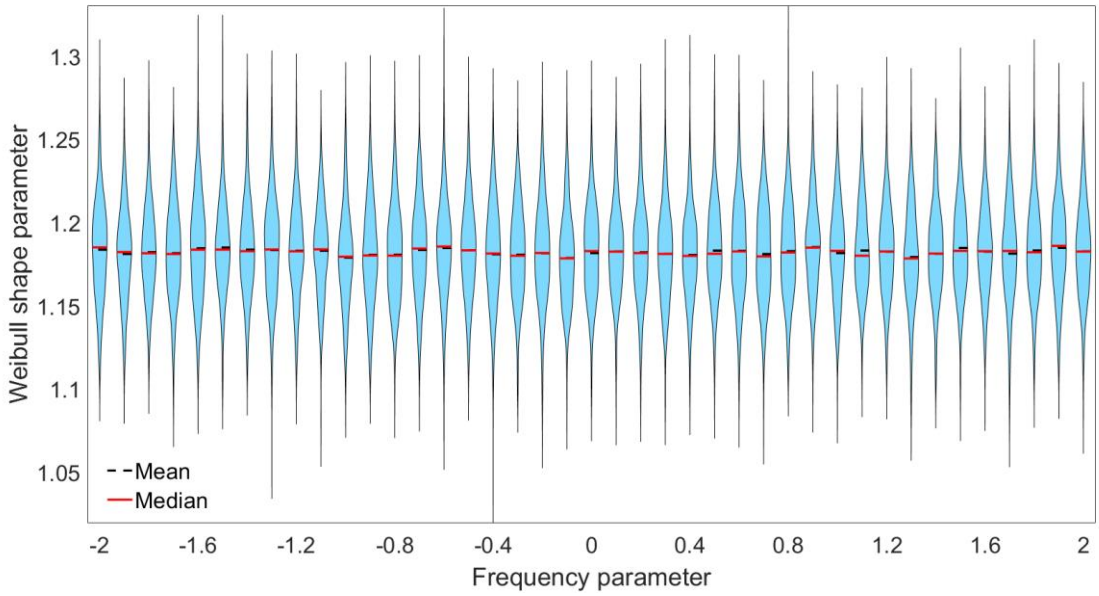

Figure 53 - Distribution of fitted shape parameters over 300 simulations for different frequency sinusoidal cortical inputs. The width of the blue area represents kernel density estimates of the count distribution of predicted shape values. There is no significant change in the shape parameter or variance of the fits.

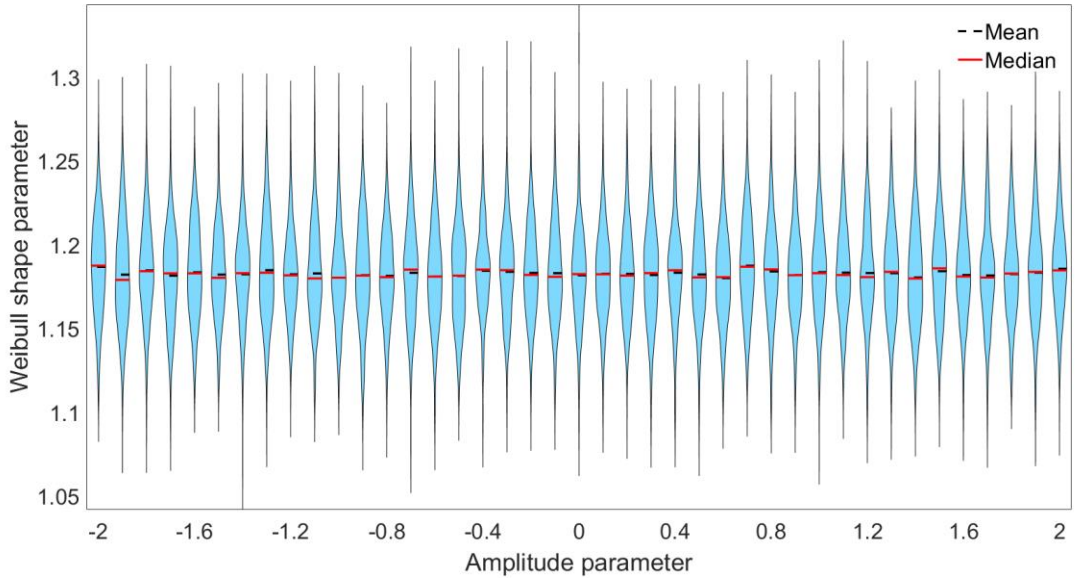

Figure 54 - Distribution of fitted shape parameters over 300 simulations for different amplitude sinusoidal cortical inputs. The width of the blue area represents kernel density estimates of the count distribution of predicted shape values. There is no significant change in the shape parameter or variance of the fits.

A spectral property that is of interest with regards to MERs from PD patients is beta band behaviour (Brown, 2009). The spectrograms of the simulations found that beta band behaviour similar to patient recordings was found when $c \leq 1$. In the previous section, the shape parameter had no connection to biological properties as the model was developed from a top down perspective. With the added brain dynamics, it can now be seen that the beta band behaviour could be related to the underlying functions of the cortex. The two random processes, Weiner and OU, can both exhibit statistics that are described using $c \leq 1$. A change from the random cortical input to a deterministic process would cause the beta band behaviour to persist. This type of behaviour could be used as a biomarker for PD and warrants further study, discussed briefly in Chapter 6.3.

To determine the usefulness of the renewal model analysis using Weibull ISI statistics we have two criteria to determine. First, does the fitted Weibull shape parameter vary over repeated simulations for the same input parameter. Second, can the Weibull shape parameter be used as a predictor of the input parameter. We will look at the first criterion and determine how well the stationary approximation is for the non-stationary MER simulations.

For every parameter for both sinusoidal inputs the variance in the fit of the shape parameter was less than 10%. This level of variance can be explained by the finite length of the

recordings simulated. This shows that the renewal model can describe the ISI times generated given a sinusoidal input. However, the mean value and variance of the shape parameter does not change when varying the input parameters. This prevents the shape parameter from being used as a predictor of sinusoidal cortical input parameters.

In both the Weiner and OU simulations the variance of the shape parameter increased more than can be explained due to the finite length or the recording. This result indicates that different realizations of the simulation using the same input produces different distributions of ISI times. Although the first criteria of describing the simulation outputs using a stationary distribution fails for certain parameter values, it does not prevent the fits from being used as a predictor of the input.

To look at how the shape parameter could be used to characterize the cortical input we can look at the OU processes. From the simulations, we can construct a 2D histogram of Weibull shape given a specific cortical parameter. Figure 55 shows an example of this for the OU process using the logarithm of the correlation parameter. This distribution of counts is equivalent to the probability of measuring a shape parameter giving a correlation parameter, $P(\lambda|\log\tau^{-1})$. If we assume *a priori* knowledge that the cortical input follows an OU process, then we can use Bayes Theorem to determine the correlation parameter given a measurement of the shape parameter using:

$$P(\log\tau^{-1}|\lambda) = \frac{P(\lambda|\log\tau^{-1})P(\log\tau^{-1})}{P(\lambda)} \qquad (51)$$

To use this formula $P(\lambda)$ and $P(\log\tau^{-1})$ are required. $P(\lambda)$ can be estimated from the simulations by summing over the correlation parameter to get the total number of counts for a given λ and dividing by the total number of simulations. Without experiments to determine $P(\log\tau^{-1})$ an uninformative prior, where the probability does not favour any value, can be used. Assuming some form of exponentially distributed parameter, one such uninformative prior that can be used is Jeffery's prior, which gives a uniform distribution when normalized for $P(\log\tau^{-1})$ over a constrained range. For an example if we assume the logarithm of correlation parameter is uniformly distributed between -1 and 1 we can produce Figure 56 using Equation (51).

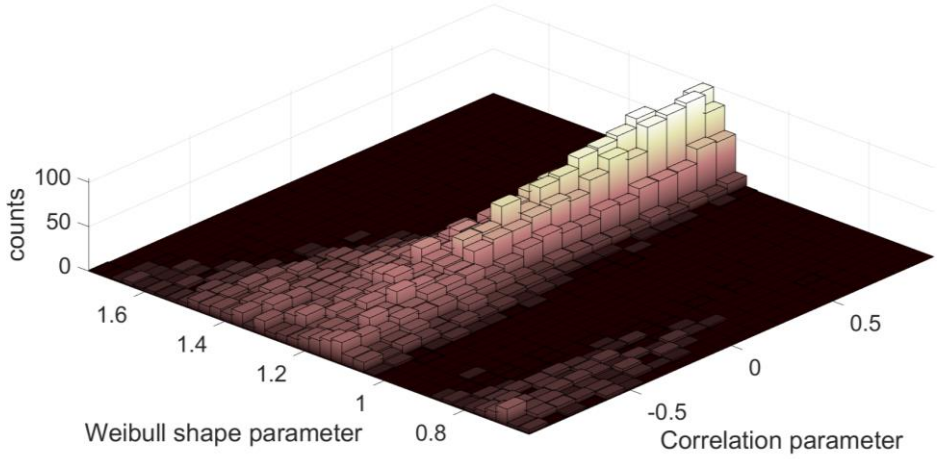

Figure 55 - Probability of finding a specific Weibull shape parameter when given an OU process cortical input with a given correlation parameter.

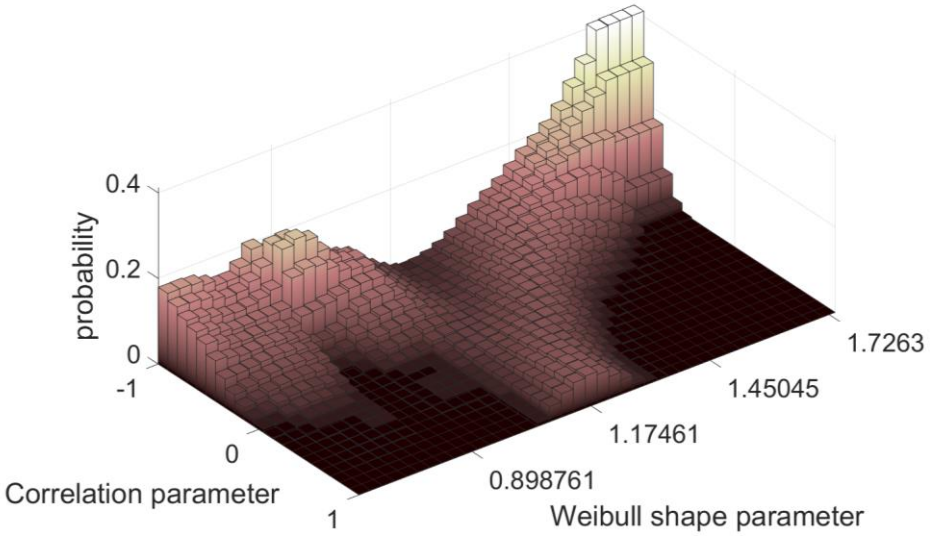

Figure 56 - Probability of a cortical input with a given correlation parameter given a measured Weibull shape parameter.

We can apply the methods presented here to the result from the patient data. In the validation of the model it was found that using a renewal model with a Weibull shape parameter of 0.8 best fit the interoperative patient recordings in a resting state. Using the analysis method presented above we can calculate the *posteri* estimate, $\mathcal{L}(x;\lambda=0.8)$, for the different types of cortical parameters we have modeled. By calculating $P(x|\lambda=0.8)$ for each of the cortical inputs and finding the maximum gives $\mathcal{L}(x;\lambda=0.8)$. For the Wiener and OU processes $P(x|\lambda=0.8)$ was found, giving Figure 57. The maximum of the *posteri* estimate for the Diffusion parameter is $\mathcal{L}(D;\lambda=0.8)=10^{1.6}=39.81s^{-1}$ and for the correlation parameter $\mathcal{L}(\tau^{-1};\lambda=0.8)=10^{-1}=0.1s^{-1}$.

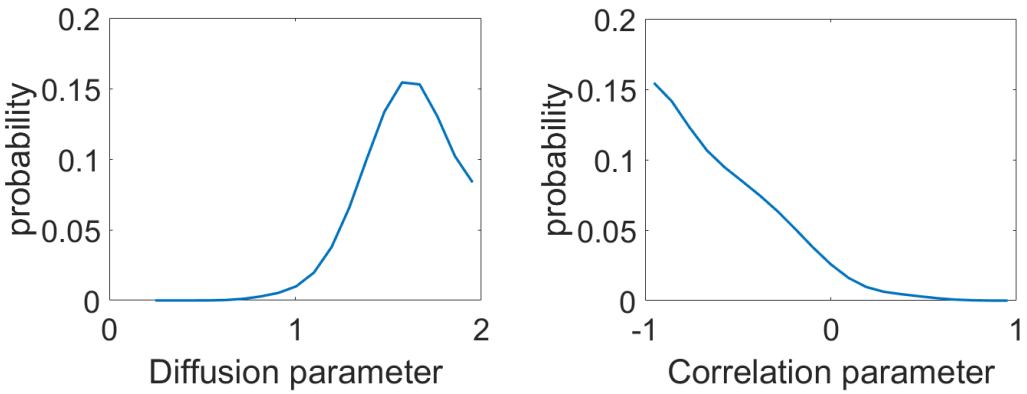

Figure 57 - Probability of a cortical parameter using a measured Weibull shape parameter of 0.8. (a) $P(logD|\lambda = 0.8)$ and (b) $P(log\tau^{-1}|\lambda = 0.8)$.

The sinusoidal inputs produce no variation in λ which means the parameters for them cannot be estimated. To demonstrate this, the results from varying the frequency parameter to produce the 2D histogram of Weibull shape and cortical frequency, Figure 58, are used. Using Jeffry's prior again, where *a prior* knowledge on the bounds of the frequency and values between these bounds are equally likely, Equation (51) can again be used to calculate $P(\log \omega|\lambda)$. Figure 59 shows the results from this calculation, with the likelihood of most frequencies being flat. The problem with this naïve probability calculation is the effect of noise, specifically low counts of rare events on the edges. Regularization can be used to correct this problem. By considering the probability range where the frequency parameter is 1.3, gives values of 0-0.001. Because of the finite number of events used to generate the histogram, the probabilities are discretised into steps of 0.00025. By assuming now that there is some finite probability of any combination of shape parameter and frequency parameter occurring, the minimum step in probability is added to all the bins. Calculating $P(\log \omega|\lambda)$ now gives Figure 60. This represents an approximately uniform distribution, indicating that a maximum *posteri* estimate cannot be made to determine the frequency of the cortical input to the BG.

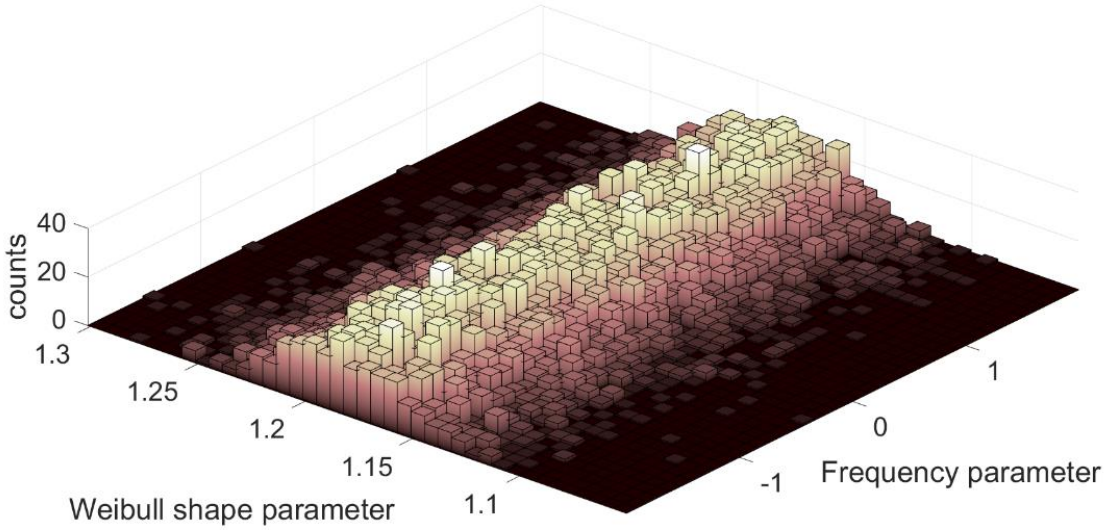

Figure 58 - 2D histogram of measured Weibull shape parameter given a frequency parameter.

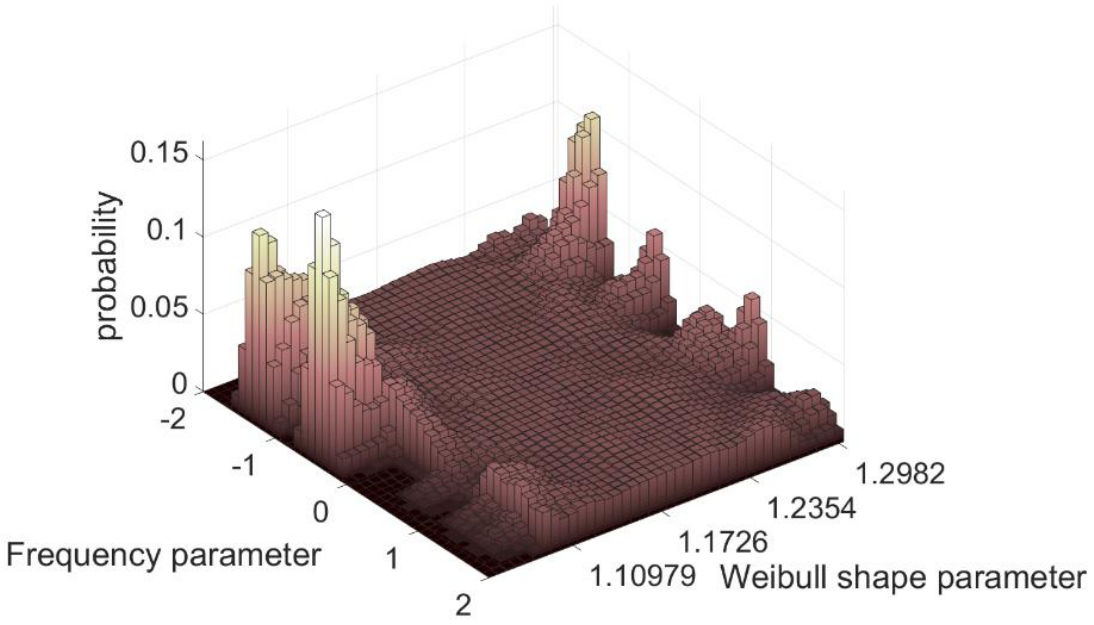

Figure 59 – Unsmoothed probability of a frequency given a Weibull shape parameter.

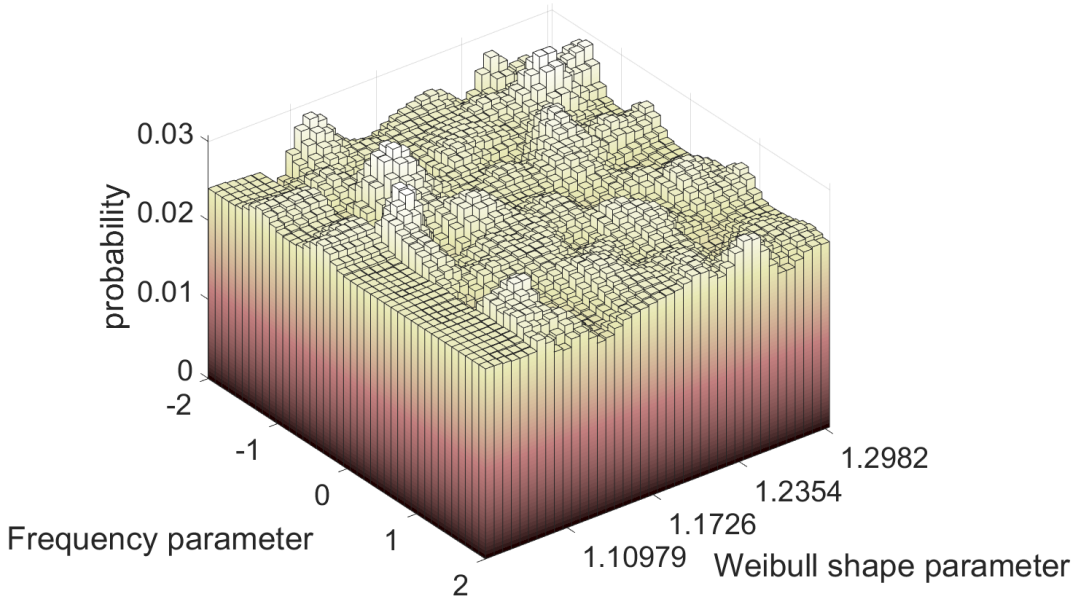

Figure 60 - Regularized probability of a frequency given a Weibull shape parameter.

Other forms of regularization could be used to assist in the calculation of the conditional probabilities of the cortical parameters. By taking a larger number of samples, the noise in the counts would reduce. If getting a large data set is a restriction, another method would be to use a kernel density estimate (KDE) on the histograms. This would be done by taking rows and using a 1D KDE, since the rows are independent using a 2D KDE would not be valid. This method could still have problems when the smoothed estimate has regions of 0 probability and the finite valued probability offset used above may also be necessary.

The estimate of the cortical parameters (x) can be improved by using multiple independent measurements of λ, and applying the Bayes Theorem recursively:

$$P(x|\lambda_1, \dots, \lambda_{N-1}, \lambda_N) = \frac{P(\lambda_N|x)P(x|\lambda_1, \dots, \lambda_{N-1})}{P(\lambda_N)} \quad (52)$$

This analysis involves assumptions on the dynamics of the cortical input to constrain the probability distributions. The assumptions used are not necessarily realistic but have been chosen arbitrarily for an example of how estimation of the input parameter would be performed. To extend this work for practical applications, such as feedback control, investigating different models of cortical input by either including the dynamics of interactions between the motor cortex and the thalamus, or recording activity from patients performing different tasks could be used.

5.4 Summary

The results for the renewal process MER model best fits the patient data with a Weibull shape parameter of 0.8 and it was found that simulation of a neuron volume of ~1mm^3, corresponding to ~10,000 neurons, was required. Introducing two different synchronisation methods to the model did not affect using the assumptions of the renewal theory (IID) to determine the ISI distribution, with the firing time statistics used for the simulations found by inverting their power spectra. The time-homogenous assumption of the renewal model could also be used to provide a description of the behaviour of the neural mass model of the BG to generate the spike times used to simulate STN MERs, as well as demonstrating under certain conditions it is possible to use the shape parameter of the Weibull distribution to predict changes of the cortical firing rate. These findings motivate further investigation into using renewal process models of STN MERs as biomarkers in feedback control of DBS and as a possible identifier of disease.

6 Conclusion

This thesis contains a novel approach to modelling and analysing microelectrode recordings of the subthalamic nucleus. Simplifications to an intractably complex physical system have been made to allow the model to be evaluated efficiently while still reproducing key features. The main underlying assumptions of the model are:

- A homogeneous population of independent neurons, where all neurons fire with the same waveform, firing times with the same statistics and are treated as point sources. This means we only consider their far-field and do not consider their spatial morphology.
- Isotropic filtering with distance, where the extracellular medium between the neurons and electrode has no spatial changes other than their radial distance to the electrode.
- A fixed number of neurons contribute to the recordings.
- Independent, identically distributed (IID) inter-spike interval times for all the neurons, characterized by the Weibull distribution.

The simplifications allow simulations to be computed for large numbers of neurons very quickly. Using this the volume of neurons, ~1mm^3 (10,000 neurons), that contribute to the background noise of STN MERs was calculated. The speed of generating simulations also allows investigations using thousands of repeated trials, for example fitting the Weibull distribution to the STN MER generated using basal ganglia dynamics (Chapter 5.3). These simplifications are also used to make the inverse problem mathematically tractable, allowing a microelectrode recording to be described using two variables; the Weibull shape parameter and the scale parameters. Opening avenues of further research into using these parameters as biomarkers for electrode location, disease state or in brain machine interfaces such as adaptive DBS.

Applying the renewal process assumptions to more complicated models where the IID assumption is no longer valid, shows that the inverse method could be used to find a time-homogeneous Weibull distribution that described the recording consistently in Chapter 4.3.2 (the variance of the Weibull parameters over 100 simulations was less than or equal to the variance of fitting an IID simulation). Fitting the Weibull parameters to the data also allowed

calculations on the probability of different cortical inputs driving the basal ganglia model for simulation of the STN MER.

Chapter 4.3 shows that the simplification of the modelled system by assuming a renewal model and parametrization of the ISI times improves the computational efficiency in simulating an MER but decreases the realistic features seen and the biological plausibility. This decrease in computational time needed for a solution allows this model to be used in studies where parameters can be varied and a large result set can be produced allowing analysis techniques such as Monte-Carlo methods.

These findings answered the two questions of this thesis proposed in the introduction:

1. What range do the neurons further from the electrode contribute to the MER background noise? It was found that modelling a volume of ~1mm^3 of STN neurons produced simulations that had the best agreement with patient data. This volume corresponds to ~10,000 neurons.
2. Can fitting the inter-spike interval probability distribution of renewal models to STN MERs be used as a potential biomarker? This was tested by modifying the STN MER model to include biologically realistic affects that break the assumptions of the renewal model. The renewal model could still be used to fit these models with varying degrees of accuracy, high fidelity when synchronization was added and an indication that it could predict some cortical dynamics using the basal ganglia model. Potential use of the renewal model as a biomarker for cortical behavior was presented in Chapter 5.3.

The rest of this chapter first outlines the contributions of the work performed. Next is details on the limitations of this research including alternative approaches and technical limitations. Finally, suggestions for further research arising from this thesis are presented.

6.1 Thesis contributions

The following results from this thesis are significant and novel contributions:

- A novel, computationally fast (ability to simulate 1s of model time in less than 1s wall time) model for subthalamic nucleus microelectrode recordings, containing contributions from 10000’s of neurons and extracellular filtering, using a renewal

model for the neuron spike timings, **Papers A and C**. The model has been produced using a top down approach to recreate interoperative patient recordings and demonstrated that volumes of ~1mm^3 contribute to the high frequency noise seen in an STN MER.

- A method of fitting the model to recordings by inverting the power spectrum using non-linear least squares to determine the inter-spike interval probability density function. The ISI PDF is found parametrically using the Weibull distribution, because it reproduces common firing patterns found in neurons, **Paper D**.
- An analysis of fitting the renewal MER model to simulations where the IID assumption relaxed by addition of synchronisation between neurons. This demonstrated that the MER model from **Papers A and C** is suitable for fitting patient recordings if synchronisation is present.
- Elucidation of how synchronisation can contribute to decreasing the signal to noise ratio of spikes found in MERs, and demonstration of the degeneracy between the number of neurons synchronised and their distance from the electrode as shown in **Paper B**.
- An analytical linearization of the axonal delays present in the neural mass model of the BG, with validation of the result and benchmarking the speed gains in numerically solving the system of PDEs.
- An analysis of fitting the renewal MER model to simulations where the IID assumption relaxed by using a neural mass model of the BG to generate the STN spike timings, **Paper D**. This demonstrated that the MER model from **Papers A and C** can be used to fit patient recordings for different classes of cortical behaviour; deterministic, Gaussian and Gauss-Markov processes.
- A novel method for determining parameters, such as the function of the cortical firing rate, of BG neural mass models, from **Paper D**, from STN MERs using Bayes Rule and fitting simulations using the model from **Paper C**.

6.2 Limitations

Specific models and assumptions on neuron behaviour were chosen for this research. These choices have technical limitations on what they can predict and simulate. The limitations of the work that has been presented in this thesis are listed below:

- A major limitation of the approach of fitting a Weibull distribution renewal model for use as a biomarker is the inability to replicate multimodal ISI distributions. There has been evidence that STN neurons exhibiting tremor behaviour can have multimodal ISI distributions.
- An assumption is that modulation of the power spectrum is only due to the renewal statistics of the neurons firing times. The model is also limited in the low frequency behaviour that is picked up by the electrode. Neurons can exhibit sub-threshold oscillations, slow exchanges of ions in and out of the cell which do not build up enough potential to trigger an action potential. These frequency components of these oscillations are low compared to the action potential. These oscillations could affect the method used to fit the model to the patient recordings, due to their contribution to the power spectrum of the MER. In the work for this thesis it was assumed that because these oscillations can be cause by action potentials arriving from afferent neurons, they would display the low frequency behaviour of the firing statistics of these neurons. This however has not been tested or modelled. This is a crucial assumption which requires further work to validate through modelling.
- The model used for this research assumes every action potential had the same shape and amplitude for a given neuron. However, neurons can exhibit a rate dependant shape change. This is where the shape of the action potential (both amplitude and frequency components) can change with the rate that the neurons fire. This is a feature that is found at high firing rates, and by assuming the mean firing rate is small compared to the maximum firing rate this effect can be ignored, for example the STN maximum firing rate is ~500 Hz, while the average firing rate is ~100 Hz.
- STN neurons can also exhibit different ISI statistics between different locations. The ability to fit the model using the inverse methods discussed in this thesis could also be investigated under this condition of different ISI statistics for different neurons. It was not considered in this study because there is evidence that the STN neurons are grouped into somatotopy regions (Theodosopoulos, et al., 2004), meaning within the size of the field of neurons seen by the electrode all the neurons exhibit the same behaviour. However, if the electrode is near the border of regions, it could pick up the electric field generated by multiple groups of neurons with different spiking statistics. The neural mass model only describes the average firing rate of the STN and this rate is applied to all the neurons in the simulation. If the neurons have different firing

rates (similar to the previous point on varying ISI distributions), but the correct average firing rate, the analysis here may not hold.

- The model in **paper D** did not include the effects of dopamine (DA) depletion on the neural pathways of the basal ganglia. DA levels are affected by the progression of PD and medication for treatment of PD symptoms is used to control the levels of DA in patients.

6.3 Suggestions for further research

The work in this thesis has opened avenues for potential research that can test the limitations outlined in 6.2 and provide directions to continue research. Due to time limitations and data availability these research directions were not pursued in this thesis. Some suggestions for further research are listed below:

- An extension to this work, by development of a parametric method of representing a more generic distribution than is possible with the Weibull distribution, can address the limitation of fitting multimodal ISI distributions.
- Extending the model to include a process that simulates sub-threshold oscillations, and a comparison by fitting the renewal model, would address the limitation of this work as to whether it is suitable to assume that modulation of the power spectrum is only due to the renewal statistics of the neurons firing times.
- Include somatotopic groups (Theodosopoulos, et al., 2004) of neurons when simulating the STN MER. This would include a study of the effects of neurons following different ISI distributions on fitting the renewal model for the MER using the IID assumptions.
- Since the neural mass model is a moment expansion of the Fokker-Plank equation, higher order moments could be added to the model to see how different distributions of firing rates would change the analysis presented in this thesis.
- By repeating the simulations with different DA levels, the usefulness of the model for predicting disease and its potential use in adaptive DBS can be determined.
- An example of future work would be to use cortical inputs recorded from patients performing different tasks. The renewal model with the IID assumption can also be used to investigate patient dopamine levels, or correlation of interoperative MERs with UPDRS scores. The Bayesian method of analysis used in the results of this

thesis could then be used to determine the values of these by the using the model and the inverse method of fitting the Weibull distribution. This work would require a larger patient data set than was available during this thesis.

- Acquisition of EEG recordings of the cortex can be used with the neural mass model to generate STN MERs. With enough recordings the Bayesian analysis, using the Weibull shape parameter, presented in this thesis can be used to see if the model can be used to predict the behaviour of the cortex.
- After validation of the Bayesian analysis using EEG recordings a potential closed loop stimulation scheme could be developed. The work presented in this thesis presents a method for estimating the cortical state in terms of a rate. Comparing the rate estimate from to a cortical measurement or a desired rate would produce an error magnitude that could be used for modifying the stimulation frequency or amplitude.
- Further experimental studies acquiring more patient recordings can allow an investigation on fitting the model to patient recordings under movement tasks. The STN, and BG on a whole, is involved in motor coordination and control. By finding the effects of movement on the STN, this model could assist in development towards adaptive DBS.
- Developing the model parameters for MERs from other deep brain structures where interoperative patient recordings can be obtained for validation of the simulations. For example, during implantation in the STN the microelectrode passes through the thalamus, the Zona Incerta, the second field of Forel and it can go past the STN into the substantia nigra.
- Determine the observability and controllability of the basal ganglia neural mass model using measurements of the STN state using the inverse method of fitting the renewal model presented in this paper. This would give an indication on the usefulness of the model in this paper in an adaptive DBS controller.

7 References

Adrian, E. & Zotterman, Y., 1926. The impulses produced by sensory nerve endings: Part II: The response of a single end organ. *J Physiol (Lond.),* Volume 61, pp. 151-171.

Akingba, A. G. & al., e., 2003. *Application of nanoelectrodes in recording biopotentials.* s.l., IEEE, pp. 870-874.

Albada, S. J. v., Gray, R. T., Drysdale, P. M. & Robinson, P. A., 2009. Mean-field modeling of the basal ganglia-thalamocortical system. II Dynamics of parkisonian oscillations. *Journal of Theoretical Biology,* Volume 257, pp. 664-688.

Albada, S. J. v. & Robinson, P. A., 2009. Mean-field modeling of the basal ganglia-thalamocortical system. I Firing rates in healthy and parkinsonian states. *Journal of Theoretical Biology,* Volume 257, pp. 642-663.

Avil-Akerberg, O. & Chacron, M. J., 2011. Nonrenewal spike train statistivs: causes and functional consequences on neural coding. *Exp. Brain Res.,* Volume 210, pp. 337-353.

Baker, K. B. & al, e., 2004. Target Selection Using Microelectrode Recordings. In: Z. Israel & K. J. Burchiel, eds. *Microelectrode recordings in movement disorder surgery.* New York: Thieme Medical Publishers, Inc.

Banta, E., 1964. A note on the correlation function of nonindependent overlapping pulse trains. *IEEE Trans. Inform. Theory,* 10(2), pp. 160-161.

Bartlett, M., 1963. The spectral analysis of point processes. *Journal of the Royal Statistical Society. Series B (Methodological),* pp. 264-296.

Bastian, J. & Nguyenkim, J., 2001. Dendritic modulation of burst-like firing in sensory neurons. *Journal of Neurophysiology,* 85(1), p. 10.

Bedard, C. & Destexhe, A., 2009. Macrascopic models of local field potentials and the apparent 1/f noise in brain activity. *Biophys. J.,* Volume 96, pp. 2589-2603.

Bedard, C., Kroger, H. & Destexhe, A., 2004. Modeling extracellular field potentials and the frequency-filtering properties of extracellular space. *Biophys. J.,* Volume 86, pp. 1829-1842.

Bedard, C., Kroger, H. & Destexhe, A., 2006. Model of low-pass filtering of local field potentials in brain tissue. *Physical Review E,* 73(5), p. 051911.

Bell, C. G. et al., 1961. Reduction of speech spectra by analysis by synthesis techniques. *J. Acoust. Soc. Amer.,* 33(12), pp. 1725-1736.

Bialek, W., Warland, D. & Steveninck, R. d. R. v., 1999. *Spikes Exploring the Neural Code.* Cambridge MA, US: The MIT Press.

Brittain, J. & Brown, P., 2014. Oscillations and the basal ganglia: Motor ontrol and beyond. *Neuroimage,* Volume 85, pp. 637-647.

Brookes, M. J. & al., e., 2011. Measuring functional connectivity using MEG: Methodology and comparison with fcMRI. *NeuroImage,* 56(3), pp. 1082-1104.

Brown, E. N. & al., e., 2001. An analysis of neural receptive field plasticity by point process adaptive filtering. *PNAS,* 98(21), pp. 12261-12266.

Burchiel, K. J. & Israel, Z., 2004. Microelectrode signal analysis techniques for improved localization. In: *Microelectrode Recordings in Movement Disorder Surgery.* New York, NY, USA: Thieme Medical, vol. 1, 2004..

Buzsaki, G., Anastassiou, A. & Koch, C., 2012. The origin of extracellular fields and currents - EEG, ECoG, LFP and spikes. *Nature Reviews Neuroscience ,* 13(6), p. 407.

Camalier, C. R., Konrad, P. E. & al., e., 2014. Methods for surgical targeting of the stn in early-stage Parkinson's disease. *Front. Neurol,* Volume 5, p. 25.

Camunas-Mesa, L. A. & Quiroga, R. Q., 2013. A detailed and fast model of extracellular recordings. *Neural Computation,* Volume 25, pp. 1191-1212.

Cateua, H. & Reyes, A. D., 2006. Relation between single neuron and population spiking statistics and effects on network activity. *Phys. Rev. Lett.,* 96(5), p. 058101.

Chen, C. C. & al., e., 2010. Complexity of subthalamic 13-35 Hz oscillatory activity directly correlates with clinical impairment in patients with Parkinson's disease. *Experimental Neurology,* 224(1), pp. 234-240.

Coffey, W., Kalmykov, Y. & Waldron, J., 1996. *The Langevin equation with applications in physics, chemistry and electrical engineering.* Singapore: World Scientific.

Coyne, T. et al., 2006. Rapid subthalamic nucleus deep brain stimulation lead placement utilising CT/MRI fusion microelectrode recording and test stimulation. *Acta Neurochirurgica Suppl.,* Volume 99, pp. 49-50.

Davie, C. A., 2008. A review of Parkinson's disease. *Br. Med. Bull. ,* 86(1), pp. 109-127.

Deco, G. et al., 2008. The Dynamic Brain: From Spiking Neurons to Neural Masses and Cortical Fields. *PLoS Computational Biology,* 4(8), pp. 1-35.

Dummer, B., Wieland, S. & Lindner, B., 2014. Self-consistent determination of the spiketrain power spectrum in a neural netowrk with sparse connectivity. *Frontiers in computational Neruoscience,* 104(8).

Eden, U. T. & al, e., 2004. Dynamic analysis of neural encoding by point process adaptive filtering. *Neural Computation,* Volume 16, pp. 971-998.

Eusebio, A. & Brown, P., 2009. Synchronisation in the beta frequency-band - the bad boy of parkinsonism or an innocent bystander?. *Experimental Neurology,* 217(1), pp. 1-3.

Favre, J. & T., B., 2004. Signal Processing and Pattern Recognition in Microelectrode Recordings. In: I. Z. & B. K. J., eds. *Microelectrode Recordings in Movement Disorder Surgery.* New York: Theime Medical Publishers.

Feng, X.-J.et al., 2007. Optimal deep brain stimulation of the subthalamic nucleus: A computational study. *J. Computational Neurosci.,* Volume 23, pp. 3265-3282.

Franklin, J. & Blair, W., 1995. The effect of a refractory period on the power spectrum of neuronal discharge. *SIAM J. Applied Math.,* 55(4), pp. 1074-1093.

Fridman, J. et al., 1984. Application of phase spectral analysis for brain stem auditory evoked potential detection in normal subjects and patients with posterior fossa tumors. *Int. J. Audiol.,* 23(1), pp. 99-113.

Garonzik, I. M. et al., 2004. Microelectrode techniques: Single-cell and field potential recordings. In: *Microelectrode Recordings in Movement Disorder Surgery.* New York, NY, USA: Thieme Medical.

Gold, C., Henze, D. A., Koch, C. & Buzsaki, G., 2006. On the origin of the extracellular action potential waveform: A modeling study. *J. Neurophsiol,* 95(5), pp. 3113-3128.

Gurney, K., Prescott, T. J. & Redgrave, P., 2001. A computational model of action selection in the basal ganglia. I. A new functional anatomy. *Biol. Cybern,* Volume 84, pp. 401-410.

Heida, T., Marani, E. & Usunoff, K. G., 2008. The subthalamic nucleus: Modelling and simulation of activity. Part II. In: *Advances in Anatomy.* Berlin, Germany: Springer-Verlag.

Heinricher, M. M., 2004. Principles of Extracellular single-unit recording. In: Z. Israel & K. J. Burchiel, eds. *Microelectrode Recordings in Movement Disorder Surgery.* New York, NY, USA: Thieme Medical.

Hines, M. L. & Carnevale, N. T., 1997. The NEURON simulation environment. *Neural computation,* 9(6), pp. 1179-1209.

Hodgkin, A. L. & Huxley, A. F., 1952. A quantitative description of membrane current and its application to conduction and excitation in nerve. *The journal of physiology,* 117(4), pp. 500-544.

Hofmanis, J. & al., e., 2011. *Propagation of electrical field in the brain using electrical intra-cerebral stimulations.* Boston, MA, IEEE.

Hosain, K., Kouzani, A. & Tye, S., 2014. Closed loop deep brain stimulation: An evolving technology. *Australas Phys. Eng. Sci. Med.,* Volume 37, pp. 619-634.

Humphrey, D. & Schmidt, E. M., 1990. Extracellular Single-Unit Recording Methods. In: *Neurophysiological Techniques.* s.l.:Humana Press, pp. 1-64.

Hutchison, W. D., Allan, R. J. & al., e., 1998. Neurophysiological identification of the subthalamic nucleus in surgery for Parkinson's disease. *Ann. Neurol.,* Volume 44, p. 622.

Israel, Z. & Schulder, M., 2004. History of electrophysiological recording for functional neurosurgery. In: Z. Israel & K. J. Burchiel, eds. *Microelectrode Recordings in Movement Disorder Surgery.* New York, NY, USA: Thieme Medical.

Izhikevich, E. M., 2003. Simple Model of SPiking Neurons. *IEEE Transactions on Neural Networks,* 14(6), pp. 1569-1572.

Izhikevich, E. M., 2004. Which model to use for Cortical Spiking Neurons?. *IEEE Transactions on Neural Networks,* 15(5), pp. 1063-1070.

Izhikevich, E. M., 2006. Polychronization: Computation with spikes. *Neural Computation,* Volume 18, pp. 245-282.

Izhikevich, E. M., 2007. *Dynamical Systems in Neuroscience.* Cambridge: MIT Press.

Izhikevich, E. M., 2007. Solving the distal reward problem through linkage of STFP and dopamine signaling. *Cerebral Cortex,* 17(October), pp. 2443-2452.

James, C. D. et al., 2004. Extracellular recordings from patterned neuronal networks using planar microelectrode arrays. *IEEE Trans. Biomed. Eng.,* 51(9), pp. 1640-1648.

Johnson, D. H., 1996. Point process models of single-neuron discharges. *Journal of computational neuroscience,* 3(4), p. 275.

Johnston, D. & Miao-Sin Wu, S., 1995. *Foundations of Cellular Neurophysiology.* Cambridge: MIT press.

Kang, G. & Lowery, M. M., 2011. *Effects of subthalamic nucleus interconnectivityat deep brain stimulation onset and offset.* Boston, Massachusetts, IEEE.

Kringelbach, M. C. & al., e., 2007. Translational Principles of Deep Brain Stimulation. *Nature Reviews, Neuroscience.*

Kuhn, A. A. & al., e., 2009. Pathological synchronisation in the subthalamic nucleus of patients with Parkinson's disease relates to both bradykinesia and rigidity. *Experimental Neurology,* Volume 215, pp. 380-387.

Kuhn, A. A. et al., 2008. High-frequeny stimulation of the subthalamic nucleus suppresses oscillatory activity in patiens with parkinson's disease in parallel with improvement in motor performance. *Journal of Neuroscience,* Volume 28, pp. 6165-6173.

Li, C., 2011. A model of neuronal intrinsic plasticity. *IEEE transactions on autonomous mental development,* Volume 99, p. 1.

Lindner, B., 2006. Superposition of many independent spike trains is generally not a renewal process. *Phys. Rev. E,* Volume 55, pp. 1074-1093.

Little, S. et al., 2013. Adaptive deep brain stimulation in advanced Parkinson disease. *Ann. Neurol.,* Volume 74, pp. 449-457.

Liu, C. et al., 2017. Neural mass models describing possible origin of the excessive beta oscillations correlated with Parkinsonian state. *Neural Networks,* Volume 88, pp. 65-73.

Long, L. N. & Fang, G., 2010. *A review of biologically plausible neuron models for spiking neural networks.* s.l., s.n., pp. 3265-3282.

Ly, C. & Tranchina, D., 2009. Spike train statistics and dynamics with synaptic input from any renewal process: a population density approach. *Neural computation,* 21(2), p. 360.

MacKay, D. M. & McCulloch, W. S., 1952. The limiting information capacity of a neuronal link. *The bulletin of mathematical biophysics,* 14(2), pp. 127-135.

Maimon, G. & Assad, J. A., 2009. Beyond Poisson: Increased spike-time regularity across primate parietal cortex. *Neuron,* 62(3), p. 426.

Marceglia, S., Foffani, G. & al., e., 2006. Dopamine-dependent non-linear correlation between subthalamic rhythms in Parkinson's disease. *The Journal of physiology,* 571(3), p. 579.

Marreiros, A. C. et al., 2013. Basal ganglia-cortical interactions in Parkinsonian patients. *Neuroimage,* Volume 66, pp. 301-310.

Mayo Foundation for Medical Education and Research (MFMER), 2017. *Progressive supranuclear palsy - Overview - Mayo Clinic.* [Online] Available at: http://www.mayoclinic.org/diseases-conditions/progressive-supranuclear-palsy/home/ovc-20312358
[Accessed 14 September 2017].

McIntyre, C. C., Grill, W. M., Sherman, D. L. & Thakor, N. V., 2004. Cellular effects of deep brain stimulation: Model-based analysis of activation and inhibition. *J. Neurophysiol.,* Volume 91, pp. 1457-1469.

McIntyre, C. C. et al., 2004. Electric field and stimulating influence generated by deep brain stimulation of the subthalamic nucleus. *Clin. Neurophysiol.,* 115(3), pp. 589-595.

McKeegan, D. E. F., 2001. Spontaneous and odour evoked activity in single avian olfactory bulb neurons. *Brain Research,* 929(1), pp. 48-58.

McKeegan, D. E. F., 2002. Spontaneous and odor evoked activity in single avian olfactory bulb neurones. *Brain Res.,* 929(1), pp. 48-58.

Medtronic, n.d. *Leadpoint user guide,* Minneapolis, MN: s.n.

Meehan, P. A. & al., e., 2011. *Investigation of the non-Markovity spectrum as a cognitive processing measure of deep brain microelectorde recordings.* Rome, Italy, SciTePress.

Meehan, P. & Bellette, P., 2009. *Chaotic signal analysis of STN brain signals.* s.l., World Scientific Publishing.

Meissner, W. & al., e., 2005. Subthalamic high frequency stimulation resets subthalamic firing and reduces abnormal oscillations. *Brain,* Volume 128, pp. 2372-2382.

Michmizos, K. & Nikita, K., 2012. Prediction of the timing and the rhythm of the parkinsonian subthalamic nucleus neural spikes using the local field potentials. *IEEE transactions on information technology in biomedicine,* 16(2), pp. 190-197.

Modolo, J., Mosekilde, E. & Beuter, A., 2007. New insights offered by a computational model of deep brain stimulation. *Journal of Physiology,* Volume 101, pp. 56-63.

Moore, G., Perkel, D. & Segundo, J., 1966. Statistical analysis and functional interpretation of neuronal spike data. *Annual Review of Physiology,* Volume 28, p. 493.

Moro, E., Poon, Y. Y. & al., e., 2006. Subthalamic nucleus stimulation: improvements in outcome with reprogramming. *Archives of neurology,* 63(9), p. 1266.

Nunez, P. & Srinivasan, R., 2006. *Electric Fields of the Brain.* 2 ed. New York: Oxford University Press, Inc.

Nykamp, D. Q. & Tranchina, D., 2000. A population density approach that facilitates large-scale modeling of neural networks: analysis and an application to orientation tuning. *Journal of computational neuroscience,* 8(1), pp. 19-50.

Omurtag, A., Knight, B. W. & Sirovich, L., 2000. On the simulation of large populations of neurons. *Journal of computational neuroscience,* 8(1), pp. 51-63.

Parastarfeizabadi, M. & Kouzani, A. Z., 2017. Advances in closed-loop deep brain stimulation devices. *Journal of neuroengineering and rehabilitation,* 14(79), pp. 1-20.

Pascual, A., Modolo, J. & Beuter, A., 2006. Is a computational model useful to understand the effect of deep brain stimulation in Parkinson's disease. *Journal of Integrative Neuroscience,* 5(4), pp. 541-559.

Pawlas, Z. & Lansky, P., 2011. Distribution of interspike intervals estimated from multiple spike trains observed in a short time window. *Physical Review E,* Volume 83, p. 259.

Pedoto, G., Santaniello, S. & al., e., 2012. *Point process modeling reveals anatomical non-uniform distribution across the subthalamic nucleus in Parkinson's disease.* s.l., IEEE.

Perkel, D. H., Gerstein, G. L. & Moore, G. P., 1967. Neuronal spike trains and stochastic point processes I. *Biophys. J.,* 7(4), pp. 391-418.

Perkel, D. H., Gerstein, G. L. & Moore, G. P., 1967. Neuronal spike trains and stochastic point processes II. *Biophys. J.,* 7(4), pp. 419-440.

Pirini, M. & al., e., 2009. A computational modelling approach to investigate different targets in deep brain stimulation for Parkinson's disease. *Journal of Computational Neuroscience,* Volume 26, pp. 91-107.

Pouzat, C., Delescluse, M., Viot, P. & Deibolt, J., 2004. Improved spike-sorting by modeling firing statistics and burst-dependent spike amplitude attenuation: a Markov chain Monte Carlo approach. *Journal of neurophysiology,* 91(6), p. 2910.

Priori, A., Foffani, G., Rossi, L. & Marceglia, S., 2013. Adaptive deep brain stimulation (aDBS) controlled by local field potential oscillations. *Experimental Neurology,* Volume 245, pp. 77-86.

Rajdl, K. & Lansky, P., 2015. Stein's neuronal model with pooled renewal input. *Biological cybernetics,* 109(3), p. 389.

Rasch, M. J., Gretton, A. & al., e., 2008. Inferring spike trains from local field potentials. *Journal of Neurophysiology,* 99(3), p. 1461.

Rasch, M., Logothetis, N. & Kreiman, G., 2009. From neurons to circuits: Linear estimation of local field potentials. *The journal of neuroscience,* 29(44), pp. 13785-13796.

Reike, F., Warland, D., van Steveninck, R. & Bialek, W., 1997. *Spikes: Exploring the neural code.* Boston, MA: MIT press.

Remple, M., Bradenham, C. & al., e., 2011. Subthalamic nucleus neuronal firing rate increases with Parkinson's disease progression.. *movement disorders,* 26(9), pp. 1657-1662.

Robinson, P. A., Rennie, C. J. & Wright, J. J., 1997. Propagation and stability of waves of electrical activity in the cerebral cortex. *Physical review E,* 56(1), pp. 827-840.

Robinson, P., Rennie, C. J. & al., e., 2005. Multiscale brain modelling. *Philosophical transactions of the Royal Society B,* Volume 360, pp. 1043-1050.

Rouse, A. G. et al., 2011. A chronic generalized bi-directional brain-machine interface. *J. Neural Eng.,* Volume 8.

Rubin, J. E. & Terman, D., 2004. High frequency stimulation of the subthalamic nucleus eliminates pathological thalamic rhythmicity in a computational model. *J. Computational Neurosci.,* Volume 16, pp. 211-235.

Rutishauser, U., Schuman, E. M. & Mamelak, A. N., 2006. Online detection and sorting of extracellularly recorded action potentials in human medial temporal lobe recordings, in vivo. *J. Neurosci. Methods,* 154(1-2), pp. 204-224.

Sanghera, M. & Grossman, R., 2004. Techniques in data analysis: General principles. In: Z. Israel & K. J. Burchiel, eds. *Microelectrode Recordings in Movement Disorder Surgery.* New York, NY, USA: Thieme Medical.

Santaniello, S., Fiengo, G., Glielmo, L. & Catapano, G., 2004. A biophysically inspired microelectrode recording-based model for the subthalamic nucleus activity in Parkinson's disease. *Biomed. Signal Processing Contr.,* Volume 3, pp. 203-211.

Sarma, S. V. & al., e., 2010. Using point process models to compare neural spiking activity in the subthalamic nucleus of Parkinsons patients and a healthy primate. *IEEE transactions on biomedical engineering,* 57(6), pp. 1297-1305.

Snellings, A., Sagher, O., Anderson, D. J. & Aldridge, J. W., 2009. Identification of the subthalamic nucleus in deep brain stimulation surgery with a novel wavelet-derived measure of neural background activity. *J. Neurosurg.,* Volume 111, pp. 767-774.

Stein, R., Gossen, E. & Jones, K., 2005. Neuronal variability: noise or part of the signal?. *Nat. Rev. Neurosci.,* 6(5), pp. 389-397.

Stevens, C. F. & Zador, A. M., 1998. Input synchrony and the irregular firing of cortical neurons. *Nature Neuroscience,* Volume 1, pp. 210-217.

Suk, J. & al., e., 1991. Anatomical localization revealed by MEG recordings of the human somatosensory system. *Electroencephalography and clinical neurophysiology,* 78(3), pp. 185-196.

Terman, D., Rubin, J. E., Yew, A. C. & Wilson, C. J., 2002. Activity patterns in a model for the subthalamopallidal network of the basal ganglia. *J. Neurosci.,* 7(22), pp. 2963-2976.

The MathWorks Inc., n.d. *MATLAB,* Natick, Massachusetts: s.n.

Theodosopoulos, P. V. et al., 2004. Electrophysiological findings in STN and SNR. In: Z. Israel & K. J. Burchiel, eds. *Microelectrode Recordings in Movement Disorder Surgery.* New York, NY, USA: Thieme Medical.

Tsirogiannis, G. L. & al., e., 2008. *Fitting local field potentials generating model of the basal ganglia to actual recorded signals.* s.l., IEEE.

Tuckwell, H. C., 1979. Synaptic transmission in a model for stochastic neural activity. *Journal of Theoretical Biology,* 77(1), pp. 65-81.

Varghese, J. J. & al., e., 2011. *Use of the non Markov parameter to detect low frequency synchronisation in time series analysis.* Boston, Massachusetts, s.n.

Weegink, K. J., 2017. *(BuzzVII) Kristian Weegink.* [Online] Available at: https://github.com/BuzzVII

Weegink, K. J. et al., 2016 . A Parametric Simulation of Neuronal Noise From Microelectrode Recordings. *IEEE Transactions on Neural Systems and Rehabilitation Engineering,* 25(1), pp. 4-13.

Weegink, K. J., Varghese, J. J. & al., e., 2012. *An efficient stochastic based model for simulating microelectrode recordings of the deep brain.* Vilamoura, Portugal, s.n., pp. 76-84.

Weegink, K., Varghese, J. & Bradley, A., 2015. *Spikes from compound action potentials in simulated microelectrode recordings.* Brisbane, IEEE, pp. 813-816.

Welch, P. D., 1967. THe use of fast Fourier transform for the estimation of power spectra: A method based on time averaging over short, modified periodograms. *IEEE Transactions on audio and electroacoustics,* 15(2), p. 70.

Wilbur, W. j. & Rinzel, J., 2983. A theoretical basis for large coefficient of variation and bimodality in neuronal interspike interval distributions. *Journal of theoretical biology,* 105(2), p. 345.

Yannaros, N., 1994. Weibull Renewal Processes. *Ann. Inst. Statist. Math,* 46(4), pp. 641-648.

Zelniker, E. E. & al., e., 2008. Estimation of neuronal firing rates with the three-stat biological point process model. *Journal of neuroscience methods,* 174(2), pp. 281-291.

8 Appendices

Paper A*, An efficient stochastic based model for simulating microelectrode recordings of the deep brain.* (2012), Kristian J. Weegink, John J. Varghese, Paul A. Bellette, Terry Coyne, Peter A. Silburn, and Paul A. Meehan, Proceedings of Biosignals 2012, International Conference on Bio-Inspired Systems and Signal Processing. 5th International Joint Conference on Biomedical Engineering Systems and Technologies (BIOSTEC), Vilamoura, Portugal, pp 76-84. 1-4 February 2012.

Paper B*, Spikes from compound action potentials in simulated microelectrode recordings.* (2015), Kristian J. Weegink, John J. Varghese, and Andrew P. Bradley, 2015 IEEE International Conference on Acoustics, Speech and Signal Processing (ICASSP). 2015 International Conference on Acoustics, Speech and Signal Processing, South Brisbane, QLD, Australia, pp 813-816. 19-24 April 2015.

Paper C, *A Parametric Simulation of Neuronal Noise from Microelectrode Recordings.* (2016), Kristian J. Weegink, Paul A. Bellette, John J. Varghese, Peter A. Silburn, Paul A. Meehan and Andrew P. Bradley, IEEE Transactions on Transactions on Neural Systems and Rehabilitation Engineering, Vol 25, no. 1, pp 4-13, Jan. 2017.

Paper D, *Bayesian Approach for Stationary Analysis of Microelectrode Recordings Using a Neural Mass Model of the Basal Ganglia.* (2017), Kristian J. Weegink, Paul A. Bellette, John J. Varghese, Andrew P. Bradley and Paul A. Meehan, submitted to IEEE Transactions on Biomedical Engineering, 2018.

Paper A - An efficient stochastic based model for simulating microelectrode recordings of the deep brain

K. J. Weegink, J. J. Varghese, P.A. Bellette, T. Coyne, P.A. Silburn and P.A. Meehan

ABSTRACT

We have developed a computationally efficient stochastic model for simulating microelectrode recordings, including electronic noise and neuronal noise from the local field of 3000 neurons. From this we have shown that for a neuron network model spiking with a stationary Weibull distribution the power spectrum can change from exhibiting periodic behaviour to non-stationary behaviour as the distribution shape is changed. It is shown that the windowed power spectrum of the model follows an analytical result prediction in the range of 100-5000 Hz. The analysis of the simulation is compared to the analysis of real patient interoperative sub-thalamic nucleus microelectrode recordings. The model runs approximately 200 times faster compared to existing models that can reproduce power spectral behaviour. The results indicate that a spectrogram of the real patient recordings can exhibit non-stationary behaviour that can be re-created using this efficient model in real time.

1 INTRODUCTION

For the treatment of progressed movement disorders, such as Parkinson's disease (PD), deep brain stimulation (DBS) may be used. This treatment involves locating a target deep brain structure, such as the sub-thalamic nucleus (STN), inserting an electrode to within 1 mm accuracy, and then applying a pulsed electric field to the area. One of the tools used to locate the correct nucleus structure is a microelectrode recording (MER).

MERs are performed by insterting a recording electrode, with a diameter around 50 um, into the nucleus structure (figure 1) located via MRI and CT scans.

To confirm the correct location of the implanted DBS electrodes, patients are awake to perform neurological tests. This gives an opportunity to monitor the candidate nucleus, for stimulation, while the patients perform tasks. Recent work has shown that with the correct measure, correlations between MER recordings and patient response to symantic tests has been demonstrated (P. A. Meehan & Bellette, 2009; Paul A. Meehan et al., 2011; Varghese et al., 2011).

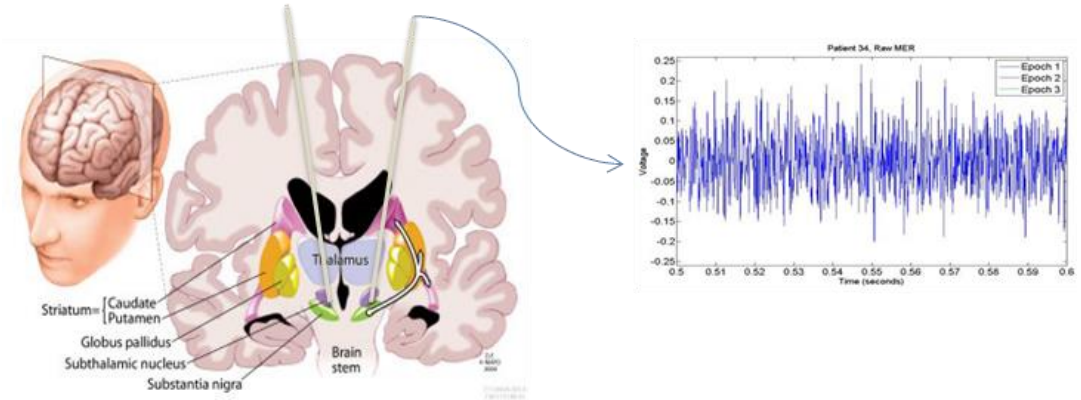

Figure 1: The micro-electrode recordings (MER) are acquired by inserting an electrode into a deep brain structure. The electrical activity of the neurons surrounding the electrode can couple to it producing a voltage time series.

Currently there has also been work on developing a bi-directional brain-machine interface for DBS treatment (Rouse et al., 2011). To further develop these research paths appropriate methods for efficient real time simulations to estimate neural network behaviour are required. For instance developing a metric that can characterise the underlying neural behaviour from a MER, a better understanding of the process in DBS could be made.

Current MER models only consider the behaviour of the closest neuron and reduce the further neurons to a local field noise (Santaniello, Fiengo, Glielmo, & Catapano, 2008). For feedback control of DBS the behaviour of the neural network needs to be modelled, as it has been shown that analysis of the closest neuron to the electrode is insufficient (Rouse, et al., 2011). Using the current non-linear neuron models of DBS (Rubin & Terman, 2004)

for this type of feedback controller would be too computationally intensive, for this reason models that can take into account a large number of neurons and display markers of pathalogical states efficiently are needed.

In this paper we develop numerical probabilistic models, using a point process (PP) in order to create a much more computationally efficient model of networked neurons. Each neuron is coupled to the electrode, using a non-homogenous model for the extracellular medium, via a filter function derived from a conductance based model for the STN extacellular current during an action potential (AP). We use the model to compare with real patient MERs and an analytical model using frequency based analysis. This type of numerical model could potentially be used in a clinical setting as part of a feedback controller for DBS, alleviating the clinical load of optimizing the device settings.

2 Methods

There are several aspects to modelling and analysing deep brain signals. The system is a complicated system with many levels of dynamics required to create a MER. Section 2.1 contains the procedure used to acquire patient MERs. The factors that contribute to modelling a MER; modelling the behaviour of a single neuron, the network behaviour, the neuron electrode interaction and the electrical equipment processing the signal are detailed in the section 2.2. A simple analytical model is presented in 2.3 for comparison to the numerical model and to provide more insight into how the statistical distribution influences the expected power spectrum. The methods of the comparative analysis are then summarized in 2.4.

2.1 Experimental Procedure - Patient MER Acquisition

MERs are acquired from participants with idiopathic PD who were considered suitable for the implantation of bilateral permanent stimulators in the STN. Fused MRI and stereotactic CT images and direct visualisation of FLAIR (Fluid-attenuated inversion recovery) MRI images displayed by Stealthstation (Medtronic Inc., Minneapolis, MN) were used to target the STN.

During surgery characteristic STN firing patterns were used to confirm the STN location by the neurologist and neurosurgeon. More details of the surgical procedure are reported in Coyne et al. (Coyne et al., 2006).

MERs were acquired with a Tungsten microTargeting® electrode (model mTDWAR, FHC, Bowdoinham, ME) with a tip diameter of less than 50µm and impedance of approximately 0.5 MΩ (± 30%) at 1 kHz. MERs were filtered (500-5000 Hz) and recorded at a sampling rate of 24 kHz from LeadPoint™ (Medtronic Inc., Minneapolis, MN).

2.2 Numerical Modelling of Micro-Electrode Recordings

A MER is created by the activity of the neurons around the recording electrode. The neurons generate currents and hence electric fields that propagate through the different structures of the brain tissue, which can attenuate and filter the signal (Garonzik, Ohara, Hua, & Lenz, 2004). Finally the field incident on the electrode is processed by the electrical equipment to produce the recording.

Models of MERs have been developed that consider single unit recordings, made from a stochastic single neuron with random noise (Santaniello, et al., 2008) and local field potentials (LFP) created using the spike trains of simultaneously recorded *in-vivo* cells (Bedard & Destexhe, 2009). However neither of these models allow for real time simulations with dynamically altering network behaviour.

To effectively model a MER which would allow real time simulations, there are several different stages that need to be taken into consideration. The four separate areas we are to model are the behaviour of the neural network, the electrical dynamics of individual neurons, the coupling of the electric fields from a neuron to the electrode and the processing of the signal by the electronics.

2.2.1 Neural Networks

For a MER a large number of neurons in the structure surrounding the electrode contribute to the signal. Dynamic models of neurons and neural networks are common for simulating brain structures(Feng, Shea-Brown, Greenwald, Kosut, & Rabitz, 2007; Izhikevich, 2007a, 2007b; Rubin & Terman, 2004; Terman, Rubin, Yew, & Wilson, 2002). These types of models, using synaptic connections between neurons with dynamical neuron models, can be very computationally intensive (Long & Fang, 2010). To reduce the computational burden of modelling individual neurons with synaptic connections, the firing times of each neuron can be characterized by a stochastic variable. This variable is produced from a probability distribution that depends upon the behaviour of the network. This type of model is a point process (Perkel, Gerstein, & Moore, 1967a, 1967b).

For single neurons the spiking statistics are often modelled by a Poisson distribution of inter spike interval (ISI) times. The participants for the deep brain MER recordings are undergoing treatment for a pathological state that is treated by altering STN function. This could imply abnormal function of the STN where the firing is not best described by a Poisson distribution in ISIs.

A probability distribution that can give the common types of behaviour found in neurons, such as bursting, Poisson and periodic behaviour, is the Weibull distribution (Li, 2011; McKeegan, 2002; Perkel, et al., 1967a, 1967b). This type of distribution can reduce to a Poisson distribution if the shape parameter is equal to one, takes the form of a Rayleigh distribution if the shape parameter is larger than two and burst fire behaviour is produced as it goes below one.

The point process simulation is performed using MATLAB 7.12.0 (R2011a) on a PC with a quad core 1.73GHz processor and 8.0 GB of RAM. A spatial distribution of 3000 neurons is randomly generated, shown in figure 2, that follows the radial density of neurons ($N(r)$) given in equation (1) using a spatial neuron density of $\rho = 10^5 cm^{-3}$.

$$N(r) = 4\pi r^2 \rho. \qquad (1)$$

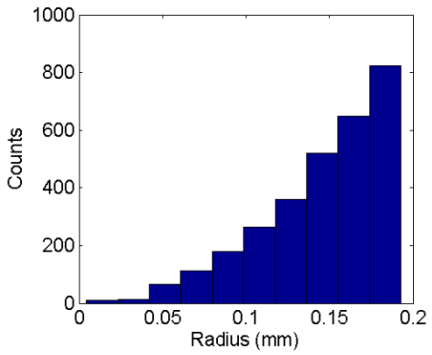

Figure 2: The radial distribution of neurons used for simulations. The volume of tissue for the simulation depends on the number of neurons simulated.

All simulations are performed over a three second period. Time series of Dirac pulses are created for each neuron by drawing interval times for spike occurrences from a probability distribution. Weibull distributions are used to generate the ISIs given by

$$P(t) = \begin{cases} \left(\frac{t-t_r}{\lambda}\right)^{c-1} \frac{c}{\lambda} e^{-\left(\frac{t-t_r}{\lambda}\right)^c} & x > t_r, \\ 0 & x \leq t_r \end{cases} \qquad (2)$$

λ is the scale parameter that controls the rate and is set to 10 Hz. The shape parameter c is varied to control the neuron behaviour; with $c \ll 1$ generating bursting, $c = 1$ Poissonian and $c \gg 1$ periodic behaviour. The parameter t_r controls the refractory time of the neuron and set to 5 ms, preventing another action potential occurring for the same neuron in this period. The first spike for each neuron uses $c = 1$ with t_r=0. Each time series is convolved with the EAP for an STN neuron by taking the product in the frequency domain. The time series data for each neuron are then superimposed to create the voltage at the electrode.

2.2.2 Neuron Dynamics

Using a PP model for the neural network, the dynamics of each neuron have been reduced to an ‘on’ or ‘off’ state. To develop the correct response for a neuron when in the ‘on’ state, conductance models such as the Hodgkin and Huxley (HH) model can be used to generate the behaviour of the individual neuron, when an action potential occurs.

The HH model can calculate the extracellular currents around a neuron which is required for determining the voltage seen by an electrode. It has previously been demonstrated STN cells can be simulated effectively using this type of model (Terman, et al., 2002). More computationally efficient mathematical models of neurons are not considered since these types of models cannot always reproduce the correct shape of the action potential waveform, and this feature is important when considering the windowed power spectrum.

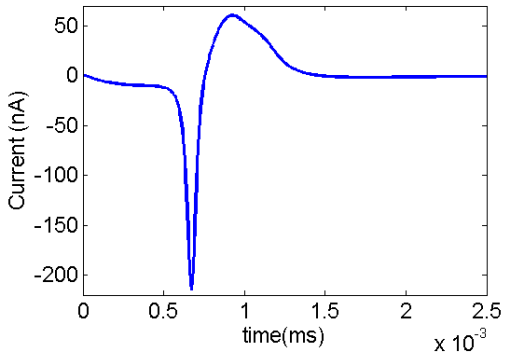

Figure 3: The extracellular current used for each neuron generated using equation (3).

The STN cell is modelled using a single compartment conductance based model described by a modified version of the HH equation, based on (Feng, et al., 2007; Rubin & Terman, 2004; Terman, et al., 2002):

$$C_m \frac{dV}{dt} = -g_L(V - v_L) - g_K n^4 (V - v_K) - g_{Na} m^3 h (V - v_{Na}) - g_T a^3 b^2 (V - v_{Ca}) - g_{Ca} s^2 (V - v_{Ca}), \quad (3)$$

where C_m is the membrane capacitance and set to $1\,pF/\mu m$; g_L, v_L are the leak conductance and reversal potential ($2.25\,nS/m^2$ and $-60.0\,mV$ respectively); g_K, v_K are the K^+ conductance and equilibrium potential ($45\,nS/m^2$ and $-80.0\,mV$ respectively); g_{Na}, v_{Na} are the Na^+ conductance and equilibrium potential ($37.5\,nS/m^2$ and $55.0\,mV$ respectively); g_T is a low-threshold T-type Ca^{2+} conductance ($0.5\,nS/m^2$); and g_{Ca}, v_{ca} are a high-threshold Ca^{2+} conductance and a Ca^{2+} equilibrium potential ($0.5\,nS/m^2$ and $140.0\,mV$ respectively). The gating variables $n,\ m,\ h,\ a$ and b follow the differential equations given in (Terman, et al., 2002) using the parameters given in their table 1. The dynamics of a single neuron are

modelled in NEURON (Hines & Carnevale, 1997) using equation (3) to generate the extracellular current during an action potential, shown in figure 3.

2.2.3 Neuron/Electrode Interaction

The electrode senses the neuron dynamics through the electric field that propagates from the neuron. This electric field is known as the extracellular action potential (EAP). The EAP is generated by ionic currents around the active neuron. As the EAP propagates through the extracellular space to the electrode it will pass through regions of space with different conductivity and permittivity. This will cause filtering effects along with attenuation of the field. This means that the electrode will record a different EAP for each neuron depending upon the distance from the electrode and the media in between.

The complex impedance ($Z_\omega(r)$) for the interaction of each neuron with the electrode over the range of radii is calculated by (Bedard, Kroger, & Destexhe, 2004),

$$Z_\omega(r) = \frac{1}{4\pi\sigma(R)} \int_r^\infty \frac{1}{r\prime^2} \frac{\sigma(R)+i\omega\epsilon(R)}{\sigma(r\prime)+i\omega\epsilon(r\prime)} dr', \tag{4}$$

where σ is the conductivity in the extracellular medium, ϵ is the permittivity in the extracellular medium and R is the spherical radial size of each neuron. An exponentially decaying conductance

$$\sigma(r) = \sigma(R)\left(\sigma_0 + (1-\sigma_0)\mathrm{e}^{\left(-\frac{r-R}{\lambda}\right)}\right), \tag{5}$$

with a space constant $\lambda = 500\,\mu m$, cell radius $R = 10\,\mu m$, conductivity at the cell $\sigma(R) = 1.5\,S/m$ and a normalized low amplitude conductivity $\sigma_0 = 2 \times 10^{-9}$; and a constant normalized permittivity $\epsilon = 10^{-11} F/m$ were used following Bedard (2004). The EAP waveform in the frequency domain for each neuron is calculated using the complex impedance and the FFT of the extracellular current.

The voltage (V_ω), in terms of the frequency components, at the electrode caused by a neuron is then calculated using Ohm's law (Bedard, et al., 2004),

$$V_\omega(r) = I_\omega Z_\omega(r), \quad (6)$$

where I_ω is the frequency component of the current at the neuron.

2.2.4 Electrical Processing

To properly analyse a MER the effects of the electrical equipment, on the recording, need to be included. These effects include the introduction of noise, such as that due to sampling rate, clock stability and thermal noise, and any filtering that occurs. These issues could greatly affect the ability of a measure to differentiate the neuronal behaviour from the electrical effects.

The first such noise source is the noise present from thermal fluctuation of electrons in the microelectrode (Akingba, Wang, Chen, Neves, & Montemago, 2003). This type of noise is known as Johnson-Nyquist noise and is characterized by having zero mean voltage and a variance dependant on the temperature, resistance and frequency bandwidth.

The phase noise is not considered in this analysis due to the stability of the 10 MHz clock typically used and the comparatively small sample rate of 24 kHz. Digitization noise can be accounted for by producing the final MER of the simulation with the same time step that the patient data is recorded at. Finally any filters can be added using the filter transfer function in the post processing of the MER simulation.

Thermal noise on the electrode is added as white noise using

$$\langle V \rangle = 0, \quad (7)$$

$$\langle V^2 \rangle = 4k_B TR\Delta f, \quad (8)$$

where k_B is Boltzmann's constant, T is the temperature, R is the resistance, Δf is the bandwidth and $\langle \ \rangle$ is the time average, it is found that for a 0.5 MΩ resistor at body temperature (37^{o}C) the thermal noise can be between 10-30% of the size of the neural signal.

The recording is filtered with a 6th order low pass Butterworth filter with a corner frequency of 5 kHz and a 3rd order high pass filter with a corner frequency of 500 Hz. The final MER from the simulation is produced with a sample rate of 24 kHz to create the same digitization effects as present in the patient data.

2.3 Simplified Analytical Model of Micro-Electrode Recordings

The MER may be analytically modelled by a superposition of independent spike trains, equivalent to the numerical model using a point process. The PSD for a PP model will be a filtered version of the PSD for the EAP waveform. For independent overlapping pulse trains, with the same shape waveform for each pulse, it has been shown (Banta, 1964) that the power spectrum ($G_0(\omega)$) for the MER can be written as

$$G_0(\omega) = \frac{\nu G(\omega)}{2\pi}\left[\overline{a^2} - 2\bar{a}^2 Re\left\{\frac{H(\omega)}{1-H(\omega)}\right\}\right], \qquad (9)$$

where $G(\omega)$ is the PSD of the waveform, $H(\omega)$ is the characteristic function (Fourier transform) of the probability distribution for the aggregate spiking statistics, ν is the number of pulses per unit time and a is the amplitude of the pulses with $\bar{}$ representing the ensemble average.

Although this equation for the PSD takes into account the attenuation caused by the extracellular medium on the spike waveform it does not take into account the frequency filtering effects.

This equation can however be used to see expected behaviour of different simulations. The bracketed term can be thought of as a filter, which is a function of the spiking probability,

applied to the waveform PSD. By looking at this term the filtering effects caused by the different probability functions can be examined.

2.4 Procedure for Comparison of Numerical and Experimental Results

The most intuitive way to analyse the noise of an MER is to look at the PSD. This was first done by in 1979 (McNames, 2004) using a circuit equivalent of a Fourier Transform (FT). In recent years analysis of MERs has progressed into the digital domain. The majority of these techniques still involve analysis of the PSD.

Neuron spiking behaviour can be examined through MER PSDs. It was shown how f^{-2} behaviour in the PSD can arise from shot noise type behaviour of neurons spiking (Milstein, Mormann, Fried, & Koch, 2009), while f^{-1} behaviour may be due to filtering by reactive extracellular media, or due to complex self-organized critical phenomena (Bedard & Destexhe, 2009).

Complex measures have been used to look at MERs, and it has been shown that some techniques, such as the Non-Markov parameter (NMP) relate to the PSD (Varghese, et al., 2011).

The windowed PSD will not capture transient behaviour in the MER. To view this transient behaviour a spectrogram can be used. This involves dividing the signal into smaller time bins. The PSD is taken for each time bin to see the PSD as a function of time for the MER.

A windowed PSD is taken of the time series data from the simulation using a Gaussian window with an e^{-2} width of 1/50th of the signal length. The PSD is then averaged of 5 trials of the simulation with the same firing statistics. This is compared to the windowed PSD of a three second signal averaged over 5 recordings.

Spectrograms are produced with the same time intervals used for the windowed PSD. The spectrograms consist of a series of instantaneous PSD over each time interval. The spectrograms are then used to compare the stationary behaviour of the power spectrum for different ISI probability distributions and the patient data.

3 Results and Discussion

The results from the numerical simulations are presented in this section and are then compared to the experimental results and analytical predictions. Subsection 3.1 summarises the numerical results and provides a comparison with MERs acquired from patients. The time series, windowed power spectrum and spectrogram for three different simulation parameters are used. Subsection 3.2 includes details of the results from the simple analytical model, comparing how the power spectrum of the EAP is modified under the different spiking statistics used to produce the MERs from the numerical models.

3.1 Numerical and Experimental Results Comparison

The time series of voltage from the simulations has been plotted for three different firing probability distributions and compared to a patient recording (Figure 4). For $c \cong 1$ the time series have similar features to the patient data. Differences can only be seen for large deviations from $c = 1$. As case examples for their characteristic behaviour extreme cases of c have been used. As $c \ll 1$, bursting behaviour is visible in the time series and for $c \gg 1$ periodic spiking becomes apparent.

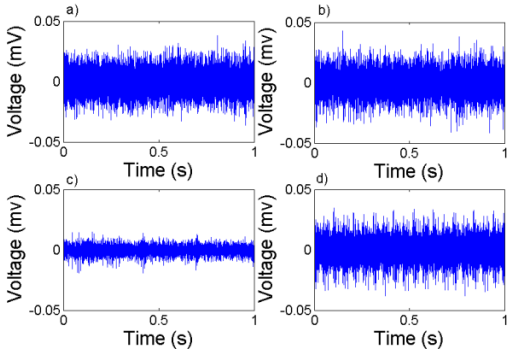

Figure 4: Comparison of a) Patient MER to simulations with b) $c = 1$, c) $c \ll 1$ and d) $c \gg 1$.

The simulations were calculated at a rate of 6 milli seconds per neuron per second of computational time, a 200 fold increase on dynamical models that reproduce accurate waveform shapes (Long & Fang, 2010).

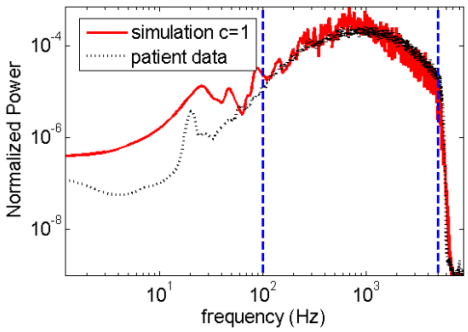

Figure 5: Overlap of the real patient windowed PSD over the windowed PSD of the simulation for $c = 1$.

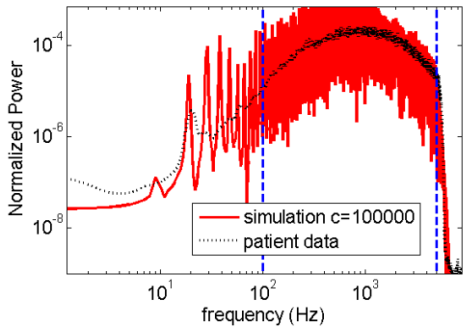

Figure 6: Overlap of the real patient windowed PSD over the windowed PSD of the simulation for $c \gg 1$.

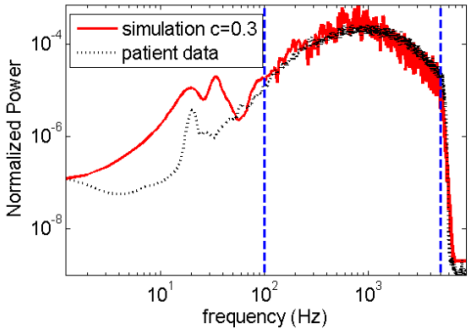

Figure 7: Overlap of the real patient windowed PSD over the windowed PSD of the simulation for $c \ll 1$.

The windowed PSD for all three simulations and the patient recordings, seen in figures 5, 6 & 7, have three main regions. The first region is the filter drop off above 5 kHz. This feature is present in all 4 PSDs with good agreement between patient data and simulations. The thermal noise term added is white noise and as such adds the same power to every frequency, shifting the PSD up. This effect is removed by normalizing the power spectrum to integrate to unity. The other electrical effects; high and low pass filtering; do however alter the normalized power spectrum, seen by the sharp falloff in power in this region.

The second region is the behaviour at high frequencies (100-5000 Hz). The two simulations

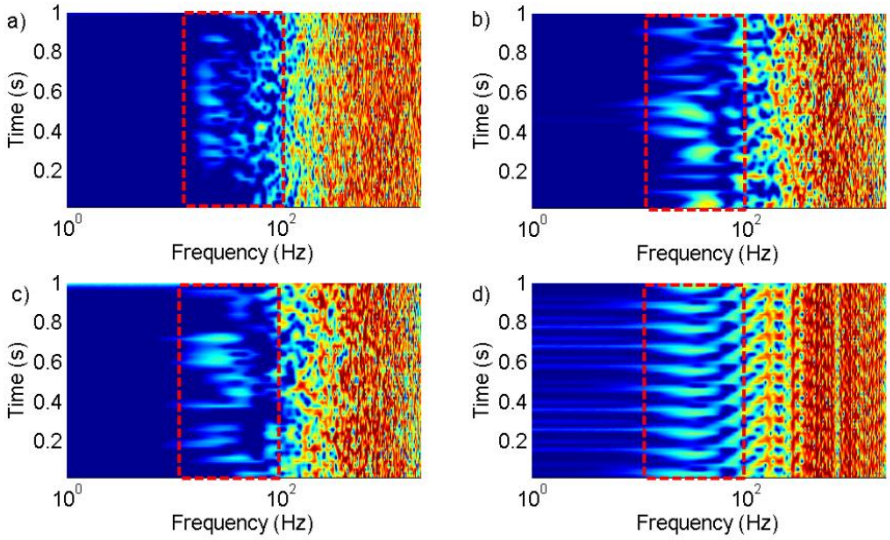

Figure 8: Spectrograms with the region displaying beta band behaviour boxed in red, a) patient MER showing transient beta band behaviour, b) simulations $c \ll 1$ showing transient beta band behaviour, c) $c = 1$ showing transient beta band behaviour and d) $c \gg 1$ showing periodic behaviour.

with $c \leq 1$ have good agreement with patient data in this region shown in figures 5 & 7. The simulation with $c \gg 1$ (figure 6) has structure in this region that can be explained as harmonics of features in the low frequency region. The overall shape in this region is dominated by the waveform of the EAP.

The final region of interest is in the region below 100 Hz. This region is thought to contain information of the Local field potential (LFP). Experimentally this region has an electronic filter, with a slow drop off. For $c \gg 1$ this region has a sharp peak at 10 Hz, the simulated spike rate, and then has peaks at the harmonic frequencies of n10 Hz, where n is an integer. The other two cases have anomalous peaks in this region similar to the 20 Hz peak in the patient data. This beta band peak (12-30 Hz) has been seen in PD MER recordings previously and has been implicated in the pathological state (Eusebio & Brown, 2009).

Besides the PSD for $c \gg 1$, the problem with comparing the average PSD is that they appear very similar between 100-5000 Hz with differences below 100 Hz. Another method to examine the spectral properties of an MER is to look at the spectrogram, figure 8, and to observe changes in the power spectrum over time.

From the spectrogram for the typical patient MER recording it can be seen that the PSD changes in time. These recordings show the feature in the beta band appearing and disappearing through the recording.

When the numerical simulations were performed with $c \gg 1$, the PSD appears periodic stationary. This behaviour can be seen in figure 8 d). When c is set to one or below features of the PSD appears to change in time in the beta band. This is similar behaviour to the PSD for the patient data.

This analysis suggests that $c \cong 1$ qualitatively represents the patient data the best from the options tried. This supports the idea that spiking behaviour in a large network appears Poisson (Câteau & Reyes, 2006; McNames, 2004; Stevens & Zador, 1998).

3.2 Analytical Predictions

The results from equation (5) show the effect of changes in the aggregate probability distribution. Equation (5) can be thought of as a spike waveform filter that is dependent on the probability distribution through $Re\left[H(\omega)/\left(1-H(\omega)\right)\right]$. Figure 9 shows the frequency behaviour of equation (5) for different values of c, if the statistics follow a Weibull distribution.

For $c \gg 1$ and $c = 1$ figure 9 shows the frequency filtering effects due to the spiking statistics are flat and will not add noticeable features in the PSD below 100 Hz. This analytical model doesn't take into account the frequency filtering of more distant neurons by the extracellular medium. Figure 9 a) shows how the extracellular medium model acts as a low pass filter. For these reasons this model is not sufficient to describe the features seen in the numerical simulations below 100 Hz.

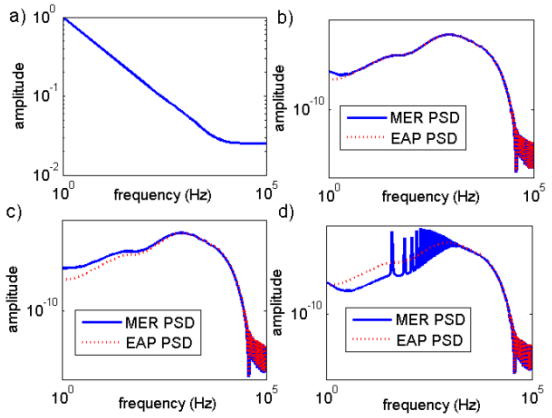

Figure 9: a) The filter function of the extracellular medium at $0.2\mu m$. Inserts b)-d) show the comparison of the power spectrum of the EAP with the MER power spectrum from the analytical model, b) the MER PSD for $c = 1$ modelled by equation (9), it can be seen that for this distribution the results of the MER and EAP PSDs are in agreement, c) the MER PSD for $c \gg 1$ modelled by equation (9), d) the MER PSD $c \ll 1$ modelled by equation (9).

For $c \gg 1$ the 10 Hz peak with harmonic peaks in the numerical simulation can be seen in the frequency effects from equation (9), shown in figure 9, if the aggregate probability distribution maintains the single neuron ISI probability shape.

The problem with this analysis is that we have assumed that the distribution controlling the ISIs is stationary in time. Equation (9) cannot account for ISI distributions that change in time. The non-stationary nature of the real patient PSD could suggest that the probability distribution describing the neuron firing may not be stationary. This behaviour can alternatively be explained by the probabilistic nature of the simulation and the time period the PSD is taken over. This is demonstrated by the simulations using the PP model showing similar non stationary behaviour under the same analysis, even though the probability distribution of ISIs was stationary in time.

4 Conclusions

MERs were efficiently simulated using a PP model with a conductance model for generating the EAP, taking into account extracellular frequency filtering and attenuation; and the effects of the recording electronics. The simulations perform approximately 200 times faster than

using a Hodgkin and Huxley model for all of the neuron dynamics (Long & Fang, 2010). With this computationally efficient model very good agreement was achieved when comparing the windowed PSD of the simulated MERs with real patient data for frequencies above 100 Hz.

Below 100 Hz the PSD of patient MERs are not stationary, which can be reproduced using a time stationary probability distribution for the ISI. Since the model is a probabilistic model that treats the neurons as point sources rather than a full dynamical model, the neurons are either in an 'on' or 'off' state. This means it cannot produce neural features such as sub-threshold oscillations and cellular activity such as synaptic currents. These features may be critical for describing the features below 100Hz sufficiently.

The analytical model using the results from Banta (1964) showed features that were present in the simulations, such as the harmonic structure present in the windowed PSD for simulations with $c \gg 1$. This type of analysis could allow for characterization of the ISI probabilities of patient MERs from the windowed PSD.

To account for the features in the beta band (10-35 Hz) more complex models; including explicit network interactions and full cell dynamics, such as sub-threshold oscillations, may be required.

Future work could include performing the inverse problem of finding the shape and rate parameters that best describe a patient MER. The results from this study could be used to find markers that may be applicable in the clinical environment for optimising DBS and potentially operating in a feedback controller.

Acknowledgements

The authors are greatly indebted to PD specialists of St. Andrew's War Memorial and The Wesley Hospitals, Australia for their motivation, guidance, interdisciplinary expertise and funding.

References

Akingba, A. G., Wang, D., Chen, P.-s., Neves, H., & Montemago, C. (2003). *Application of nanoelectrodes in recording biopotentials*. Paper presented at the IEEE-NANO 2003.

Banta, E. (1964). A note on the correlation function of nonindependent, overlapping pulse trains. *Information Theory, IEEE Transactions on, 10*(2), 160-161.

Bedard, C., & Destexhe, A. (2009). Macrascopic Models of Local Field Potentials and the Apparent 1/f Noise in Brain Activity. *Biophysical Journal, 96*, 2589-2603.

Bedard, C., Kroger, H., & Destexhe, A. (2004). Modeling Extracellular Field Potentials and the Frequency-Filtering Properties of Extracellular Space. *Biophysical Journal, 86*, 1829-1842.

Câteau, H., & Reyes, A. D. (2006). Relation between Single Neuron and Population Spiking Statistics and Effects on Network Activity. *Physical Review Letters, 96*(5), 058101.

Coyne, T., Silburn, P. A., Cook, R., Silberstein, P., Mellick, G., Sinclair, F.,& Stowell, P. (2006). Rapid subthalamic nucleus deep brain stimulation lead placement utilising CT/MRI fusion, microelectrode recording and test stimulation. *Acta Neurochirurgica Suppl*(99), 49-50.

Eusebio, A., & Brown, P. (2009). Synchronisation in the beta frequency-band--the bad boy of parkinsonism or an innocent bystander? *Experimental Neurology, 217*(1), 1-3.

Feng, X.-J., Shea-Brown, E., Greenwald, B., Kosut, R., & Rabitz, H. (2007). Optimal deep brain stimulation of the subthalamic nucleus—a computational study. *J. Comput. Neurosci.*(23), 265–282.

Garonzik, I. M., Ohara, S., Hua, S. E., & Lenz, F. A. (2004). Microelectrode Techniques: Single-Cell and Field Potential Recordings. In Z. Israel & K. J. Burchiel (Eds.), *Microelectrode recordings in movement disorder surgery* (Vol. 1). New York: Thieme Medical Publishers, Inc.

Hines, M. L., & Carnevale, N. T. (1997). The NEURON Simulation Environment. *Neural Computation, 9*(6), 1179-1209. doi: 10.1162/neco.1997.9.6.1179

Izhikevich, E. M. (2007a). *Dynamical Systems in Neuroscience*. Cambridge: MIT Press.

Izhikevich, E. M. (2007b). Solving the distal reward problem through linkage of STDP and dopamine signaling. *Cerebral Cortex, October*(17), 2443-2452.

Li, C. (2011). A Model of Neuronal Intrinsic Plasticity. *Autonomous Mental Development, IEEE Transactions on, PP*(99), 1-1.

Long, L. N., & Fang, G. (2010). *A Review of Biologically Plausible Neuron Models for Spiking Neural Networks*. Paper presented at the AIAA InfoTech@Aerospace Conference, Atlanta, GA.

McKeegan, D. E. F. (2002). Spontaneous and odour evoked activity in single avian olfactory bulb neurones. *Brain Research, 929*(1), 48-58. doi: 10.1016/s0006-8993(01)03376-5

McNames, J. (2004). Microelectrode Signal Analysis Techniques for Improved Localization. In Z. Israel & K. J. Burchiel (Eds.), *Microelectrode recordings in movement disorder surgery* (Vol. 1). New York: Thieme Medical Publishers, Inc.

Meehan, P. A., & Bellette, P. A. (2009). *Chaotic Signal Analysis of Parkinson's Disease STN Brain Signals*. Paper presented at the Topics in Chaotic Systems.

Meehan, P. A., Bellette, P. A., Bradley, A. P., Castner, J. E., Chenery, H. J., Copland, D. A.,& Silburn, P. A. (2011). *Investigation of the Non-Markovity Spectrum as a Cognitive Processing Measure of Deep Brain Microelectrode Recordings*. Paper presented at the BIOSIGNALS 2011- International Conference on Bio-Inspired Systems and Signal Processing, Rome, Italy.

Milstein, J., Mormann, F., Fried, I., & Koch, C. (2009). Neuronal Shot Noise and Brownian 1/f^2 Behavior in the Local Field Potential. *PLoS One, 4*(2), e4338 4331-4335.

Perkel, D. H., Gerstein, G. L., & Moore, G. P. (1967a). Neuronal Spike Trains and Stochastic Point Processes I. *Biophys J., 7*(4), 391–418.

Perkel, D. H., Gerstein, G. L., & Moore, G. P. (1967b). Neuronal Spike Trains and Stochastic Point Processes II. *Biophys J., 7*(4), 419–440.

Rouse, A. G., Stanslaski, S. R., Cong, P., Jensen, R. M., Afshar, P., Ullestad, D., & Denison, T. J. (2011). A Chronic Generalizaed Bi-directional Brain-Machine Interface. *J. Neural Eng., 8*(036018).

Rubin, J. E., & Terman, D. (2004). High Frequency Stimulation of the Subthalamic Nucleus Eliminates Pathological Thalamic Rhythmicity in a Computational Model. *Journal of Computational Neuroscience*(16), 211–235.

Santaniello, S., Fiengo, G., Glielmo, L., & Catapano, G. (2008). A biophysically inspired microelectrode recording-based model for the subthalamic nucleus activity in Parkinson's disease. *Biomedical Signal Processing and Control*(3), 203–211.

Stevens, C. F., & Zador, A. M. (1998). Input synchrony and the irregular firing of cortical neurons. *Nature Neuroscience 1*, 210 - 217. doi: 10.1038/659

Terman, D., Rubin, J. E., Yew, A. C., & Wilson, C. J. (2002). Activity Patterns in a Model for the Subthalamopallidal Network of the Basal Ganglia. *The Journal of Neuroscience, 7*(22), 2963–2976.

Varghese, J. J., Weegink, K. J., Bellette, P. A., Meehan, P. A., Coyne, T., & Silburn, P. A. (2011). *Theoretical & Experimental Analysis of the Non Markov Parameter to Detect Low*

Frequency Synchronisation in Time Series Analysis. Paper presented at the Engineering in Medicine and Biology Society, Annual International Conference of the IEEE, Boston Massachusetts.

Paper B - SPIKES FROM COMPOUND ACTION POTENTIALS IN SIMULATED MICROELECTRODE RECORDINGS

K. J. Weegink, J. J. Varghese, and A. P. Bradley

ABSTRACT

In this paper we demonstrate by simulation, that the spike features apparent in low-impedance deep brain stimulation (DBS) targeting microelectrode recordings (MER) may not reflect the action potentials of individual neurons. Rather, they are more likely to be compound action potentials from a synchronized group of neurons local to the electrode. Initially we simulate the MER by combining the electric fields from a large number of independent neurons surrounding the microelectrode tip. When synchronization is introduced amongst neurons the resulting discernible spikes in an MER are far more likely to relate to compound action potentials from sub-sets of synchronized neurons than individual action potentials. Different sub-sets of neurons are then synchronized to see how well a conventional spike sorting algorithm can differentiate the compound action potentials from different groups of neurons. These simulations offer insight into the clinical interpretation of DBS MERs used to target deep brain structures.

1 INTRODUCTION

During the treatment of Parkinson's Disease with deep brain stimulation (DBS) a microelectrode is used to confirm the target location, e.g. the Subthalamic Nucleus (STN), in the brain. This electrode is used to both stimulate and record neuronal activity. A design

consequence of using the recording electrode for stimulation is that it has a 50μm tip to increase the volume of stimulation and to prevent neuronal damage by minimizing the current density around the electrode tip. A typical MER consists of a baseline noise component and features, larger in amplitude than the noise, often referred to as spikes. These spikes are commonly interpreted as action potentials (APs) from single neurons [1, 2, 3, 4]. Characteristics of the microelectrode recording (MER), such as an increase in the noise amplitude when entering the STN, are used by the surgical team to locate the target for stimulation [5, 6].

Previous work has modeled how an increase in MER noise can be attributed to neural structure, showing that the electric field from a large number of neurons, up to 10,000 neurons, can contribute to the recording [7, 8]. In these models each neuron is simulated as a filtered point process with independent identically distributed interspike interval (ISI) times. As these neurons are also modelled independent from one another, there is no synchronous activity, other than by chance. These models are not representative of the STN. Studies have shown that there can be up to 25% of cells are involved in synchronous activity in the STN [5].

In this paper we demonstrate that synchronization of neuronal firing times can produce spikes in an MER known as compound action potentials (CAPs). This paper has the following structure: The methods section describes how synchronization is added to the simulation. The results section details the properties of these spikes under different conditions. The discussion section is focused on the analysis of two different synchronization mechanisms, their plausibility and the implication of these results to spike sorting of MERs from DBS. The final section summarizes the conclusions of this study.

2 METHODS

The model used in this paper is an extension of the work presented in [7, 8]. For each neuron the ISI times are drawn from the same Weibull distribution, with a shape parameter of 0.8 and a mean firing rate of 10Hz. These parameters match the values found for a STN given in [8]. A subset of synchronized neurons are defined at random during the initialization of the simulation. An additional point process time series is generated, using a Poisson distribution for ISI of synchronized firing running in parallel. A Poisson distribution is chosen so that the synchronized events are independent and evenly distributed in time (it is not

biologically based). At the spike times of this second point process a spike is added to the subset of neurons selected to be synchronized. If a neuron fires as part of a synchronized subset, the next firing time is reset and redrawn from the single neuron ISI distribution. The neuronal spike trains produced are coupled to the modeled electrode using the extracellular filtering model in [8].

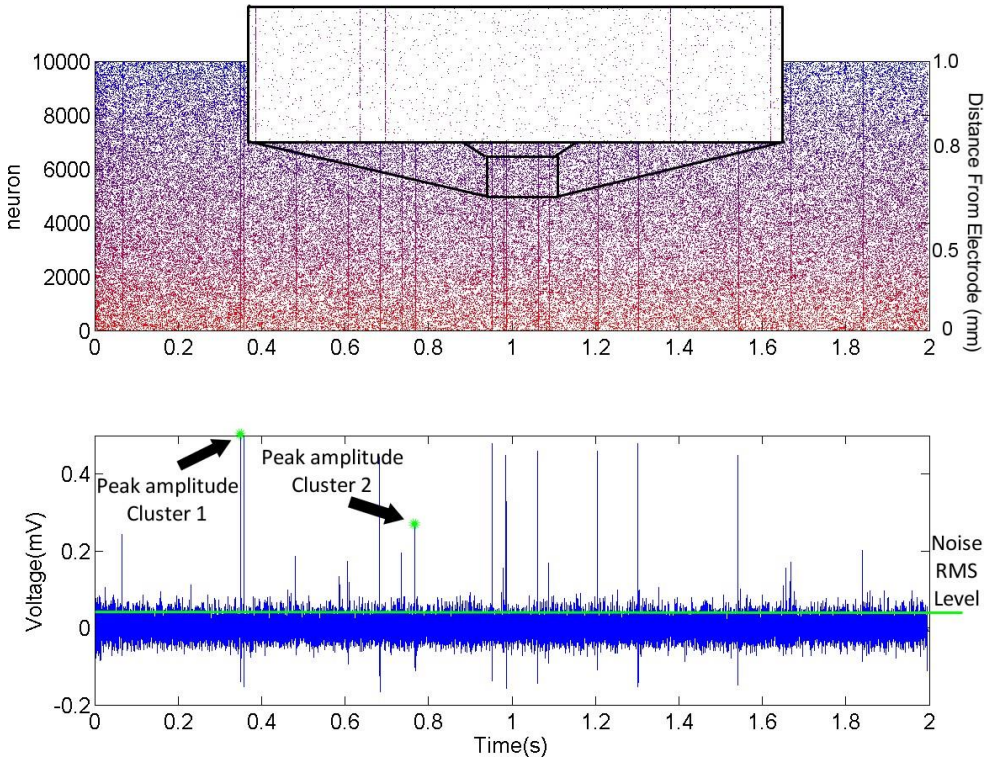

Fig. 1. Raster plot of the simulated neuron firing times and the MER time series. The vertical lines of increased density in the raster plot correspond to the synchronized firing events, with a fraction of 0.15 synchronization. There are two synchronized subsets of neurons, giving two different spike shapes/amplitudes.

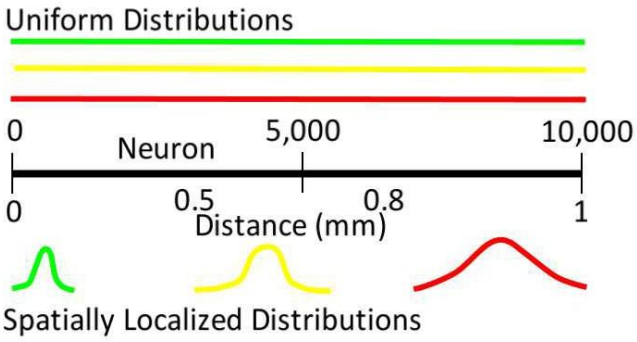

Fig. 2. Comparison of the probability of a neuron belonging to a synchronized subset for uniform distributed and spatially localized selections. The three coloured lines represent three different synchronized subsets (above the graph uniformly distributed and below spatially localized).

In order to generate another synchronized neural sub-set the same process can be used,

with a different group of neurons selected and a separate probability distribution for synchronized timing events generated. Neurons that synchronize in one group can still synchronize in another group. For spatial localization of groups, the neurons are selected using a Gaussian distribution in space centered on the group with a standard deviation based on the spatial spread of the desired group as shown in Figure 2.

The signal to noise ratio (SNR) of the spikes is calculated by taking the average maximum peak amplitude for a spike and comparing it to the root mean square (RMS) voltage of the noise (shown in Figure 1). Spike sorting of the recordings is performed using Osort [9], with compact support bi-orthogonal '1.5' wavelet at individual wavelet scales corresponding to between 0.1 and 1ms. The clustering is unsupervised, with cluster validity checked by comparing s pike timing to the synchronized times in the simulation.

3 RESULTS

A raster plot, Figure 1, of the simulated neuron firings shows how the synchronized firing times correspond to a spike with a large signal to noise ratio. In the raster plot two separate synchronized subsets can be seen. Although there are two subsets with the same percentage of total neurons synchronized, their spatial arrangement around the electrode are different. The effects of this spatial arrangement can be seen in the MER time series, where two different spike shapes are present.

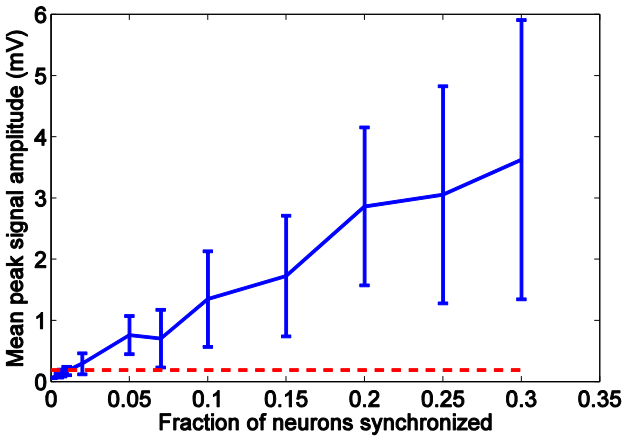

Fig. 3. Mean peak signal amplitude as the fraction of neurons in the synchronized sub-set changes. The mean is taken over 20 simulations and the error bars are one standard deviation. The dashed line represents the average RMS value of the recordings, shown in Figure 1.

As the number of neurons that are synchronized increases Figure 3 shows a linear increase of the mean peak amplitude of the CAP spike, averaged over 20 simulations. The variance of the peak amplitude also increases significantly, depending on the spatial distribution of the sub-set of synchronized neurons, i.e. as more neurons are synchronized they are more likely to come from a wide spread of locations. Figure 3 shows synchronization over the biologically plausible range of 0-0.30 for the STN [5]. For synchronization above 0.5 the mean peak signal amplitude becomes constant at 8.06 ± 0.52 *mV*, with variance decreasing to zero when all neurons are synchronized.

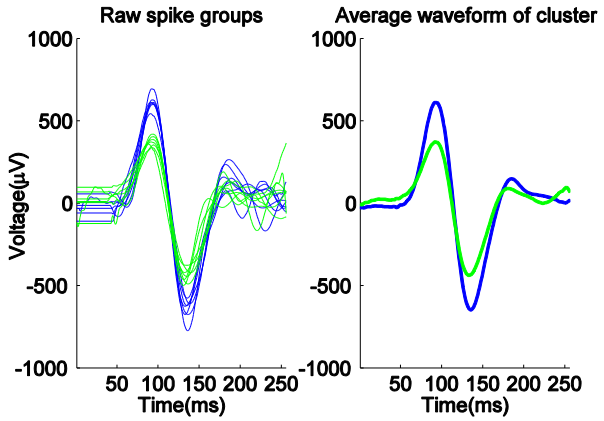

Fig. 4. Comparison of two CAPs after spike sorting from a simulation with synchronization percentage of 25% total synchronization. For this simulation there were two synchronized subsets of neurons with each subset uniformly distributed across all the neurons and 12.5% of neurons in each set.

Figure 3 shows when two sub-sets of synchronized neurons differ substantially in their spatial distribution, spike sorting can be successfully achieved. This occurs more often when the neurons are spatially localized, however it can occur when the two sub-sets are uniformly distributed as per Figure 2.

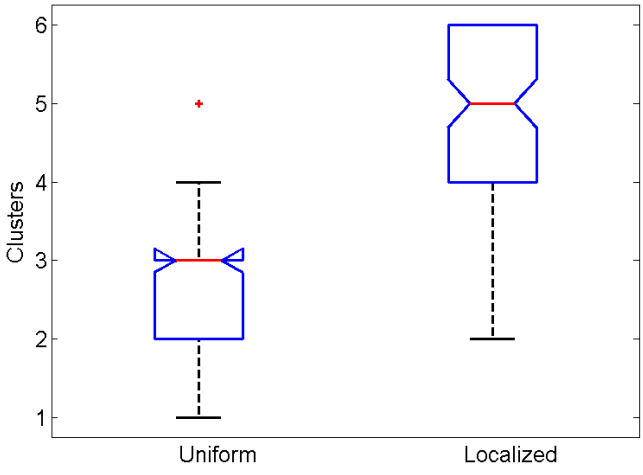

Fig. 5. The number of groups clustered for six spatially localized and six uniformly distributed subsets of synchronized groups of neurons over 100 simulations. The sticks represent the maximum and the minimum number of groups, the box represents the 25th and 75th percentile and the notch is the mean.

Figure 5 shows that when the synchronization of six neural subsets is changed from uniform across space, to spatially localized, the spike sorting algorithm can distinguish more clusters. For the uniform distribution only two to three clusters are found 50% of the time. For the spatially localized neural subsets more than four clusters are found 75% of the time.

4 DISCUSSION

Figure 3 shows that for no synchronization there is a chance of having a peak signal amplitude two times above the RMS noise. In this case a neuron current source (the axon hillock) is located close enough to the electrode tip for its action potential to be significantly larger than the background noise and thus appear as a spike. This shows that it is possible for DBS MER spikes to represent single neuron activity. However, the likelihood of two or more neurons contributing AP spikes in these MER simulations is very low because of their spatial distribution.

There are two methods to produce visible spikes in the MER simulations. The first method is to place a neuron very close to the electrode (where the current source is adjacent to the tip of the electrode). The second method is to introduce synchronization and produce a CAP. For DBS MERs the spikes are often thought to be APs produced by single neurons. Spike sorting techniques, based on shape, amplitude and rate, are then used to determine if the MER spikes all correspond to the same neuron, or multiple neurons firing at different times [9]. It can be seen that these spike sorting methods can also be used to sort CAP spikes generated by synchronization, depending on the spatial distribution of the synchronization within the STN.

When synchronization was uniformly spread through the STN the spike sorting of different synchronized subsets failed to produce the correct number of clusters. This is due to the effective shape of the CAP produced by a subset of synchronized neurons being too similar. Their similarity in shape of the spike is an average effect of the action potentials from each neuron that is synchronized. As the distribution of the synchronized subsets has a uniform probability of selecting any neuron, the average spike shape for each subset is on average the same. In general, the CAP shape is dominated by the closest neurons to the electrode, with minimal extracellular filtering. On average neurons that are further away are more likely

to be selected because the number of neurons located at a distance depends on the square of the radial distance from the electrode, r^2. However, the further the neuron is from the electrode, the more the electric field is filtered by the extracellular medium [7, 8, 10, 11], with an amplitude decay larger than $1/r^2$. Therefore, the main difference between the two CAPs produced by a subset of synchronized neurons will be the total number of closer neurons, which will change the amplitude of the spike, as seen in the example in Figure 4.

When the synchronized subsets are defined to be spatially localized, rather than across all of the STN, the compound action potentials are no longer dominated by the closest neurons. Rather they reflect the average AP at the mean spatial location of the cluster. This increases the success of the spike sorting because each CAP not only differs in amplitude but also in shape due to extracellular filtering.

A point to note from Figure 5 is that the spike sorting never overestimates the number of synchronized subsets. The low likelihood of two neurons producing AP spikes in the recording combined with this point would suggest that spatially localized synchronization is the most likely explanation for a DBS MER when the spikes can be sorted into multiple clusters. A limitation of this model is that the peak amplitude for a single neuron AP is limited in size to the minimum distance a neuron can be generated at. In practice there is no limit to the neuron-electrode distance, meaning that peak amplitude cannot be used to differentiate between spikes from CAPs and very close APs.

Simultaneous MERs cannot be obtained in a target structure during a DBS surgery. The exact location of neurons around the electrode is also currently unmeasurable. These limitations, along with the spike mechanisms presented in this paper, mean that it would be unlikely to differentiate between APs, a single synchronous neuronal subset and multiple uniformly distributed synchronous neuronal subsets. Due to this complication, DBS MER spikes are most sensibly considered as an indication of the target structures overall activity. If the spikes can be sorted into multiple clusters, it indicates that there is most likely spatially localized synchronized neuronal subsets. Alternatively, the spikes can be sorted into a single group to obtain a measure of overall activity.

The method used for adding the synchronization uniformly in this paper is artificial and not based on a biological mechanism. This was chosen only to demonstrate that with

synchronization, sortable spikes can emerge from the CAPs in MERs. The model was extended to include spatially localized synchronization to improve biological plausibility and making the CAPs differ in amplitude and shape. This distribution relates to the idea of somatotropic maps of the STN, which show that there is localized organization in the STN related to different movement tasks [5].

Future work will focus on increasing the biological plausibility of this model, structures external to the STN, such as the entire Basal Ganglia, can be included. These external structures can be used to control the amount of synchronization, and the statistics of the synchronized spikes. Controlling the ISI times using an external structure allows for non-stationary ISI statistics, which could be used to analyze MERs when patients are performing transient tasks.

5 CONCLUSION

This work shows that synchronized firing between different neurons located near a microelectrode can produce what appears to be a single neuron action potential but is actually more likely to be a compound action potential. As the number of synchronized neurons, within a biologically plausible range, increases the signal to noise ratio for these spikes increases. Standard spike sorting methods cannot appropriately cluster spikes which occur when the neuronal synchronization is uniformly distributed. The spike sorting methods perform better when the synchronized groups are spatially localized.

6 REFERENCES

[1] S. Santaniello, G. Fiengo, L. Glielmo, and G. Catapano, “A biophysically inspired microelectrode recording-based model for the subthalamic nucleus activity in parkinson’s disease,” *Biomedical Signal Processing and Control*, vol. 3, pp. 203– 211, 2008.

[2] I. M. Garonzik, S. Ohara, S. E. Hua, and F. A. Lenz, “Microelectrode techniques: Single-cell and field potential recordings,” in *Microelectrode recordings in movement disorder surgery*, Z. Israel and K. J. Burchiel, Eds., vol. 1. Thieme Medical Publishers, Inc., New York, 2004.

[3] K.P. Michmizos and K.S. Nikita, “Addition of deep brain stimulation signal to a local field potential driven izhikevich model masks the pathological firing pattern of an stn neuron,” in *Proceedings from the 33rd Annual International Conference of the IEEE EMBS*, Boston,

Massachusetts USA, 2011, IEEE EMBS.

[4] M. Rasch, N.K. Logothetis, and G. Kreiman, “From neurons to circuits: Linear estimation of local field potentials,” *The Journal of Neuroscience*, vol. 29, no. 44, pp. 13785–13796, 2009.

[5] P. V. Theodosopoulos, R. S. Turner, and P. A. Starr, “Electrophysiological findings in stn and snr.,” in *Microelectrode recordings in movement disorder surgery*, Z. Israel and K. J. Burchiel, Eds., vol. 1. Thieme Medical Publishers, Inc., New York, 2004.

[6] A. Snellings, O. Sagher, D. J. Anderson, and J. W. Aldridge, “Identification of the subthalamic nucleus in deep brain stimulation surgery with a novel wavelet-derived measure of neural background activity,” *J Neurosurg*, vol. 111, pp. 767–774, 2009.

[7] K. J. Weegink, J. J. Varghese, P. A. Bellette, Coyne, P. A. T., Silburn, and P. A. Meehan, “An efficient stochastic based model for simulating microelectrode recordings of the deep brain,” in *Proceedings of Biosignals 2012, International Conference on Bio-Inspired Systems and Signal Processing. 5th International Joint Conference on Biomedical Engineering Systems and Technologies (BIOSTEC)*, Sabine Van Huffel, Carlos Correia, Ana Fred, and Hugo Gamboa, Eds., Vilamoura, Portugal, Ferbruary 2012, pp. 76–84.

[8] K. J. Weegink, P. A. Bellette, J. J. Varghese, P. A. Silburn, P. A. Meehan, and A. P. Bradley, “Efficient micro-electrode recording modelling using a filtered point process.,” *Preprint available http://arxiv.org/abs/1307.5250*.

[9] U. Rutishauser, E. M. Schuman, and A. N. Mamelak, “Online detection and sorting of extracellularly recorded action potentials in human medial temporal lobe recordings, in vivo.,” *J. Neurosci. Methods*, vol. 154, no. 1-2, pp. 204–224, 2006.

[10] C. Gold and et al., “On the origin of extracellular action potential waveform: A modeling study.,” *Journal of Neurophysiology*, vol. 95, pp. 3113–3128, 2006.

[11] C. Bedard, H. Kroger, and A. Destexhe, “Modeling extracellular field potentials and the frequency-filtering properties of extracellular space.,” *Biophysical Journal*, vol. 86, pp. 1829–1842, 2004.

Paper C - A Parametric Simulation of Neuronal Noise from Microelectrode Recordings

K. J. Weegink, J. J. Varghese, P. A. Bellette, P. A. Silburn, P. A. Meehan and A. P. Bradley

ABSTRACT

In this paper we present an efficient model of microelectrode recordings (MER) from the subthalamic nucleus acquired during deep brain stimulation surgery. The model shows how changes in the “noise” relate to the neuronal spike time statistics. A top-down approach is used with analysis by-synthesis of the MER power spectra. The model is built around a sum of filtered point processes consisting of thousands of neurons and including extracellular filtering. The quality of the model is demonstrated through comparisons to recordings from eight individuals (both hemispheres in six) who have undergone DBS implantation for the treatment of Parkinson’s disease. The simulated recordings were compared using their voltage amplitude distributions, power spectral density estimates and phase synchrony while varying only one free parameter (The shape of the inter-spike interval distribution). Through this simple model, we show that the noise present in a DBS MER contains properties that match that of patient recordings when a Weibull distribution with shape parameter of 0.8 is used for the inter-spike interval.

I. INTRODUCTION

Deep brain stimulation (DBS) has become a common treatment for neurological movement disorders such as Parkinson’s disease (PD) [1], [2]. DBS involves applying a pulsed electric field to a deep brain structure with the electrode positioned to within 1 mm accuracy. DBS applies chronic stimulation, using no feedback based on patient state, except for periodic clinical adjustment [3]. The subthalamic nucleus (STN) is a common target for the treatment of PD [1]. The role of the STN as a DBS target for PD is not fully understood and for this reason many models of the brain areas associated with Parkinson’s disease have been developed to aid interpretation [4], [5], [6], [7].

To help determine whether the DBS stimulation electrode is implanted at the correct surgical target a micro-electrode recording (MER) is used [1], [8]. A typical MER contains baseline noise and spikes with a peak amplitude above the background activity [9]. Changes in the noise level can be used to confirm electrode placement [8]. This suggests that the “noise” component of a DBS MER has a neuronal component. Microelectrodes used in targeting during a DBS implantation procedure have a 50µ*m* tip diameter. This tip size is larger than electrodes used for single cell recordings (≈ 1 µ*m*) and considerably smaller than the implanted electrode (≈1 *mm*). This intermediate size allows the electrode to record high frequency electrical activity, associated with the behaviour of single neurons and apply electrical stimulation without causing damage to the surrounding tissue. However, a consequence of the microelectrode tip size is that it contains a large degree of background activity compared to a high impedance single neuron recording electrode [10].

Using the same electrode to both stimulate and record electrical activity within a neuronal structure would minimize the impact and risks to patients. It could also improve the surgical out-come by removing the need to replace the targeting electrode with the permanent electrode while ensuring it ends up at the same position. Combined with a top down parametric model, this type of electrode would have the potential to aid in the development of adaptive stimulation and thus improve the clinical effectiveness of stimulation, reduce unwanted side effects and increase the energy efficiency leading to longer battery life.

The aim of this paper is to develop an efficient model capable of modeling the neuronal activity in MERs recorded from the STN. This model has the potential to be used as a basis for metrics of patient state through analysis by synthesis of the recording, inspired by the approaches in speech coding [11]. This method of analysing MERs can provide a computationally efficient parametric method for characterizing patient state, thereby providing a robust method suitable for use in adaptive feedback control [3].

The model we demonstrate in this paper is a summed filtered point process model of an STN MER. The model is a parametric model with the inter-spike interval statistics adapted to reproduce patient data. The model couples the electric field of the neurons to the micro-electrode with a spatial dependence. We demonstrate that this type of model is significantly more computationally efficient than current bottom up modeling techniques. To evaluate the

quality of the model, we compare the distribution of recorded amplitudes, linear correlations of the modeled power spectrum and the synchronous phase components to patient MER signals.

The paper is structured as follows; section one provides the background and motivation for the modeling and analysis methods used. Section two outlines the methodology used for the simulations, the acquisition of patient recordings and the techniques used to quantify the quality of the model reproducing patient data. Section three presents the results of the comparison, section four includes a discussion of this work and section five provides the conclusions.

A. Adaptive Stimulation

Adaptive stimulation for DBS requires the development of a feedback loop to control the behaviour of the electrode stimulation based on the patient state. For DBS there is a single system input (the stimulation electrode) that changes the neuronal firing patterns in the patient. Measuring the state of every neuron in the patient would be experimentally impossible while modelling the state would be a mathematically monumental and computationally expensive task which is for all intents and purposes not practicably feasible. Instead a single-input single-output model can be developed to reduce the complexity.

A simple parametric model of the STN/electrode system would allow for a single-output protocol that could be useful for adaptive stimulation. This type of model needs to be able to be computed in real time and change with the patient state in a manner that can be compared to a desired reference to produce an appropriate stimulator output.

In this paper we propose the development of a computationally simple parametric model of the STN-neuron interaction that fits patient data as a first step towards the type of model needed for a feedback control system of DBS. Most importantly this model has minimal free parameters, is near on-line efficient and has a conceptual link back to the underlying neuro-biology.

B. Subthalamic Nucleus Models

The types of STN models previously used vary from phase oscillators [7] to conductance based spiking neuron models [6]. Current STN models involving a large number of individual neurons are computationally intensive [12]. DBS MER models that simulate a single neuron with background noise are computationally efficient but may not reflect neuronal noise processes. These methods to simulate STN MERs involve a single spiking neuron and additive white noise to produce the background activity [7]. These models assume a spectrally white background noise, while we show the patient recordings have non-white statistics. How neuronal activity changes this type of background activity hasn't previously been modeled. To model the noise with a biologically plausible method a large number of individual spiking neurons are required in the simulation. The conductance-based Hodgkin-Huxley (HH) model used in [4] can be used to simulate individual STN neurons. These types of models are computationally intensive and require context (input signals) from the surrounding structures in the basal ganglia be modeled to produce correct spike timing [4]. To overcome this requirement of a large model we propose using a top-down approach by using a filtered point process (FPP) model of the STN firing times where parameters relate to biologically important properties, e.g. rate and inter-spike interval (ISI) distribution.

C. Filtered Point Process Models

Filtered point processes are a subset of linear stochastic processes. Stochastic models reduce an observable variable of a neuron, such as the timing of spikes, from being described by a deterministic equation, e.g. HH, to being randomly drawn from a probability distribution. Features like spike timing can be described using only a probability distribution [13], [14]. The probability distribution used simplifies the factors that cause a neuron to fire, such as the network inputs and noise inputs to a neuron. For our point process model, to reduce complexity, each neuron is considered independently. The firing times of the point process model are convolved with the neuronal action potential shape. The action potential shape acts as a filter to create the current time series for a neuron.

A filtered renewal process is a special type of FPP where the time interval between two spikes, the ISI, is drawn from a common distribution not conditional on the previous ISI [15]. Each ISI time is assumed independent of any previous spike times satisfying the independent identical distribution assumption. The simplification of a filtered renewal process allows the neuron time series to be modeled with just the shape of the action

potential and the ISI probability distribution [16]. This significantly reduces the complexity as compared to other neuronal models such as [6].

The firing times for neurons are often described by a Poisson process, a special case of the renewal process where the ISI distribution is exponential. However, there are many counter examples of non-Poisson neuron firing patterns [17], [18]. A Poisson process is described by only a single parameter, the rate, where the spikes are uniformly distributed in time. It cannot model cell behaviors seen in the STN such as bursting and periodic firing [19]. Therefore, we propose that a Weibull distribution is a more suitable ISI distribution for reproducing this range of STN behaviors of which Poisson is a special case.

D. Electric Field Models for Extracellular Recordings

The coupling of each neuron to the micro-electrode is dependent on the distance of that neuron to the electrode and the properties of the extracellular media in-between [20]. As the electric field from the action potential propagates to the electrode it passes through the extracellular space which has varying conductivity and permittivity. This process modifies the frequency behaviour recorded by the electrode for that neuron. These effects change the power spectra of a neuronal recording and need to be considered when producing a model of MER power spectra. Finite element models (FEM) have been created to describe the electric field of neurons as it propagates through the extracellular medium [21]. The FEM simulations show that the extracellular medium causes low pass filtering and attenuation of the potential measured at the electrode. The spatial composition of the extracellular medium is required to use these methods and these methods are computationally expensive. Complications can be reduced by assuming average properties of the extracellular medium [22]. This also removes the need to define the exact extracellular composition for each neuron-electrode interface.

The average extracellular filtering of the neuronal electric field at the electrode can be described by a complex transfer function relating the cellular current to the voltage recorded by the electrode, i.e. the impedance of the extracellular material [20], [22]. This assumes the neurons act as a point current source and a decoupled magnetic field. However, obtaining the transfer function for the extracellular medium is computationally expensive as a numerical integral is calculated for each frequency component and for all neuronal positions.

A circuit model simplification of this extracellular filtering can be used to find a simplified form of the transfer function [23], [24]. The effect of the radial distance to the electrode for each neuron is reduced to a “seal” resistance. This type of model also includes the frequency effects of the electrode geometry with Faradic resistance and capacitance.

E. Analysis of Recordings

The key to the analysis-by-synthesis approach is to measure how closely the proposed top down model can synthesis MER data. Here we use three different analysis methods common to compare simulations and patient recordings. A standard method for analysing an MER is to use spike sorting [19]. In many cases an MER may not contain spikes that can be separated from noise. However, by its very nature spike sorting removes the noise and thus is unsuitable for analysing the neuronal noise. To compare the simulations including noise to the in vivo recordings, time averaged statistical properties need to be used, such as the autocorrelation function, power spectrum or equivalent. Using renewal theory [16] it has been shown that a filtered renewal process has a closed form power spectral density (PSD). The PSD can be written as a function dependent on the impulse filter (the action potential) and ISI probability density function. This result shows that as the parameters of the ISI distribution change the power spectrum changes for a summed filtered renewal process [16].

Since the MER simulation will be modeled as a stochastic process, the voltage history will not be deterministic. Random processes can be compared against their statistical moments, such as the mean and variance. In this paper a Kolmogorov-Smirnov test, [25], is used to compare the voltage distributions of simulated MERs to patient MERs.

Another feature of a stochastic process is random phase. To look at the phase properties of neural signals the component synchrony measure can be used [26]. This measure is also used in this paper to determine the quality of the model for simulating patient recordings.

II. METHODS

The methods of this paper are organized into three sections. Section 2.1 contains patient information and the surgical method used to obtain the recordings. Section 2.2 describes

how the simulations were performed. Section 2.3 contains the analysis methods used to compare simulations to patient recordings.

A. Patient Recordings

Eight participants (five male, three female) with idiopathic PD who were considered suitable for the implantation of bilateral permanent stimulator in the STN were included in this study. The patient age was 67 ±5 years (none of the patients were “young onset”), with disease duration of 14 ±6 years. Participants were all right handed and had no further neurological impairment. The participants had undergone psychiatric screening prior to DBS surgery. A summary of the patients is given in TABLE I.

TABLE I - SUMMARY OF PARTICIPANTS FOR WHOM MER RECORDINGS WERE USED FOR THE VALIDATION OF THE MODEL

Participant	Age	Gender	Education	Handedness	Disease Duration	Severity (H&Y)	UPDRS III score	Side of MER
32	73	M	14	Right	8	NA	NA	Left
38	58	M	11	Right	11	2	3	Bilateral
53	71	M	13	Right	16	4	20	Bilateral
61	71	F	10	Right	17	3	17	Bilateral
69	66	F	14	Right	22	NA	NA	Bilateral
74	65	F	7	Right	15	2	11	Bilateral
103	62	M	9	Right	20	2	8	Right
104	71	M	10	Right	3	NA	NA	Bilateral

Note: H&Y = Hoehn and Yahr; UPDRS = Unified Parkinson’s Disease Rating Scale; NA not available.

The dorsolateral aspect of the STN was targeted using a Cosman-Roberts-Wells stereotactic frame with coordinates based on CT images fused with 3T MRI t1 and FLAIR sequences. The electrode placement was confirmed interoperatively by an MER. The surgical procedure is described in detail in [1]. Tungsten microTargeting electrodes (model mTDWAR, FHC, Bowdoinham, ME) with a tip diameter of less than 50 µ*m* were used for the MER acquisition. The electrodes had a typical impedance of 0.5 (±0.15) *M*Ω at 1*kHz*. A LeadPoint™ system (Medtronic Inc., Minneapolis,MN) was used to record the signals at a sampling rate of 24 *kHz*. Three filters were applied (high pass: 500 *Hz* first order, low pass: 5*k Hz* first order and anti-aliasing: 5 *kHz* fourth order) as recommended by Medtronic. Each MER was recorded during resting phases, when the participant was lying still and not performing any cognitive or movement tasks.

B. Simulations

The simulation method presented here are an extension of those presented in [27]. A summary of the simulation method is given in Figure 1. Simulations were performed for 10,000 neurons over one second to model the patient recordings. The use of 10,000 neurons is based on calculations in [27].

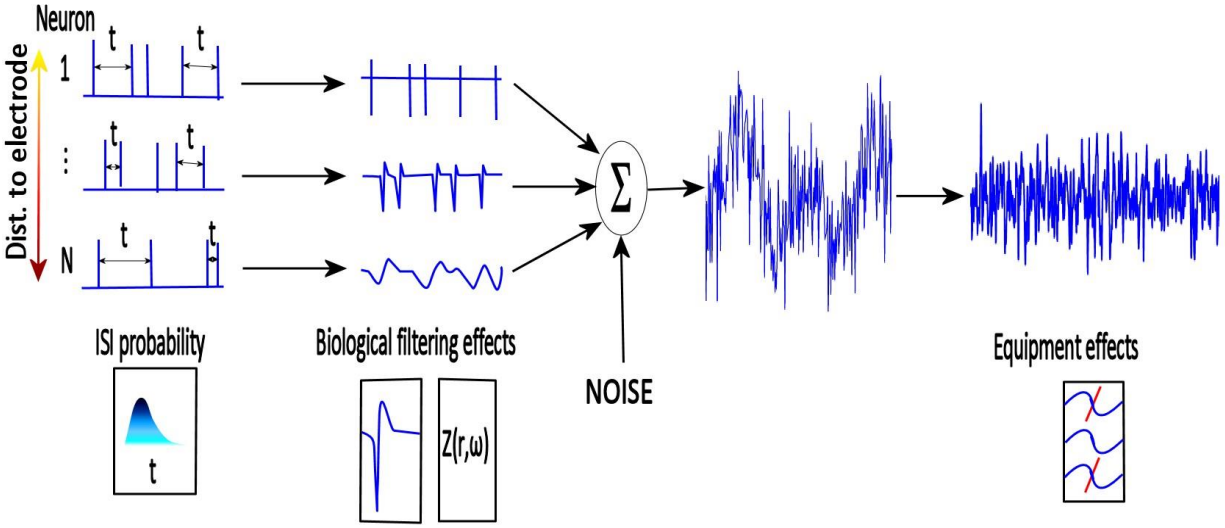

Fig. 1. A summary of the method used for the MER simulations. Spike times for each neuron are produced using the ISI probability distribution. The action potential shape is applied, and the spike trains are filtered based on their distance from the electrode. The filtered spike trains are then summed together, and noise is added before passing the signal through filters based on the equipment used in acquisition.

We validate the number of neurons to use by calculating the RMS value of the MER simulations for different numbers of neurons. All steps in the simulation were performed on a PC with a quad core 1.73 GHz processor and 8 GB or RAM using 64-bit MATLAB 7.14.0 (R2012a) [28]. A time step of 1/24,000 *s* was used to match the sampling rate of the patient recordings.

The STN behavior is modeled by assuming the ISI times form a random variable drawn from a Weibull distribution in time:

$$P(t) = \left(\frac{t - t_r}{\lambda}\right)^{c-1} \frac{c}{\lambda}\, e^{-\left(\frac{t-t_r}{\lambda}\right)^c} \quad for\ t > t_r$$

$$otherwise\ P(t) = 0,$$

where $P(t)$ is the probability density function for the ISIs and λ is the scale parameter that controls the firing rate. The shape parameter c influences the neuronal behavior; with $c<1$ generating burst firing, $c=1$ Poisson statistics and $c>2$ firing times with a common mode, as shown in Figure 2. In the limit as $c \to \infty$ periodic behavior emerges. The parameter t_r controls the refractory time of the neuron, preventing another action potential occurring within this period. The scale, rate and refractory parameters relate to the rate of firing(v) by:

$$v = (t_r + \lambda \ \Gamma(1+1=c)) \ -1;$$

where Γ is the complete gamma function. The point process consists of a time series of Kronecker-delta pulses which are first created by drawing the ISI times from the Weibull distribution with shape parameter (c) values of 0.5, 0.8, 1, 10 and 100, and a rate parameter that corresponds to 30 *Hz*. A refractory time of 5 *ms* was used [19]. Neuronal current time series are produced by convolving the Kronecker-delta pulses with the action potential shape. The time series was generated for each neuron independently.

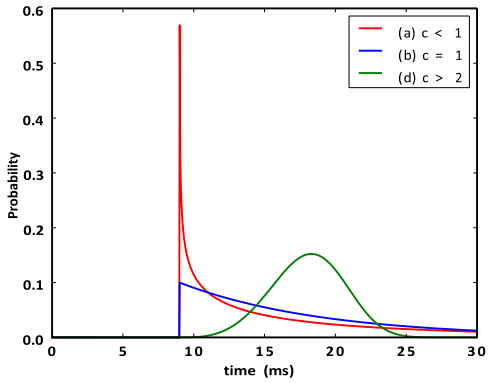

Fig. 2. Examples of the Weibull distribution. The neuron can exhibit burst firing (a), Poisson statistics (b), or semi periodic firing (c) depending upon the shape parameter c.

The action potential shape was generated by numerically solving a Hodgkin and Huxley model using a variable order solver (ODE15s [28]). The Hodgkin and Huxley model parameters used were for the medium spiny neuron based on [4]:

$$C_m = \frac{dV}{dt}$$

$$C_m = -g_L(V - v_L) - g_K n^4 (V - v_K) - g_{Na} m^3 h (V - v_{Na}) - G_T a^3 b^2 (V - v_{Ca}) - g_{Ca} s^2 (V - v_{Ca})$$

where C_m is the membrane capacitance (1 pF/μm^2); g_L, v_L are the leak conductance and reversal potential (2.25 nS/μm^2 and -60.0 mV respectively); g_K, v_K are the K^+ conductance and equilibrium potential (45 nS/μm^2 and -80.0 mV respectively); g_{Na}, v_{Na} are the Na^+

conductance and equilibrium potential (37.5 nS/µm^2 and 55.0 mV respectively); g_T is a low-threshold T-type Ca^{2+} conductance (0.5 nS/µm^2); and g_{Ca}, v_{Ca} are a high-threshold Ca^{2+} conductance and a Ca^{2+} equilibrium potential (0.5 nS/µm^2 and 140.0 mV respectively). The gating variables *n*, *m*, *h*, *a* and *b* follow the differential equations and parameters given in [4]. This produces the filter function used for each neuron.

Each neuron is modeled as a point source, with the current being generated from the axon hillock. The current time series was then filtered using an impedance based on the distance of the neuron from the electrode to find the potential contributed by each neuron. This model assumes a far-field approximation to the electric field incident on the electrode. This allows us to sum the voltages linearly after they are found through the relation:

$$V_{\omega(r)} = I_{\omega}\, Z_{\omega(r)}$$

where *I*ω is the frequency components of the current at the neuron found by solving eq. 4. The impedance filter *Z*ω is found using a symbolic maths package by determining the transfer function *I*ω/*V*ω for the circuit model of the neuron-electrode interaction, shown in Figure 3.

The circuit model used evaluates the propagation of the electric field through the extracellular medium and uses circuit element values that depend on the radial distance between the electrode and neuron, the size of the electrode tip and the impedance of the electrode, where C_l is the membrane-electrolyte interface capacitance (9.38*nF*), R_L is the body resistance to ground (the spread of the field from the neuron, 100*M*Ω), C_b is the body's capacitance (2.22µ*F*), R_l is the resistance between the cell and the electrode (seal of the electric field by the neuron to the electrode [23], [24], R_l , R_f and C_f are the electrode Faradic resistance (960Ω) and capacitance (1.56µ*F*) of the electrode and R_e is the electrode resistive load (0.5*M*Ω). The voltage for the recording, *V*ω, is taken across the load resistance (R_e).

While the extracellular medium is known to be anisotropic over a scale of mm^3 [29] there is currently no data available to model this anisotropy at sub-mm levels. Therefore, we assume the extracellular medium between the neuron and probe can be treated as isotropic.

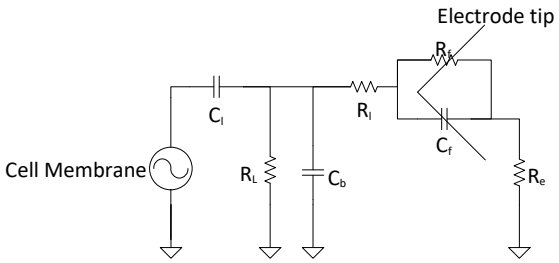

Fig. 3. The circuit configuration used for coupling each neuron to the electrode.

As the distance from the electrode increases the number of neurons contributing to the time-series follows the neuron radial distribution density $N(R)$ is randomly generated using a uniform spatial distribution with density, $\rho = 10^5\, cm^{-3}$ [19].

$$N(R) = 4\pi r^2 \rho.$$

The complete time series from all neurons are then summed together linearly to create the potential across the electrode.

Thermal white noise (Johnson-Nyquist noise) is added to the electrode to match experimental conditions. The statistics of the noise are described by:

$$\langle V \rangle = 0, \;\; \langle V^2 \rangle = 4k_B T R(f) \Delta f$$

where k_B is Boltzmann's constant, T is the temperature (assumed to be average body temperature 310K(37^{o}C)), $R(f)$ is the electrode resistance, $\langle \cdots \rangle$ represents the time average. The product $R(f)\Delta f$ is the bandwidth and $R(f)\Delta f$ is calculated by integrating the product of $R(f)$ with the gain function $G(f)$ of the equipment over frequency:

$$R(f)\Delta f = \int_0^\infty R(f)G(f)\, df$$

To match simulations to the surgical conditions the simulated voltage time series is passed through three filters described in section 2.1. The filters are Butterworth models of the two software filters with a 500 *Hz* first order high pass, 5 *kHz* first order low pass and the hardware 5 *kHz* fourth order anti-aliasing filter. $G(f)$ is found by multiplying a flat, unity power spectra, $P(f) = 1$, by the filter gains.

C. Comparative analysis of modeled and patient recordings

The quality analysis of the model is broken into three sections. The sections look at the distribution of recorded amplitudes in the time domain, linear correlations of the modeled PSD estimate to patient PSD estimates and comparisons of synchronous phase

components. Patient recordings that contained movement artefacts, defined by amplitude > 10 *mV*, or had recording times less than 1 *s* were removed from the analysis. After this removal process, 84 MERs from 14 patient-hemispheres were analysed.

1) Test of Voltage Distribution: The first test performed was a two-sided Kolmogorov-Smirnov (KS) test on the distribution of the voltages in time. This test was used to check if the voltage amplitude distribution for the simulations have a different distribution to the voltage amplitude distribution seen in patient recordings. Rather than use the KS test to assign statistical significance, we use the p-value from the test as a measure of distance between the patient recordings and the modeled results.

2) Power Spectrum Comparisons: PSDs for the recordings and simulations were calculated using Welch's overlapping segment method with a Hamming window [28]. The PSDs obtained using the five different simulation parameters were compared to the 14 patient hemisphere recordings using linear regression. The linear regression used the value of the patient PSD against the simulated PSD for each frequency. The correlation coefficient (R^2) was used to assess the goodness of fit.

3) Phase comparisons: The individual recordings are divided into 100 ms non-overlapping sections. The component synchrony measure (CSM) can be calculated by using [26]:

$$CSM(\omega) = \left[\frac{1}{N}\sum_{i=1}^{N}\cos\varphi_i(\omega)\right]^2 - \left[\frac{1}{N}\sum_{i=1}^{N}\sin\varphi_i(\omega)\right]^2$$

where the signal is divided into N non-overlapping segments. $\phi_i(m)$ is the phase of the signal at frequency *m* for signal *i*, where the phase is found by taking the tangent of the real and imaginary components of the FFT of the signal.

III. RESULTS

The results are divided as follows; Section 3.1 contains a summary of the computation time and features of the MER simulation. Section 3.2 contains the results from the comparison

with patient recordings. Section 3.3 contains the results from the parameter estimations of the patient recordings.

A. Simulations

To illustrate the speed advantages of the summed FPP model over a deterministic HH model, a comparison of the time required to compute an MER using the proposed electrode model and a coupled HH network is shown in Figure 4. The points are averaged over three data samples. The dashed line is a line of unity slope, to show that the computational order of the summed FPP is approximately $O(N)$, where N is the number of neurons. Due to the long computation time, no simulations of the Hodgkin and Huxley network with over 1,000 neurons were performed. The comparison of the computational time compared to neuron number shows that the FPP model is significantly (100x) faster than the equivalent Hodgkin and Huxley network model.

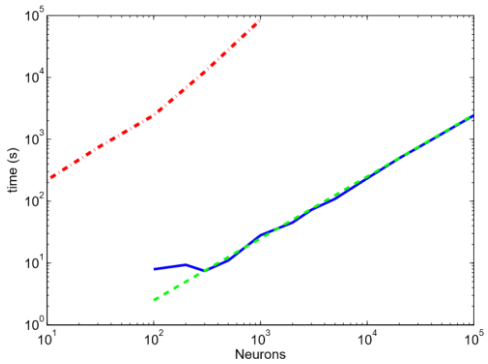

Fig. 4. The computational time to simulate an MER using the method presented in this paper (solid), a Hodgkin and Huxley neural network (dot dash). A line with slope one (dashed) is layered on top to indicate $O(N)$.

Figure 5 shows how the RMS value of the simulated MERs changes as the neuron number is changed. Above 3,000 neurons the RMS value plateaus. The peak RMS value approaches 49 μV. This is within one standard deviation of the mean RMS value for all the patient recordings of 56 ±12 μV over.

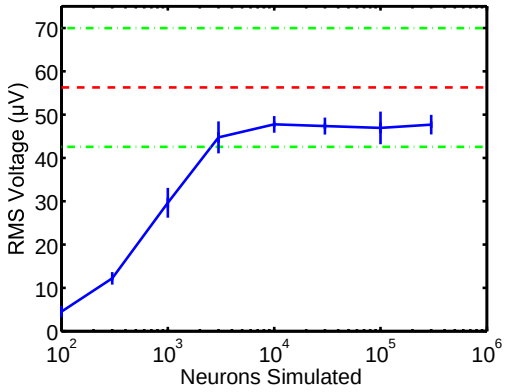

Fig. 5. The effect of changing the number of neurons simulated on the RMS value of the MER. The dashed lines represent the mean RMS (dark line) of patient recordings and one standard deviation (light line).

B. Comparative analysis of modeled and patient recordings

Figure 6 shows comparisons of the patient DBS MER to a simulation with a Weibull shape parameter of 0.8. This comparison visually shows the difficulty to compare the simulation and patient recordings as a time series. A clearer comparison of how well the parametric MER simulation models the patient data PSD is shown in figure 7.

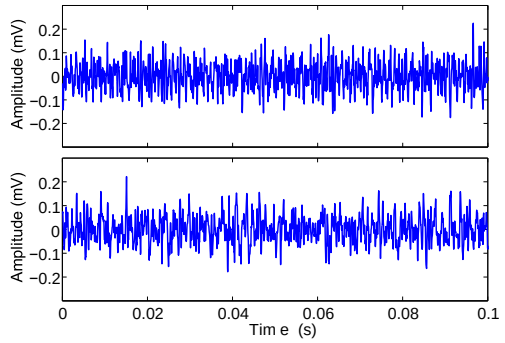

Fig. 6. Examples of a patient recording (top) and a simulated recording (bottom) on a fine time scale with a simulation parameter *c*=0.8.

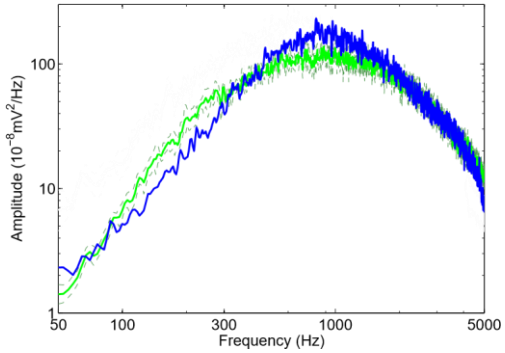

Fig. 7. Examples of the spectral estimates for P32L with 95 % confidence interval (dashed) and a simulation with *c*=0.8 (Dark line).

1) Test of Voltage Distributions: Figure 8 shows a box-plot of p-values from the KS test on the voltage distributions of the 14 hemisphere recordings against simulation parameters c = 0.5 to c = 100. As all p-values are above 0.05 we cannot reject the null hypothesis that the variables are drawn from the same distribution. Using the KS test as a distance measure, it can be seen that the closest simulated amplitude distribution to the patient recordings is c = 0.8.

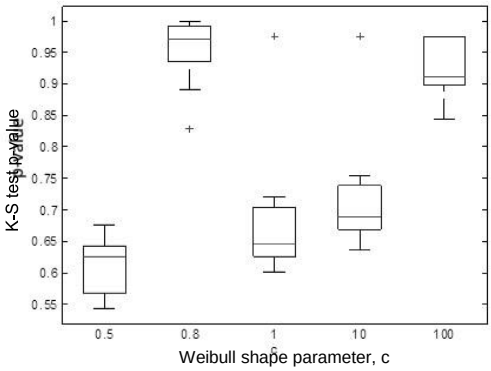

Fig. 8. Box plot of the KS test p-value of each patient voltage distribution matching the simulation distribution for each shape parameter. The Box represents the 25 and 75 percentiles, the lines represent the maximum and minimum values, the mid line represents the median value and the '+' represents outliers.

2) Power Spectrum Comparisons: Linear regression of the simulated PSD against the patient MER PSD was used to assess the model fit to the patient recordings. Figure 9 shows a box plot of the correlation coefficient for the linear fit for the 14 patient-hemisphere recordings. The outlier point is patient 61 right side for all values of c. This figure also shows that the R^2 value is greater than 0.89 for all values of the shape parameter.

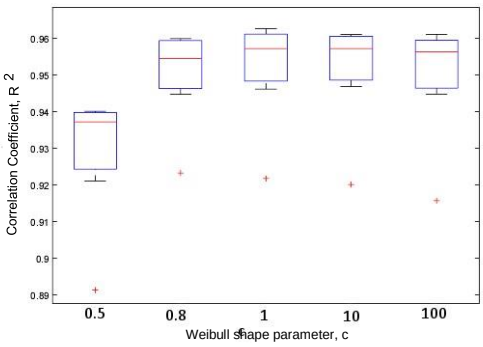

Fig. 9. Box plot of the R^2 value from fitting each patient spectrum to the simulated spectrums for different c values.

3) Phase Comparisons: The method used to see if there are any features in the phase spectrum of the recordings was the component synchrony measure (CSM). The amplitude of the largest peak in each CSM spectrum is shown in Figure 10 for both simulation and patient data. Figure 10 shows there are no peaks with amplitude above 0.3 in any of the recordings or simulations and therefore no significant phase structure.

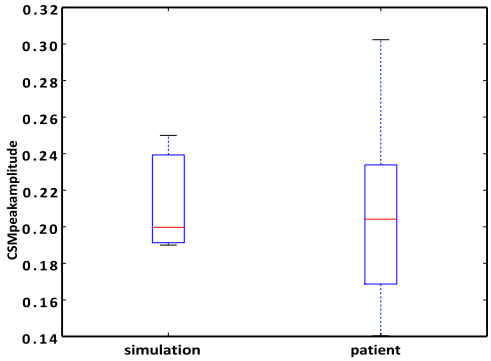

Fig. 10. Box plot of the amplitudes of the highest peak from each CSM spectra.

IV. DISCUSION

The implications from the model presented in this paper are given in section 4.1. Section 4.2 looks at the results of the analysis and section 4.3 discusses the assumptions and limitations for the model with possible future extensions. Section 4.4 summarizes the discussion.

A. Modeling

The computational time of the FPP model diverges from O(N) at low neuron number seen in Figure 4. This divergence from O(N) is due to the minimum time to initialize the simulation.

Other dynamic models of neurons, which reduce the complexity of the differential equations of the Hodgkin and Huxley model were not used to compare the computational time to this model. Computationally efficient spiking neuron (leaky integrate and fire and Izhekivich) models cannot produce accurate enough action potential shapes and are generally only used to produce the correct spike timing [30]. Because the PSD in the frequency range of interest has a contribution from the shape of the action potential these models were not considered. The model we have presented is a linear top-down model to analyse patient data via synthesis, where the complexity of spike timing is buried in the stochastic process.

A similar ‘cut and paste’ method for the spike shape can be used in the previous dynamical models where the spike timing is determined by the nonlinear dynamics. However, using these models for parametric fitting to patient data, without pre-calculating accurate waveforms or ISI timings, would be a significant and computationally intensive task. This is because the dynamics of each neuron cannot be modeled individually since the network activity and neuron to neuron coupling is required to produce the individual neuron dynamics.

The model proposed in this paper only produces the timing and shape of action potentials. The model does not account for any of the electrical activity below threshold that activates the spike. This type of activity, called subthreshold oscillations, are typically low frequency (1-100Hz). Slow oscillations are not clearly seen in the patient recordings due to the shape of the electrode (50 μ*m* tip) and the high pass filter at 500Hz. Due to these factors, sub threshold oscillations are not required to accurately model a DBS MER. The main feature that the model is used to simulate is the power spectrum of MERs. Figure 11 demonstrates how the power spectrum changes with the Weibull shape parameter. For the same recording length c = 0.5 (small dotted line) shows the least power density across the frequency band of interest in the patient recordings (unfiltered region, 500 Hz < ω< 5000 Hz). At the other extreme of c = 100 (dashed line) shows harmonic spikes. For c = 0.8 the PSD has a more spread out frequency distribution compared to the other simulations. The PSD for c = 1 follows the action potential power spectrum as expected from Carson’s theorem for a Poisson process. Although c=0.8 and c=1 have a very similar shape of their ISI times distribution (exponential), they display different distributions of power in their PSD estimates, see figure 11.

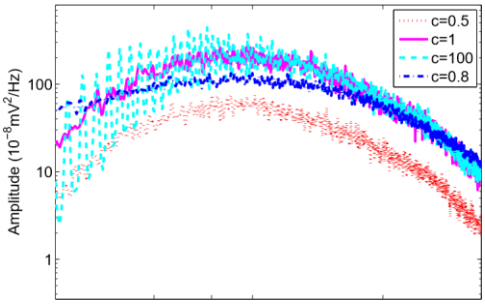

Fig. 11. PSD estimates for the simulations using c=0.5(dots), c=1(solid), c= 100(dashed) and c=0.8 (dot dash).

The change in RMS values in Figure 5 numerically show that when choosing a neuron number over 10,000 the extra neurons do not contribute significant power. Additional neurons do not have a significant contribution to the model due the extracellular filtering effects. Increasing the number of neurons places them further from the electrode. When the distance becomes too large their electric fields do not contribute to the recordings.

B. Analysis

Three different methods were used to analyse the MER data. These methods were used to build a comprehensive comparison between the patient and simulated recordings. The first order analysis, using the voltage distribution, demonstrates matching behavior of the probability distribution of voltage levels. The second order analysis, using the PSD, allows the correlation properties of the model and patient recordings to be analysed using different inter-spike interval statistics. The phase properties are used to verify the random phase assumption of a stochastic process.

1) Voltage Distribution: The KS test estimated the p-value for the null-hypothesis that voltage for the simulation and patient recordings are drawn from the same distribution. For all values of *c* the test statistic, *p*, was greater than 0.05. This means that for each *c* value on these series of data we cannot reject the null-hypothesis. However, using the KS test as a distance measure, we find that *c* = 0.8 has the closest distribution of voltage amplitudes to the patient data.

2) Power Spectral Comparisons: The linear regression of patient and simulated PSD, with Weibull shape factor, *c*, ranges from 0.8 to 100 give good agreement with the patient recordings. Assuming constant action potential shape between patients, the changes in inter-patient PSD estimates are indicative of changes in the ISI statistics. Qualitatively it was shown in Figure 7 that simulations with *c* = 0.8 has the most similar PSD to a patient recording. The 95% confidence interval is also plotted for five repeated recordings from the same patient. Figure 13 shows the linear regression of the PSD estimates for simulations using *c* = 0.8 against two different patients. This demonstrates the variation in patient recordings. For comparison, Figure 12 shows the regression of a patient PSD against white noise with equipment filtering effects described in section IB. This regression has a low

correlation coefficient, R^2= 0.0306, indicating that the noise of the patient recordings contains structure not adequately modelled by filtered white noise.

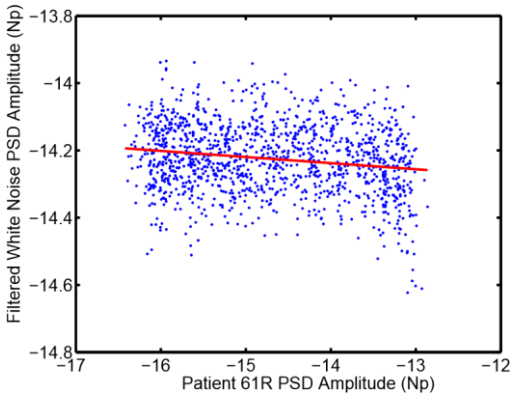

Fig. 12. Linear regression of the PSD of the P61R with white noise passed through the equipment filters. The regression line has the form y=−0.0182x−14.4920 with a correlation coefficient R^2=0.0306.

Variation in fits between the different patient's data sets can be explained by the fact that an "average" electrode impedance of 0.5 $M\Omega$ at 1kHz was used for the model. The impedance changes slightly for each patient [31]. This model could be used to improve the fit to individual patients by measuring the electrode impedance prior to recording.

3) Phase Properties: Since a stochastic process in time will have random phase, the phase information should show no synchrony between any frequency components. CSM values above 0.5 show a significant amount of phase synchrony across the recordings at a specific frequency [26]. Figure 10 shows there are no peaks above 0.3 in the CSM spectra for the patients or simulations with patients being slightly more variable. This indicates that there is no phase synchrony present in either the model or patient recordings verifying the stochastic assumption for MERs.

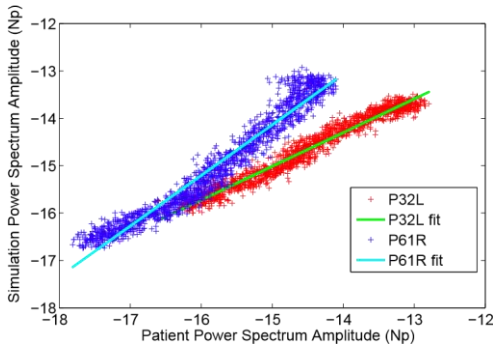

Fig. 13. Example of linear fits of the patient frequency power versus simulation frequency power for P32L (light) and P61R (dark).

The difference in the distribution of CSM peaks in the model can be explained by an additional white noise source in the patient recordings that isn't modeled. A white noise source would not affect the spectral colour, as it would add power across all frequencies, however it can add noise to the phase spectrum. This noise has a variance that scales with the amplitude of the source [26]. This could increase the CSM peaks that are not above the significance of 0.5 and would be spread across a wider frequency range than the simulation currently displayed.

C. Limitations and Future Work

Simplifications to an intractably complex physical system have been made to allow the model to be evaluated efficiently while still reproducing key features. The main underlying assumptions of the model are:

1) A homogeneous population of independent neurons, where all neurons fire with the same waveform, firing times with the same statistics and are treated as point sources. This means we only consider their far-field and do not consider their spatial morphology.
2) Isotropic filtering with distance, where the extracellular medium between the neurons and electrode has no spatial changes other than their radial distance to the electrode.
3) A fixed number of neurons contribute to the recordings. 4) Linear MER-neuron interaction dynamics.

These simplifications are used to make the inverse problem mathematically tractable. By fixing the number of sources and how they interact with the electrode there are less degrees of freedom in the model and hence less measurements are required to fit model parameters.

The simplification of the modeled system by parametrization improves the computational efficiency in simulating an MER but decreases the realistic features seen, described by [30] and the biological plausibility. One feature that can be seen in neurons that this model fails to reproduce is synchronization in the neural network. Although several network features can be modeled through the shape of the ISI probability, there is no ability for two or more neurons to fire synchronously or to have any firing correlations.

This model assumes a decoupling between the firing statistics and shape. The situation is more complicated, with the firing pattern driving changes in the action potential shape. The

prime example of this is a rate dependent action potential shape. This is where the shape of the action potential (both amplitude and frequency components) can change with the rate that the neurons fire [32]. If the target neuron displays rate dependent action potential shape, the model cannot account for this effect. Neurons that do display this behavior usually have two distinctive action potential types. One shape when the neuron is firing slowly and a sharp change to another other when the neuron is firing near its maximum rate [32]. Assuming the neuron only fires in a rate range, the effect of rate dependent action potential shapes can be minimized by approximating a single waveform over that range.

Synchrony may be present between neurons, even though both the simulations and patient recordings do not indicate any phase synchrony. This type of behavior is not present in the model due to the neurons being modeled as independent. The result by Lindner [33] also shows that the cross-correlation terms, when summing independent filtered renewal processes, do not affect the PSD. This means the relative timing between neurons will not affect the PSD. Future work will include neuron synchrony by including synchronous firing events as a second process with different statistics to the individual neurons ISI to investigate the effects on the time series. The assumption of stationary statistics could be replaced with a model of the basal ganglia that produces the instantaneous spike rate for the STN. The usefulness of this model in a clinical setting can also be found by finding the parameters of the model for patients undergoing different tasks.

To advance the model presented for use in a feedback controller, experiments are required that correlate the model parameters with the patient's physical state and how it changes with state. There is also a requirement for the loop to be closed by adapting the stimulation based on the parametric state and a reference. Methods such as PID or lead-lag controllers could be used in this step.

V. CONCLUSION

In this paper we have proposed an efficient model of an MER acquired from the STN during DBS implantation for PD. We have shown, on a set of 84 recordings from 14 patient hemispheres, that this MER model simulates recordings from patients, in terms of the voltage amplitude distribution, the power spectral estimates and phase synchrony. The model uses a top down approach that simulates the neural structure by synthesis of MERs.

The results indicate that a large number of neurons may contribute to the MER background activity and that there is information in this often-discarded noise. In our simulations background activity arises from “competition” between the filtering properties of the extracellular medium model and the electrode geometry. This noise was shown to be dependent on a model parameter that controlled the “shape” of the ISI time distribution (changing the firing patterns). Using values of the ISI times drawn from a Weibull distribution with a rate of 30*Hz* and a shape parameter of 0.8 corresponded to the best agreement with the patient data.

REFERENCES

1) T. Coyne, P. A. Silburn, R. Cook, P. Silberstein, G. Mellick, F. Sinclair, and P. Stowell. Rapid subthalamic nucleus deep brain stimulation lead placement utilising ct/mri fusion, microelectrode recording and test stimulation. Acta Neurochirurgica Suppl, 99:49–50, 2006.
2) J. McNames. Microelectrode signal analysis techniques for improved localization. In Z. Israel and K. J. Burchiel, editors, Microelectrode recordings in movement disorder surgery, volume 1. Thieme Medical Publishers, Inc., New York, 2004.
3) A. G. Rouse, S. R. Stanslaski, P. Cong, R. M. Jensen, P. Afshar, D. Ullestad, and T. J. Denison. A chronic generalizaed bi-directional brain-machine interface. J. Neural Eng., 8, 2011.
4) D. Terman, J. E. Rubin, A. C. Yew, and C. J. Wilson. Activity patterns in a model for the subthalamopallidal network of the basal ganglia. The Journal of Neuroscience, 7(22):2963–2976, 2002.
5) J. E. Rubin and D. Terman. High frequency stimulation of the subthalamic nucleus eliminates pathological thalamic rhythmicity in a computational model. Journal of Computational Neuroscience, 16:211–235, 2004.
6) X.-J. Feng, E. Shea-Brown, B. Greenwald, R. Kosut, and H. Rabitz. Optimal deep brain stimulation of the subthalamic nucleus: a computational study. J. Comput. Neurosci., 23:3265–282, 2007.
7) S. Santaniello, G. Fiengo, L. Glielmo, and G. Catapano. A biophysically inspired microelectrode recording-based model for the subthalamic nucleus activity in parkinson’s disease. Biomedical Signal Processing and Control, 3:203–211, 2004.

8) A. Snellings, O. Sagher, D. J. Anderson, and J. W. Aldridge. Identification of the subthalamic nucleus in deep brain stimulation surgery with a novel wavelet-derived measure of neural background activity. J Neurosurg, 111:767–774, 2009.

9) I. M. Garonzik, S. Ohara, S. E. Hua, and F. A. Lenz. Microelectrode techniques: Single-cell and field potential recordings. In Z. Israel and K. J. Burchiel, editors, Microelectrode recordings in movement disorder surgery, volume 1. Thieme Medical Publishers, Inc., New York, 2004.

10) Donald R. Humphrey and Edward M. Schmidt. Extracellular single-unit recording methods. 15, September 1990.

11) B. G. Bell, H. Fujisaki, J. M. Heinz, K. N. Stevens, and A. S. House. Reduction of speech spectra by analysis by synthesis techniques. J. Acoust. Soc. Am., 33(12):1725–1736, 1961.

12) Lyle N. Long and Guoliang Fang. A review of biologically plausible neuron models for spiking neural networks. AIAA InfoTech@Aerospace Conference, 23(Atlanta):3265–282, 2010.

13) B. H. Perkel, G. L. Gerstein, and G. P. Moore. Neuronal spike trains and stochastic point processes i. Biophys J., 7(4):391–418, 1967.

14) B. H. Perkel, G. L. Gerstein, and G. P. Moore. Neuronal spike trains and stochastic point processes ii. Biophys J., 7(4):419–440, 1967.

15) Joel Franklin and Wyeth Bair. The effect of a refractory period on the power spectrum of neuronal discharge. SIAM Journal of Applied Mathematics, 55(4):1074–1093, 1995.

16) E. Banta. A note on the correlation function of nonindependent, overlapping pulse trains. IEEE Transactions on Information Theory, 10(2):160–161, 1964.

17) E. E. F. McKeegan. Spontaneous and odour evoked activity in single avian olfactory bulb neurones. Brain Research, 929(1):48–58, 2002.

18) H. Cateau and A. D. Reyes. Relation between single neuron and population spiking statistics and effects on network activity. Physical Review Letters, 96(5):058101, 2006.

19) P. V. Theodosopoulos, R. S. Turner, and P. A. Starr. Electrophysiological findings in stn and snr. In Z. Israel and K. J. Burchiel, editors, Microelectrode recordings in movement disorder surgery, volume 1. Thieme Medical Publishers, Inc., New York, 2004.

20) C. Bedard and A. Destexhe. Macrascopic models of local field potentials and the apparent 1/f noise in brain activity. Biophysical Journal, 96:2589–2603, 2009.

21) C. Gold and et al. On the origin of extracellular action potential waveform: A modeling study. Journal of Neurophysiology, 95:3113–3128, 2006.

22) C. Bedard, H. Kroger, and A. Destexhe. Modeling extracellular field potentials and the frequency-filtering properties of extracellular space. Biophysical Journal, 86:1829–1842, 2004.

23) C.D. James, A.J.H. Spence, N.M. Dowell-Mesfin, R.J. Hussain, K.L. Smith, H.G. Craighead, M.S. Isaacson, W. Shain, and J.N. Turner. Extracellular recordings from patterned neuronal networks using planar microelectrode arrays. Biomedical Engineering, IEEE Transactions on, 51(9):1640–1648, sept. 2004.

24) Cameron C. McIntyre, Warren M. Grill, David L. Sherman, and Nitish V. Thakor. Cellular effects of deep brain stimulation:model-based analysis of activation and inhibition. The Journal of Neurophysiology, 91:1457–1469, 2004.

25) M. H. DeGroot. Probability and Statistics. Addison-Wesley, Boston, 1986.

26) J. Fridman, R. Zappulla, M. Bergelson, E. Greenblatt, L. Malis, F. Morrell, and T. Hoeppner. Application of phase spectral analysis for brain stem auditory evoked potential detection in normal subjects and patients with posterior fossa tumors. International Journal of Audiology, 23(1):99–113, 1984.

27) K. J. Weegink, J. J. Varghese, P. A. Bellette, Coyne, P. A. T., Silburn, and P. A. Meehan. An efficient stochastic based model for simulating microelectrode recordings of the deep brain. In Sabine Van Huffel, Carlos Correia, Ana Fred, and Hugo Gamboa, editors, Proceedings of Biosignals 2012, International Conference on Bio-Inspired Systems and Signal Processing. 5th International Joint Conference on Biomedical Engineering Systems and Technologies (BIOSTEC), pages 76–84, Vilamoura, Portugal, Ferbruary 2012.

28) MATLAB. version 7.10.0 (R2010a). The MathWorks Inc., Natick, Massachusetts, 2010.

29) Cameron C McIntyre, Susumu Mori, David L Sherman, Nitish V Thakor, and Jerrold L Vitek. Electric field and stimulating influence generated by deep brain stimulation of the subthalamic nucleus. Clinical Neurophysiology, 115(3):589–595, 2004.

30) D. M. Izhikevich. Dynamical Systems in Neuroscience. MIT Press, Cambridge, 2007.

31) Medtronic. Leadpoint user guide. Minneapolis, MN.

32) T. Heida, E. Marani, and K.G. Usunoff. The Subthalamic Nucleus: Modelling and simulation of activity. Part II. Advances in anatomy. Springer-Verlag Berlin Heidelberg, 2008.

33) B. Lindner. Superposition of many independent spike trains is generally not a renewal process. Physical Review E, 55:1074–1093, 2006.

Paper D - Bayesian Approach for Stationary Analysis of Microelectrode Recordings Using a Neural Mass Model of the Basal Ganglia

K. J. Weegink, J. J. Varghese, P. A. Bellette, P. A. Meehan and A. P. Bradley

ABSTRACT

Analysis methods in electrophysiology typically assume that over a short period of time the statistical distribution of inter-spike timing does not change. This assumption can be used even if the dynamics of the brain structure are changing in time. In this study, we investigate using a stationary distribution for analysis of subthalamic nucleus microelectrode recordings while the underlying statistics change. Microelectrode recordings are simulated using a neural mass model to generate the statistics. The neural mass model is driven using a sinusoidal input, a Weiner process and an Ornstein–Uhlenbeck process and the Weibull distribution is used to fit the statistics of the inter-spike intervals. It was found that stationary statistics fit the sinusoidal input, but are not predictive of the input. For the Weiner and Ornstein-Uhlenbeck processes the variance between repeated measurements of the Weibull shape parameter changes with changing parameters. We perform an analysis of experimental results to demonstrate the usefulness of these methods. This work shows that that properties of microelectrode recordings related to the distribution of inter-spike timing can be analyzed using a stationary model.

INTRODUCTION

How the neurons in the brain carry and encode information is one of the fundamental questions of neuroscience. There are several models how a neuron’s spikes could encode information [1]. One approach, temporal encoding, relies on the precise timing of spikes in relation to a stimulus or neighboring spike times [1]. This approach has been used successfully in Hebbian learning models and models of spike timing dependent plasticity{ref}. An alternate approach, developed using concepts from information theory,

attempts to characterize the spike train by using the statistical distribution of the time between spikes (inter-spike interval, ISI) [1]. One of the first hypotheses to adopt this approach was used by Adrian and Zotterman [2], where the first statistical moment, the firing rate, was used to characterize neuron activity in the presence of different stimuli. A problem with the rate hypothesis is that the ISI timing can vary while the same overall rate is produced. This means the rate alone cannot be used as a measure to always explain the neurons behavior and more sophisticated coding schemes are needed (R.B., et al., 2005). This variability can be characterized using the next statistical moment in the unitless form of the coefficient of variation, C_V, defined as the standard deviation of the ISI time divided by the mean ISI time [4]. The extension of analysis to measuring the C_V can describe the variability in ISI times and how they relate to the information capacity of a neuron [5]. As the understanding of the complexity of the signals increases Information Entropy can be used, which encodes all the statistical moments. These approaches where the signal is characterized by statistical moments of the ISI times can be described mathematically using renewal theory, where a fundamental assumption is that the distribution is stationary in time.

Decoding how neurons carry information is not just a question of philosophical but biological importance, as it can be used to create brain interfaces, characterize pathological processes or to diagnose disease {ref}. Detecting when a patient enters a diseased state would allow treatment to be tuned to when it is needed, a prime example of this is deep brain stimulation (DBS) where treatment is moving towards intelligent systems that use adaptive stimulus [6] [7] [8] [9]. This type of treatment could reduce side effects and improve the effectiveness of the treatment.

The basal ganglia (BG) is a closed neural system that has been highly studied with applications for the treatment of movement disorders such as Parkinson's disease [10]. An increase in treatment of Parkinson's disease using DBS has increased access to electrical recordings of neuron activity of the BG and allowed an opportunity to bridge the theories of neural coding to application. These *in vivo* recordings, known as microelectrode recordings (MER), contain electrical spikes caused by activation of neurons surrounding the electrode tip [10] [11]. These types of recordings can be analyzed by locating the timing of spikes or looking at the statistics of their ISI. The ISI statistics of these recordings are fundamentally non-stationary due to the dynamic nature of the brain structures involved (Theodosopoulos, et al., 2004). For instance, the patient may not be in the same condition while performing

the same task for each recording, or the length of the recording may be longer than the time for a patient to perform a task (Theodosopoulos, et al., 2004).

To capture the dynamics causing the non-stationary behavior of the statistics, the neural structures of the BG are modelled. The subthalamic nucleus (STN), a common structure targeted using MERs, has on the order of 10^5 neurons, where each neuron can be described using a multi-variable non-linear partial differential equation (PDE). In addition to inter-nucleus connections the neurons are also highly connected to surrounding structures in the brain. This connectivity leads to an extremely large number of states to model, a problem when modelling parts of the brain as a dynamical system. When modelling these complex system, to reduce the size of this state space, a neural field model can be used [5]. These models reduce a highly-interconnected structure of the brain into the time evolution of the distribution of firing times throughout the structure which is described by a non-linear PDE. These field models can be expanded into the distribution's moments, giving a second order ordinary differential equation for each moment. Basal ganglia field models of the first moment, the mean firing rate, have been developed [5]. These models have been used with great success for analysis of movement disorders that are treated with DBS [11] [12] [13]. The advantage of these models is to reduce the high dimensionality of the state space down to two states per brain structure, the mean firing rate and the rate of change of the firing rate.

Previous models have been successful in modelling MERs using stationary statistics and renewal theory, with good quantitative agreement to experimental data [6] [7]. In this article, we extend these types of MER simulations to include non-stationary behavior by modelling the dynamic nature of underlying structures within the brain and their effect on the firing statistics. We repeatedly fit a stationary multivariate ISI time distribution, the Weibull distribution, to the simulated MERs to determine how well the fundamentally non-stationary behavior can be approximated by using renewal theory. This type of approximation is explored as it could allow easier analysis of MERs produced by a complex system evolving in time, with potential applications in patient monitoring and adaptive DBS.

METHODS

The type of MER recordings modeled are interoperative STN recordings taken during implantation of a DBS pacemaker to treat Parkinson's disease as described in [8]. The model consists of two parts; a series of differential equations that describes the average

rates of the groups of neurons in the different nuclei and a filtered point process to describe the electrical output of the STN as measured by the MER. The neural mass model of the cortex and basal ganglia derived from [5]. The filtered point process to producing the microelectrode recordings follow the methodology in [6].

Basal Ganglia model

For the neural mass model the classical direct-indirect pathway model of the basal ganglia is used (Figure 21) [14]. This involves modelling the cortex with excitatory (Glutamate) projections into the D1 and D2 cells in the striatum. From the straitum D1 cells inhibit the globus palidus internal (GPi). The D2 cells inhibit the globul palidus external (GPe), which in turn inhibits the STN. The STN then has excitatory projections into the GPi. The GPe has inhibitory (GABA) projections into itself and the GPi. The STN also has excitatory connections into itself and the GPe. The GPi then projects into the thalamus and the brainstem, but this feature is not included in this paper. This seemingly simple model is successful at describing the pathophysiological processes, such as those involved in Parkinson's Disease [14] [15] [16].

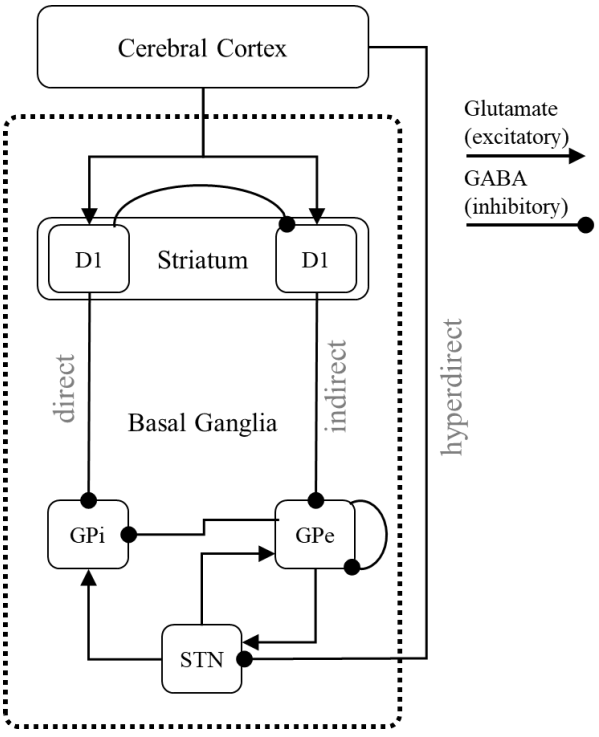

Figure 61 - Direct and indirect pathways in the Basal Ganglia

In the neural field model each of the various nuclei are modelled by using the Fokker-Plank equation to describe how the distribution of firing probabilities for a given group of neurons and how they evolve over time [15]. These equations can be simplified by performing a first

order expansion about the statistical moments, resulting in a system of ordinary differential equations which describes their average firing rate for a body of neurons given by:

$$\dot{\mu_v} = y_v \tag{53}$$

$$\dot{y_v} = ab\left[\sum_n \alpha_{vn}\zeta(\mu_n(t-\tau_{vn})) - \left(\frac{1}{a}+\frac{1}{b}\right)y_v - \left(\frac{1}{ab}\right)\mu_v\right] \tag{54}$$

$$\zeta(\mu_v) = \frac{S_{max}}{1+e^{k(\theta-\mu_v)}} \tag{55}$$

where y_v is a dummy variable used to represent the second order system as a first order, μ_v is the mean voltage of the target nuclei, α_{vn} is the strength of coupling from the nuclei n to the target and τ_{vk} is the axonal propagation delay, S_{max} is the maximum firing rate of the target, a is the decay time constant of the membrane and b is the rise time constant, θ is the potential that gives half the maximum firing rate and k controls the slope of the sigmoid to give realistic rates for a given input potential.

Equation 2 introduces the delays caused by axonal propagation between structures. The delays increase the time for a numerical solution. When the delays are small compared to the characteristic times of the dynamics the system can be approximated using perturbation analysis. All the delays are passed through the sigmoid function; therefore, we can perform a Taylor expansion and truncate insignificant terms. We can first perform an expansion around t:

$$\zeta\big(\mu_v(t-\tau)\big) = \zeta\big(\mu_v(t)\big) + (t-\tau-t)\frac{d\zeta\big(\mu_v(t)\big)}{dt} + \frac{(t-\tau-t)^2}{2!}\frac{d^2\zeta\big(\mu_v(t)\big)}{dt^2} + O(\tau^3) \tag{56}$$

$$\zeta\big(\mu_v(t-\tau)\big) = \zeta(\mu_v) - \tau\zeta'(\mu_v)\frac{d\mu_v}{dt} + \frac{\tau^2}{2!}\left[\zeta'(\mu_v)\frac{d^2\mu_v}{dt^2} + \zeta''(\mu_v)\left(\frac{d\mu_v}{dt}\right)^2\right] + O(\tau^3) \tag{57}$$

where $\zeta'(\mu_v(t))$ denotes the derivative with respect to μ_v and has been introduced into the equations using the chain rule and for convenience $\mu_v(t)$ is written as μ_v. Considering the faster time constant, membrane potential gain, is on the order of 2 ms, the τ^2 term is very small in comparison. This allows us to neglect terms $O(\tau^2)$ and substituting into the dynamics for the neural structures yields a nonlinear first order differential equation:

$$\dot{y_v} = ab\left[\sum_n \alpha_{vn}(\zeta(\mu_n) - \tau_{vn}\zeta'(\mu_n)y_n) - \left(\frac{1}{a} + \frac{1}{b}\right)y_v - \mu_v\right] \quad (58)$$

This linearization decreases the time for a numerical solution which allows large numbers of simulations to be performed. The large number of simulations allows production of a large sample of the statistics using random processes for cortical simulation. It also allows Monte Carlo simulations to be performed for analysis of the system. Using the linearized delay for solving the system over 5 s, using a fixed time step (1 ms) and a random cortical input decreased the solver time to 3.7±0.4 s from 51±11s for the full system.

Table 7 - TIME PERFORMANCE AND ERROR USING THE FULL BG MODEL, ZEROTH ORDER AND FIRST ORDER APPROXIMATIONS.

Model	Solver time (s)	Maximum Error (%)
With delays	51±11	0
Without delays	3.1±0.5	0.18
Linearized delay	3.7±0.4	0.07

The decreased computational time is only advantageous if the numerical solution is accurate. Comparing the solution of the linearized delays to the solution without delays allows us to validate the accuracy of the linearized approximations of the model. Figure 49 shows the absolute error for the simulations using zero-time delay and the first order approximation. The maximum error fraction compared to the model with full delays for the simulation without delays was $1.8e^{-3}$ and using the first order approximation the error reduced to $2.677e^{-4}$. The error level for the first order approximation is acceptable for simulating the MER, while significantly increasing the time to for a simulation.

Microelectrode Model

The microelectrode recording used to estimate the state of the STN is simulated using methods following the models described in [5] [6]. The electrical activity of the STN is generated by simulating the firing times for 10000 neurons, distributed homogenously around the electrode with a density of neurons in the STN, 10^5 cm^{-3}, using an inhomogeneous Poisson process. The Poisson process is a special type of renewal process where the firing times of the neurons are completely independent of each other, resulting in ISI times being exponentially distributed. The Poisson process can be extended to have a rate parameter as a function of time. This type of Poisson process is an inhomogeneous Poisson process. The Cox process, also known as doubly Poisson, is a special type of inhomogeneous Poisson process where the rate parameter is stochastically distributed. It

has been shown that the firing times of the non-stationary Cox process can also be modelled using a stationary Weibull distribution. In [5] it was found the Weibull distribution could also be used to model ISI times of interoperative patient MERs.

The instantaneous Poisson firing rates of the neurons (ν) are now drawn from the neural mass model rate at each time using equation 8 to determine if there is at least one spike in the sampling time. We can consider the probability of N spikes in the time window since neurons have a refractory period which prevents them from successive firing in short intervals. The basal ganglia model is sampled at 24kHz ($\delta t = 41.6\mu s$); the recording frequency of the MER. The instantaneous rate is then used to determine if a given neuron has fired at that time using:

$$P(N = n) = \frac{(\nu\delta t)^n}{n!} e^{\nu\delta t} \tag{59}$$

$$P(N \geq 1) = 1 - P(N = 0) = 1 - e^{\nu\delta t} \tag{60}$$

As the firing times are generated for each neuron, an action potential wave form is generated using the Hodgkin and Huxley model from Rubin et al [7]. To model the extracellular fluid the spike trains are filtered according to the distance of each neuron to the electrode [8]. The signal generated is then passed through filters to simulate the acquisition hardware, with the addition of white noise, to simulate an MER [5].

Stationary Analysis

To analyze the signals generated by the MER simulations we model the spike trains generated as renewal processes. For a renewal process the ISI times are independently drawn from a single probability distribution that does not change in time.

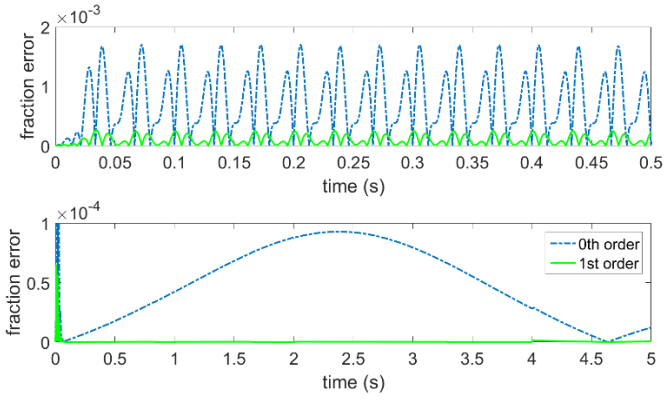

Figure 62 - absolute error compared to the full model without delays for 0th and 1st order delay approximations for a) sinusoidal cortical input, B) linearly increasing cortical input

We fit the ISI distributions over multiple simulations, with randomized initialization, to see if the fitting parameters are reproducible.

Modelling the ISI times (t) as independent events drawn from a Weibull distribution, shown in equation 9 (where k is the shape parameter and λ is the scale), can capture common firing patterns of neurons (ranging from bursting to Poisson to periodic), as shown in [5].

$$f(t;\lambda,k) = \frac{k}{\lambda}\left(\frac{t}{\lambda}\right)^{k-1} e^{-\left(\frac{t}{\lambda}\right)^{k}} \quad , \ \forall \ t > 0 \tag{61}$$

The coefficient of variation is a normalized metric of the spread of neural firing times [4]. The coefficient of variation (C_v) of the Weibull distribution can also be fully described using only the shape parameter:

$$C_v = \frac{\sigma}{\bar{\mu}} = \frac{\sqrt{\Gamma\left(1+\frac{2}{k}\right) - \Gamma\left(1+\frac{1}{k}\right)^2}}{\Gamma\left(1+\frac{1}{k}\right)}, \tag{62}$$

where $\Gamma(\ \ )$ is the gamma function, $\bar{\mu}$ is the mean ISI time and σ is the standard deviation of ISI times. Because the coefficient of variation is a common metric for neural recordings and can be entirely described using the Weibull shape parameter, we fit the Weibull distribution shape parameter to simulated MERs. To find the shape parameter we take the power spectral density of the simulated MER using Welch's method with five non-overlapping rectangular windows. The power spectral density is then fit to Eqn. 11 using least squares to the predicted power spectrum with the Marquardt-Levenberg algorithm. The predicted power spectrum of a renewal process ($P(\omega)$) is given by [9]:

$$P(\omega) = A \cdot G(\omega)\left[1 + Re\left\{\frac{H(\omega,k)}{1 - H(\omega,k)}\right\}\right], \qquad \forall \ \omega > 0 \tag{63}$$

where $G(\omega)$ is the action potential power spectrum including extracellular filtering, $H(\omega,k)$ is the characteristic function of the Weibull distribution for shape parameter k, and A is a scaling factor that accounts for factors that contribute to the total power; the rate of firing, the number of neurons contributing to the signal and the distance of the neurons to the electrode. The factor A creates a degeneracy between the rate, neuron distance and number of neurons. This degeneracy causes the rate parameter found with the least squares fit to not accurately represent the rate used for the simulation. However, because the coefficient of variation is defined in terms of only the shape parameter the rate parameter may not be important in characterizing the ISI distribution for the neural signals analyzed.

Simulations

To simulate MER recordings, we need to know the cortical input to the model and what length of time is required for the analysis. The cortical input for the BG model can vary

depending upon the patient state and task being performed. Due to the ability of this input to change in a non-deterministic way [21] [22] [23], we choose to look at how the model responds to specific classes of functions. We explore whether the stationary Weibull distribution can be used to consistently numerically characterize fundamentally non-stationary processes, specifically, four different cortical inputs ($\mu_{ctx}(t)$, shown in Figure 22) are used; sinusoidal ($\mu_{ctx}(t) = C + B[\sin(Dt)]$), where B and D are varied, a Weiner process ($\frac{d\mu_{ctx}}{dt} = DW_t$), where D is varied and an Ornstein–Uhlenbeck (O-U) process ($\frac{d\mu_{ctx}}{dt} = -\frac{1}{\tau}\mu_{ctx} + DW_t$) where τ is varied. These functions are chosen as they represent a deterministic process, a Gaussian process, and a Gauss-Markov process respectively.

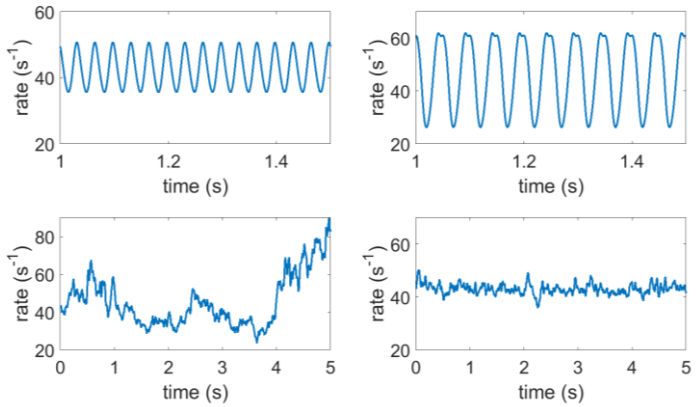

Figure 63. example STN rate evolution using different cortical inputs a) Varying the sinusoidal frequency, B) Varying the sinusoidal amplitude to the point that the non-linearities begin to affect the system C) varying the Diffusion constant of a Weiner process and D) varying the correlation time of a damped weiner process.

To validate the methodology of using the Weibull distribution to characterize the ISI distribution for finite time length recordings, small sets of ISI times are generated that make different length recordings. The shape parameter is then fitted using the time series and the spectral methods described above.

To determine the shape parameter, many spikes need to have occurred to build up a representative sample of the ISI distribution. This means that the recordings need to run for a certain length before there are enough spikes to build up an

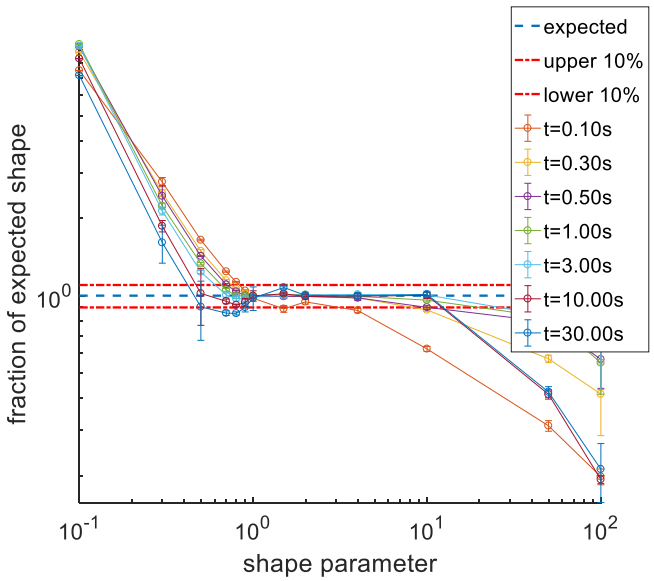

Figure 64 - Accuracy of Weibull shape prediction from 1000 MER simulations of varying time length.

estimate of the statistics. To determine what length of simulation is required, and hence what length of patient recording would be needed, simulations were produced drawing the firing times from a stationary distribution. The shape parameter was then determined from the simulation. This was repeated 1000 times for 13 shape parameters. Figure 42 shows that over the expected range of shape values, 0.5 to 10, that a 3-10s recording is needed. For the rest of the study 5s recordings are simulated to allow a large range of valid shape parameters.

RESULTS

In this section, we present the results from fitting stationary statistics for the ISI times to different numerical simulations of MERs with time dependent statistics. To validate the methods used, we fit MERs that have been generated using a Cox process. The results from the four different cortical inputs tested are then shown.

To look at how non-stationary statistics can be modeled using a stationary distribution, MERs were simulated using a Cox process to generate ISI times. By fitting the expected power spectrum of Weibull ISI statistics to the power spectrum it was found that as the Cox parameter is increased, the average value of the Weibull shape parameter increased. It also shows the variance of the fit, over 300 simulations, increased with the Cox parameter, Figure 50 shows these results.

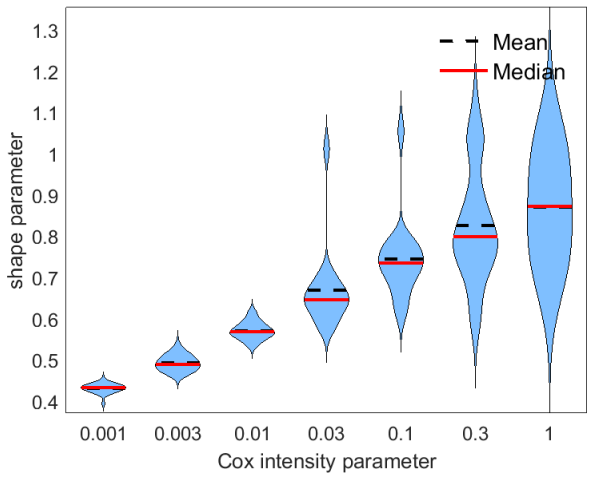

Figure 65 - distribution of fitted shape parameters over 100 simulations for different cox process intensity parameters. as the intensity parameter increases the shape parameter increases. The variance in fitting the shape parameter also increases.

For the neural mass model, the cortical input was first modeled using a stochastic input, the Weiner process. It can be seen in Figure 51 that the diffusion parameter has no effect on the expected shape parameter. There was an increase in the variance of the fitted shape value as the diffusion parameter increased. Adding in a correlation time to the Weiner process creates an O-U process. Using a fixed diffusion parameter of 30, the variance decreases as the correlation parameter is increased, see Figure 52.

The cortical input was then changed to a sinusoid to mimic the oscillations common in the cortex. The frequency of oscillations was varied with a fixed rate of 1 Hz and an offset of 14 Hz. Figure 53 shows that varying the frequency of oscillations has no effect on the predicted shape parameter. Next, fixing the frequency at 20 Hz and varying the amplitude has no effect on the predicted shape parameter, as seen in Figure 54.

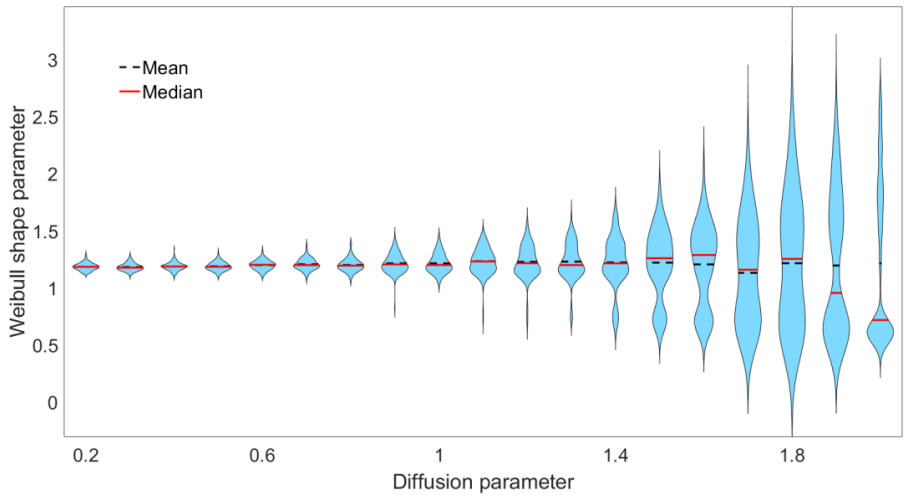

Figure 66 distribution of fitted shape parameters over 300 simulations for different diffusion parameters in a weiner process. as the diffusion parameter increases there is no affect on the shape parameter. the variance increases significantly as the diffusion parameter is increased.

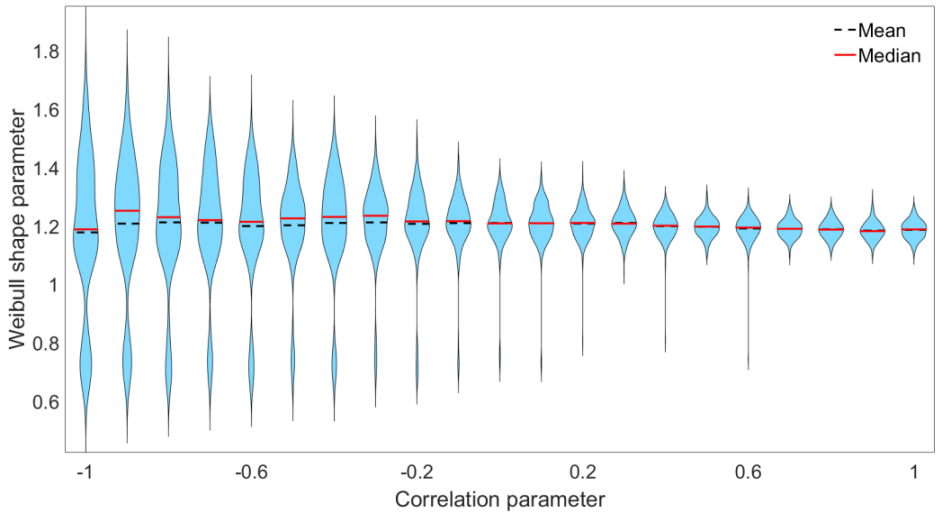

Figure 67 - distribution of fitted shape parameters over 300 simulations for different correlation parameter in a Ornstein–Uhlenbeck process. the variance is large for small correlation parameters and reduces as the parameter is increased.

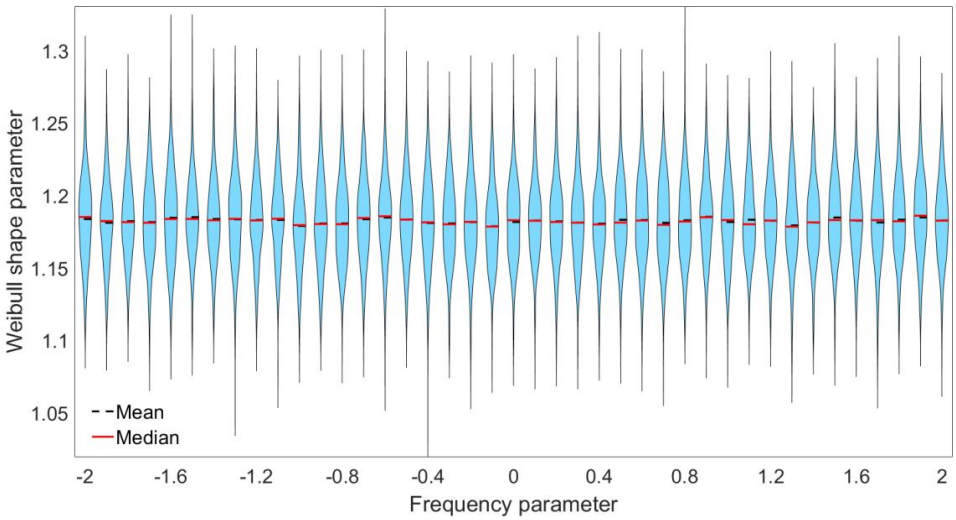

Figure 68 - distribution of fitted shape parameters over 300 simulations for different frequency sinusoidal cortical inputs. there is no significant change in the shape parameter or variance of the fits.

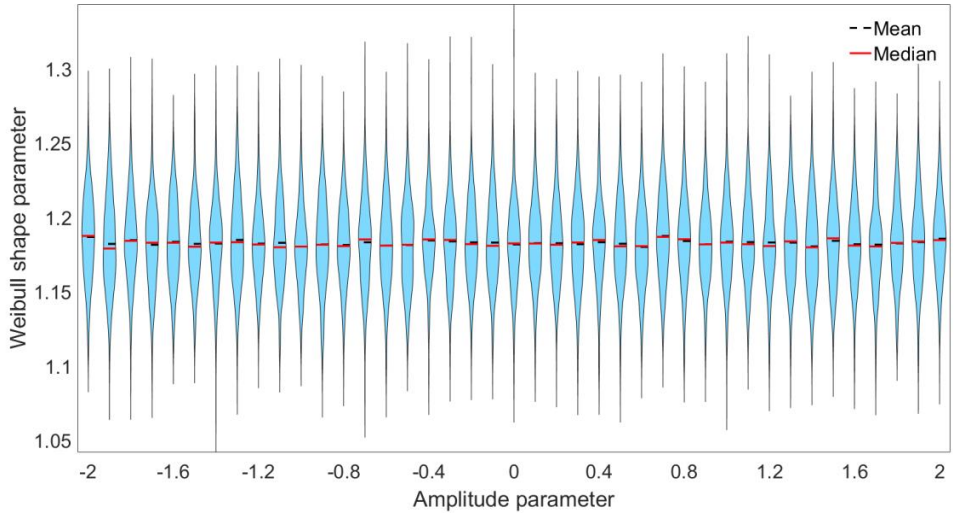

Figure 69 - distribution of fitted shape parameters over 300 simulations for different amplitude sinusoidal cortical inputs. there is no significant change in the shape parameter or variance of the fit

DISCUSSION

To determine the usefulness of the stationary analysis presented we have two criteria to determine. First, does the fitted Weibull shape parameter vary over repeated simulations for the same input parameter. Second, can the Weibull shape parameter be used as a predictor of the input parameter. We will look at the first criteria and determine how well the stationary approximation is for the non-stationary MER simulations. We then address the second criteria by an example using the experimental result from [5].

The results show that the Cox process rate parameter is correlated with the shape parameter determined from the power spectrum. This result is expected based on the results of [10] and along with Figure 42 validates the method for finding the shape parameter. Based on Figure 42, a simulation time was chosen that would result in approximately 10% variance in the Weibull shape parameter, however when the Cox parameter was increased past 0.1 the variance of the fit increased beyond 10%. This result indicates that the non-stationary nature of the Cox process over the time length of the simulation is introducing variance of the shape parameter that cannot be accounted for using a stationary model.

For every parameter in both sinusoidal inputs the variance in the fit of the shape parameter was less than 10%. This level of variance can be explained by the finite length of the recordings simulated. This shows that the stationary model can describe the ISI times generated given a sinusoidal input. However, the mean value and variance of the shape

parameter does not change when varying the input parameters. This prevents the shape parameter from being used as a predictor of sinusoidal cortical input parameters.

In both the Weiner and O-U simulations the variance of the shape parameter increased more than can be explained due to the finite length or the recording. This result indicates that different realizations of the simulation using the same input produces different distributions of ISI times. Although the first criteria, the variance of the fitted shape parameter, of describing the simulations using a stationary distribution fails for certain parameter values, it does not prevent the fits from being used as a predictor of the cortical state.

To look at how the shape parameter could be used to characterize the cortical input we can look at the O-U processes. From the simulations, we can construct a 2D histogram of Weibull shape given a specific cortical parameter, Figure 55 shows an example of this for the O-U process using the logarithm of the correlation parameter, $\log \tau^{-1}$. This distribution of counts is equivalent to the probability of measuring a shape parameter, λ, giving a correlation parameter, $P(\lambda | \log \tau^{-1})$. If we assume *a priori* knowledge that the cortical input follows an O-U process, then we can use Bayes Theorem to determine the correlation parameter given a measurement of the shape parameter using:

$$P(\log \tau^{-1} | \lambda) = \frac{P(\lambda | \log \tau^{-1}) P(\log \tau^{-1})}{P(\lambda)} \qquad (64)$$

To use this formula $P(\lambda)$ and $P(\log \tau^{-1})$ are required. $P(\lambda)$ can be estimated from the simulations by summing over the correlation parameter to get the total number of counts for a given λ and dividing by the total number of simulations. Without experiments to determine $P(\log \tau^{-1})$ an uninformative prior can be used. Assuming some form of exponentially distributed parameter, one such uninformative prior that can be used is Jeffery's prior, which gives a uniform distribution when normalized for $P(\log \tau^{-1})$ over a constrained range. For an example if we assume the logarithm of correlation parameter is uniformly distributed between -1 and 1 we can produce Figure 56 using equation 12.

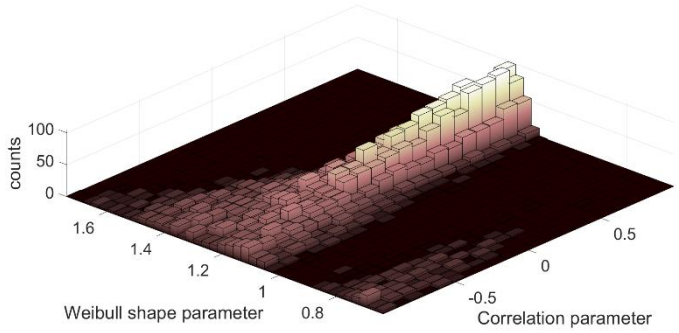

Figure 70 - probability of finding a specific Weibull shape parameter when given an OU process coritcal input with a given correlation parameter.

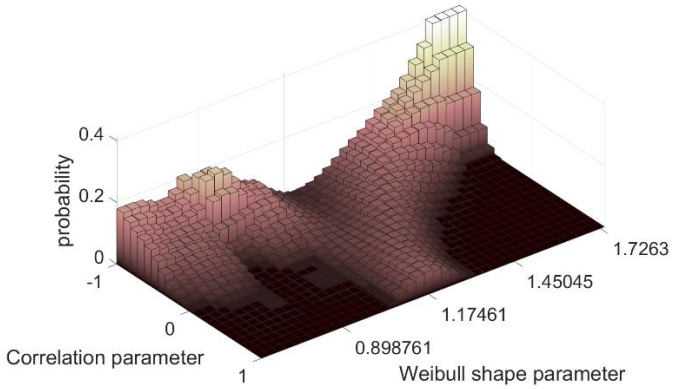

Figure 71 - probability of a cortical input with a given correlation parameter given a measured Weibull shape parameter.

We can apply the methods presented here to the experimental result given in [5]. It was found that a using a renewal model a Weibull shape parameter of 0.8 best fit interoperative patient recordings in a resting state. Using the analysis method presented above we can calculate the *posteri* estimate, $\mathcal{L}(x;\lambda = 0.8)$, for the different types of cortical parameters we have modeled. By calculating $P(x|\lambda = 0.8)$ for each of the cortical inputs and finding the maximum gives $\mathcal{L}(x;\lambda = 0.8)$. The sinusoidal inputs produce no variation in λ which means the parameters for them cannot be estimated. For the Wiener and O-U processes $P(x|\lambda = 0.8)$ was found, giving Figure 57. The maximum of the *posteri* estimate for the Diffusion parameter is $\mathcal{L}(D;\lambda = 0.8) = 10^{1.6} = 39.81s^{-1}$ and for the correlation parameter $\mathcal{L}(\tau^{-1};\lambda = 0.8) = 10^{-1} = 0.1s^{-1}$.

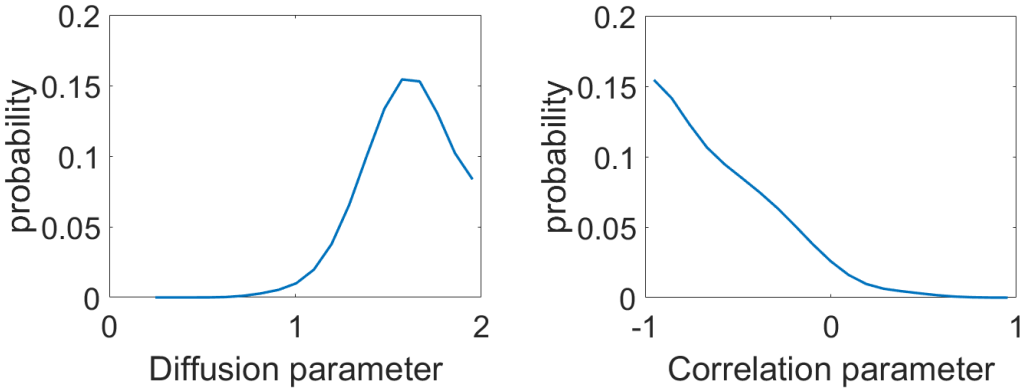

Figure 72 - Probability of a cortical parameter using a measured Weibull shape parameter of 0.8. (a) $P(logD|\lambda = 0.8)$ and (B) $P(log\tau^{-1}|\lambda = 0.8)$.

The estimate of the cortical parameters (x) can be improved by using multiple independent measurements of λ, and applying the Bayes Theorem recursively:

$$P(x|\lambda_1, \dots, \lambda_{N-1}, \lambda_N) = \frac{P(\lambda_N|x)P(x|\lambda_1, \dots, \lambda_{N-1})}{P(\lambda_N)} \quad (65)$$

Applications of this to a smart device could also involve improving the state estimate, $P(x)$, by incorporating the measurements into a Kalman filter.

This analysis involves assumptions on the dynamics of the cortical input to constrain the probability distributions. The assumptions used are not necessarily realistic, but have been chosen to allow an example of how estimation of the input parameter would be performed.

To extend this work for practical applications, such as feedback control, investigating different models of cortical input by either including the dynamics of interactions between the motor cortex and the thalamus, or recording activity from patients performing different tasks could be used.

CONCLUSION

It was found that stationary statistics fit the sinusoidal input, but cannot be used as a predictor for the input parameters. For the Weiner and Ornstein-Uhlenbeck processes the variance between repeated measurements changes with changing parameters. It was shown that this changing variance can be used to predict the most likely values of the input parameters. This work shows that that properties of microelectrode recordings related to the distribution of inter-spike timing can be analyzed using a stationary model for certain cases of time varying dynamics.

REFERENCES

[1] W. Bialek, D. Warland and R. d. R. v. Steveninck, Spikes Exploring the Neural Code, Cambridge MA, US: The MIT Press, 1999.

[2] E. Adrian and Y. Zotterman, "The impulses produced by sensory nerve endings: Part II: The response of a single end organ," *J Physiol (Lond.),* vol. 61, pp. 151-171, 1926.

[3] S. R.B., G. E.R. and J. K.E., "Neuronal variability: noise or part of the signal?," *Nat. Rev. Neurosci.,* vol. 6, no. 5, pp. 389-397, 2005.

[4] H. C. Tuckwell, "Synaptic transmission in a model for stochastic neural activity," *Journal of Theoretical Biology,* vol. 77, no. 1, pp. 65-81, 1979.

[5] D. M. MacKay and W. S. McCulloch, "The limiting information capacity of a neuronal link," *The bulletin of mathematical biophysics,* vol. 14, no. 2, pp. 127-135, 1952.

[6] A. Priori, G. Foffani, L. Rossi and S. Marceglia, "Adaptive deep brain stimulation (aDBS) controlled by local field potential oscillations," *Experimental Neurology,* vol. 245, pp. 77-86, 2013.

[7] S. Little, A. Pogosyan, S. Neal, B. Zavala, L. Zrinzo, M. Hariz, T. Foltynie, P. Limousin, K. Ashkan, J. FitzGerald, A. L. Green, T. Z. Aziz and P. Brown, "Adaptive deep brain stimulation in advanced Parkinson disease," *Ann. Neurol.,* vol. 74, pp. 449-457, 2013.

[8] K. Hosain, A. Kouzani and S. Tye, "Closed loop deep brain stimulation: An evolving technology," *Australas Phys. Eng. Sci. Med.,* vol. 37, pp. 619-634, 2014.

[9] A. G. Rouse, S. R. Stanslaski, P. Cong, R. M. Jensen, P. Afshar, D. Ullestad and T. J. Denison, "A chronic generalized bi-directional brain-machine interface," *J. Neural Eng.,* vol. 8, 2011.

[10] C. A. Davie, "A review of Parkinson's disease," *Br. Med. Bull. ,* vol. 86, no. 1, pp. 109-127, 2008.

[11] D. Humphrey and E. M. Schmidt, "Extracellular Single-Unit Recording Methods," in *Neurophysiological Techniques*, Humana Press, 1990, pp. 1-64.

[12] I. M. Garonzik, S. Ohara, S. E. Hua, F. A. Lenz, Z. Israel and K. J. Burchiel, "Microelectrode techniques: Single-cell and field potential recordings," in *Microelectrode Recordings in Movement Disorder Surgery*, New York, NY, USA, Thieme Medical, 2004.

[13] P. V. Theodosopoulos, R. S. Turner, P. A. Starr, Z. Israel and K. J. Burchiel, "Electrophysiological findings in STN and SNR," in *Microelectrode Recordings in Movement Disorder Surgery*, New York, NY, USA, Thieme Medical, 2004.

[14] S. J. v. Albada and P. A. Robinson, "Mean-field modeling of the basal ganglia-thalamocortical system. I Firing rates in healthy and parkinsonian states," *Journal of Theoretical Biology,* vol. 257, pp. 642-663, 2009.

[15] S. J. v. Albada, R. T. Gray, P. M. Drysdale and P. A. Robinson, "Mean-field modeling of the basal ganglia-thalamocortical system. II Dynamics of parkisonian oscillations," *Journal of Theoretical Biology,* vol. 257, pp. 664-688, 2009.

[16] C. Liu, Y. Zhu, F. Liu, J. Wang, H. Li, B. Deng, C. Fietkiewicz and K. A. Loparo, "Neural mass models describing possible origin of the excessive beta oscillations correlated with Parkinsonian state," *Neural Networks,* vol. 88, pp. 65-73, 2017.

[17] K. J. Weegink, P. A. Bellette, J. J. Varghese, P. A. Silburn, P. A. Meehan and A. P. Bradley, "A Parametric Simulation of Neuronal Noise From Microelectrode Recordings," *IEEE Transactions on Neural Systems and Rehabilitation Engineering,* vol. 25, no. 1, pp. 4-13, 2016 .

[18] L. A. Camunas-Mesa and R. Q. Quiroga, "A Detailed and Fast Model of Extracellular Recordings," *Neural Computation,* vol. 25, pp. 1191-1212, 2013.

[19] T. Coyne, P. A. Silburn, R. Cook, P. Silberstein, G. Mellick, F. Sinclair and P. Stowell, "Rapid subthalamic nucleus deep brain stimulation lead placement utilising CT/MRI fusion microelectrode recording and test stimulation," *Acta Neurochirurgica Suppl.,* vol. 99, pp. 49-50, 2006.

[20] G. Deco, V. K. Jirsa, P. A. Robinson, M. Breakspear and K. Friston, "The Dynamic Brain: From Spiking Neurons to Neural Masses and Cortical Fields," *PLoS Computational Biology,* vol. 4, no. 8, pp. 1-35, 2008.

[21] J. E. Rubin and D. Terman, "High frequency stimulation of the subthalamic nucleus eliminates pathological thalamic rhythmicity in a computational model," *J. Computational Neurosci.,* vol. 16, pp. 211-235, 2004.

[22] C. Bedard and A. Destexhe, "Macrascopic models of local field potentials and the apparent 1/f noise in brain activity," *Biophys. J.,* vol. 96, pp. 2589-2603, 2009.

[23] E. Banta, "A note on the correlation function of nonindependent overlapping pulse trains," *IEEE Trans. Inform. Theory,* vol. 10, no. 2, pp. 160-161, 1964.

[24] J. Brittain and P. Brown, "Oscillations and the basal ganglia: Motor ontrol and beyond," *Neuroimage,* vol. 85, pp. 637-647, 2014.

[25] A. A. Kuhn, F. Kempf, C. Brucke, L. G. Doyle, I. Martinez-Torres, A. Pogosyan, T. Trottenberg, A. Kupsch, G. H. Schneider, M. I. Hariz, W. Vandenberghe, B. Nuttin and P. Brown, "High-frequeny stimulation of the subthalamic nucleus suppresses oscillatory activity in patiens with parkinson's disease in parallel with improvement in motor performance," *Journal of Neuroscience,* vol. 28, pp. 6165-6173, 2008.

[26] A. C. Marreiros, H. Cagnan, R. J. Moran, K. J. Friston and P. Brown, "Basal ganglia-cortical interactions in Parkinsonian patients," *Neuroimage,* vol. 66, pp. 301-310, 2013.

[27] N. Yannaros, "Weibull Renewal Processes," *Ann. Inst. Statist. Math,* vol. 46, no. 4, pp. 641-648, 1994.